UNIVERSITY OF CALIFORNIA

Santa Barbara

Optimizing Soft and Stretchable Electronics Made with Novel Polymers through Predictive Modeling

A dissertation submitted in partial satisfaction of the requirements for the degree

Doctor of Philosophy in Materials

by

Veronica Gail Reynolds

Committee in charge:

Professor Michael L. Chabinyc, Committee Chair

Professor Christopher M. Bates

Professor Craig J. Hawker

Professor Megan T. Valentine

March 2022

The dissertation of Veronica Gail Reynolds is approved.

Megan T. Valentine

Craig J. Hawker

Christopher M. Bates

Michael L. Chabinyc, Committee Chair

February 2022

Optimizing Soft and Stretchable Electronics Made with Novel Polymers through Predictive Modeling

by

Veronica Gail Reynolds

ACKNOWLEDGEMENTS

To my family, for their love and support.

VITA OF VERONICA GAIL REYNOLDS

March 2022

Education

University of California, Santa Barbara | 2017 – 2022
Doctor of Philosophy in Materials

Columbia University | 2010 – 2014
Bachelor of Science in Materials Science and Engineering

Publications

1. Self, J. L., **Reynolds, V. G.**, Blankenship, J., Mee, E., Guo, J., Albanese, K., Xie, R., Hawker, C. J., Read de Alaniz, J., Chabinyc, M. L., Bates, C. M. "Soft Carbon Nanotube Composites with Bottlebrush Polymer Networks for Compliant Electrodes." *ACS Polymers Au* 2, 1: 27–34 (2021)

2. Nie, H.*, Schauser, N. S.*, Self, J. L., Tabassum, T., Oh, S., Geng, Z., Jones, S., Zayas, M. S., **Reynolds**, **V. G.**, Chabinyc, M. L., Hawker, C. J., Han, S., Bates, C. M., Segalman, R. A., and Read de Alaniz, J. "Light-Switchable and Self-Healable Polymer Electrolytes Based on Dynamic Diarylethene and Metal Ion Coordination." *Journal of the American Chemical Society* 143, 3: 1562–1569 (2021) * Equal contribution

3. Xie, R., Mukherjee, S., Levi, A. E., **Reynolds, V. G.**, Wang, H., Chabinyc, M. L., and Bates, C. M. "Room temperature 3D printing of super-soft and solvent-free elastomers." *Science Advances* 6: eabc6900 (2020).

4. **Reynolds, V. G.**, Oh, S., Xie, R., and Chabinyc, M. L. "Model for the electro-mechanical behavior of elastic organic transistors." *Journal of Materials Chemistry C* 8, 27: 9276–9285 (2020).

5. Mukherjee, S.*, Xie, R.*, **Reynolds, V. G.**, Uchiyama, T., Levi, A. E., Valois, E., Wang, H., Chabinyc, M. L., and Bates, C. M. "Universal Approach to Photo-Crosslink Bottlebrush Polymers." *Macromolecules* 53, 3: 1090–1097 (2020). * Equal contribution

6. **Reynolds, V. G.***, Mukherjee, S.*, Xie, R., Levi, A. E., Atassi, A., Uchiyama, T., Wang, H., Chabinyc, M. L., and Bates, C. M. "Super-soft solvent-free bottlebrush elastomers for touch sensing." *Materials Horizons* 7, 1: 181–187 (2020). * Equal contribution

Contributed Presentations

1. Oral presentation at the APS March Meeting 2021 (March 15–19, 2021, virtual). Reynolds, V. G., Oh, S., Xie, R., and Chabinyc, M. L. "Model for the electro-mechanical behavior of elastic organic transistors."
2. Oral presentation at the UCSB Center for Polymers and Organic Solids seminar series (March 10, 2021, virtual). “Optimizing Soft and Stretchable Electronics Made with Novel Polymers through Predictive Modeling.”
3. Oral presentation at the 2020 Materials Research Society Spring/Fall Meeting (November 28–December 4, 2020, virtual). Reynolds, V. G., Mukherjee, S., Xie, R., Levi, A. E., Atassi, A., Uchiyama, T., Wang, H., Chabinyc, M. L., and Bates, C. M. "Super-soft solvent-free bottlebrush elastomers for touch sensing."
4. Poster presentation at the Robotics Gordon Research Conference (January 12–17, 2020, Ventura, CA). Reynolds, V. G., Mukherjee, S., Xie, R., Levi, A. E., Atassi, A., Uchiyama, T., Wang, H., Chabinyc, M. L., and Bates, C. M. "Super-soft solvent-free bottlebrush elastomers for touch sensing."

Awards and Fellowships

2017 NSF Graduate Research Fellowship

2020 Edward J. Kramer Prize in Materials
Award for best poster presentation at the UCSB Materials Research Outreach Program

2020 MRL Education Program Outstanding K–12 Volunteer Award
Award for dedicated contributions to K–12 education, UCSB Materials Research Laboratory

2020 Dow Materials Institute & UCSB Materials Research Laboratory Travel Fellowship

Abstract

Optimizing Soft and Stretchable Electronics Made with Novel Polymers through Predictive Modeling

by

Veronica Gail Reynolds

The combination of contemporary synthetic chemistry and application-driven materials design accentuates the opportunities available at the intersection of science and engineering to advance soft, flexible, and biocompatible devices. Designing devices which will undergo deformation can be approached in two ways: (1) mitigating deformation to realize strain-tolerant devices that maintain functionality in dynamic environments, e.g., wearable devices that bend and stretch with the body, or (2) leveraging deformation as a device input or output, e.g., strain sensing or actuation. In both cases device performance can be optimized through materials development, guided by electro-mechanical modeling.

Devices which leverage deformation have figures of merit that are closely linked to material mechanics. It is of interest to develop novel materials that defy conventional boundaries of mechanical behavior. Bottlebrush elastomers are an emerging class of solid materials that exhibit extremely low elastic moduli. Super-soft bottlebrush elastomer dielectrics and conductive composites have utility in enhancing the performance of flexible devices such as capacitive pressure sensors. Mitigating deformation requires quantitative modeling of strain-dependent device parameters. One particularly interesting device to model is the thin film transistor (TFT), an

important building block of modern circuits. Organic TFTs can be made with materials that allow them to be deformed during electrical operation. Mechanical models of the elasticity of polymers can be applied to predict the electrical characteristics of deformable TFTs.

Table of Contents

Chapter 1: Introduction

Soft and stretchable electronics represent a paradigm shift in the way we interact with the digital world. In the decades since the invention of the computer, the size of electronic devices has decreased dramatically (from computers that fill an entire room to a smartphone that fits in your pocket). The high density of computing power currently achievable means that the devices we use have incredible functionality. Modern electronics, however, are rigid devices with planar form factors. The field of stretchable electronics aims to create devices that can be operated in challenging, dynamic environments and designed with unconventional form factors, e.g., wearable electronics. Stretchable electronics may also gain functionality through the mechanical compliance of the device, e.g., strain sensing or actuation. The materials set needed is dramatically different from conventional silicon-based electronics.

Stretchable electronics could be either (1) stretched (e.g., upon installation) and remain stretched or (2) functionally cycled through stretched and unstretched states. The former can be prepared from plastic materials and the latter from elastic materials. This Dissertation focuses on the latter, elastic materials for stretchable electronics.

Elastomers—polymer networks which can be deformed and subsequently recover their shape—are the materials of choice for elastic devices. Elastomers are typically dielectrics (non-conductive) but can be mixed with conductive particles to make elastic conductive composites or blended with semiconducting polymers to form elastic semiconductive blends.[1,2] In the case of composites and blends, careful formulation is required to achieve the desired electrical properties while maintaining the target mechanical properties of the elastomer base. Advances in elastic electronic materials are an enabling factor in designing new stretchable device architectures.

The field of flexible and stretchable electronics has experienced tremendous progress over the past few decades. Major advances have been shown in the development of electronic skin (large area devices mimicking the functionality of human skin).[3,4] Optoelectronics with unique geometries, such as hemispherical arrays that mimic the curvature of the eyeball, have been demonstrated using compliant interconnects.[5] In the field of soft robotics, a related area of research which aims to realize new robotic capabilities through compliant actuators, there has been dynamic growth in the invention of new form factors and actuation mechanisms.[6] The application-inspired development of novel materials has been and will continue to be a critical factor in the invention and commercialization of stretchable electronics.

The studies presented in this Dissertation aim to develop new materials, models, and methods for understanding and improving the performance of soft and stretchable electronics. The remainder of Chapter 1 gives an overview of the materials currently used in stretchable electronics and challenges in new materials development. Chapter 2 demonstrates how super-soft bottlebrush elastomers can be applied to increase the sensitivity of capacitive pressure sensors. Chapter 3 describes soft, conductive, and self-healable composites prepared by the incorporation of carbon nanotubes into a dynamic bottlebrush elastomer matrix. Chapter 4 focuses on the development of an electro-mechanical model describing the behavior of stretchable thin film transistors and its application to predict which types of materials will enable stable stretchable circuits. Chapter 5 reports an approach to studying the microstructure of self-assembled block copolymers using simulation-guided resonant soft X-ray scattering. In Chapter 6, I share a handful of lessons learned over the course of my graduate research and key developments that enabled the work presented in the previous chapters. The final chapter of this Dissertation summarizes the work presented and briefly details future research that I believe will contribute to progress in the field of stretchable electronics.

1.1 Strategies for designing stretchable electronics

Designing devices which will undergo deformation can be approached in two ways: (1) mitigating deformation to realize strain-tolerant devices that maintain functionality in dynamic environments, e.g., wearable devices that bend and stretch with the body, or (2) leveraging deformation as a device input or output, e.g., strain sensing or actuation.

Mitigating deformation: Many of the original architectures for creating flexible or stretchable devices involved engineering compliance on a macroscale through the use of rigid electronics connected by compliant interconnects, termed island–bridge structures. Generally, the goal of this design scheme is to preserve the functionality of the rigid islands while enabling a non-planar device conformation or stretchability. Figure 1.1 shows an example of this design scheme applied to create a hemispherical electronic eye camera, in which rigid silicon-based devices (photodetectors and p–n diodes) are connected by compressible metal interconnects supported by a flexible and stretchable silicone substrate.[5] The devices used in island–bridge structures are generally prepared through conventional silicon fabrication processing and the flexibility or stretchability of the device is determined by the mechanics of the substrate and interconnects.

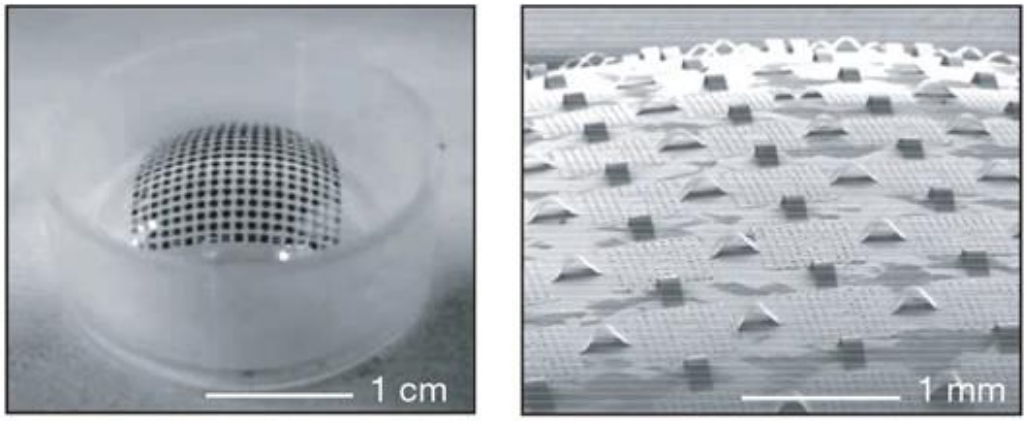

Figure 1.1 *Left*: photograph of the electronic eye camera focal plane array on the hemispherical silicone substrate; *Right*: scanning electron micrograph of the focal plane array showing the compressible interconnects.[5] Reprinted with permission from Springer Nature, Nature, "A hemispherical electronic eye camera based on compressible silicon optoelectronics," Heung Cho Ko et al. © 2008

Recently, enabled by new materials development, researchers have demonstrated devices prepared entirely with intrinsically stretchable electronic

materials.[7] Benefits of using intrinsically stretchable materials relative to structurally-engineered compliance include increased robustness, higher skin compatibility, and potential for higher device density.[7] A transistor array prepared with intrinsically stretchable materials exhibited varying mobilities and threshold voltages with strain; the relationship between these device parameters and strain differed depending on the mode of deformation (parallel or perpendicular to the semiconducting channel).[7] In investigating the impact of materials selection, device geometry, and circuit layout on device behavior, researchers are often seeking strain-tolerant configurations. Through investigation of the interplay between materials behavior and device physics, deformation can potentially be mitigated to enable stable device operation.

Leveraging deformation: Stretchable devices that leverage deformation include strain sensors and dielectric actuators—a key aspect to the functionality of the device involves deformation, either as an input to be read out as an electrical signal or as the output resulting from an applied electrical signal. Devices which leverage deformation generally have figures of merit closely linked to material mechanics, meaning limits on the mechanical properties of a material (e.g., how soft the material can be) is what limits the performance of the device.

There have been numerous demonstrations of flexible and stretchable strain/pressure sensors, particularly for electronic skin, biomechanical measurements, and human–machine interfacing.[4,8–10] Sensors which can bend and stretch with the human body are valuable for wearable consumer and medical devices. Two common sensing mechanisms are resistive and capacitive sensing—in the former, an applied strain causes a change in the measured resistance of the device and in the

latter, a change in the measured capacitance. Capacitive sensors are generally sensitive to the proximity of approaching objects (e.g., a human finger) in addition to applied strain, which may or may not be desirable depending on the use case. For both sensing mechanisms, the response function of the sensor is determined by material mechanics and strain-dependent electrical properties. Strong understanding of these materials properties enables not only an understanding of device response but also cycling stability/lifetime.

Dielectric elastomer actuators (DEAs), which translate an applied voltage into mechanical work (dielectric deformation caused by electrostatic force), also have figures of merit governed by the electrical and mechanical properties of the constituent materials. It has been shown that polymer design can be used to target specific stress–strain responses for optimized performance in DEA applications.[11] There are unique opportunities in integrating electronic circuits into DEAs due to the self-sensing capability, where measurable electrical properties of the device relate to the extent of deformation.[12] This class of devices is an interesting demonstration of the complex interplay between the mechanical and electrical properties of materials and their relation to device performance.

1.2 Materials challenges in soft and stretchable electronics

Soft electronics for which device behavior is impacted by deformation have modulus-dependent performance. This impact could be desirable (e.g., a strain sensor) or undesirable (e.g., a simple circuit designed to be strain-tolerant). In either case, it is

useful to probe limiting circumstances — based on the limits of material mechanics, where are the limits of device behavior?

Dielectrics: Off-the-shelf silicones are ubiquitous in the stretchable electronics literature, whether serving as a device substrate or dielectric layer. This family of materials, which includes the Sylgard™ (Dow Silicones Corporation) and Ecoflex™ (Smooth-On, Inc.) product lines, are incredibly useful for prototyping due to their low cost and ease of use. These are typically platinum-catalyzed two-part cure systems, in which crosslinking proceeds after the two parts are mixed together. This results in a limited pot life (amount of time the material remains liquid and moldable). The time to reach a complete cure is slow at room temperature, but this can be accelerated using higher temperatures. Once the silicone is fully cured, it is notoriously challenging to bond to other surfaces (silicone or otherwise) which complicates device fabrication.

The challenges with off-the-shelf silicones described above highlight the utility of application-driven polymer design to precisely target desired properties. Contemporary synthetic chemistry can access an incredible diversity of polymer chemistries and architectures. Macromolecular design can be applied to improve materials properties, enable different types of processing, and impart recyclability. Novel polymer architectures have been shown to enable mechanical properties inaccessible to typical linear polymers. It has been demonstrated that super-soft elastomers can be prepared using bottlebrush polymers[13], which have long side chains densely grafted to a main chain called the backbone (Figure 1.2). Bottlebrush elastomers can exhibit elastic moduli in the same range as gels and biological tissue, but without solvent or plasticizer (which can evaporate or leach out over time, causing

a change in properties). For devices with performance determined by material mechanics, there are opportunities in using materials such as bottlebrush elastomers which defy conventional limits of mechanical behavior.

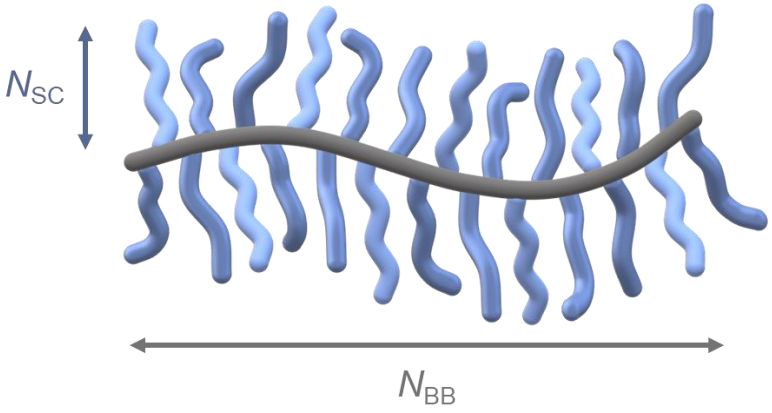

Figure 1.2 Cartoon of the bottlebrush polymer architecture. Key parameters include the degree of polymerization of the backbone, N_{BB}, and the degree of polymerization of the side chains, N_{SC}. The grafting density of the side chains along the backbone is another important parameter governing bottlebrush polymer properties.

Targeted polymer design can also improve processability through the use of alternative curing mechanisms; one example is using light to initiate elastomer curing (photocuring). Photocuring allows for indefinite pot life, with the reaction only proceeding when the material is exposed to certain wavelengths of light; photocuring additionally allows for photolithography, where masks can be used to create patterned elastomer films.[14] Another useful property achievable through alternative network formation chemistries is recyclability/reprocessability. Conventional elastomers cannot be recycled like thermoplastics—they cannot be melted and reprocessed. Researchers have shown that elastomers prepared with dynamic network chemistries can be thermally reprocessed, enabling self-healing and reforming.[15] Novel network

formation chemistries offer unique opportunities across the material lifecycle, from initial processing to end-of-life recyclability.

Conductors: One major challenge in stretchable electronics is the lack of compliant conductors. In the realm of common materials, there is a clear trade-off between compliance and conductivity. At one extreme, metals exhibit the highest conductivities (10^5–10^7 S/m) but also some of the highest moduli (10^{10}–10^{11} Pa).[16] On the opposite end, elastomers have the lowest moduli (10^5–10^8 Pa) but exhibit poor conductivity (10^{-20}–10^{-7} S/m).[16] It is a materials science challenge to access new regions of the compliance–conductivity property map.

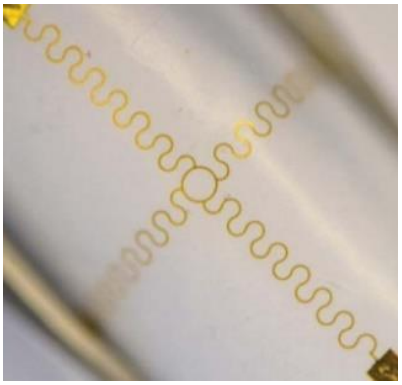

Figure 1.3 The wave geometry of this gold interconnect enables stretching up to 285% strain before failure, although not without plastic deformation along the way.[17] Copyright © 2013, IEEE.

Scientists and engineers have tackled this trade-off from a variety of angles. One tactic is to engineer geometric compliance into otherwise stiff materials by using zig-zag or wave designs to enable strain relief upon deformation (Figure 1.3).[17] This technique is promising for applications in which strains remain below the plastic deformation limit (*circa* 20% for the system shown in Figure 1.3)[17] but is limited with respect to achievable device structures (best suited to interconnects) and involves

complex fabrication. An opposite and complementary tactic is to impart conductivity to elastic polymeric materials. There are two primary methods of developing electrically conductive polymers. The first is to design intrinsically conductive polymers with conjugated chemistries which enable conduction via overlapping p-orbitals with delocalized π-electrons. These materials require doping to achieve useful conductivities and are generally limited in their mechanical compliance.[18] Conjugated polymers are typically semi-crystalline and primarily deform plastically rather than elastically; additionally, the very feature that enables conductivity (conjugation) also increases chain rigidity. The second method of developing conductive polymers is to add conductive particles to the polymer matrix, forming a composite. If the conductive particles form connected pathways through the polymer (percolate), the conductivity of the material will increase by orders of magnitude. In the design of compliant conductive composites, this need for particle percolation poses a challenge—the same pathways that conduct electricity also stiffen the composite. Despite this complexity, composites hold promise to deliver compliant conductors with suitable mechanics for stretchable electronics.

Semiconductors: As with conductors, conventional semiconductors (e.g., silicon) are hard, inextensible materials. Semiconducting polymers are softer than silicon, but they have a known trade-off between deformability and charge transport.[19] In a similar manner to achieving stretchable conductors by dispersing conductive particles in an elastomer matrix, stretchable semiconductors can be prepared by blending semiconducting polymers and elastomers.[2] The development of intrinsically

soft and stretchable semiconductors is ongoing, but the current materials set has enabled preliminary demonstrations of stretchable circuits.

1.3 The utility of predictive modeling in materials development

In either case of mitigating or leveraging deformation, it is critical to develop electro-mechanical models of device functionality using knowledge of both material mechanics and deformation-dependent parameters governing device behavior. To mitigate deformation, modeling provides a compensation function, $f_{compensation}(\lambda)$, that can be used to correct device output over a variety of strain states (defined here by the extension ratio, λ). To leverage deformation, modeling provides a response function, $f_{response}(\lambda)$, that can be used to link device inputs and outputs (e.g., a sensor response function linking an applied force to a change in capacitance).

Creating electronics that bend and stretch adds new variables to the equations governing device behavior. For example, the source–drain current of a field–effect transistor, typically controlled by the applied voltage, can be additionally modulated by dimensional changes resulting from an applied stress. These additional variables influencing device behavior can be captured in electro-mechanical models which combine equations describing the electrical operation of a device with scaling relationships describing changes in materials properties and device parameters with strain. Electro-mechanical models for device behavior can also be used to identify performance limits for properties which are impacted or controlled by the mechanical behavior of the constituent materials.

The development of electro-mechanical models requires not only theoretical efforts applying fundamental equations of mechanics and device physics, but also experimental efforts to probe the complex relationships between deformation, device operation, and materials properties. These models will be critical for the commercialization of stretchable electronics, particularly in a medical context. The insights gained and uncertainties raised in the development of electro-mechanical models serve to guide future research.

1.4 References

1. Mutiso, R. M. & Winey, K. I. Electrical properties of polymer nanocomposites containing rod-like nanofillers. *Progress in Polymer Science* 40 63–84 (2015).
2. Xu, J. et al. Highly stretchable polymer semiconductor films through the nanoconfinement effect. *Science* 355, 59–64 (2017).
3. Hammock, M. L., Chortos, A., Tee, B. C. K., Tok, J. B. H. & Bao, Z. 25th anniversary article: The evolution of electronic skin (E-Skin): A brief history, design considerations, and recent progress. *Advanced Materials*. 25, 5997–6038 (2013).
4. Bauer, S. et al. 25th anniversary article: A soft future: From robots and sensor skin to energy harvesters. *Advanced Materials* 26 149–162 (2014).
5. Ko, H. C. et al. A hemispherical electronic eye camera based on compressible silicon optoelectronics. *Nature* 454, 748–753 (2008).
6. Whitesides, G. M. Soft Robotics. *Angewandte Chemie International Edition* 57 4258–4273 (2018).
7. Wang, S. et al. Skin electronics from scalable fabrication of an intrinsically stretchable transistor array. *Nature* 555, 83–88 (2018).
8. Mannsfeld, S. C. B. et al. Highly sensitive flexible pressure sensors with microstructured rubber dielectric layers. *Nature Materials* 9, 859–864 (2010).
9. Lei, K. F., Lee, K. F. & Lee, M. Y. Development of a flexible PDMS capacitive pressure sensor for plantar pressure measurement. *Microelectronic Engineering* 99, 1–5 (2012).
10. Amjadi, M., Kyung, K. U., Park, I. & Sitti, M. Stretchable, Skin-Mountable, and Wearable Strain Sensors and Their Potential Applications: A Review. *Advanced Functional Materials* 26, 1678–1698 (2016).
11. Vatankhah-Varnoosfaderani, M. et al. Bottlebrush Elastomers: A New Platform for Freestanding Electroactuation. *Advanced Materials* 29, 1604209 (2017).
12. Jung, K., Kim, K. J. & Choi, H. R. A self-sensing dielectric elastomer actuator. *Sensors and Actuators A: Physical* 143, 343–351 (2008).

13. Daniel, W. F. M. et al. Solvent-free, supersoft and superelastic bottlebrush melts and networks. *Nature Materials* 15, 183–189 (2016).
14. Mukherjee, S. et al. Universal Approach to Photo-Crosslink Bottlebrush Polymers. *Macromolecules* 53, 1090–1097 (2020).
15. Self, J. L. et al. Dynamic Bottlebrush Polymer Networks: Self-Healing in Super-Soft Materials. *Journal of the American Chemical Society* 142, 7567–7573 (2020).
16. Ashby, M. F. Materials Selection in Mechanical Design. Elsevier (2011).
17. Hsu, Y. Y. et al. Novel strain relief design for multilayer thin film stretchable interconnects. *IEEE Transactions on Electron Devices* 60, 2338–2345 (2013).
18. Roth, B. et al. Mechanical Properties of a Library of Low-Band-Gap Polymers. *Chemistry of Materials* 28, 2363–2373 (2016).
19. Printz, A. D. & Lipomi, D. J. Competition between deformability and charge transport in semiconducting polymers for flexible and stretchable electronics. *Applied Physics Reviews* 3 021302 (2016).

Chapter 2: Super-soft solvent-free bottlebrush elastomers for touch sensing

2.1 Abstract

The sensitivity of capacitive pressure sensors is primarily determined by the modulus of a soft dielectric layer that reversibly deforms to produce an electrical signal. Unfortunately, the mechanical properties of conventional linear networks are constrained such that a lower limit on softness translates to poor capacitive pressure sensor performance. Here, we overcome this paradigm by leveraging the intrinsic "super-soft" characteristic of bottlebrush polymers. A simple light-induced

crosslinking strategy is introduced to facilitate device fabrication and parallel plate capacitive pressure sensors constructed with these bottlebrush polymer networks exhibit up to a 53× increase in sensitivity compared to traditional material formulations, e.g., Sylgard 184. This combination of contemporary synthetic chemistry and application-driven materials design accentuates the opportunities available at the intersection of science and engineering.

2.2 Introduction

Sensor skins are large area electronic devices that translate input stimuli into electrical signals for robotics and wearable electronics.[1,2] Pressure is a critical input in these applications because it provides environmental awareness that can be used to tune interaction with the surroundings. Key regimes include 1–10 kPa (touch sensing; intraocular and intracranial pressures) and 10–100 kPa (pulse monitoring).[3] Pressure sensors can be formed using a variety of materials, but dielectric polymers provide unique advantages versus inorganic options, such as high elongation at break and ease of processing for large area devices.

Capacitive pressure sensors (CPSs) are devices that report a capacitance change upon deformation of a dielectric layer.[3] The most basic CPS architecture is a parallel plate capacitor, which can be readily formed with soft materials. Elastomer-based CPSs comprise an elastic dielectric layer sandwiched between two electrodes. In these devices, the sensitivity (S) is governed by the elastomer modulus (Figure 2.1) – softer materials produce higher sensitivity because an applied pressure causes a larger change in thickness (and thus a bigger change in the capacitance). However, CPSs have traditionally suffered from low sensitivity; often, more complex devices are

needed to amplify signals in the low pressure regime, for example where a dielectric layer is also the gate of a transistor.[3,4] While traditional polymers do not satisfy current demands for soft dielectric elastomers, recent synthetic advances in macromolecular design present opportunities to control macroscopic properties with unprecedented tunability.

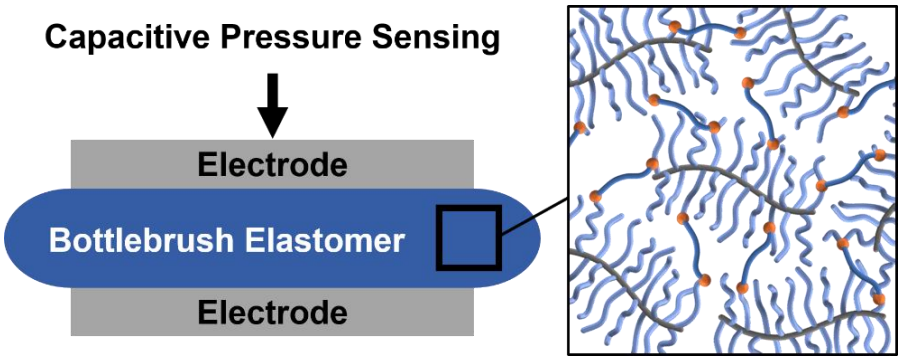

Figure 2.1 Illustration of a parallel plate capacitive pressure sensor fabricated with a bottlebrush polymer dielectric elastomer. Since sensor response scales inversely with elastomer modulus, "super-soft" bottlebrush networks improve sensitivity relative to traditional linear analogues. In the network illustration on the right, orange spheres represent productive crosslinking points that connect individual bottlebrush molecules.

Conventional elastomeric dielectric layers are usually formed from crosslinked networks of linear polymeric precursors. For example, poly(dimethylsiloxane) (PDMS) is commonly used in soft robotics and sensor skins because it is commercially available in various formulations such as Sylgard 184 (Dow Corning) and Ecoflex (Smooth-On, Inc.).[5] Additional benefits of PDMS include its modest dielectric constant *circa* 2.3–2.8, high electrical resistivity, and nontoxicity.[6] In the field of dielectric elastomers, the VHB series of polyacrylate foam adhesives (3M) is also widely used for dielectric actuation.[7] Unfortunately, these and other linear elastomer networks exhibit a well-known lower bound on stiffness (*circa* 10^3 kPa) that is

characteristic of entangled polymers, thus placing an upper limit on the sensitivity of CPSs formulated therefrom.[2]

Numerous strategies have been devised to achieve higher sensitivity CPSs with conventional elastomers. One way to reduce the modulus of an elastomer involves partial crosslinking, effectively rendering the uncrosslinked polymer chains diluents and turning the resulting material into a gel (swollen network). The use of partially crosslinked or solvent-swollen networks can improve the conformability and sensitivity of CPSs,[8,9] but risks leachability and sacrifices rheological stability. An alternative to using gels is reducing the effective modulus of the dielectric layer by incorporating air. Sylgard 184 can be micropatterned using a multistep molding process to create linear and pyramidal features on the micron scale.[4] These air–elastomer composites reduce the effective modulus of the dielectric layer by removing material, therefore amplifying pressure and providing space for the elastomer to deform. Elastomer foams – a different type of air–elastomer composite – have similar mechanical properties but are made through different processing routes. For example, porous elastomer layers can be formed by incorporating sacrificial particles, commonly sugar or salt granules, that are dissolved after curing the network (referred to as solid particle leaching).[10–13] Another technique involves the dispersion of water droplets into the elastomer matrix and subsequent evaporative removal post-curing.[14] While these routes have been shown to reduce effective modulus and improve CPS sensitivity, they require complex fabrication techniques and result in devices that are susceptible to contaminant ingress and response drift due to humidity.

Here, we introduce a new approach to create high sensitivity CPSs by designing dielectric elastomers based on bottlebrush polymers. This highly branched architecture tends to minimize chain entanglements, resulting in "super-soft" materials with a significantly lower bulk shear modulus than linear analogues (*circa* 1–100 kPa).[15,16] Figure 2.2 illustrates the two key ingredients in our formulations: (1) well-defined bottlebrush precursors comprising a long backbone and densely-grafted side-chains with chemical degrees of polymerization denoted as N_{BB} and N_{SC}, respectively,[17–19] and (2) a photo-crosslinkable bis-benzophenone additive that includes a customized linker to promote miscibility with the bottlebrushes at room temperature for facile mixing without solvent. We demonstrate that using PDMS-based bottlebrush elastomers in CPSs increases their sensitivity by 3–53× compared to conventional elastomers. These improvements are comparable to, or better than, previous microstructuring strategies, yet involve significantly simpler processing steps.

2.3 Results and Discussion

Molecular design and synthesis

Our initial design for solvent-free bottlebrush dielectric elastomers is based on PDMS due to its favorable rheological properties, optical transparency, non-toxic nature, and relatively high entanglement molecular weight (M_e = 21–33 kDa).[6] A PDMS macromonomer (M_n = 5.3 kg mol^{-1}, Đ = 1.1, N_{SC} = 68) was synthesized from commercially-available poly(dimethylsiloxane) by installing a norbornene group on one end (see Appendix A for details). Subsequent grafting-through ring-opening metathesis polymerization (ROMP) catalyzed by a Grubbs 3rd generation catalyst

produced a library of bottlebrush polymers with constant PDMS side-chain degree of polymerization (N_{SC} = 68) and variable poly(norbornene) backbone lengths (N_{BB}). An advantage of this synthetic approach is the ability to fully characterize well-defined bottlebrush precursors[20,21] (see Table A1 for a summary, Appendix A) before subsequent crosslinking reactions, in contrast to in situ polymerization methods that simultaneously construct the bottlebrush architecture and crosslink chains.[22]

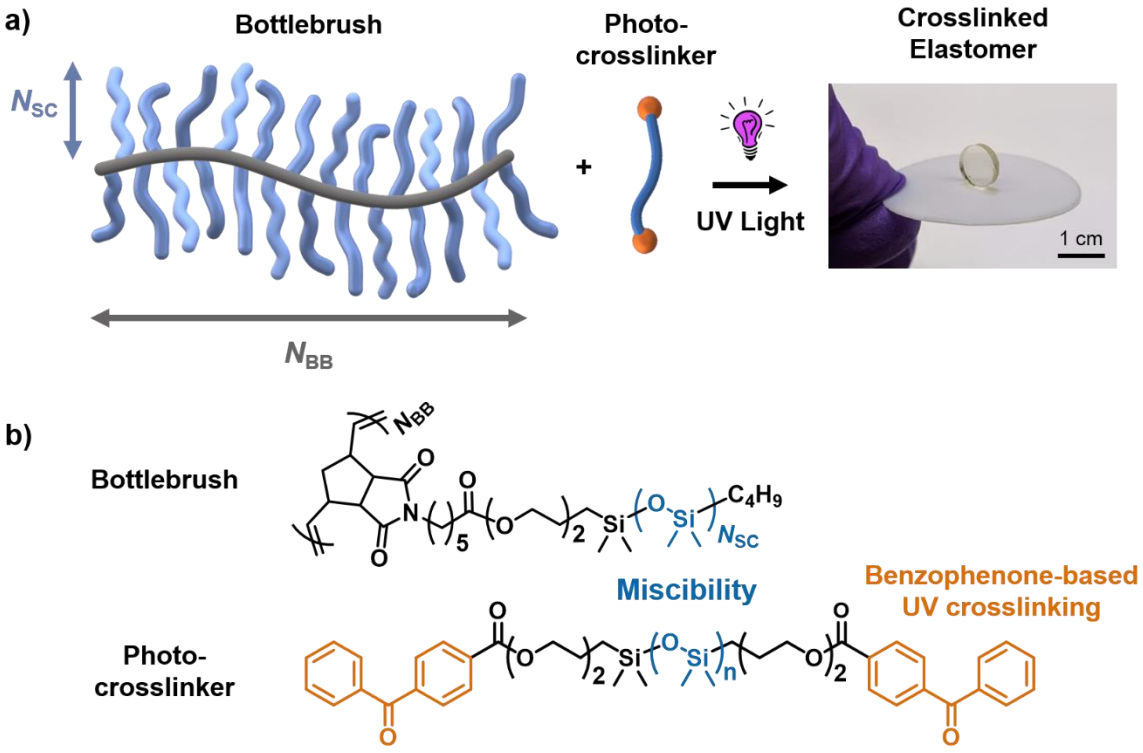

Figure 2.2 Photo-crosslinkable bottlebrush dielectric elastomer formulations. (a) Key ingredients include well-defined bottlebrush molecules with backbone and side-chain degrees of polymerization N_{BB} and N_{SC}, respectively, and a bis-benzophenone-based photo-crosslinker. All components are miscible at room temperature to produce a viscous liquid mixture. Subsequent crosslinking with UV light creates an elastomeric solid. (b) Chemistry of the PDMS bottlebrush polymer and PDMS-based bis-benzophenone photo-crosslinker. Full synthetic details are available in Appendix A.

The PDMS bottlebrush polymers are viscous liquids (zero-shear viscosity η_0 = 2–55 Pa s) that require crosslinking to form a solid elastomer network. Network

formation was achieved by designing a PDMS-based benzophenone (BP) photo-crosslinker, which we envisioned would simplify the synthesis of solvent-free elastomers and facilitate integration of bottlebrush materials into useful devices. The BP unit has a relatively weak absorption band near 350 nm (n → π*) and strong absorption bands near 200–250 nm (π → π*). When irradiated with a 350 nm light source, triplet excited states of benzophenone abstract hydrogen atoms from nearby alkyl moieties via radical pathways. The resulting reactive species can undergo C–C coupling reactions; through this mechanism, a molecule with two BP moieties can covalently crosslink distinct polymer chains. To obtain a photo-crosslinker that homogeneously mixes with PDMS bottlebrushes without any additional solvent, we functionalized di-hydroxy telechelic PDMS (M_n = 6.0 kg mol^{-1}, Đ = 1.3, N = 72) with BP moieties at both termini. This design is critical since small molecule bis-benzophenones lacking a bridging PDMS chain were immiscible with PDMS-based bottlebrush polymers, even at elevated temperatures. Our solvent-free mixing strategy provides a facile route to an all-solids, super-soft dielectric layer.

Rheology of benzophenone-crosslinked PDMS bottlebrush elastomers

Various formulations of PDMS bottlebrush polymer and PDMS crosslinker were prepared to investigate the effects of molecular design on network properties and CPS performance. Samples are referred to as $PDMS_{68}^{N_{BB}} - XX$, where N_{BB} is variable, N_{SC} = 68 is held constant, and XX is the number of crosslinkers per bottlebrush molecule. The range of architectures and formulations explored produced bottlebrush elastomers with moduli spanning nearly two decades.

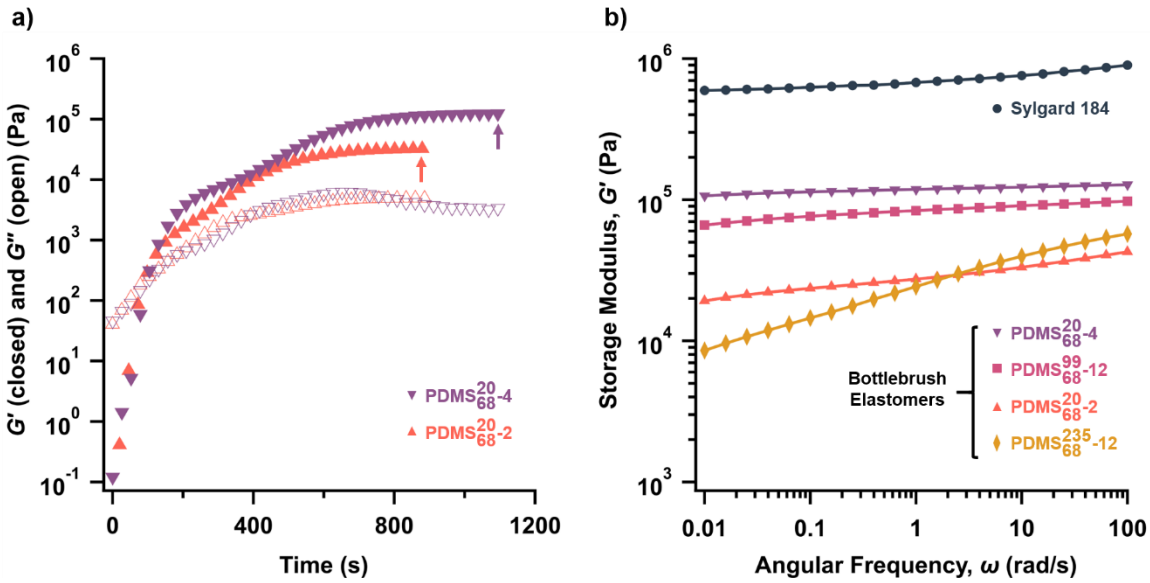

Figure 2.3 (a) PDMS bottlebrush formulations are photo-crosslinkable as evidenced by rheological analysis of $PDMS_{68}^{20}-2$ and $PDMS_{68}^{20}-4$ under UV light exposure (365 nm, 150 mW cm^{-2}; exposure begins at t = 0). (b) Frequency sweeps indicate the plateau storage modulus can be tuned by N_{BB} and crosslinker loading. Measurements were taken at 21 °C and 1% strain. Loss moduli and FFT results are available in Appendix A.

Rheological analysis with *in situ* light exposure (365 nm, 150 mW cm^{-2}) indicates the PDMS bottlebrush formulations described above are UV-crosslinkable at room temperature with a relatively fast gel time ($G' = G''$) *circa* 100 s for thick layers (≈0.4 mm) (Figure 2.3a). Continued illumination further increases the shear modulus over the course of about 1000 s, resulting in a plateau value that depends on crosslinker loading. As expected, higher crosslinker concentration increases both curing time and the final modulus. Frequency sweeps (Figure 2.3b) of fully cured samples at room temperature further indicate the plateau storage modulus (defined at 0.001 rad s^{-1} by Fast Fourier Transformed (FFT) stress relaxation or creep results) depends on N_{BB}. The softest formulations occur at large N_{BB}, which produces longer network strands on average, in agreement with previous work.[23] Importantly, all of these materials are considerably softer – by 1–2 orders of magnitude – than linear

PDMS that was thermally cured at 150 °C for 30 min (*cf.*, Sylgard 184 in Fig. 3b). Moreover, for three different backbone lengths (N_{BB} = 20, 99, and 235), low crosslinker loadings still produce excellent gel fractions (>85%) as measured via mass loss after solvent soaking (24 h in toluene). The gel fraction correlates with curing completeness (percentage of polymer chains incorporated into the elastic network) and is critical for elasticity, non-leachability, and device stability. This combination of soft mechanical properties (G' = 104–105 Pa) and high gel fraction highlights the advantages of the bottlebrush architecture in comparison to linear alternatives.

Capacitive pressure sensor fabrication and performance

Capacitive pressure sensors were fabricated by laminating molded elastomer discs to flexible and transparent indium-tin-oxide (ITO)-coated poly(ethylene terephthalate) (PET) electrodes mounted on glass substrates (Figure 2.4). The choice of electrode enabled visual inspection of the elastomer–electrode interface (the quality of which is critical to device performance) and additionally resulted in transparent and flexible (Fig. A17, Appendix A) sensors. The dielectric constant of the PDMS bottlebrush networks is 2.6 at frequencies of 100 to 105 Hz, a value identical to Sylgard 184 (Fig. A11, Appendix A). Based on parallel plate capacitance and rubber elasticity models, CPS sensitivity (defined as the slope of the sensor response curve, $S = d(\Delta C/C_0)/d\sigma$) should scale inversely with the modulus of the elastomer (see Appendix A). The pressure sensors were tested by simultaneously measuring capacitance with an LCR (inductance, capacitance, resistance) meter and applied force. Sensor response curves were collected in the 0–50 kPa range with an S-beam load cell in a displacement-controlled compression tester. Pressure cycling curves of the sensors were collected

using a TA Instruments Dynamic Mechanical Analyzer (DMA) 850 to apply a sinusoidal force program at specific frequencies. Note that for the cycling data, the relative change in capacitance was calculated relative to a pre-loaded (rather than unloaded) state. Care was taken to eliminate stray capacitive effects so that the sensor response was dominated by the mechanics of the elastomer layer. The sensors would ideally be fully shielded from stray capacitance of the leads, but the requirements of our mechanics-focused design – complete transfer of applied pressure to the elastomer disc and freedom for lateral expansion of the elastomer – limited such a setup. The test environment was grounded and kept constant for each elastomer tested.

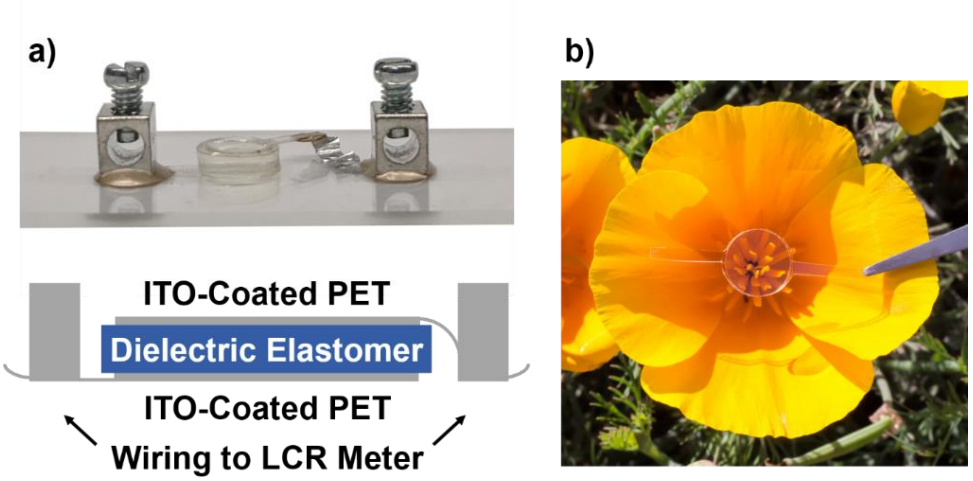

Figure 2.4 (a) Optical photograph and accompanying schematic of the capacitive pressure sensor devices studied herein. ITO-coated PET electrodes enabled a visual check of interfaces and screw terminals attached with conductive epoxy ensured repeatable connection to the LCR meter. (b) The sensor has excellent optical properties with <1% haze over the majority of the visible spectrum (transmittance and haze spectra are available in Appendix A, Figure A12).

The modulus of the bottlebrush elastomers is controllable by crosslinker concentration and can improve the sensitivity of CPSs. Figure 2.5a shows the sensor response curves for four PDMS bottlebrush networks ($PDMS_{68}^{20}-2$, $PDMS_{68}^{20}-4$, $PDMS_{68}^{99}-12$, $PDMS_{68}^{235}-12$) and a reference linear elastomer (Sylgard 184). The

response of the Sylgard 184 sensor quickly saturates relative to the bottlebrush elastomer sensors. For the bottlebrush networks, moving from 4 to 2 crosslinkers per chain produces a significant increase in sensitivity concomitant with a reduced G0. The sensor made with the softest polymer, $\mathrm{PDMS}_{68}^{235}-12$ (G_0 = 6.2 kPa) exhibits extremely high sensitivity. As compared with the Sylgard 184 sensor, it has 22× higher sensitivity in the low pressure (0–10 kPa) regime and 53× higher sensitivity in the high pressure (20–50 kPa) regime. Sensitivities for all sensors measured are summarized in Table 2.1; note that S_{Y-Z} indicates the sensitivity in pressure regime Y–Z kPa. At the highest pressure of 50 kPa, strains occurring in the sensors ranged from 0.03 (Sylgard 184) to 0.38 ($\mathrm{PDMS}_{68}^{235}-12$). All sensors tested exhibited response hysteresis at the strain rate used, meaning the unloading curve appears different than the loading curve. Hysteresis is common for sensors with dielectric elastomers and is most evident here for the lowest modulus elastomers with the largest magnitude signals. The capacitance of the two lowest modulus bottlebrush elastomer sensors did not return to the baseline at the end of the high pressure (0–50 kPa) response test, indicating either an undesirably slow relaxation response or permanent sample damage. The former seems more likely based on the low-frequency rheology data (Figure 2.3b) and visual evidence that suggests sample integrity. Further investigation into cycling stability using the DMA revealed a trade-off between sensitivity and baseline stability in pressure regimes that approach significant strains. Figure 2.5b shows that in the medium pressure regime (1–21 kPa), the sensor prepared with $\mathrm{PDMS}_{68}^{235}-12$ undergoes some baseline drift over time while one prepared with $\mathrm{PDMS}_{68}^{99}-12$ remains relatively stable. These data suggest that high sensitivity and

baseline stability may be achieved by appropriately matching a bottlebrush elastomer with the pressure range of interest.

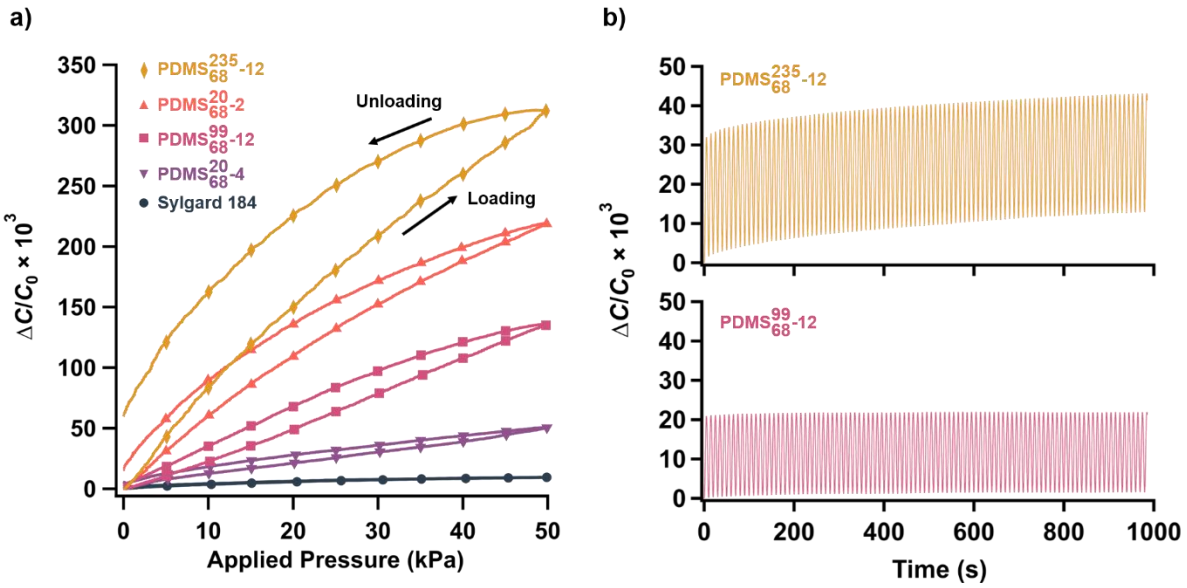

Figure 2.5 (a) Sensor response curves (relative change in capacitance *vs.* applied pressure) show the bottlebrush elastomers enable improved sensitivity compared to crosslinked linear PDMS (Sylgard 184). Sensors were loaded and unloaded at a strain rate of 0.001 s^{-1}. (b) Cycling tests show a trade-off between sensitivity and baseline stability. The sensors were cycled at 0.1 Hz with an 11 kPa pre-load and a 10 kPa wave amplitude, resulting in oscillation between 1–21 kPa. Note that the amplitude of oscillation remains relatively constant even as the baseline drifts.

The bottlebrush elastomer sensors exhibit high sensitivity at pressures under 1 kPa and additionally show rapid response times to pressure oscillations at 0.1 Hz (Figure 2.6). In considering higher frequency pressure application, the frequency-dependent modulus curves from our rheological studies can be used to identify appropriate limits. The two stiffer bottlebrush elastomers exhibit less frequency-dependent shear moduli between 0.01 and 100 rad s^{-1}, which is correlated with smaller hysteresis in the sensor response. The two softer bottlebrush elastomers exhibit some relaxation into the low frequency regime (i.e., <0.1 rad s^{-1}), possibly resulting in the pronounced hysteresis for the sensor response at the strain rate of

0.001 s^{-1}. Further studies investigating the effect of bottlebrush architecture on frequency response may elucidate the cause of this slow relaxation and help minimize hysteresis through informed molecular design.

Table 2.1 Measured sensitivities for the bottlebrush elastomer and Sylgard 184 sensors.

Sample ID	G_0 (kPa)	S_{0-10} (kPa^{-1})	$S_{0-10}/S_{Sylgard}$	S_{20-50} (kPa^{-1})	$S_{20-50}/S_{Sylgard}$
Sylgard 184	520	0.0004	-	0.0001	-
$PDMS_{68}^{20}$-4	92	0.0013	3.3	0.0009	9.0
$PDMS_{68}^{99}$-12	53	0.0023	5.8	0.0029	29
$PDMS_{68}^{20}$-2	16	0.0062	16	0.0036	36
$PDMS_{68}^{235}$-12	6.2	0.0087	22	0.0053	53

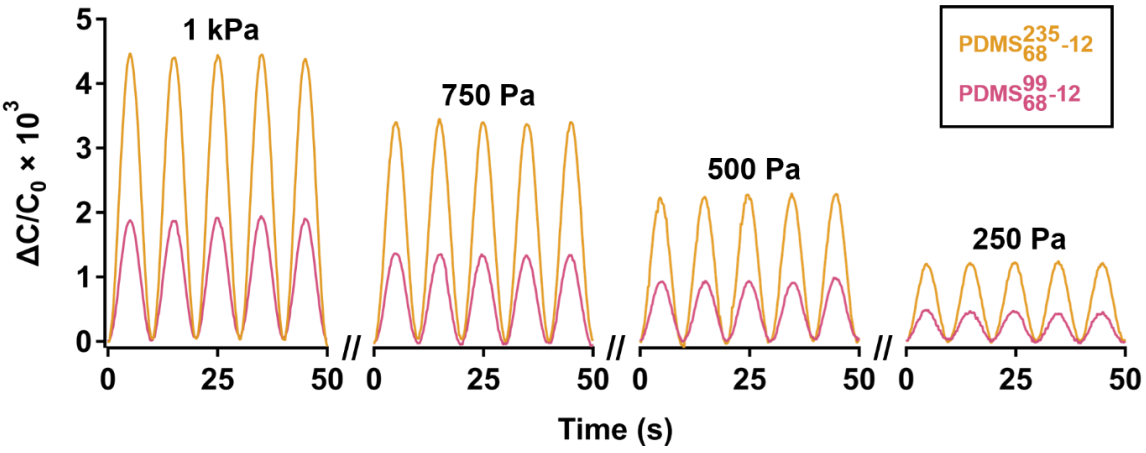

Figure 2.6 Low pressure cycling of the bottlebrush elastomer sensors shows high sensitivity in the 250 Pa–1 kPa regime. The data shown were collected at a frequency of 0.1 Hz with the amplitude of pressure oscillation labeled above each dataset.

Modeling the modulus–sensitivity relationship

The expected response of CPSs prepared with a uniform elastomer layer is more easily modeled than micropatterned or foamed alternatives. The compression of a dielectric elastomer layer between stretchable electrodes, assuming constant relative permittivity and incompressibility (Poisson's ratio, ν = 0.5), will result in the relationship between relative change in capacitance $\Delta C/C_0$ and extension ratio in the direction of applied pressure λ shown in Eqn (2.1):

$$\frac{\Delta C}{C_0} = \lambda^{-2} - 1 \tag{2.1}$$

The ITO-coated PET film electrodes used in this work are undersized and inextensible relative to the soft and elastic dielectric. Applying a constant area assumption to the derivation with stretchable electrodes gives the new relationship shown in Eqn (2.2):

$$\frac{\Delta C}{C_0} = \lambda^{-1} - 1 \tag{2.2}$$

Following this constant area relationship, the pressure sensor sensitivity S can be related to the shear modulus, G, using the network theory of rubber elasticity,[24] as:

$$S = \frac{1}{G(\lambda+\lambda^{-1}+1)} \Longrightarrow \frac{1}{3G} \text{ (small strain limit)} \tag{2.3}$$

Derivations of the above expressions may be found in Appendix A. We expect that practical sensors will deviate from the predicted behavior. In practice there are parasitic circuit elements in the detection circuit and the adhesion of the elastomer to the electrodes will limit free deformation of the polymer. The effect of parasitic circuit elements was found to be similar for all sensors (evaluated by comparing the measured

capacitive signal to that expected by calculations using the measured strain). The adhesion of the elastomer to the electrodes inhibits lateral expansion, promoting bulging of the disc sidewall; the impact of this on stress–strain behavior has been described through a geometric correction factor that increases the apparent modulus.[25,26] The effect of adhesion to the electrodes was found to become significant in the lower modulus elastomers, which deformed to higher strains in the pressure range tested. Further details can be found in Appendix A. Despite the aforementioned non-idealities, the simple model (Eqn (2.3)) was found to roughly capture the sensitivity–modulus scaling found in this work (Figure 2.7), with a good fit for low pressure (0–10 kPa) sensitivities of all sensors except for the lowest modulus bottlebrush elastomer, $\mathrm{PDMS}_{68}^{235} - 12$.

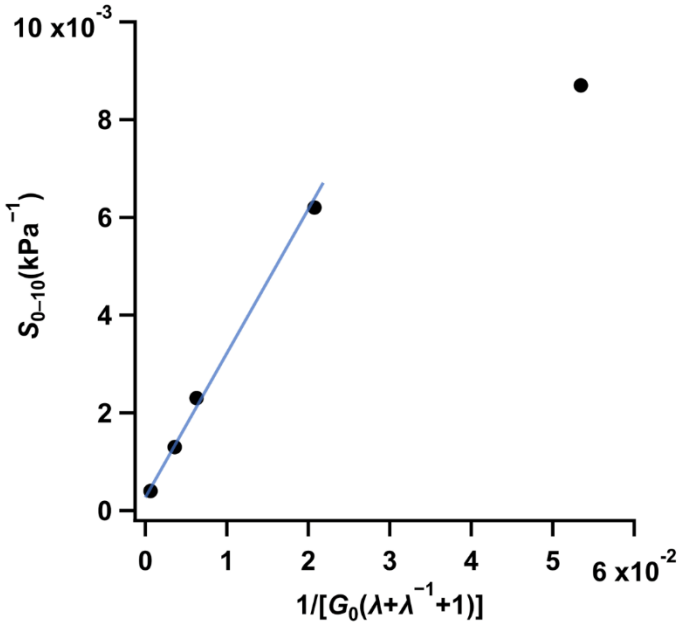

Figure 2.7 The simple model, which predicts a linear relationship between sensitivity and the modulus/extension ratio term, fits for all but the softest bottlebrush elastomer sensor.

The performance of CPSs is highly dependent on device design in addition to material selection and fair comparisons of sensitivity should therefore be made relative to a control sensor of the same design. Our work demonstrates sensitivity increases relative to a control ranging from 3.3× to 22× in the 0–10 kPa range and 9.0× to 53× in the 20–50 kPa range by using bottlebrush elastomers instead of traditional linear elastomers. In comparison, the micropatterning method for PDMS reportedly leads to a 28× sensitivity increase in the 0–2 kPa range and a 7.5× increase in the 2–7 kPa range compared to an unstructured Sylgard 184 layer.[4] Introduction of microporosity reportedly results in an 8.2× sensitivity increase in the 0–10 kPa range and a 1.3× increase in the 10–100 kPa range (via processing with 10:1 sugar: Sylgard 184, 89.3% porosity).[12] In another study, a 38× sensitivity increase in the 0–5 kPa range was reported for a sensor with both a microporous dielectric layer and stretchable electrodes.[11] The performance of a broader range of sensors can be found in Appendix A (Table A2). Notably, the air–elastomer composites exhibit declining sensitivities at high pressures – as air is displaced, the dielectric layer increasingly behaves like a bulk elastomer layer. The non-negligible gas permeability of PDMS adds complexity to this deformation behavior, i.e., it is not clear whether the gas simply leaks out of the sensor or permeates the PDMS.[6] Here, we achieve comparable, or better, performance through the use of a rationally designed all-solids material, rather than through complex processing. A combination of bottlebrush materials and porosity could conceivably result in even larger increases in sensitivity than achievable with either strategy alone.

2.4 Conclusion

The use of super-soft bottlebrush elastomers as dielectric layers in solvent-free capacitive pressure sensors produces significant performance enhancements while preserving a simple and easily manufacturable design. Formulations that include a bis-benzophenone-based additive can be UV cured in minutes and the resulting mechanical properties are highly tunable via crosslinker loading and bottlebrush backbone degree of polymerization. Optimal designs reach moduli circa 10^4–10^5 Pa, a factor of 10–100× smaller than conventional linear analogues. This greater deformability results in device sensitivities up to 53× higher than commercially available Sylgard 184, highlighting the potential of applying new polymeric materials in well-established device architectures.

2.5 Experimental Methods

PDMS bottlebrush elastomers were prepared by the addition of PDMS bis-benzophenone at molar concentrations varying between 2–12 crosslinkers per bottlebrush molecule. Rheology samples were cured *in situ* with the UV LED curing accessory for a TA Instruments AR-G2 rheometer (150 mW cm^{-2}, 365 nm). Pressure sensor samples were cured using a collimated LED (approximately 1 mW cm^{-2}, 365 nm; M365L2-C1, Thorlabs) or on the rheometer. These narrowband light sources avoid sample degradation issues that can occur with broadband UV sources (e.g., metal halide bulbs). Mixtures of bottlebrush polymer and photo-crosslinker were degassed in a vacuum oven at 100 °C for 3 hours before UV crosslinking to ensure the elimination of any air bubbles. The sensors were fabricated by crosslinking

bottlebrush polymers in a poly(tetrafluoroethylene) mold (6.35 mm diameter by 1.55 mm thick disc) and laminating to ITO-coated PET electrodes (Thorlabs). The use of transparent electrodes enabled visual inspection of the electrode–polymer interface for bubbles and delamination. Electrical connection to the sensor was established by installing screw terminals (Keystone Electronics Corp.) with conductive epoxy (CW2400, Chemtronics).

For pressure sensor response curve measurements, a compression tester with a precision ball screw stage actuated by a micro-stepper motor was used to compress the sensors at a strain rate of 0.001 s^{-1}; a 5 N load cell was used to measure applied force, with its signal conditioned by a standalone strain gage amplifier. A laser extensometer (Electronic Instrument Research LE-01) was used to monitor sub-micron displacements for high resolution strain measurement. A glass spacer was used to electrically insulate the sensor from the compression tester and distribute pressure across the sensor face; a rounded probe was used to ensure level compression. Pressure sensor cycling tests were collected with a TA Instruments DMA 850 using the parallel plate compression clamp. A PTFE spacer was used to electrically insulate the sensor from the clamp. For both response curve and cycling tests, capacitance measurements were collected with a Keysight E4980A LCR meter, using a probing AC signal of 1 V/100 kHz. To the greatest extent possible, the sensor test environment was grounded to the LCR meter to reduce electromagnetic interference effects.

2.6 Acknowledgements

Materials characterization was supported by NSF DMR 1436263. V.G.R. gratefully acknowledges the National Science Foundation Graduate Research Fellowship Program under Grant 1650114. The research reported here made use of shared facilities of the UCSB MRSEC (NSF DMR 1720256), a member of the Materials Research Facilities Network (http://www.mrfn.org). Special thanks to Kirk Fields, Mechanical Test Lab, Department of Mechanical Engineering, UCSB and Prof. Yon Visell, Department of Electrical and Computer Engineering and Media Arts and Technology Program, UCSB for assistance with the pressure sensor test method development. Special thanks to the Helgeson Lab, UCSB for access to the AR-G2 rheometer and UV curing accessory.

2.7 Appendix A

I. Synthesis

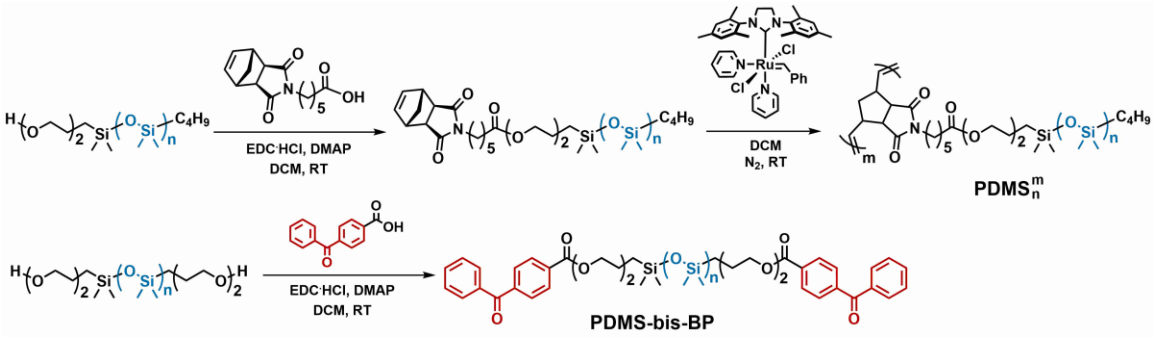

Scheme A1. Synthesis of PDMS bottlebrush polymers (top) and PDMS bis-benzophenone crosslinker (bottom).

Materials and Methods

N-(hexanoic acid)-*cis*-5-norbornene-*exo*-dicarboximide was prepared according to literature. Grubbs' second-generation metathesis catalyst [$(H_2IMes)(PCy_3)(Cl)_2Ru$=CHPh] was generously provided by Materia. Grubbs' third-generation metathesis catalyst [$(H_2IMes)(pyr)_2(Cl)_2Ru$=CHPh] (G3) was prepared according to literature. Methanol (Fisher Scientific — A412; purity >99.8%), dichloromethane (Fisher Scientific — D37, purity >99.5%), and ethyl vinyl ether (Fisher Scientific / ACROS Organics, AC119082500, purity >99%) were used as received. $CDCl_3$ (99.8%) was purchased from Cambridge Isotope Laboratories (DLM-7) and used as received. Bis(hydroxyalkyl)-terminated PDMS (Sigma — 481246), hydroxyalkyl-terminated PDMS (Gelest — MCR-C18), 4-benzoylbenzoic acid (Sigma — B12407, purity 99%), *N,N*-dimethylaminopyridine (Alfa Aesar, H51715, purity 99%) and EDC (Oakwood chemical-024810, purity 99%) were used as received.

Synthesis of PDMS-bis-BP Crosslinker

In a round-bottom flask, a mixture of 4-benzoylbenzoic acid (1.21 g, 5.36 mmol), bis(hydroxyalkyl)-terminated 5.6 kDa PDMS (10 g, 1.79 mmol), DMAP (109 mg, 0.9 mmol), and EDC•HCl (1.37 g, 7.14 mmol) in DCM (100 mL) was stirred for 24 hours. The reaction mixture was washed with dilute HCl (1 M) and repeatedly washed with water, followed by drying over anhydrous $MgSO_4$. The solution was passed through a plug of activated basic alumina and evaporated to dryness to obtain the desired compound as a transparent colorless liquid. Yield: 5.75 g (53 %). ^{1}H NMR (600 MHz, Chloroform-*d*) δ: 8.18 (d, *J* = 8.2 Hz, 4H), 7.84 (d, *J* = 8.2 Hz, 4H), 7.81 (d, *J* = 8.1 Hz, 4H), 7.61 (t, *J* = 7.4 Hz, 2H), 7.50 (t, *J* = 7.7 Hz, 4H), 4.53 – 4.50 (m, 4H), 3.81 – 3.77

(m, 4H), 3.50 (t, *J* = 6.9 Hz, 4H), 1.64 (dd, *J* = 15.3, 8.0 Hz, 4H), 0.58 – 0.54 (m, 4H), 0.08 (s, 475H). ^{13}C NMR (151 MHz, Chloroform-*d*) δ: 195.88, 165.73, 141.33, 136.97, 133.25, 132.85, 130.05, 129.68, 129.57, 128.40, 74.15, 68.45, 64.58, 23.39, 14.10, 1.23, 1.12, 0.99, 0.74, 0.07.

Synthesis of PDMS Macromonomer

In a round-bottom flask, a mixture of mono-hydroxy 5 kDa PDMS (54.3 g, 10.9 mmol), *N*-(hexanoic acid)-*cis*-5-norbornene-*exo*-dicarboximide (7.53 g, 27.2 mmol), DMAP (663 mg, 5.43 mmol), and EDC•HCl (7.3 g, 38.0 mmol) in DCM (250 mL) was stirred for 48 hours. The reaction mixture was washed with dilute HCl (1 M) and repeatedly washed with water, followed by drying over anhydrous $MgSO_4$. The solution was passed through a plug of activated basic alumina and evaporated to dryness to obtain the desired compound as a transparent colorless liquid. Yield: 50.1 g (88%). ^{1}H NMR (600 MHz, Chloroform-*d*) δ: 6.28 (t, *J* = 1.8 Hz, 2H), 4.22 – 4.19 (m, 2H), 3.48 – 3.44 (m, 2H), 3.42 (t, *J* = 7.1 Hz, 2H), 3.27 (s, 2H), 2.67 (s, 2H), 2.33 (t, *J* = 7.5 Hz, 2H), 1.62 (ddt, *J* = 34.6, 15.2, 7.6 Hz, 8H), 1.51 (d, *J* = 9.8 Hz, 1H), 1.36 – 1.26 (m, 6H), 1.21 (d, *J* = 9.9 Hz, 1H), 0.88 (t, *J* = 7.0 Hz, 4H), 0.57 – 0.49 (m, 4H), 0.07 (s, 278H).

Synthesis of Bottlebrush Polymers

Polymerizations of the macromonomers using G3 catalyst were performed in dilute solutions of the macromonomer (0.02 g mL^{-1}) in dry DCM. Catalyst was injected as a dilute solution in dry DCM (e.g., 500 μL of 0.029 g mL^{-1}) and the equivalents relative to macromonomer were varied depending on the target backbone degree of polymerization (N_{BB}). Polymerizations were terminated using ethyl vinyl ether after 6

hours. The resulting reaction mixtures were concentrated *in vacuo* and the polymers were precipitated in methanol. After two more consecutive precipitations of the polymers in methanol, the bottlebrush polymers were collected and dried under vacuum.

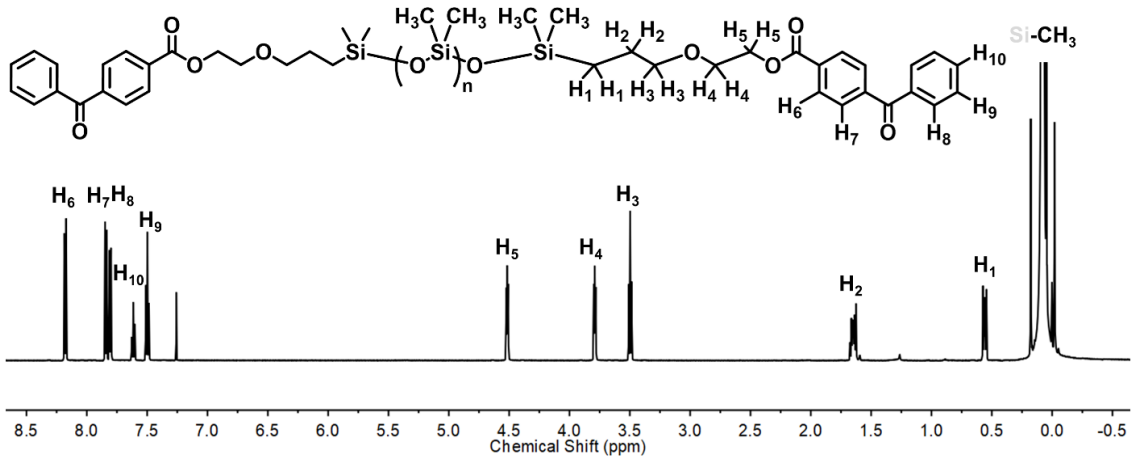

Figure A1 ^{1}H NMR of PDMS-bis-BP in $CDCl_3$.

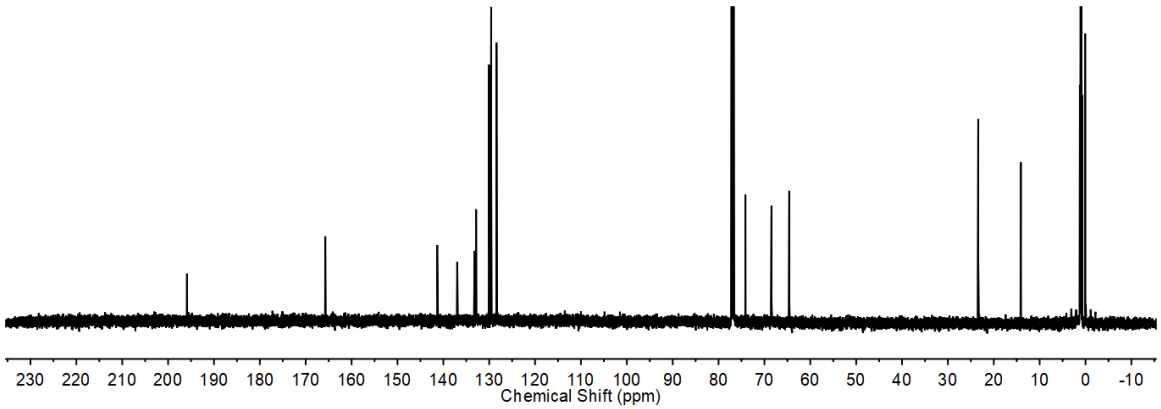

Figure A2 ^{13}C NMR of PDMS-bis-BP in $CDCl_3$.

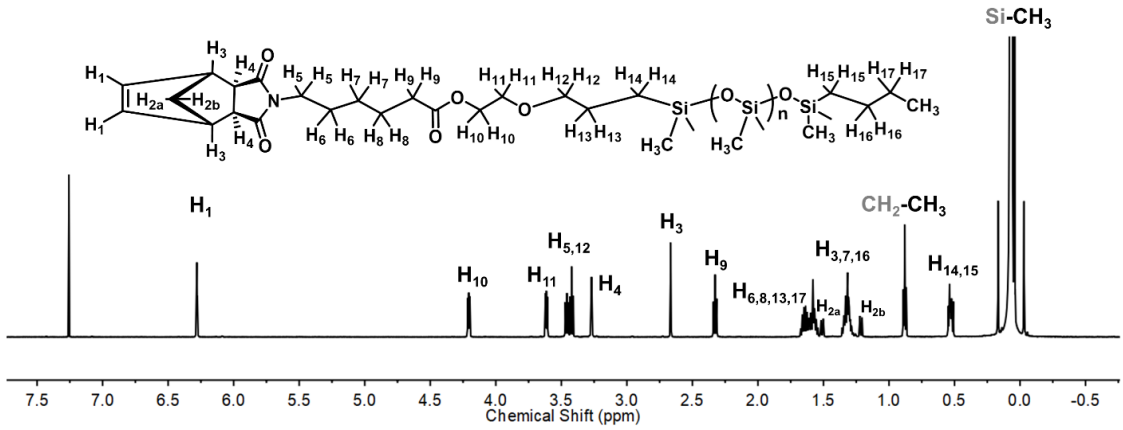

Figure A3 ^{1}H NMR of PDMS macromonomer in $CDCl_3$.

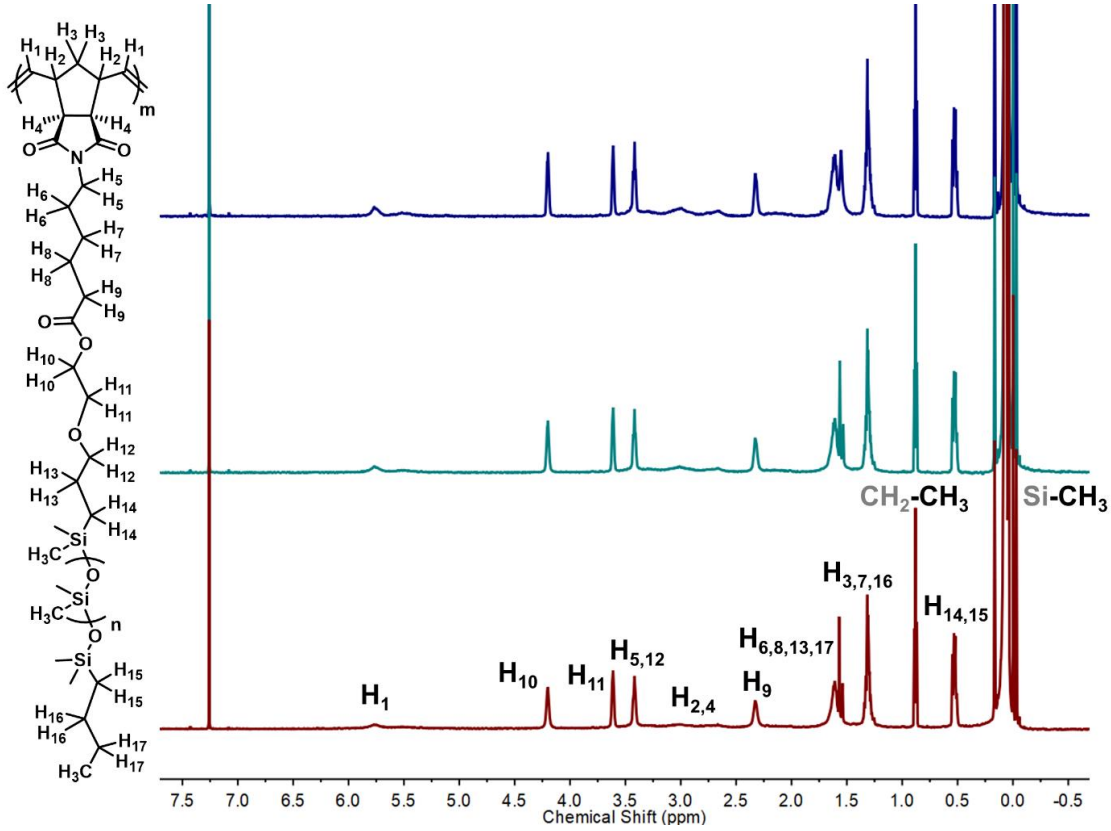

Figure A4 ^{1}H NMRs of the bottlebrush polymers in $CDCl_3$. From top to bottom: $PDMS_{68}^{20}$ (navy), $PDMS_{68}^{99}$ (teal), and $PDMS_{68}^{235}$ (maroon).

Size exclusion chromatography (SEC) was performed on a Waters Alliance HPLC System 2695 Separation Module equipped with two Agilent PLgel MiniMixed-D bed

columns and multi-angle light scattering (Wyatt DAWN HELEOS-II, 663 nm laser light) and differential refractive index (Wyatt Optilab rEX) detectors. The absolute molar mass and molar mass distribution of PDMS bottlebrush polymers was measured in tetrahydrofuran (THF) at 30 ^{0}C. Polymers were first dissolved in THF overnight with known and dilute concentrations (≤4.0 mg/mL) and then filtered through a 0.45 μm PTFE filter. The differential refractive index increment (dn/dc) was calculated by integrating the refractive index signal assuming 100% mass recovery as shown in Table A1. Although the values of dn/dc are very small (≈0.01 mL/g), the bottlebrush polymer molecular weights are still high enough to provide sufficient scattering signal in dilute solution. The number-average molar mass (M_n), molar mass dispersity (M_w/M_n), and the z-average radius of gyration ($R_{g,z}$) were determined by constructing a Zimm plot for each slice of the elution profile in Figure A5; the data are summarized in Table A1.

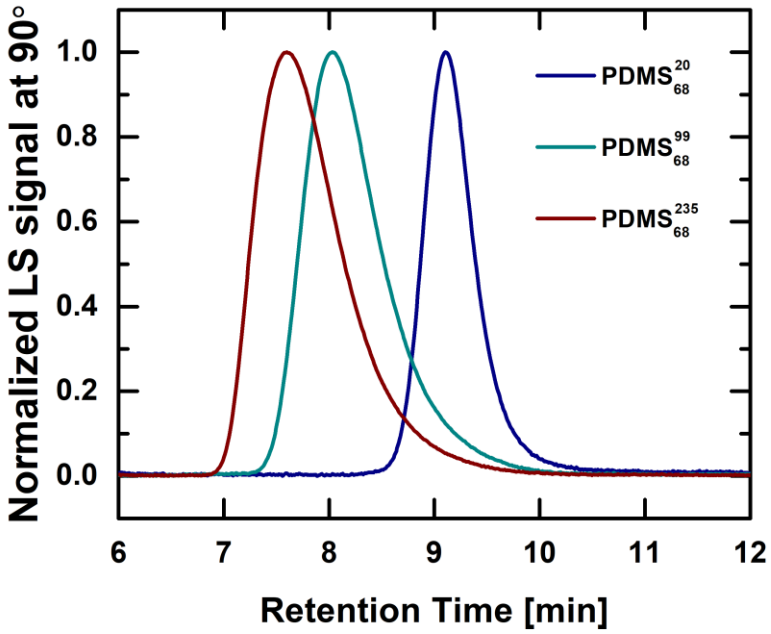

Figure A5 SEC profiles (light-scattering signal at 90°) of the bottlebrush polymers in THF.

Table A1 Characterization of the bottlebrush polymers by SEC-MALS

Material	M_n (kDa)	M_w/M_n	dn/dc (mL/g)	$R_{g,z}$ [nm]
$PDMS_{68}^{20}$	110	1.4	0.0196	6.5 ± 4.1
$PDMS_{68}^{99}$	520	1.4	0.0137	17.8 ± 0.9
$PDMS_{68}^{235}$	1200	1.4	0.0106	28.1 ± 0.5

II. Rheology

To determine the network moduli of PDMS elastomers, PDMS/crosslinker mixtures were first crosslinked *in situ* in an AR-G2 rheometer (TA Instruments). A 20-mm-diameter parallel plate geometry with a sample thickness of 0.4 mm was used for all rheology measurements in this work. For Sylgard 184, the mixture was cured by heating the sample to 150 ^{0}C for 30 mins using a Peltier plate. The frequency-dependent moduli are shown before and after this curing process in Figure A6. For photo-crosslinking PDMS bottlebrush polymers, a UV LED light source with a 365 nm wavelength and irradiance of 150 mW/cm^2 was used to cure the sample *in situ* through a UV-transparent quartz bottom plate. The curing process was monitored by tracking the time evolution of shear moduli from a viscoelastic liquid to fully crosslinked elastomer as shown in Figure 2.4a. When curing, a constant oscillatory frequency of 10 rad/s and strain amplitude of 0.01 were used.

After complete curing as indicated by a plateau in the storage modulus during light exposure, the frequency dependence of the shear moduli at 21 ^{0}C was collected

by both a small-amplitude oscillatory shear test and stress relaxation test. Specifically, Figures A7–A10 show the frequency sweep response between 100 and 0.01 rad/s with an oscillatory strain amplitude of 0.01, which is well within the linear region for $PDMS_{68}^{20}$-2, $PDMS_{68}^{20}$-4, $PDMS_{68}^{99}$-12, and $PDMS_{68}^{235}$-12. Due to the presence of slow relaxation in PDMS elastomers, a stress relaxation test with a step strain of 0.01 was also conducted to probe the long-time (or low-frequency) behavior and reach the plateau storage modulus faster. In the linear viscoelastic regime, the stress relaxation result should be equivalent to the oscillatory shear result. Thus, by fast Fourier transforming (FFT) the stress relaxation response from the time to the frequency domain,[27] its frequency response is extended to an even lower frequency value of 0.001 rad/s, where the plateau storage modulus starts to appear. Finally, the equilibrium network modulus (G_0) is determined as the plateau storage modulus at the lowest experimentally measured frequency (i.e., $G_0 = G'(0.001\ \text{rad/s})$).

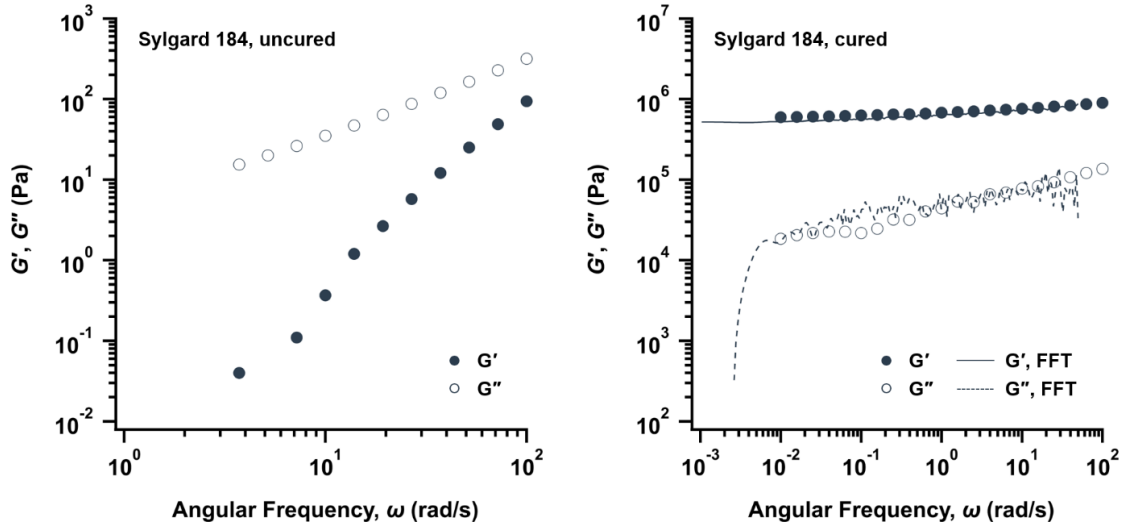

Figure A6 Frequency dependence of the shear moduli for uncured Sylgard 184 at 21 ^{0}C with an oscillatory strain amplitude of 0.05 (left) and for crosslinked Sylgard 184 at 21 ^{0}C with an oscillatory strain amplitude of 0.01 after curing at 150 ^{0}C for 30 mins (right). The stress relaxation response with a step strain of 0.01 was fast Fourier transformed (FFT) to extend the frequency range to 0.001 rad/s.

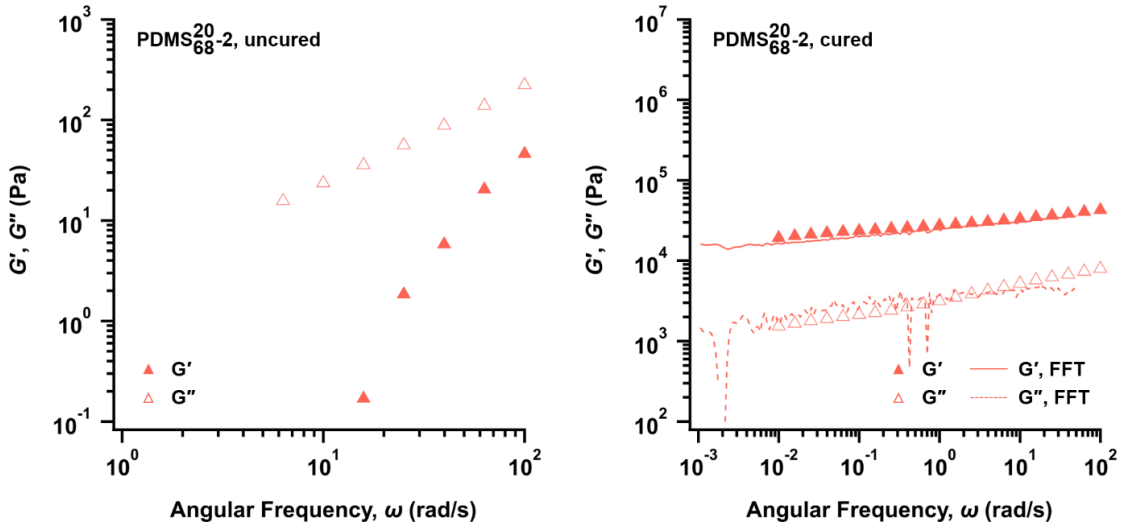

Figure A7 Frequency dependence of the shear moduli for uncured PDMS$_{68}^{20}$-2 at 21 ^{0}C with an oscillatory strain amplitude of 0.05 (left) and for crosslinked PDMS$_{68}^{20}$-2 at 21 ^{0}C with an oscillatory strain amplitude of 0.01 after complete UV curing (right). The stress relaxation response with a step strain of 0.01 was fast Fourier transformed (FFT) to extend the frequency range to 0.001 rad/s.

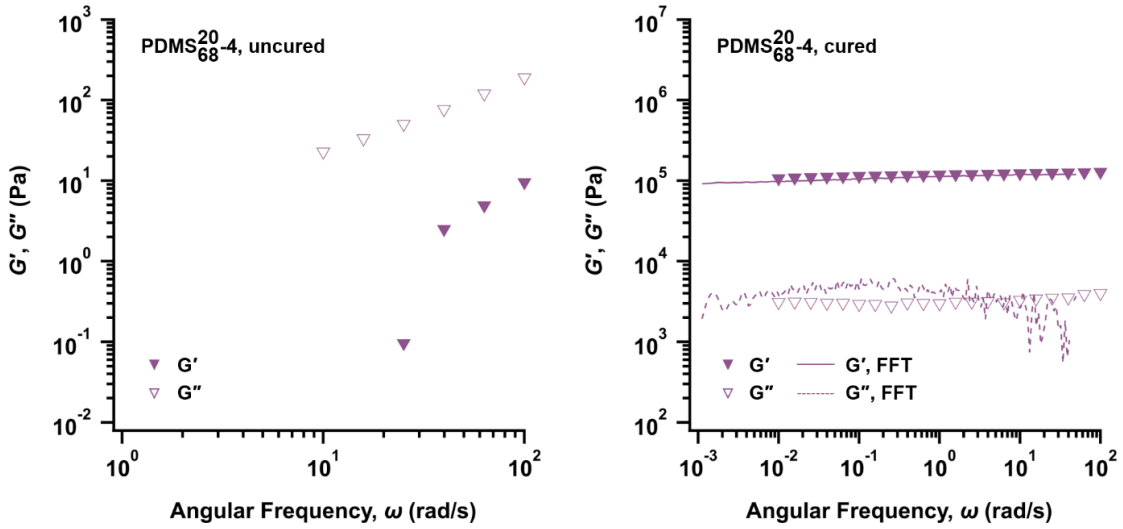

Figure A8 Frequency dependence of the shear moduli for uncured PDMS$_{68}^{20}$-4 at 21 ^{0}C with an oscillatory strain amplitude of 0.05 (left) and for crosslinked PDMS$_{68}^{20}$-4 at 21 ^{0}C with an oscillatory strain amplitude of 0.01 after complete UV curing (right). The stress relaxation response with a step strain of 0.01 was fast Fourier transformed (FFT) to extend the frequency range to 0.001 rad/s.

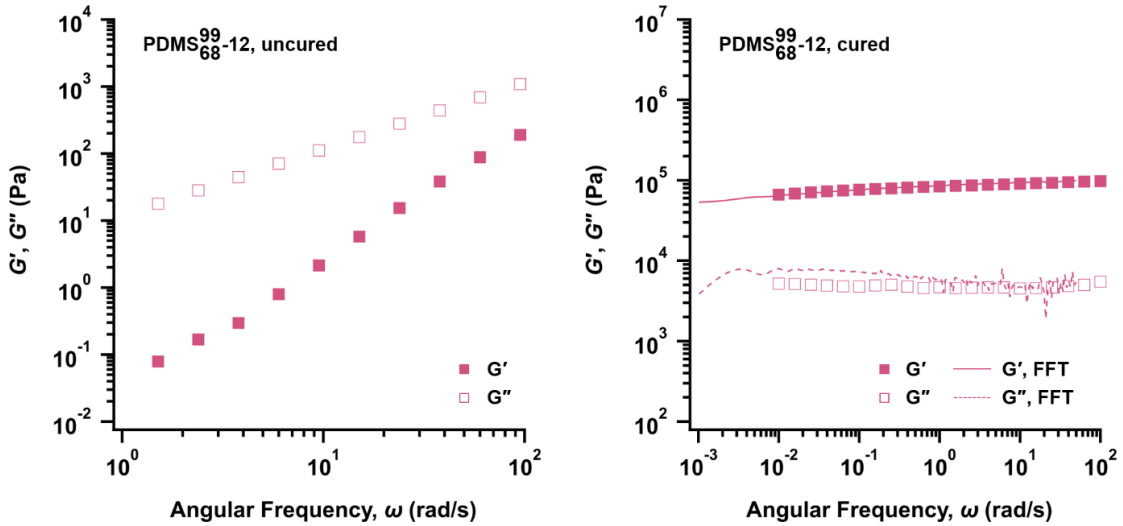

Figure A9 Frequency dependence of the shear moduli for uncured PDMS$_{68}^{99}$-12 at 21 ºC with an oscillatory strain amplitude of 0.05 (left) and for crosslinked PDMS$_{68}^{99}$-12 at 21 ºC with an oscillatory strain amplitude of 0.01 after complete UV curing (right). The stress relaxation response with a step strain of 0.01 was fast Fourier transformed (FFT) to extend the frequency range to 0.001 rad/s.

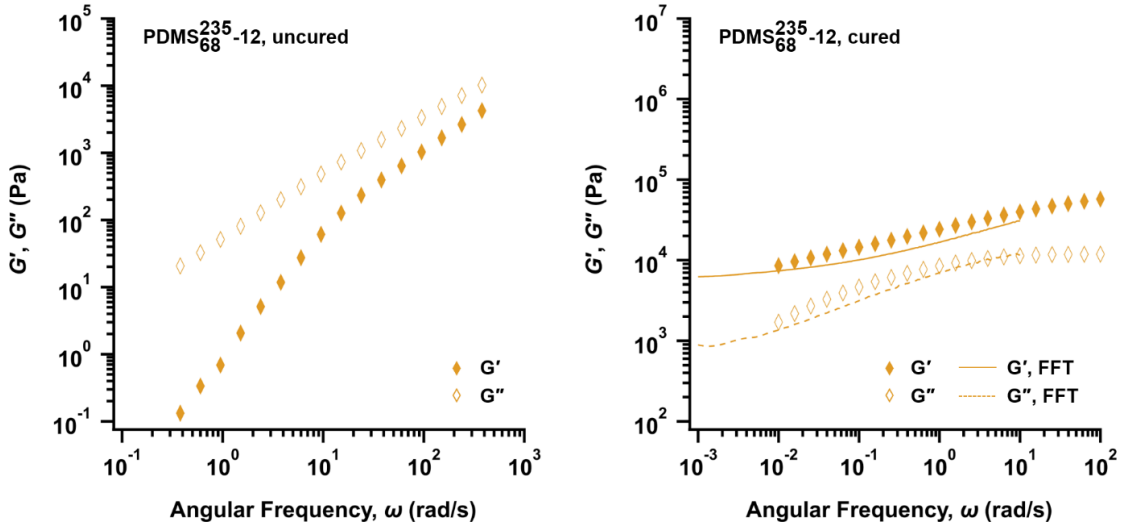

Figure A10 Frequency dependence of the shear moduli for uncured PDMS$_{68}^{235}$-12 at 21 ºC with an oscillatory strain amplitude of 0.05 (left) and for crosslinked PDMS$_{68}^{235}$-12 at 21 ºC with an oscillatory strain amplitude of 0.01 after complete UV curing (right). The stress relaxation response with a step strain of 0.01 was fast Fourier transformed (FFT) to extend the frequency range to 0.001 rad/s.

III. Dielectric and Optical Characterization

Dielectric Constant by Impedance Spectroscopy

The dielectric constants of a representative PDMS bottlebrush ($PDMS_{68}^{131}$-12) and Sylgard 184 were measured in the range of 100 Hz – 100 kHz with a 1 V amplitude using a Solartron 1260 Frequency Response Analyzer and 12962A room temperature sample holder. Figure A11 shows that the dielectric constant of the PDMS bottlebrush is 2.6 over the frequency range measured, matching that of Sylgard 184.

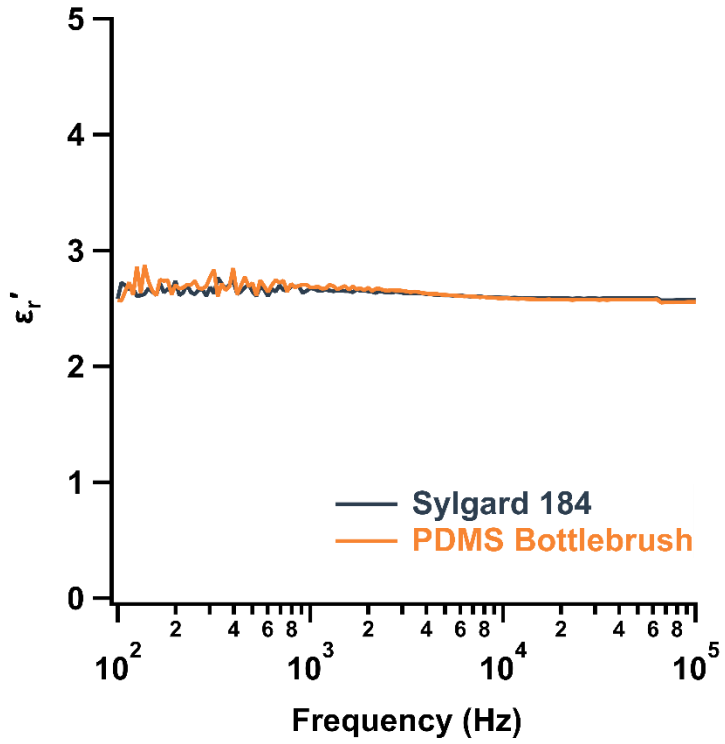

Figure A11 The frequency-dependent dielectric constant of a representative PDMS bottlebrush closely matches that of Sylgard 184.

Transmittance and Haze by UV-Vis Spectroscopy

The transmittance and haze of ITO-coated PET film (electrode material) and a sensor stack prepared with a representative PDMS bottlebrush ($PDMS_{68}^{20}$-2) were measured using a Shimadzu UV-3600 Spectrophotometer with an integrating sphere. Figure A12 shows that the transmittance and haze spectra of the sensor stack are closely matched with that of the ITO-coated PET film alone. The sensor has extremely low haze, < 1% over most of the visible spectrum.

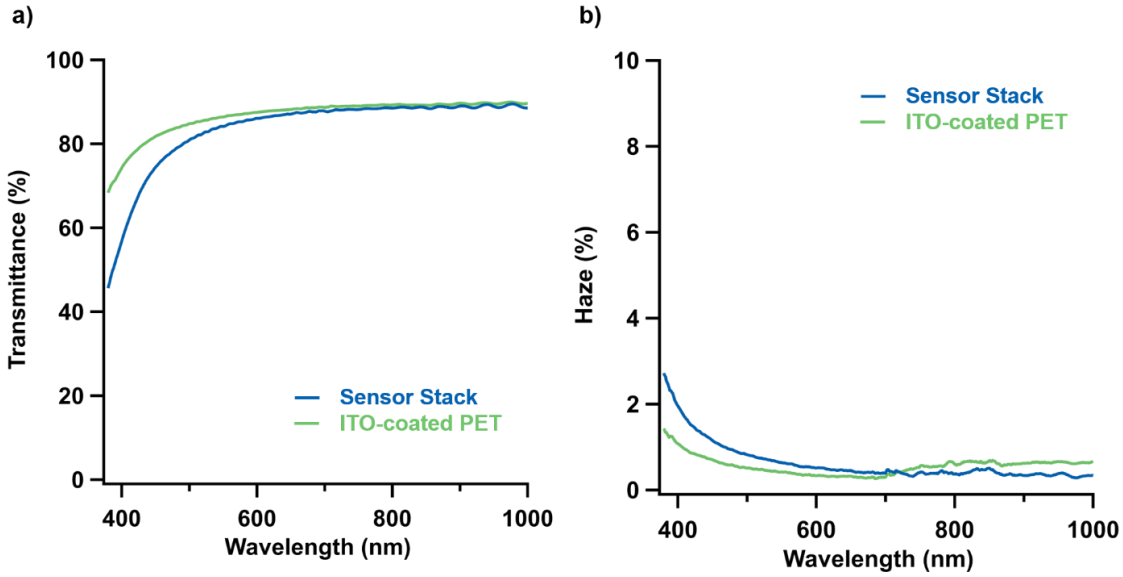

Figure A12 a) Transmittance spectra of ITO-coated PET film and a full sensor stack (two ITO-coated PET electrodes sandwiching a 0.2 mm PDMS bottlebrush film, $PDMS_{68}^{20}$-2). b) haze spectra of the same two samples.

Haze, defined as the ratio of diffuse transmittance, T_d, to total transmittance, T_t, was calculated using the following equations from ASTM D1003–13:[28]

$$T_t = \frac{T_2}{T_1}$$

$$T_{\mathrm{d}} = \frac{1}{T_1}\left[T_4 - T_3\left(\frac{T_2}{T_1}\right)\right]$$

$$\text{Haze}\ (\%) = 100 \times \frac{T_{\mathrm{d}}}{T_{\mathrm{t}}}$$

In the above equations, T_1 represents the incident light transmitted without the sample in position, T_2 represents the total light transmitted by the sample, T_3 represents the light scattered by the instrument, and T_4 represents the light scattered by the instrument and sample.

IV. Relationship Between Elastomer Modulus and Device Sensitivity

Dielectric Elastomer Between Stretchable Electrodes:

The sensor geometry implemented in this work can be simply described as a parallel plate capacitor with capacitance C given as a function of dielectric permittivity $\varepsilon_0\varepsilon_{\mathrm{r}}$, electrode area A, and dielectric thickness d:

$$C = \frac{\varepsilon_0\varepsilon_{\mathrm{r}}A}{d}$$

Assuming elastomer incompressibility (Poisson's ratio, $\nu = 0.5$), deformation of the elastomer disc in uniaxial compression can be described by the following equations for extension ratios λ (z-direction, normal to the disc face; compression) and λ' (x and y directions, in the plane of the disc face; extension):

$$\lambda = \frac{d}{d_0}$$

$$\lambda\lambda'^2 = 1$$

$$\lambda' = \frac{1}{\sqrt{\lambda}}$$

$$A = \frac{A_0}{\lambda}$$

where A_0, d_0 are defined before deformation and A, d after deformation. Combining the above equations gives the relative change in capacitance ($\Delta C/C_0$) in terms of the disc normal extension ratio λ:

$$\frac{\Delta C}{C_0} = \frac{\frac{A}{d} - \frac{A_0}{d_0}}{\frac{A_0}{d_0}}$$

$$\frac{\Delta C}{C_0} = \lambda^{-2} - 1$$

The sensitivity of the sensor is defined as the relative change in capacitance divided by the applied compressive stress σ:

$$S = \frac{\frac{\Delta C}{C_0}}{\sigma} = \frac{\lambda^{-2} - 1}{\sigma}$$

Applying the network theory of rubber elasticity,[24] the final relationship between sensitivity S, shear modulus G, and extension ratio λ is:

$$\sigma = -G\left(\lambda - \frac{1}{\lambda^2}\right)$$

$$S = \frac{1}{G[\lambda + (\lambda + 1)^{-1}]}$$

Small strain limit: $\lambda \approx 1$, $S = \frac{2}{3G}$

Dielectric Elastomer between Rigid Electrodes (Constant Area Assumption):

A similar relationship can be derived for the case of rigid electrodes (capacitive response limited to that of the thickness change):

$$\frac{\Delta C}{C_0} = \frac{\frac{1}{d} - \frac{1}{d_0}}{\frac{1}{d_0}} = \frac{d_0}{d} - 1 = \lambda^{-1} - 1$$

$$S = \frac{1}{G(\lambda + \lambda^{-1} + 1)}$$

Small strain limit, $\lambda \approx 1$: $S = \frac{1}{3G}$

Note that in the small strain limit, the sensitivity of a device with stretchable electrodes is predicted to be double that of a device with rigid electrodes.

V. Experimental Stress–Strain Data Compared to Rubber Elasticity Models

The experimental stress–strain curves for each sensor were compared to curves predicted by two different models — the network theory of rubber elasticity[24] and the bonded rubber model from Gent & Lindley[25] and Gent & Meinecke[26] (to account for the effects of elastomer adhesion to the rigid electrodes). The three highest modulus elastomers showed behavior roughly tracking the network elasticity model while the curves for the two lowest modulus elastomers moved closer to that predicted by the bonded rubber model (Figure A13 and A14). Figure A15 shows the experiment stress–strain curves plotted together for reference.

(a) Network Theory of Rubber Elasticity[24]

$$\sigma = G\left(\lambda - \frac{1}{\lambda^2}\right)$$

(b) Compression of Bonded Rubber Blocks[25,26]

$$\sigma = \frac{E_a}{3}\left(\lambda - \frac{1}{\lambda^2}\right)$$

$$E_a = 3G\left(1 + \frac{r^2}{2d_0^2}\right)$$

$$\sigma = G\left(1 + \frac{r^2}{2d_0^2}\right)\left(\lambda - \frac{1}{\lambda^2}\right)$$

r = disc radius

d_0 = initial disc thickness

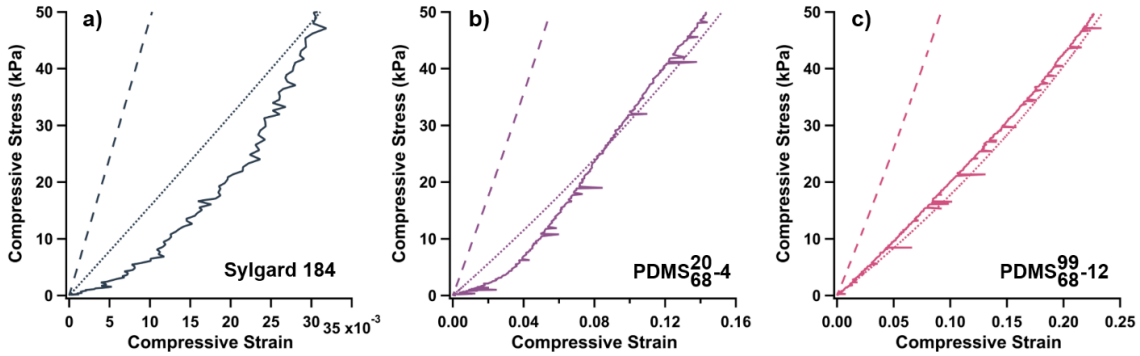

Figure A13 Stress-strain curves for the **a)** Sylgard 184, **b)** PDMS$_{68}^{20}$-4, and **c)** PDMS$_{68}^{99}$-12 sensors (solid lines) compared to theoretical curves predicted by the network theory of rubber elasticity (dotted lines) and the bonded rubber model (dashed lines). These three highest modulus conditions are roughly captured by the network theory of rubber elasticity.

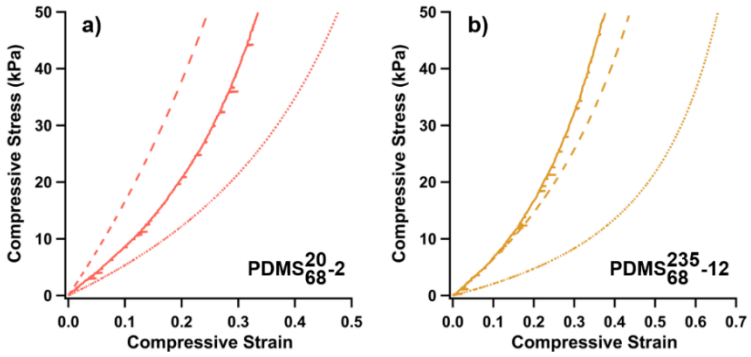

Figure A14 Stress-strain curves for the **a)** PDMS$_{68}^{20}$-2 and **b)** PDMS$_{68}^{235}$-12 sensors (solid lines) compared to theoretical curves predicted by the network theory of rubber elasticity (dotted lines) and the bonded rubber model (dashed lines). These two lowest modulus conditions show evidence of the influence of elastomer adhesion to the electrodes.

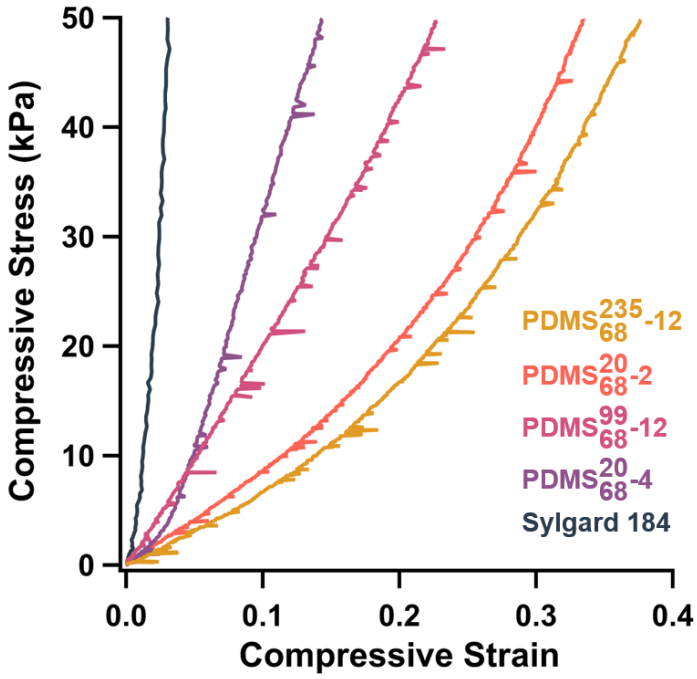

Figure A15 Stress–strain curves for the sensors tested.

VI. Table of Sensitivity Data for Elastomer-Based CPSs from Literature

Table A2 Sensitivity Data for Elastomer-Based CPSs from Literature

Elastomer Technology	Electrodes	Pressure Range (kPa)	Sensitivity (kPa^{-1})	$S/S_{control}$	Reference
Microporous Elastomer					
Prepared by sacrificial particle dispersion:					
Ecoflex + sugar granules, 44% porosity	Conductive fabric	0–100	0.0121	5.3	Atalay et al. (2018)[10]
Ecoflex + sugar cube, 63% porosity	CNT-Ecoflex composite	0–5 30–120	0.601 0.077	38 4.8	Kwon et al. (2016)[11]
Sylgard 184 + sugar granules, 89% porosity	ITO-coated PET	0–10 10–100	0.51285 0.01097	8.2 1.3	Yoon et al. (2017)[12]
Sylgard 184 + 6 μm poly(styrene) beads	ITO-coated PET	0–1	0.63	7.9	Kang et al. (2016)[13]
Prepared by water droplet dispersion:					
Sylgard 184 + 30 w% dispersed water	ITO-coated PET	0–0.1	0.8	4.0	Lee et al. (2016)[14]
Micropatterned Elastomer					
Sylgard 184, 6 μm pyrimidal features	ITO-coated PET	0–2 2–7	0.55 0.15	28 7.5	Mannsfeld et al. (2010)[4]
Polyurethane nano-needles	Aluminum foil	0–1 1–6	1.76 0.0268	17 1.1	Kim et al. (2012)[29]
Bulk Bottlebrush Elastomer					
PDMS Bottlebrush Elastomers	ITO-coated PET	0–10 20–50	0.0087 0.0053	22 53	This work

VII. Step Compression Examples

Step compressions of 1 kPa and 10 kPa were applied to the $PDMS_{68}^{99}$-12 and $PDMS_{68}^{235}$-12 sensors using a TA Instruments DMA 850. As expected from rheology studies, the $PDMS_{68}^{99}$-12 sensor exhibits more rapid response times than the $PDMS_{68}^{235}$-12 sensor (Figure A16).

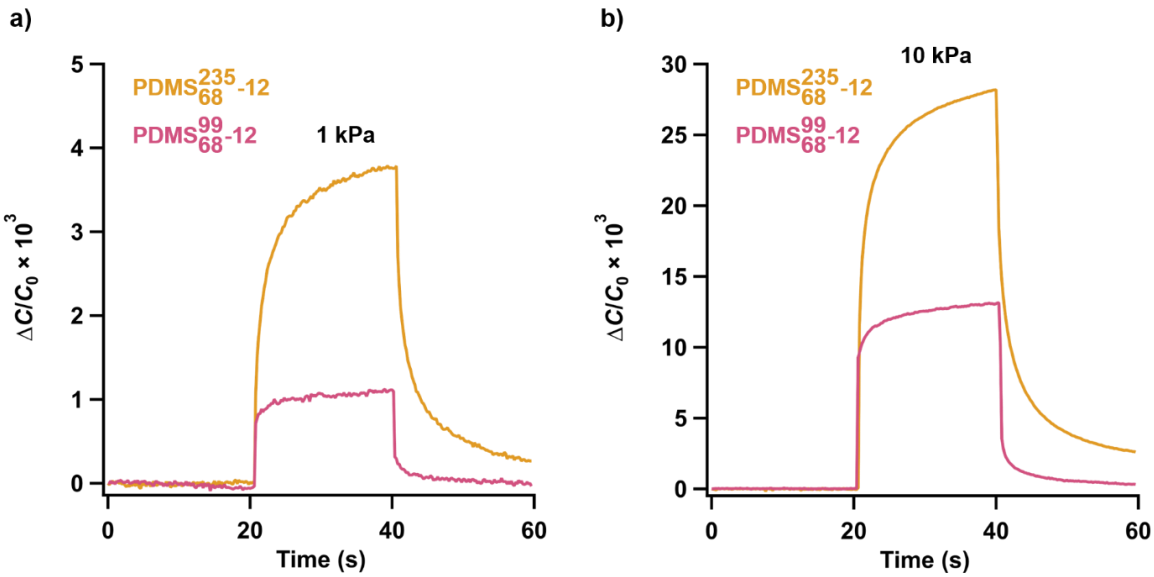

Figure A16 Sensor response to step compressions of **a)** 1 kPa, and **b)** 10 kPa.

VIII. Sensor Flexibility Demonstration

To demonstrate the mechanical flexibility of the sensor, a fixture was designed to apply compressive strain in a bent configuration (see inset of Figure A17; curvature κ = 0.55 cm^{-1}). The response curve of a representative PDMS bottlebrush elastomer sensor (prepared with $PDMS_{68}^{131}$-12; 12.7 mm diameter electrodes and elastomer) was measured using the strain-controlled test set-up with a 44 N load cell (Figure A17). The bent configuration applies a gradient pre-strain with a point of zero strain in the middle of the layer.

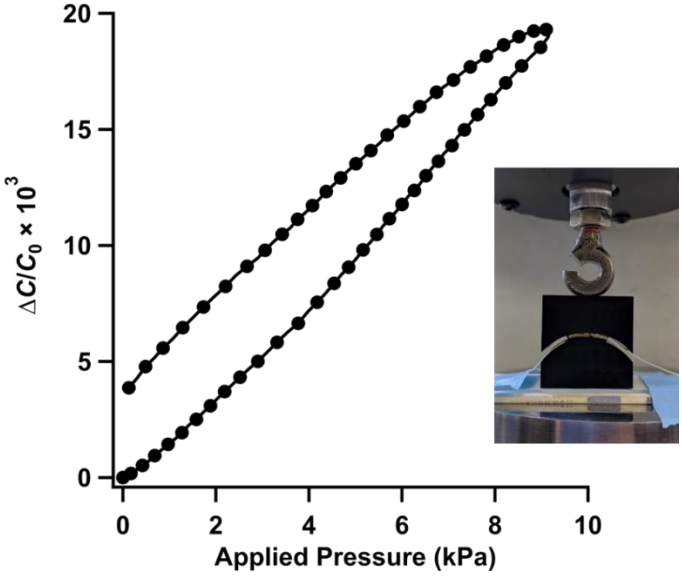

Figure A17 Sensor response curve for a bottlebrush elastomer CPS in a bent configuration.

2.8 References

1. Sun, J.-Y., Keplinger, C., Whitesides, G. M. & Suo, Z. Ionic skin. *Advanced Materials* 26, 7608–7614 (2014).
2. Wagner, S. & Bauer, S. Materials for stretchable electronics. *MRS Bulletin* 37, 207–213 (2012).
3. Zang, Y., Zhang, F., Di, C. A. & Zhu, D. Advances of flexible pressure sensors toward artificial intelligence and health care applications. *Materials Horizons* 2 140–156 (2015).
4. Mannsfeld, S. C. B. et al. Highly sensitive flexible pressure sensors with microstructured rubber dielectric layers. *Nature Materials* 9, 859–864 (2010).
5. Ilievski, F., Mazzeo, A. D., Shepherd, R. F., Chen, X. & Whitesides, G. M. Soft robotics for chemists. *Angewandte Chemie International Edition* 50, 1890–1895 (2011).
6. Mark, J. E. Polymer Data Handbook. Oxford University Press (2009).
7. Brochu, P. & Pei, Q. Advances in Dielectric Elastomers for Actuators and Artificial Muscles. *Macromolecular Rapid Communications* 31, 10–36 (2010).
8. Lei, K. F., Lee, K. F. & Lee, M. Y. Development of a flexible PDMS capacitive pressure sensor for plantar pressure measurement. *Microelectronic Engineering* 99, 1–5 (2012).
9. Lei, Z., Wang, Q., Sun, S., Zhu, W. & Wu, P. A Bioinspired Mineral Hydrogel as a Self-Healable, Mechanically Adaptable Ionic Skin for Highly Sensitive Pressure Sensing. *Advanced Materials* 29, 1700321 (2017).
10. Atalay, O., Atalay, A., Gafford, J. & Walsh, C. A Highly Sensitive Capacitive-Based Soft Pressure Sensor Based on a Conductive Fabric and a Microporous Dielectric Layer. *Advanced Materials Technologies* 3, 1700237 (2018).
11. Kwon, D. et al. Highly Sensitive, Flexible, and Wearable Pressure Sensor Based on a Giant Piezocapacitive Effect of Three-Dimensional Microporous Elastomeric Dielectric Layer. *ACS Applied Materials & Interfaces* 8, 16922–16931 (2016).
12. Yoon, J. Il, Choi, K. S. & Chang, S. P. A novel means of fabricating microporous structures for the dielectric layers of capacitive pressure sensor. *Microelectronic Engineering* 179, 60–66 (2017).
13. Kang, S. et al. Highly Sensitive Pressure Sensor Based on Bioinspired Porous Structure for Real-Time Tactile Sensing. *Advanced Electronic Materials* 2, 1600356 (2016).
14. Lee, B. Y., Kim, J., Kim, H., Kim, C. & Lee, S. D. Low-cost flexible pressure sensor based on dielectric elastomer film with micro-pores. *Sensors and Actuators A: Physical* 240, 103–109 (2016).
15. Neugebauer, D., Zhang, Y., Pakula, T., Sheiko, S. S. & Matyjaszewski, K. Densely-grafted and double-grafted PEO brushes via ATRP. A route to soft elastomers. *Macromolecules* 36, 6746–6755 (2003).
16. Daniel, W. F. M. et al. Solvent-free, supersoft and superelastic bottlebrush melts and networks. *Nature Materials* 15, 183–189 (2016).

17. Sheiko, S. S., Sumerlin, B. S. & Matyjaszewski, K. Cylindrical molecular brushes: Synthesis, characterization, and properties. *Progress in Polymer Science* 33 759–785 (2008).
18. Rzayev, J. Molecular bottlebrushes: New opportunities in nanomaterials fabrication. *ACS Macro Letters* 1 1146–1149 (2012).
19. Lin, T. P. et al. Control of Grafting Density and Distribution in Graft Polymers by Living Ring-Opening Metathesis Copolymerization. *Journal of the American Chemical Society* 139, 3896–3903 (2017).
20. Xia, Y., Kornfield, J. A. & Grubbs, R. H. Efficient synthesis of narrowly dispersed brush polymers via living ring-opening metathesis polymerization of macromonomers. *Macromolecules* 42, 3761–3766 (2009).
21. Jha, S., Dutta, S. & Bowden, N. B. Synthesis of ultralarge molecular weight bottlebrush polymers using Grubbs' catalysts. *Macromolecules* 37, 4365–4374 (2004).
22. Cai, L. H. et al. Soft Poly(dimethylsiloxane) Elastomers from Architecture-Driven Entanglement Free Design. *Advanced Materials* 27, 5132–5140 (2015).
23. Vatankhah-Varnosfaderani, M. et al. Mimicking biological stress-strain behaviour with synthetic elastomers. *Nature* 549, 497–501 (2017).
24. Treloar, L. R. G. The Physics of Rubber Elasticity, 3rd Ed. Oxford University Press, Oxford, UK (2005).
25. Gent, A. N. & Lindley, P. B. The Compression of Bonded Rubber Blocks. *Proceedings of the Institution of Mechanical Engineers* 173, 111–122 (1959).
26. Gent, A. N. & Meinecke, E. A. Compression, bending, and shear of bonded rubber blocks. *Polymer Engineering & Science* 10, 48–53 (1970).
27. Tassieri, M. et al. i-Rheo: Measuring the materials' linear viscoelastic properties "in a step"! *Journal of Rheology* 60, 649–660 (2016).
28. Standard Test Method for Haze and Luminous Transmittance of Transparent Plastics. https://www.astm.org/Standards/D1003.htm.
29. Kim, J., Nga Ng, T. & Soo Kim, W. Highly sensitive tactile sensors integrated with organic transistors. *Applied Physics Letters* 101, 103308 (2012).

2.9 Permissions and Attributions

Chapter 3: Soft carbon nanotube composites with bottlebrush polymer networks for compliant electrodes

3.1 Abstract

Wearable electronics and biointerfacing technology require materials that are both compliant and conductive. The typical design strategy exploits polymer composites containing conductive particles, but the addition of a hard filler generally leads to a substantial increase in modulus that is not well-matched to biological tissue. Here, we

report a new class of supersoft, conductive composites comprising carbon nanotubes (CNT) embedded in bottlebrush polymer networks. By virtue of the bottlebrush polymer architecture, these materials are several orders of magnitude softer than comparable composites in the literature involving linear polymer networks. For example, a CNT content of 0.25 wt % yields a shear modulus of 66 kPa while maintaining a typical conductivity for a CNT composite (ca. 10^{-2} S/m). An added benefit of this bottlebrush matrix chemistry is the presence of dynamic polyester bonds that facilitate thermal (re)processing. This unique strategy of designing soft composites provides new opportunities to tailor the structure and properties of sustainable advanced materials.

3.2 Introduction

Electronic devices made with soft and elastic components offer unique functionality compared to conventional, rigid silicon-based materials.[1] These compliant electronics have been developed for applications such as monitoring of physiological signals (e.g., electrocardiography, electroencephalography),[2] electronic skin for prosthetics and soft robotics,[3–5] and body motion tracking for injury rehabilitation and the assessment of motor control disorders.[6] These and other biointerfacing/mimicking devices require elastomers with electrical and mechanical properties that are atypical of conventional (insulating) rubbery networks. A variety of strategies have been developed to improve the electrical properties of elastomers by adding a second material, including blends with semiconducting polymers and composites containing conductive hard particles.[7–12] Carbon nanotubes (CNTs) are an ideal conductive filler due to their flexibility and high aspect ratio, which enable percolation at lower

loadings than spherical particles.[13] However, adding any type of hard filler into a polymer presents an intrinsic challenge with respect to mechanical properties — the percolated filler network that imparts conductivity also significantly increases stiffness beyond values that are ideal for biointerfacing devices.[14]

A potential solution to this dichotomy lies in controlling polymer architecture. Bottlebrush polymer networks are known to be ~1–2 orders of magnitude softer than comparable linear networks because architecture effects suppress entanglements.[15] This results in mechanical properties comparable to hydrogels and soft biological tissue but without the use of solvent or plasticizer.[15–17] Such unusually low moduli[15] have already been exploited to improve the performance of functional devices such as capacitive pressure sensors with enhanced sensitivity,[18] dielectric actuators,[19] and stimuli-responsive composites.[20] We reasoned this class of materials would also overcome current and future challenges in elastomeric conductors by maintaining a low stiffness even in the presence of conductive CNT fillers.

To address this opportunity, here we report a new class of supersoft (shear moduli 66–140 kPa), electrically conductive (1×10^{-2} – 9×10^{-2} S/m) bottlebrush polymer composites containing CNT fillers. In addition to excellent CNT dispersion as facilitated by a novel, solvent-free curing method, these materials include a rubbery polyester side-chain chemistry that is dynamic at elevated temperatures (180 °C). This facilitates (re)processing while also maintaining excellent mechanical integrity under ambient conditions — important attributes in sustainable device design. Collectively, these findings establish a new materials platform for conductive composites and

highlight the utility of exploiting highly branched polymer architectures in advanced applications.

3.3 Results and Discussion

Composite Design and Synthesis

Our process for forming soft, conductive composites consists of several key steps: (1) synthesizing and characterizing bottlebrush polymer precursors, (2) dispersing carbon nanotubes in a solvent-free formulation containing the bottlebrush precursor, a cross-linker, and a reactive plasticizer, and (3) curing the mixture to form all-solid elastomeric composites. Below, we detail the design and chemistry used in each step.

While there are a number of synthetic strategies available to form bottlebrush networks,[21–30] we selected a versatile two-step process[17,18,23,29,30] involving (i) the synthesis of well-defined bottlebrush precursors via "grafting-through" polymerization followed by (ii) formulation and cross-linking. As previously demonstrated, this approach allows for the rigorous characterization of bottlebrush precursors prior to cross-linking.[17,18,30,31]

Poly(4-methylcaprolactone) (P4MCL) was selected as the bottlebrush side-chain chemistry, since it forms robust elastomers at room temperature due to its low glass transition temperature ($T_g \approx -60$ °C) and lack of crystallinity.[17,32] Two bis-telechelic P4MCL homopolymers (2.1 and 1.7 kDa, both below the reported entanglement molecular weight of 2.9 kDa[33]) were synthesized via ring-opening polymerization (ROP) from a norbornene–alcohol initiator using tin ethylhexanoate (SnOct2) as the catalyst following reported procedures.[17] This results in P4MCL

macromonomers with a single norbornene end group that can undergo ring-opening metathesis polymerization to construct the bottlebrush backbone as well as a single hydroxy chain end. The latter serves two purposes: (1) as a reactive nucleophile for cross-linking and (2) as a source of hydroxyl units for dynamic polyester exchange reactions at elevated temperatures in the presence of a Lewis acid.[17,34,35]

P4MCL macromonomers were subjected to the Grubbs third-generation catalyst in various stoichiometries to synthesize bottlebrush homopolymers with different backbone (N_{BB}) and side-chain (N_{SC}) degrees of polymerization (see Appendix B, Figures B1 and B2). In principle, larger values of N_{BB} are preferable, since they yield softer networks,[17,30] but in the context of composites, there is a practical upper limit due to the viscosity before curing, which also increases with the bottlebrush precursor molecular weight. High-N_{BB} (~400) bottlebrush polymers were too viscous to be compatible with our solvent-free, centrifugal-mixing-based CNT dispersion process (see below). Instead, we found that intermediate-N_{BB} bottlebrush polymers (~100) optimally balanced the trade-off between precured viscosity and postcured softness.

Even with reduced N_{BB} values, these bottlebrush polymers have high molecular weights and viscosities, making it difficult to mix CNTs in the bulk without solvent. To facilitate mixing during CNT dispersion, we plasticized the bottlebrush polymer with 4-methylcaprolactone (4MCL) monomer. Typically, the use of a nonreactive plasticizer would be undesirable as leaching can occur over time from the final material. However, due to the living nature of ring-opening polymerization (which was used to synthesize the macromonomer), 4MCL is incorporated directly into the

bottlebrush network during thermal cross-linking by reinitiation and propagation from the hydroxyl groups at the ends of side chains or those formed after reaction with the cross-linker (shown schematically in Figure 3.1a and structurally in Figure 3.1b). This approach conveniently allows for the use of plasticizer during processing while ensuring the final material lacks residual small molecules.

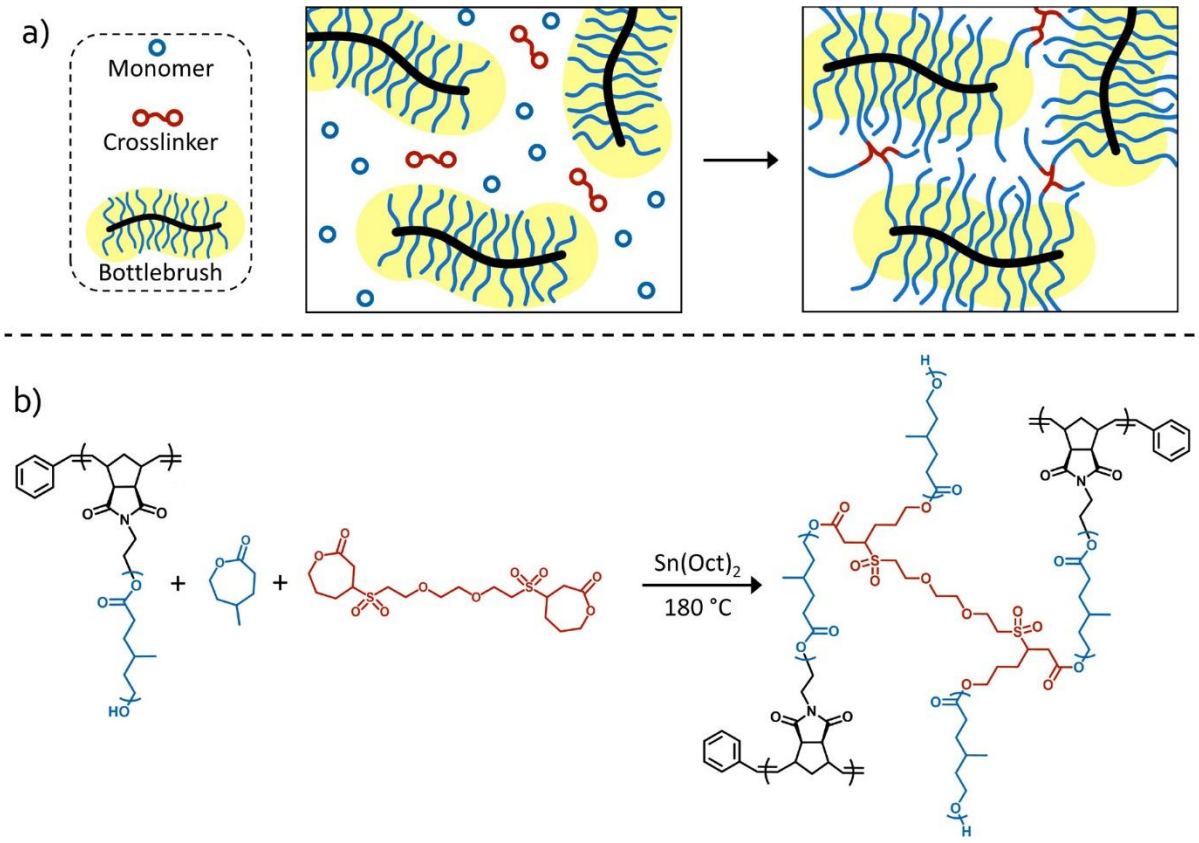

Figure 3.1 (a) Schematic representation of bottlebrush polymer network formation; note the bottlebrush polymer side chains are capable of reinitiation and complete incorporation of the monomer, which results in an all-solid material after cross-linking. (b) Chemical structures of the various resin components and the resulting bottlebrush polymer network.

To further complement this strategy, we designed a new bis-lactone-based cross-linker with improved solubility in 4MCL monomer and P4MCL bottlebrush over previous analogues (Appendix B, Figures B3 and B4).[17,32,36] The two-step synthesis enables the inclusion of a bridging chain between two caprolactone units, promoting

improved solubility and reduced crystallinity. Using thiol–ene chemistry, a thiol-terminated triethylene glycol was used to tether two cyclic ketones. The thioethers generated in the first step were then oxidized to sulfones, which have far greater oxidative stability than thioethers,[37] while simultaneously generating the bis-lactone structure necessary to drive network formation.

Mechanical Characterization of Polymer Networks and Composites

We first focus on the curing of neat P4MCL bottlebrush networks without CNTs to assess the efficiency of our new cross-linker. A series of formulations was prepared from a 170 kDa bottlebrush polymer (N_{BB} = 85, N_{SC} = 15) with varying amounts of cross-linker (0.5–3 wt %) at constant catalyst (1.5 wt %) and monomer (20 wt %) loading (see Appendix B, Tables B1–B4). Network formation proceeds rapidly at 180 °C, nearing complete conversion within 10 min as evidenced by *in situ* rheometry (Figure 3.2a); the storage (G′) and loss (G″) moduli quickly increase and plateau with a ~10× separation that indicates robust network formation. After curing, the samples were immediately cooled to 25 °C and frequency sweeps were used to measure the rubbery plateau modulus (Figure 3.2b). The final materials showed low-plateau moduli from 18 to 160 kPa (values well within the range of various biological tissue[38]) that were easily tuned through formulation. To ensure the low moduli values were not a result of unreacted monomer plasticizing the networks, sol–gel measurements were performed in duplicate for both the 0.5 and 1 wt % cross-linker samples. The average gel fractions were found to be 86 and 94% (Appendix B, Table B5), respectively, indicating that the monomer introduced during processing is successfully

incorporated into the networks. The lowest cross-linker loading (0.5 wt %) was selected for CNT composites to target supersoft materials.

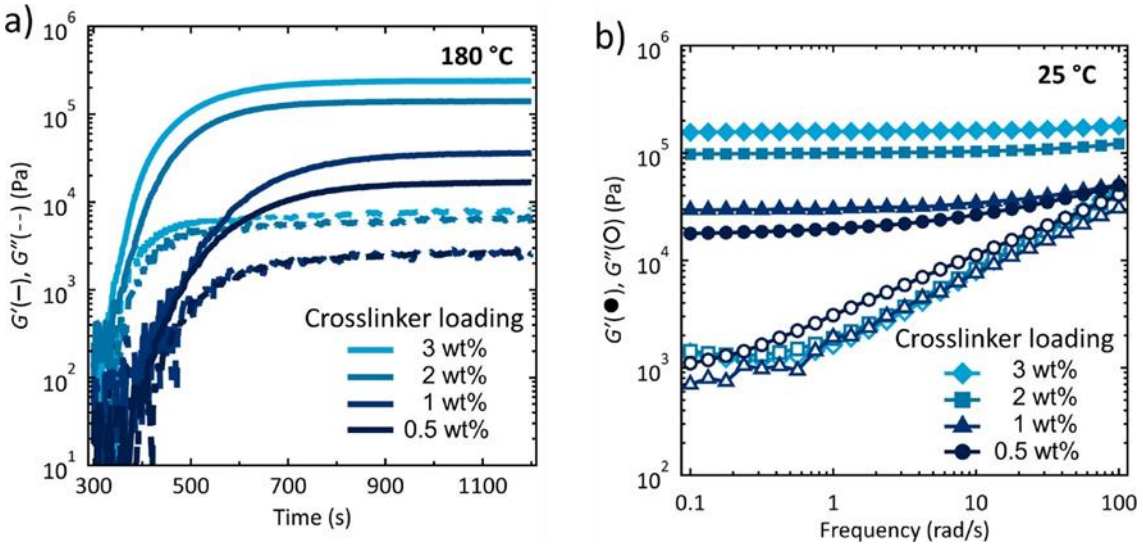

Figure 3.2 Rheological characterization of neat bottlebrush networks (no added CNTs) starting from a 170 kDa bottlebrush precursor (N_{BB} = 85, N_{SC} = 15). (a) *In situ* curing of various bottlebrush polymer resins truncated to highlight the region of interest; for full traces, refer to Appendix B, Figure B5. (b) Frequency-dependent modulus data capturing the room temperature rubbery plateau.

Various strategies have been developed to improve the dispersion of CNT filler in polymer networks, which is crucial for optimizing composite properties. Examples include increasing the chemical compatibility of CNTs with a polymer matrix (e.g., CNT surface functionalization or adding surfactant/dispersant molecules) and employing aggressive mixing techniques including ultrasonication or bead milling. Here, uniform CNT dispersions were achieved by mechanically mixing CNT powder into a 150 kDa bottlebrush polymer precursor (N_{BB} = 88, N_{SC} = 12) plasticized by 14 wt % 4MCL monomer. To better promote shear forces and break up of CNT agglomerates, ceramic cylinders were added; see Appendix B, Figure B6. As evidenced by optical microscopy (Figure 3.3), scanning electron microscopy (Appendix B, Figure B7), and small-angle X-ray scattering (Appendix B, Figure B8), this simple mixing

process yields homogeneously dispersed CNT-doped bottlebrush polymer resins. The batch sizes in this study were approximately 1 g, which is amenable for screening various formulations and small-scale prototyping; we note that this mixing process is readily scaled up.

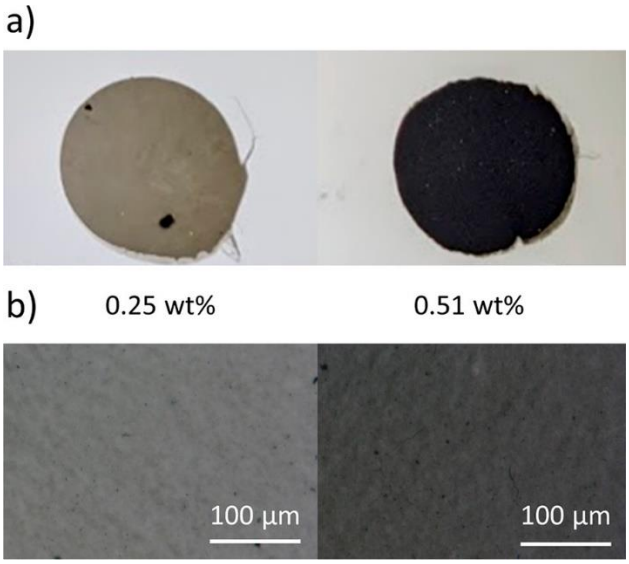

Figure 3.3 (a) Photographs of two thin films with 0.25 and 0.51 wt % CNTs after mechanical mixing. (b) Optical micrographs confirm the efficient dispersion of CNTs in P4MCL bottlebrush polymers.

For the composite materials, guided by our results on unfilled formulations, a cross-linker loading of 0.5 wt % was selected to minimize the resulting sample stiffness while retaining excellent curing characteristics. The final formulation of these samples was analogous to those shown in Figure 3.2 but with 0.25% and 0.51% CNTs by weight (full details are provided in Appendix B, Tables B6–B8). Although many filler materials require substantially higher loadings to form percolating networks, the high aspect ratio of CNTs enables percolation at these low percentages.[39,40] Note that even prior to network formation, these samples showed characteristic elasticity induced by

the presence of CNTs as observed in precuring frequency sweeps, which contain a rubbery plateau at low frequencies (Appendix B, Figure B9).

The curing traces in Figure 3.4a show that CNTs prevent the development of a flat plateau at long times. When heated beyond the 20 min required to cure the matrix network, composite samples exhibit a small and steady rise in modulus (~1 kPa/min). An effect of this magnitude would be negligible in typical composite systems where the moduli are several orders of magnitude higher, but in these soft materials (G' ≈ 10–100 kPa), it is readily apparent. We hypothesize this secondary curing stems from reactions between the bottlebrush polymer (specifically, hydroxyl groups at the ends of side chains) and functional group defects on the CNT surface (e.g., carboxylic acids and esters).[41] In the absence of cross-linker and catalyst, this behavior persists (as shown in Appendix B, Figure B10), further indicating that side reactions between the bottlebrush polymer and CNT surface could account for the rise in modulus.

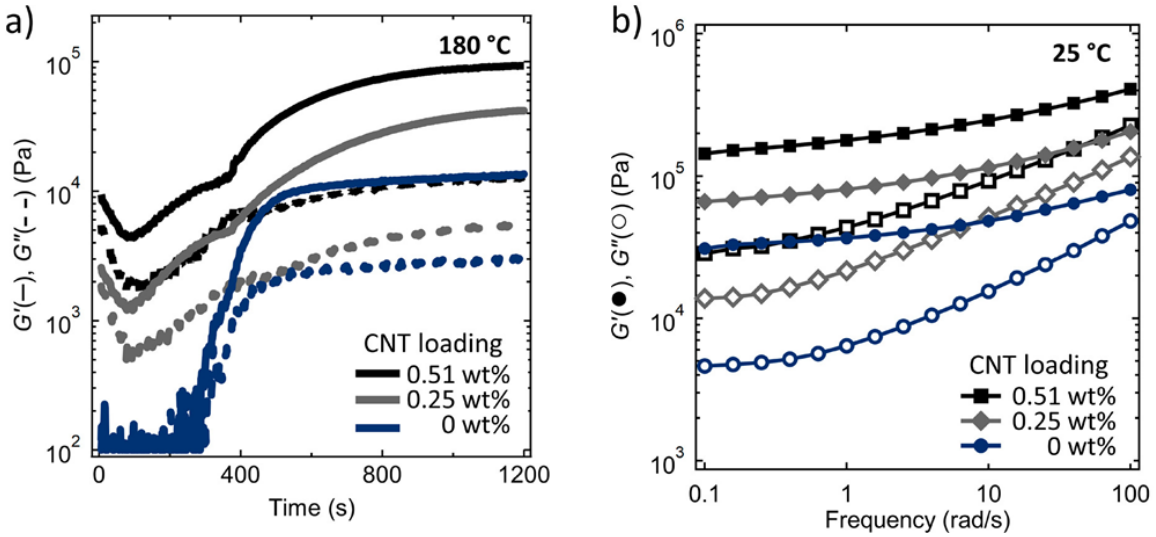

Figure 3.4 (a) Bottlebrush–CNT composites cure rapidly at 180 °C starting from a 150 kDa bottlebrush precursor (N_{BB} = 88, N_{SC} = 12). (b) Room temperature frequency sweeps after curing show a soft rubbery plateau.

Significantly, this behavior only occurs at elevated temperatures and not under ambient conditions.

When cooled to room temperature, samples with 0, 0.25, and 0.51 wt % CNTs have shear moduli (G') of 31, 66, and 140 kPa, respectively (as measured by rheometry, Figure 3.4b). Note that the 0% CNT sample is stiffer than the sample of similar composition reported in Figure 3.2 due to the lower molecular weight of the bottlebrush polymer precursor. Dynamic polyester–CNT composites of similar filler loading (0.25 wt % CNT) but prepared with a linear polymer reportedly have a shear modulus ~70 MPa, nearly 3 orders of magnitude stiffer than the composites described here.[42] Notably, a recent report achieved a dynamic composite with a similar modulus to our materials (0.5 wt % CNT, 64 kPa) but only after 70 wt % plasticizer was added.[43] We caution that directly comparing the modulus of different composites can be problematic, as it is highly dependent on both the dispersion process and polymer matrix chemistry.[14,39] Nevertheless, our bottlebrush composites are significantly softer than others reported in the literature.

Electrical Properties of Bottlebrush–CNT Composites

Next, we sought to characterize the electrical impedance of our samples to understand the relationship between CNT loading and conductivity. The electrical properties of our bottlebrush–CNT composites were measured by AC impedance spectroscopy. Both the 0.25 and 0.51 wt % CNT composites exhibited stable conductivity across a wide frequency range (Figure 3.5a). Samples had frequency-independent resistance and in-phase current and voltage (typical of ideal resistors) in this frequency range, with negligible capacitance (Appendix B, Figure B11). The DC conductivity, σ_{DC}, was

calculated from the plateau value of the resistance in the low-frequency limit (0.1 Hz). The 0.25 and 0.51 wt % samples had DC conductivities of 1×10^{-2} and 9×10^{-2} S/m, respectively, as shown in Table 3.1. Conductivity increased with CNT loading as expected, and the values were in the range of previously reported composites with similar CNT loadings (Appendix B, Figure B12). The measured conductivity of the composites improved with increasing DC bias, which indicates contact resistance at the electrode–elastomer interfaces (Appendix B, Figure B13). Therefore, the intrinsic conductivities may be higher than reported. Both composites exhibited relatively steady conductivity over time under a 4.5 V DC bias (Appendix B, Figure B14). To show that the composite is functional in a practical application, we used one in a simple light-emitting diode (LED) circuit (Figure 3.5b). A 0.51 wt % CNT sample formed with appropriate dimensions acted as a resistor in series with a green LED and a 9 V battery; this circuit shows that device-relevant voltages can be applied to the

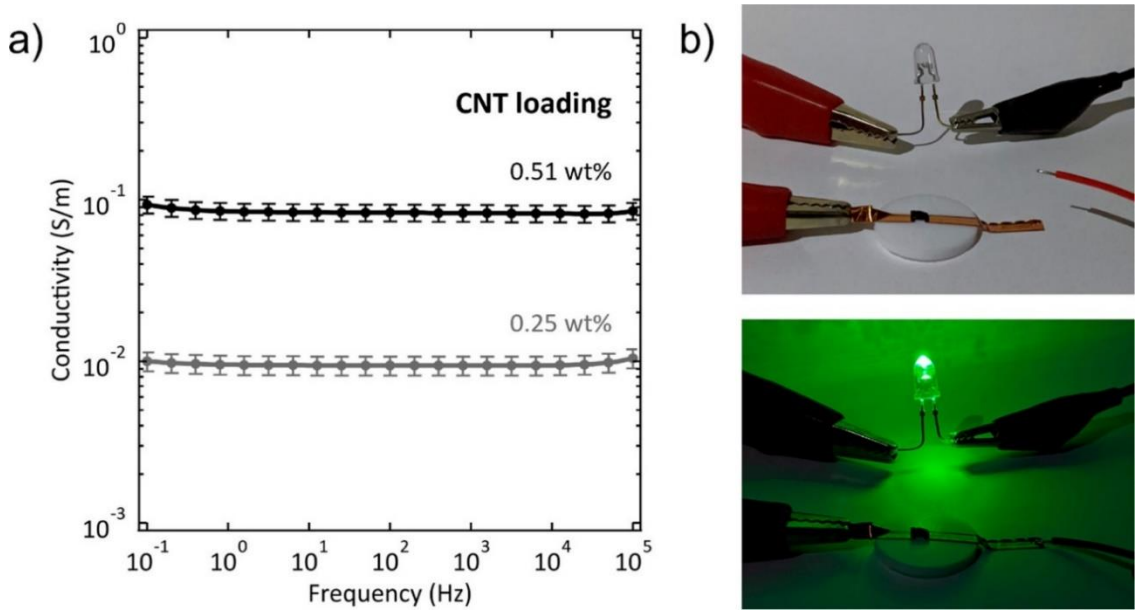

Figure 3.5 (a) Conductivity of the 0.25 and 0.51 wt % CNT composite samples measured in the frequency range of 0.1 Hz to 100 kHz (100 mV AC amplitude, no bias). (b) Photographs of the 0.51 wt % CNT sample used as a resistor to modulate the current in an LED circuit.

bottlebrush–CNT composite and that DC electrical current does not lead to degradation.

Table 3.1 Summary of Bottlebrush–CNT Composite Properties

CNT Concentration (wt%)	Shear Modulus (kPa)	Conductivity (S/m)
0	31	-
0.25	66	$(1 \pm 0.1) \times 10^{-2}$
0.51	140	$(9 \pm 1) \times 10^{-2}$

Reprocessing

Previously, polyester bottlebrush polymer networks have been shown to be dynamic and reprocessable at elevated temperatures as a result of alcohol–polyester exchange with a Lewis acid.[17] Unlike typical experiments used to establish dynamic covalent bond exchange, stress-relaxation measurements were not performed at elevated temperatures on our composites given the stiffening we observed during extended heating in the presence of CNTs. Instead, to gauge whether the dynamic bottlebrush matrix can be used to facilitate reprocessing CNT composites, dynamic mechanical analysis (DMA) was used to study samples before and after compression molding (Figure 3.6). Two rectangular samples were fashioned; one was kept as a pristine control, while the other was cut into multiple, discrete pieces and then repressed by annealing in a mold at 180 °C for 1 h. Macroscopically, the damaged pieces reformed a cohesive solid but with greater surface roughness. The pristine sample had a tensile modulus (E') of 200 kPa, which agrees with the value predicted from rheometry under

the assumption of elastomer incompressibility (Poisson's ratio ν = 0.5): $E' = 3G' = 3(66\text{ kPa}) = 198\text{ kPa}$.[44] In contrast, the healed sample had a significantly lower E' = 82 kPa, indicating the material recovers approximately 40% of its original stiffness after reprocessing. Longer times or larger compression may improve this recovery, although we note in the spirit of producing soft and conductive elastomers, it is not necessarily bad to reduce the modulus after reprocessing.

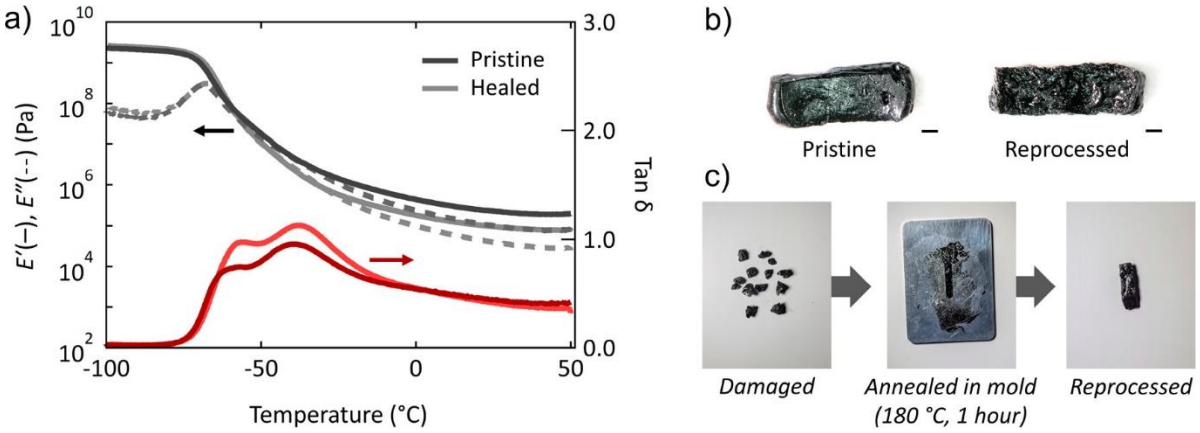

Figure 3.6 Reprocessing of a 0.25 wt % CNT bottlebrush composite with 0.5 wt % cross-linker. (a) Dynamic mechanical thermal analysis showing partial recovery of the tensile modulus (measured on cooling at 5 °C/min). (b) Optical microscopy of pristine and reprocessed samples; the scale bars are 1 mm. (c) Pictures taken throughout the process.

3.4 Conclusion

In conclusion, we have developed a class of supersoft, conductive elastomers by leveraging the highly branched bottlebrush polymer architecture. Incorporating carbon nanotubes as filler particles results in composites that achieve electrical percolation at relatively low loadings (e.g., 0.25 and 0.51 wt %). Although stiffer than unfilled samples of similar composition (G' = 31 kPa), the CNT composites have modulus values (G' = 66 and 140 kPa) about 2 orders of magnitude smaller than analogous linear networks yet comparable conductivities (1×10^{-2} and 9×10^{-2} S/m).

We anticipate this unique combination of properties will be of use to the materials science community in applications where both softness and conductivity are valuable.

3.5 Acknowledgements

Material synthesis and characterization were supported by NSF Award No. DMR-1844987 and Award No. CMMI-2053760, respectively. J.L.S. and V.G.R. gratefully acknowledge the National Science Foundation Graduate Research Fellowship Program under Grant 1650114. Any opinions, findings, and conclusions or recommendations expressed in this material are those of the author(s) and do not necessarily reflect the views of the National Science Foundation. The research reported here made use of shared facilities of the UC Santa Barbara Materials Research Science and Engineering Center (MRSEC, NSF DMR-1720256), a member of the Materials Research Facilities Network (http://www.mrfn.org). Special thanks to Dr. David Goldfeld for assistance with scanning electron microscopy.

3.6 Appendix B

Experimental methods

Reagents and solvents

Reagents and solvents were used as received except where otherwise noted. Methylene chloride ("DCM", ACS grade, ≥99.5%), methanol ("MeOH", 99%), and ethyl vinyl ether ("EVE", 99%) were purchased from Fischer Scientific and used as received. Tin(II) ethyl hexanoate (Sn(Oct)2, Aldrich, 92.5–100%) was purified by fractional distillation (3×) under reduced pressure (0.05 Torr, 150 °C) and kept in a nitrogen-filled glovebox. 2,2′-(Ethylenedioxy)diethanethiol (95%), 2-cyclohexen-1-one (≥95%),

and 3-chloroperbenzoic acid (>70%) were purchased from Millapore Sigma. 4-Methylcaprolactone ("4MCL") was prepared according to previously reported methods[33] and further purified by three consecutive fractional distillations over calcium hydride (CaH2, Fisher Scientific, 93%). Macromonomer initiator (N-(hydroxyethyl)-cis-5-norborneneexo-2,3-dicarboximide, "NbOH") was also prepared according to previously reported methods[23] and further purified by recrystallization from chloroform. Grubbs second-generation metathesis catalyst [(H2IMes)(PCy3)2(Cl)2Ru=CHPh, "G2"] was generously provided by Materia. G2 was converted to Grubbs third-generation metathesis catalyst [(H2IMes)(Pyr)2(Cl)2Ru=CHPh, "G3"] following a previously reported method.[44]

Size-exclusion chromatography instrumentation

Size-exclusion chromatography with multi-angle light scattering detection (SEC MALS) was performed using two Agilent columns (PLgel, 5 μm Mini MIX-D, 250×4.6 mm) connected to a Waters Alliance HPLC System, 2690 separation module pump, Wyatt 18-angle DAWN HELEOS-II light scattering detector, and Wyatt REX differential refractive index detector using THF as the mobile phase. The absolute molar mass was determined by light scattering using online determination of dn/dc by assuming 100% mass elution under the peak of interest. Mass spectrometry data were collected on a Waters GCT Premier high-resolution time-of-flight mass spectrometer in electron ionization mode. This instrument has a working mass range up to 800 m/z.

Mechanical analysis

Frequency sweeps and in situ curing traces were obtained on a TA Instruments ARES-G2 with an 8 mm parallel-plate geometry and a nitrogen-purged forced-convection oven. Strain sweeps were first collected to ensure subsequent experiments would be within the linear viscoelastic regime (with a typical strain value being 1%). Frequency sweeps were collected from 100 rad/s to 0.1 rad/s and the reported plateau moduli correspond to the modulus as measured at the lowest frequency. Temperature-dependent modulus data were obtained on a TA Instruments DMA 850 with a film clamp geometry and a nitrogen-purged oven using a strain of 0.01% at a frequency of 1 Hz and a temperature ramp rate of 3 °C/min. Samples were approximately 3 mm by 8 mm by 1.5 mm.

Impedance spectroscopy and LED circuit demonstration

Samples for impedance spectroscopy were prepared by applying gold electrodes to cut pieces of the samples which had been cured on the rheometer. The complex impedance was measured in the range of 0.1 Hz – 100 kHz using a Solartron 1260 Frequency Response Analyzer (100 mV AC amplitude). Conductivity was extracted from the resistance using the sample dimensions. The LED circuit demonstration was prepared by using a cut piece of the cured 0.51 wt % CNT sample connected by copper tape (spanning an appx. 1.7 mm gap) in series with a green LED to modulate the current supplied by a 9 V battery.

Small angle X-ray scattering (SAXS)

SAXS data were collected using the SAXS Diffractometer in the X-ray Facility of the Materials Research Laboratory at the University of California, Santa Barbara. This instrument has a XENOCS Genix 50W X-ray microsource (50 μm focus size, 1.54 Å wavelength) and a Dectris EIGER R 1M detector. The sample-to-detector distance was calibrated using a silver behenate standard. The 2D-to-1D data reduction was performed using the Nika software.[45]

Scanning electron microscopy (SEM)

Scanning electron microscopy was performed using a Thermo Fisher Apreo S SEM with an ETD detector operating at a 10 keV accelerating voltage with a beam current of 13 nA. The sample was prepared by cryo-fracturing a cured sample of the 0.51 wt % CNT composite.

Synthetic Details

Synthesis of macromonomer and bottlebrush polymer

Macromonomer and bottlebrush polymers were synthesized according to reported procedures.[17] The SEC traces and characterization for the first macromonomer and bottlebrush system described are given below.

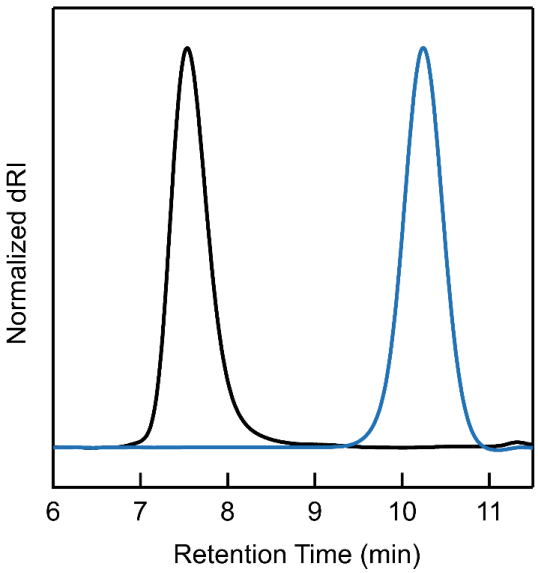

Figure B1 SEC trace of macromonomer in blue (M_n = 2.1 kDa, M_w = 2.3 kDa, $Đ$ = 1.1) and bottlebrush polymer in black (M_n = 170 kDa, M_w = 190 kDa, $Đ$ = 1.1).

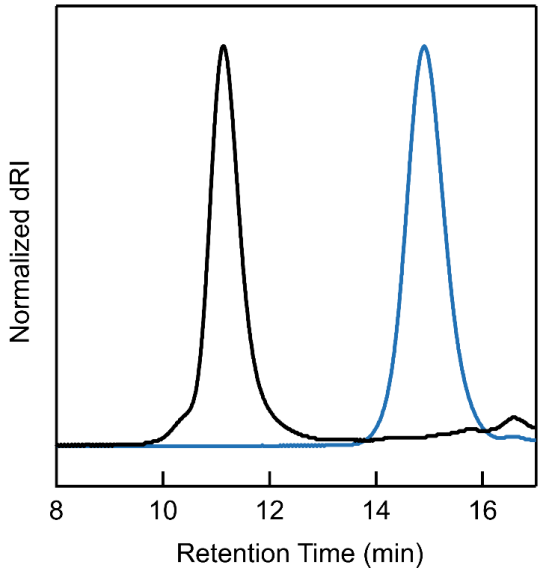

Figure B2 SEC trace of macromonomer in blue (M_n = 1.7 kDa, M_w = 1.9 kDa, $Đ$ = 1.1) and bottlebrush polymer in black (M_n = 150 kDa, M_w = 170 kDa, $Đ$ = 1.1).

Synthesis of bis-lactone crosslinker

The bifunctional crosslinker was synthesized by a two-step method as shown in Figure B3 and Figure B4. In the first step, 2.6 g (14.2 mmol, 1 eq) of 2,2′ (ethylenedioxy)diethanethiol was diluted in 20 mL of dichloromethane. To the stirred solution, 0.14 g (1.4 mmol, 0.1 eq) of triethylamine was added and the reaction vessel was cooled to 0 °C. To the cooled solution, 3.0 g (31.2 mmol, 2.2 eq) of 2-cyclohexen-1-one was added dropwise. The reaction was stirred overnight warmed to room temperature, at which point the conversion was determined to be near quantitative. The product was isolated by removing the excess reagents *in vacuo*, giving 4.6 g (14.2 mmol, 98% yield), and used in the subsequent transformation without further purification. ^{1}H NMR (600 MHz, Chloroform-d) δ = 3.60 (t, J = 6.8 Hz, 4H), 3.57 (s, 4H), 3.10 (tt, J = 10.3, 4.1 Hz, 2H), 2.71 (t, J = 6.69 Hz, 4H), 2.67 (m, 2H), 2.33 (ddd, J = 1.3, 10.56, 14.26 Hz, 4H), 2.27 (m, 2H), 2.1 (m, 4H), 1.67 (m, 4H).

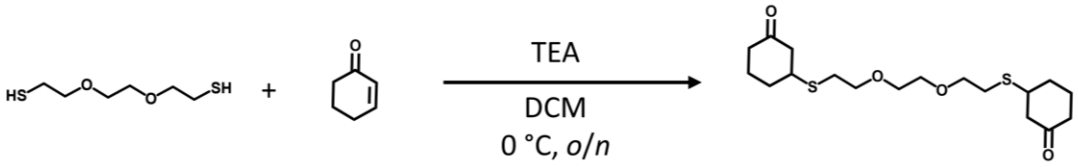

Figure B3 First step in the synthesis of a bifunctional crosslinker.

For the following reaction, 2 g of the product from the previous reaction (5.3 mmol, 1 eq) was diluted in 50 mL dichloromethane and cooled to 0 °C. To the stirring and chilled solution, 11.1 g (48.1 mmol, 9 eq) of *meta*-chloroperoxybenzoic acid was added and allowed to react overnight. Conversion was monitored by ^{1}H NMR and upon complete conversion, the reaction was filtered (to remove precipitated *meta*

chlorobenzoic acid, "mCPBA") and purified by column chromatography using a solvent gradient from pure dichloromethane to pure acetone. The final product was isolated as 1.46 g (58% yield) of a waxy solid. ^{1}H NMR (600 MHz, $CDCl_3$) δ = 4.34 (dd, J = 13.1, 5.5 Hz, 2H), 4.22 (dd, J = 13.2, 10.4 Hz, 2H), 3.93 – 3.83 (m, 4H), 3.60 (d, J = 4.2 Hz, 4H), 3.43 (td, J = 11.6, 2.8 Hz, 2H), 3.42 – 3.22 (m, 4H), 3.18 (dd, J = 13.8, 3.3 Hz, 2H), 2.93 (dd, J = 13.7, 11.6 Hz, 2H), 2.49 – 2.43 (m, 2H), 2.21 (dq, J = 14.8, 4.7 Hz, 2H), 2.01 – 1.91 (m, 2H), 1.90 – 1.81 (m, 2H). ^{13}C NMR (126 MHz, $CDCl_3$) δ 171.52, 171.43, 70.40, 70.36, 70.30, 68.59, 68.57, 64.58, 64.46, 57.77, 57.69, 50.93, 50.86, 33.46, 33.40, 33.18, 32.64, 30.92, 27.27, 27.22, 27.14, 27.04, 26.83, 21.05.

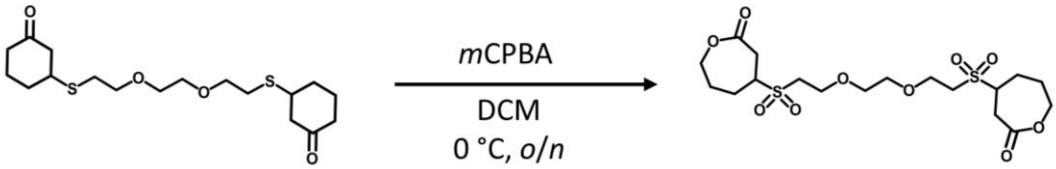

Figure B4 Second step in the synthesis of a bifunctional crosslinker.

Network formation procedure

For samples without CNT filler, the crosslinker and catalyst were first weighed into a tared vial. 4MCL monomer was then added to help homogenize the crosslinker and catalyst in solution. Lastly, P4MCL bottlebrush polymer was weighed into the vial and the contents were stirred until the solution was well-mixed. The resulting viscous paste was held under vacuum overnight to remove any bubbles that formed during the mixing step. The reaction mixture was then loaded onto the parallel plates of a rheometer and cured in situ at 180 °C for 20 minutes. Full formulation details for these

samples are provided in Tables B1 to B4. The non-truncated curing traces of unfilled samples are shown in Figure B5.

Table B1 Formulation details of the sample with 0.5 wt % crosslinker from Figure 3.2.

Compound	Molar mass (g mol^{-1})	Mass (mg)	wt %	mmol ×10^3	Eq.
P4MCL bottlebrush polymer	170,000	250.0	77.9%	1.47	1.0
4MCL monomer	470.13	64.2	20.0%	501	341
Crosslinker	405.12	1.7	0.5%	3.68	2.5
$Sn(Oct)_2$	128.17	5.0	1.6%	12.4	8.4

Table B2 Formulation details of the sample with 1 wt % crosslinker from Figure 3.2.

Compound	Molar mass (g mol^{-1})	Mass (mg)	wt %	mmol ×10^3	Eq.
P4MCL bottlebrush polymer	170,000	250.0	77.4	1.47	1.0
4MCL monomer	470.13	64.6	20.0	504	343
Crosslinker	405.12	3.5	1.1	7.35	5.0
$Sn(Oct)_2$	128.17	5.0	1.5	12.4	8.4

Table B3 Formulation details of the sample with 2 wt % crosslinker from Figure 3.2.

Compound	Molar Mass (g mol^{-1})	Mass (mg)	wt %	mmol ×10^3	Eq.
P4MCL bottlebrush polymer	170,000	250.0	76.4	1.47	1.0
4MCL monomer	470.13	65.5	20.0	511	347
Crosslinker	405.12	6.9	2.1	14.7	10.0
$Sn(Oct)_2$	128.17	5.0	1.5	12.4	8.4

Table B4 Formulation details of the sample with 3 wt % crosslinker from Figure 3.2.

Compound	Molar mass (g mol^{-1})	Mass (mg)	wt %	mmol ×10^3	Eq.
P4MCL bottlebrush polymer	170,000	250.0	75.4	1.47	1.0
4MCL monomer	470.13	66.3	20.0	518	352
Crosslinker	405.12	10.4	3.1	22.1	15.0
$Sn(Oct)_2$	128.17	5.0	1.5	12.4	8.4

Table B5 Sol-gel data for low crosslinker samples

Sample	Crosslinker (wt %)	Gel-fraction (%)
1A	0.5	85
1B	0.5	87
2A	1.0	94
2B	1.0	94

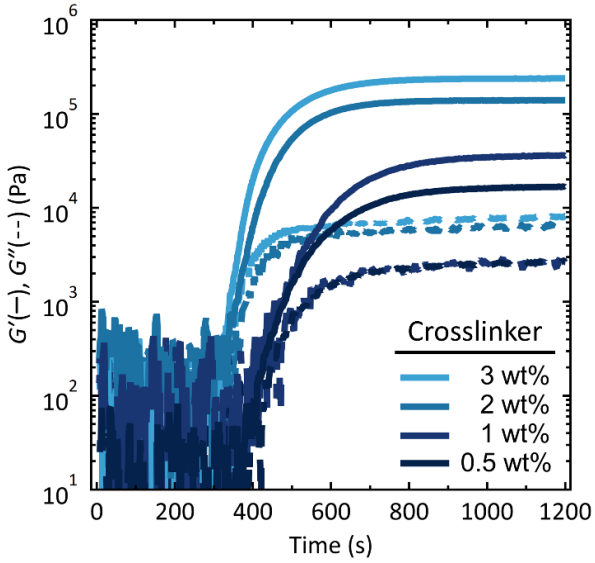

Figure B5 Non-truncated curing traces of the unfilled samples.

For CNT-composite samples, a similar procedure was used. First, the crosslinker and catalyst were weighed into a tared vial. Then, a portion of the 4MCL monomer was added to help homogenize the crosslinker and catalyst in solution. Lastly, a mixture of P4MCL bottlebrush polymer with approximately 14% by weight 4MCL monomer and a variable amount of dispersed carbon nanotubes was added to the tared vial. This mixture was rigorously stirred until it was well-mixed. The resulting composite paste was held under vacuum overnight to remove any bubbles that formed during the

mixing step. The reaction mixture was loaded onto the parallel plates of a rheometer and cured in situ at 180 °C for 20 minutes, exactly analogous to the non CNT samples.

Carbon nanotube dispersion

Single-walled carbon nanotubes (TUBALL Single Walled Carbon Nanotubes, OCSiAl) were incorporated into P4MCL bottlebrush polymers using centrifugal mixing (FlackTek SpeedMixer) with ceramic cylinders to promote particle dispersion. Advantages of this dispersion method include solvent-free processing and safe, contained mixing suitable for powders such as CNTs; one requirement of this technique is a minimum batch size of approximately 1 g to achieve proper mixing. To promote good mixing, the bottlebrush polymer was plasticized with approximately 14% by weight 4MCL monomer. The mixing protocol began with a slow ramp in the mixing speed to 1500 RPM, at which point the sample was mixed for 30 minutes (alternating 5-minute increments with 5 minutes of cooling in a water bath). The ceramic cylinders are not stable at speeds above 1750 RPM. Images of a sample at various points of the mixing and curing process are shown in Figure B6.

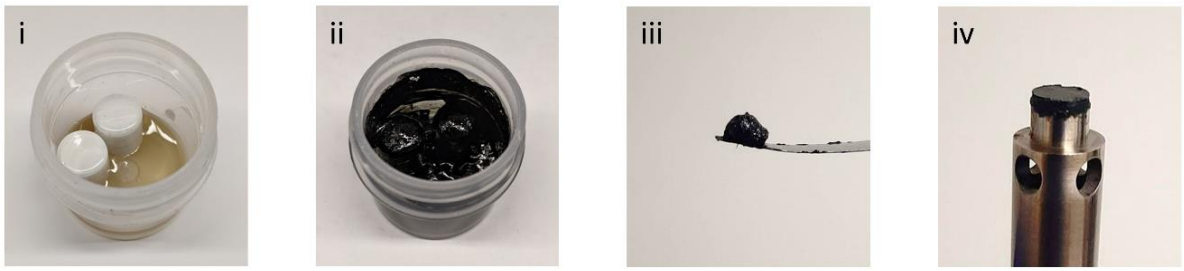

Figure B6 Images of representative sample throughout processing. (i) Bottlebrush polymer with plasticizing monomer in a mixing cup with ceramic cylinders visible directly prior to the addition of CNTs. (ii) Sample from the previous image directly after addition and dispersion of CNTs via centrifugal mixing. (iii) Portion of dispersed CNT sample after adding the rest of the formulation (including crosslinker, catalyst, and monomer, as given in Tables B5–B7), but prior to annealing. (iv) Cured composite sample directly after annealing and successful network formation.

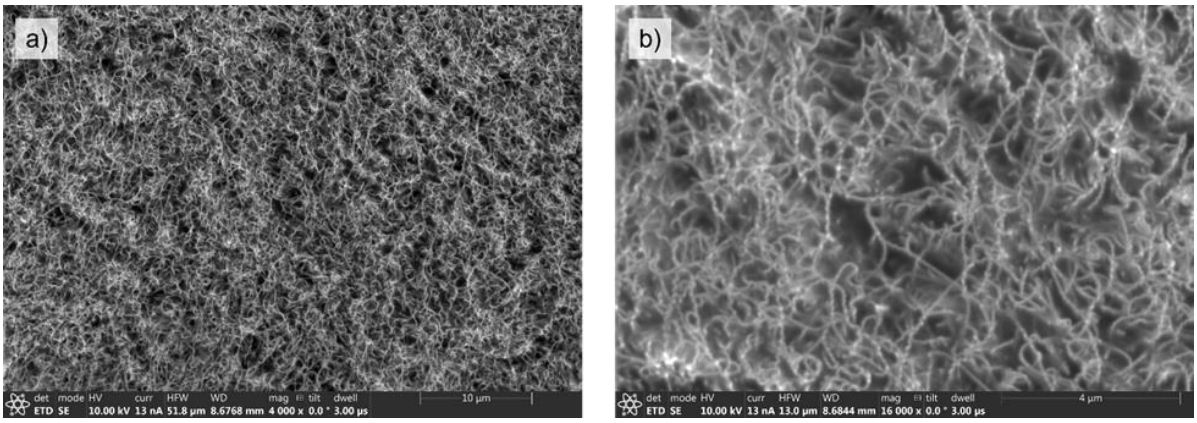

Figure B7 SEM images at (a) 4000× and (b) 16000× of the cryo-fractured surface of a cured 0.51 wt % CNT composite sample. The images show an even, isotropic network of CNT bundles. The high magnification in (b) shows that a portion of the population has a coiled conformation, which is known to occur in CNTs produced by catalytic chemical vapor deposition.[46]

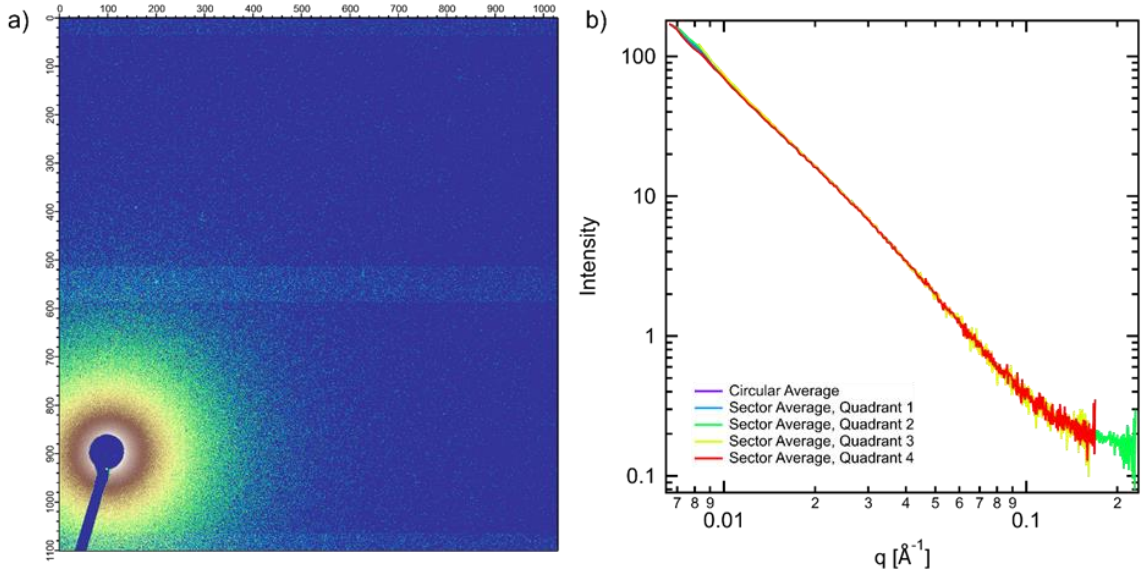

Figure B8 Small angle X-ray scattering of a rheometer-cured 0.51 wt % CNT composite sample shows no sign of orientation in the CNT network (isotropic distribution). (a) 2D scattering pattern (intensity displayed on a log color scale). (b) Reduced 1D data containing a full circular average and sector averages over 4 quadrants. The overlap of the circular and quadrant averages indicates an isotropic distribution of CNTs (no preferred orientation).

Before curing, the non-filled samples flow like viscous polymers as expected, but the CNT-filled samples behave very differently as shown in Figure B9. Once the CNT-filler is dispersed, the CNT/bottlebrush polymer mixture has distinct elasticity. This is presumably due to mechanical percolation of the filler.

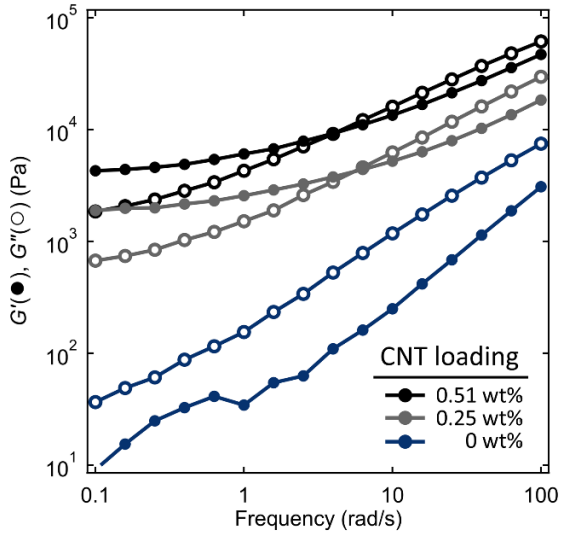

Figure B9 Frequency sweeps of the samples from Figure 3.4 before curing. Samples with CNT-filler show solid-like behavior even prior to network formation.

Table B6 Formulation details of the 0 wt % CNT composite sample from Figure 3.4.

Compound	Molar mass (g mol^{-1})	Mass (mg)	wt %	mmol ×10^3	Eq.
P4MCL bottlebrush polymer	170,000	350.0	77.9	2.22	1.0
4MCL monomer	470.13	90.0	20.0	702	317
Crosslinker	405.12	2.4	0.5	5.10	2.3
$Sn(Oct)_2$	128.17	6.7	1.5	16.3	7.5
Carbon nanotubes	*n/a*	0.0	0.00	*n/a*	*n/a*

Table B7 Formulation details of the 0.25 wt % CNT composite sample from Figure 3.4.

Compound	Molar mass (g mol^{-1})	Mass (mg)	wt %	mmol ×10^3	Eq.
P4MCL bottlebrush polymer	170,000	170.9	77.5	1.08	1.0
4MCL monomer	470.13	44.6	20.2	348	322
Crosslinker	405.12	1.2	0.5	2.55	2.4
$Sn(Oct)_2$	128.17	3.3	1.5	8.15	7.5
Carbon nanotubes	*n/a*	0.5	0.25	*n/a*	*n/a*

Table B8 Formulation details of the 0.5 wt % CNT composite sample from Figure 3.4.

Compound	Molar mass (g mol^{-1})	Mass (mg)	wt %	mmol ×10^3	Eq.
P4MCL bottlebrush polymer	170,000	171.6	77.5	1.09	1.0
4MCL monomer	470.13	44.3	20.0	345	318
Crosslinker	405.12	1.2	0.5	2.55	2.4
$Sn(Oct)_2$	128.17	3.3	1.5	8.15	7.5
Carbon nanotubes	*n/a*	1.1	0.51	*n/a*	*n/a*

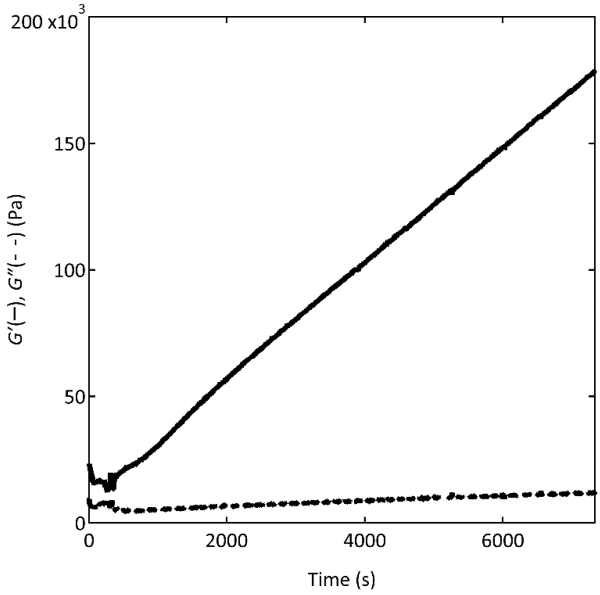

Figure B10 Curing of a 0.25 wt % CNT bottlebrush polymer mixture in the absence of catalyst or crosslinker shows secondary curing events over a long timescale.

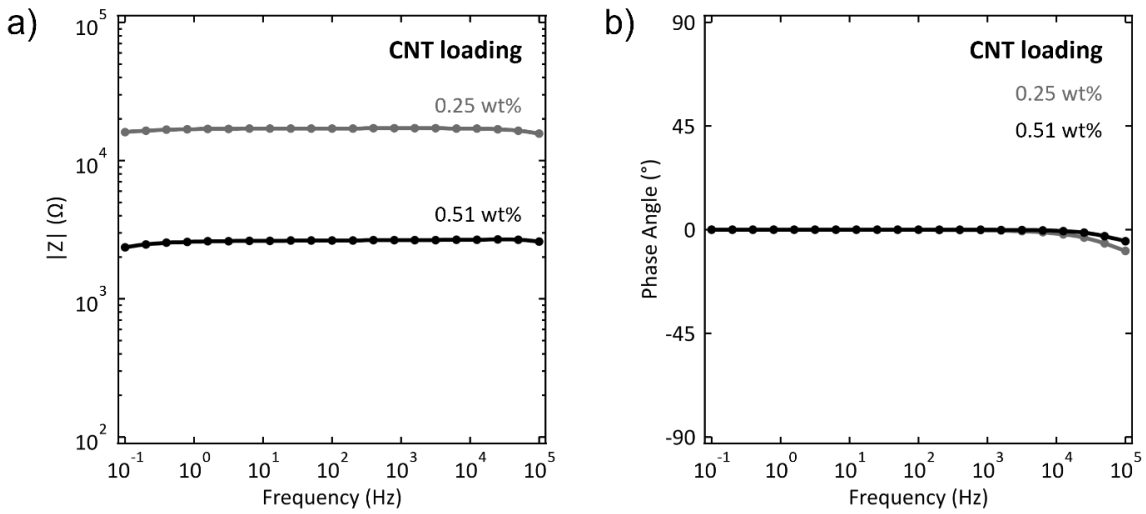

Figure B11 (a) Magnitude of impedance and (b) phase angle of the 0.25 and 0.51 wt% CNT composite samples showing ideal resistor behavior in the range of 0.1 Hz to 100 kHz (100 mV AC amplitude, no bias).

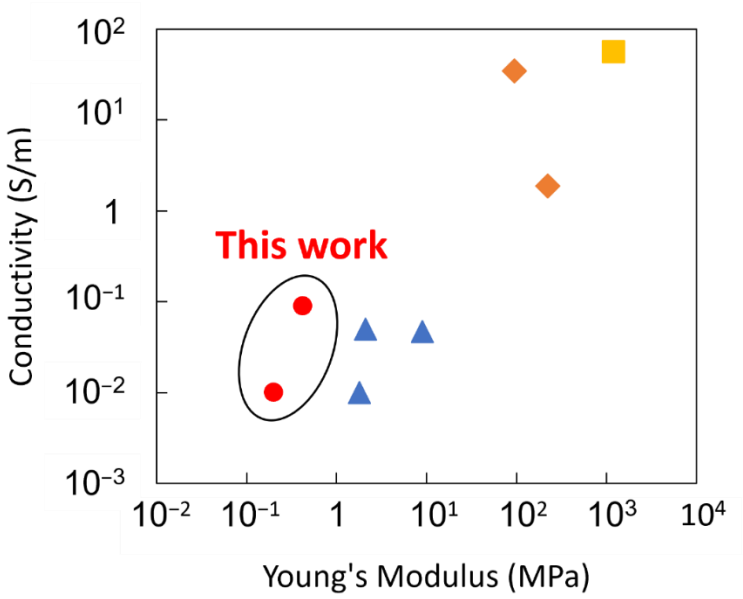

Figure B12 Comparison of CNT–bottlebrush polymer composite properties with linear polymer composite systems from literature. Blue triangles: Stopler et al.;[47] orange diamonds: Yuan et al.;[42] yellow square: Zhang et al.[48]

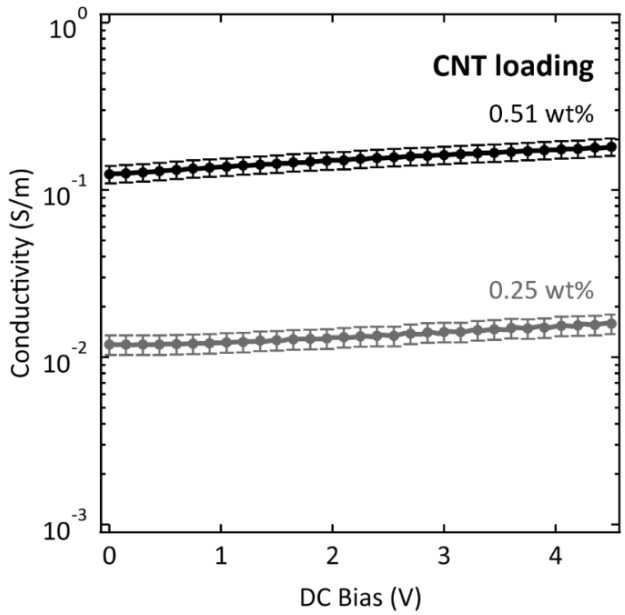

Figure B13 Conductivity of the 0.25 and 0.51 wt % CNT composite samples from 0–4.5 V DC bias (100 mV AC amplitude). The increase in measured conductivity is hypothesized to be a result of contact resistance.

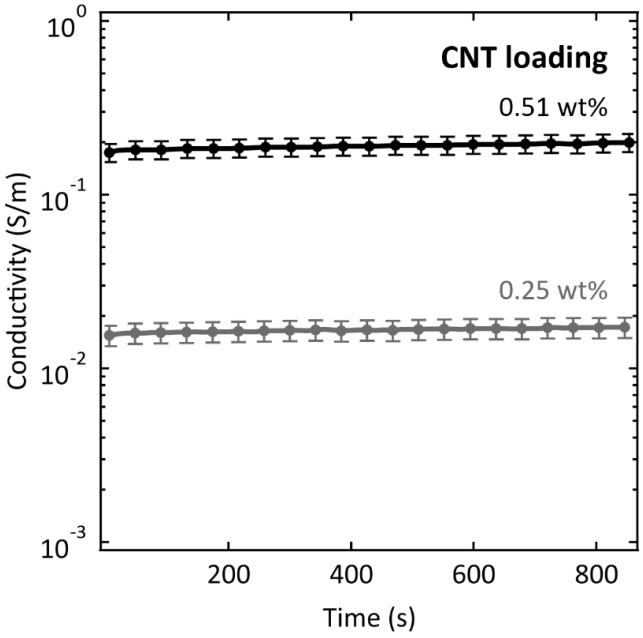

Figure B14 Conductivity vs. time of the 0.25 and 0.51 wt % CNT composite samples at a DC bias of 4.5 V (100 mV AC amplitude). The signal is relatively steady over time, with the conductivity drifting up by 12% (0.25% CNTs) and 14% (0.51% CNTs).

3.7 References

1. Rogers, J. A., Someya, T. & Huang, Y. Materials and mechanics for stretchable electronics. *Science* 327, 1603–7 (2010).
2. Weigel, M. et al. iSkin: Flexible, stretchable and visually customizable on-body touch sensors for mobile computing. *Proceedings of the 33rd Annual ACM Conference on Human Factors in Computing Systems* (2015).
3. Xu, S. et al. Soft microfluidic assemblies of sensors, circuits, and radios for the skin. *Science* 344, 70–74 (2014).
4. Shih, B. et al. Electronic skins and machine learning for intelligent soft robots. *Science Robotics* 5, eaaz9239 (2020).
5. Gomez, E. F. et al. 3D-Printed Self-Healing Elastomers for Modular Soft Robotics. *ACS Applied Materials & Interfaces* 13, 28870–28877 (2021).
6. Amit, M., Chukoskie, L., Skalsky, A. J., Garudadri, H. & Ng, T. N. Flexible Pressure Sensors for Objective Assessment of Motor Disorders. *Advanced Functional Materials* 30 1905241 (2020).
7. Xu, J. et al. Highly stretchable polymer semiconductor films through the nanoconfinement effect. *Science* 355, 59–64 (2017).
8. Shin, M. et al. Polythiophene Nanofibril Bundles Surface-Embedded in Elastomer: A Route to a Highly Stretchable Active Channel Layer. *Advanced Materials* 27, 1255–1261 (2015).
9. Song, E. et al. Stretchable and Transparent Organic Semiconducting Thin Film with Conjugated Polymer Nanowires Embedded in an Elastomeric Matrix. *Advanced Electronic Materials* 2, 1500250 (2016).
10. Moniruzzaman, M. & Winey, K. I. Polymer nanocomposites containing carbon nanotubes. *Macromolecules* 39, 5194–5205 (2006).
11. Kim, J. H. et al. Simple and cost-effective method of highly conductive and elastic carbon nanotube/polydimethylsiloxane composite for wearable electronics. *Scientific Reports* 8, 1375 (2018).
12. Yu, Z., Niu, X., Liu, Z. & Pei, Q. Intrinsically Stretchable Polymer Light-Emitting Devices Using Carbon Nanotube-Polymer Composite Electrodes. *Advanced Materials* 23, 3989–3994 (2011).
13. Mutiso, R. M. & Winey, K. I. Electrical properties of polymer nanocomposites containing rod-like nanofillers. *Progress in Polymer Science* 40 63–84 (2015).
14. Mensah, B., Kim, H. G., Lee, J. H., Arepalli, S. & Nah, C. Carbon nanotube-reinforced elastomeric nanocomposites: a review. *International Journal of Smart and Nano Materials* 6, 211–238 (2015).
15. Daniel, W. F. M. et al. Solvent-free, supersoft and superelastic bottlebrush melts and networks. *Nature Materials* 15, 183–189 (2016).
16. Abbasi, M., Faust, L. & Wilhelm, M. Comb and Bottlebrush Polymers with Superior Rheological and Mechanical Properties. *Advanced Materials* 31, 1806484 (2019).
17. Self, J. L. et al. Dynamic Bottlebrush Polymer Networks: Self-Healing in Super-Soft Materials. *Journal of the American Chemical Society* 142, 7567–7573 (2020).

18. Reynolds, V. G. et al. Super-soft solvent-free bottlebrush elastomers for touch sensing. *Materials Horizons* 7, 181–187 (2020).
19. Vatankhah-Varnoosfaderani, M. et al. Bottlebrush Elastomers: A New Platform for Freestanding Electroactuation. *Advanced Materials* 29, 1604209 (2017).
20. Kostrov, S. A., Dashtimoghadam, E., Keith, A. N., Sheiko, S. S. & Kramarenko, E. Y. Regulating Tissue-Mimetic Mechanical Properties of Bottlebrush Elastomers by Magnetic Field. *ACS Applied Materials & Interfaces* 13, 38783–38791 (2021).
21. Sarapas, J. M., Chan, E. P., Rettner, E. M. & Beers, K. L. Compressing and Swelling to Study the Structure of Extremely Soft Bottlebrush Networks Prepared by ROMP. *Macromolecules* 51, 2359–2366 (2018).
22. Vatankhah-Varnosfaderani, M. et al. Mimicking biological stress-strain behaviour with synthetic elastomers. *Nature* 549, 497–501 (2017).
23. Arrington, K. J., Radzinski, S. C., Drummey, K. J., Long, T. E. & Matson, J. B. Reversibly Cross-linkable Bottlebrush Polymers as Pressure-Sensitive Adhesives. *ACS Applied Materials & Interfaces* 10, 26662–26668 (2018).
24. Bates, C. M., Chang, A. B., Momčilović, N., Jones, S. C. & Grubbs, R. H. ABA Triblock Brush Polymers: Synthesis, Self-Assembly, Conductivity, and Rheological Properties. *Macromolecules* 48, 4967–4973 (2015).
25. Liang, H., Sheiko, S. S. & Dobrynin, A. V. Supersoft and Hyperelastic Polymer Networks with Brushlike Strands. *Macromolecules* 51, 638–645 (2018).
26. Pakula, T. et al. Molecular brushes as super-soft elastomers. *Polymer* 47, 7198–7206 (2006).
27. Zhang, Y. et al. Super soft elastomers as ionic conductors. *Polymer* 45, 6333–6339 (2004).
28. Choi, C. et al. Light-Mediated Synthesis and Reprocessing of Dynamic Bottlebrush Elastomers under Ambient Conditions. *Journal of the American Chemical Society* 143, 9866–9871 (2021).
29. Mei, H. et al. Rapid Processing of Bottlebrush Coatings through UV-Induced Cross-Linking. *ACS Macro Letters* 9, 1135–1142 (2020).
30. Mukherjee, S. et al. Universal Approach to Photo-Crosslink Bottlebrush Polymers. *Macromolecules* 53, 1090–1097 (2020).
31. Xie, R. et al. Room temperature 3D printing of super-soft and solvent-free elastomers. *Science Advances* 6, (2020).
32. Self, J. L., Dolinski, N. D., Zayas, M. S., Read De Alaniz, J. & Bates, C. M. Brønsted-Acid-Catalyzed Exchange in Polyester Dynamic Covalent Networks. *ACS Macro Letters* 7, 817–821 (2018).
33. Watts, A., Kurokawa, N. & Hillmyer, M. A. Strong, Resilient, and Sustainable Aliphatic Polyester Thermoplastic Elastomers. *Biomacromolecules* 18, 1845–1854 (2017).
34. Brutman, J. P., Delgado, P. A. & Hillmyer, M. A. Polylactide vitrimers. *ACS Macro Letters* 3, 607–610 (2014).
35. Montarnal, D., Capelot, M., Tournilhac, F. & Leibler, L. Silica-like malleable materials from permanent organic networks. *Science* 334, 965–968 (2011).
36. Wiltshire, J. T. & Qiao, G. G. Degradable core cross-linked star polymers via ring-opening polymerization. *Macromolecules* 39, 4282–4285 (2006).

37. Weh, R. & De Klerk, A. Thermochemistry of Sulfones Relevant to Oxidative Desulfurization. *Energy and Fuels* 31, 6607–6614 (2017).
38. Levental, I., Georges, P. C. & Janmey, P. A. Soft biological materials and their impact on cell function. *Soft Matter* 3 299–306 (2007).
39. Xie, X. L., Mai, Y. W. & Zhou, X. P. Dispersion and alignment of carbon nanotubes in polymer matrix: a review. *Materials Science and Engineering R: Reports* 49 89–112 (2005).
40. Ponnamma, D., Sadasivuni, K. K., Grohens, Y., Guo, Q. & Thomas, S. Carbon nanotube based elastomer composites-an approach towards multifunctional materials. *Journal of Materials Chemistry C* 2, 8446–8485 (2014).
41. Shaffer, M. S. P., Fan, X. & Windle, A. H. Dispersion and packing of carbon nanotubes. *Carbon* 36, 1603–1612 (1998).
42. Yuan, D., Guo, H., Ke, K. & Manas-Zloczower, I. Recyclable conductive epoxy composites with segregated filler network structure for EMI shielding and strain sensing. *Composites Part A: Applied Science and Manufacturing* 132, 105837 (2020).
43. Zhang, G. et al. Macromolecularly Engineered Thermoreversible Heterogeneous Self-Healable Networks Encapsulating Reactive Multidentate Block Copolymer-Stabilized Carbon Nanotubes. *Macromolecular Rapid Communications* 42, 2000514 (2021).
44. Love, J. A., Morgan, J. P., Trnka, T. M. & Grubbs, R. H. A Practical and Highly Active Ruthenium-Based Catalyst that Effects the Cross Metathesis of Acrylonitrile. *Angewandte Chemie International Edition* 41, 4035–4037 (2002).
45. Ilavsky, J. Nika: Software for two-dimensional data reduction. *Journal of Applied Crystallography* 45, 324–328 (2012).
46. Hernadi, K., Thiên-Nga, L. & Forró, L. Growth and microstructure of catalytically produced coiled carbon nanotubes. *The Journal of Physical Chemistry B* 105, 12464–12468 (2001).
47. Stopler, E. B. et al. Carbon nanotube enhanced dynamic polymeric materials through macromolecular engineering. *Materials Advances* 1, 1071–1076 (2020).
48. Zhang, J. et al. Malleable and Recyclable Conductive MWCNT-Vitrimer Composite for Flexible Electronics. *ACS Applied Nano Materials* 3, 4845–4850 (2020).

3.8 Permissions and Attributions

Chapter 4: Model for the electro-mechanical behavior of elastic organic transistors

4.1 Abstract

Organic thin film transistors (TFTs) can be made with materials that allow them to be mechanically stretched during electrical operation. We describe the application of mechanical models of the elasticity of polymers to predict the electrical characteristics of elastic TFTs. The model predicts the current–voltage behavior of TFTs under uniaxial and biaxial deformation assuming stretchable elements for contacts, dielectrics, and the semiconducting layer. The behavior of complementary inverters

using elastic TFTs is presented along with criteria for stable operation as digital circuit elements. The mechanical model was also applied to organic electrochemical transistors (OECTs). The behavior of elastic OECTs differs substantially from TFTs and the model predicts that they can provide benefits for the stability of simple digital circuits.

4.2 Introduction

The mechanical properties of polymers significantly differ from inorganic materials providing potential advantages for unconventional electronic devices.[1,2] In contrast to inorganic semiconductors that can only be deformed elastically with strains of a few percent, polymers can be deformed to many times their initial dimensions.[3,4] Despite this potential, developing mechanically stretchable semiconducting polymers, dielectrics, and conductors for stretchable electronic devices is a challenge.[5–7] There have been a number of demonstrations of stretchable thin film transistors (TFTs) and circuits with good performance upon deformation.[8–12] These advances demonstrate the need for models for the expected electro-mechanical behavior of stretchable TFTs that can be used to understand their operation.

Here we describe the application of mechanical models of the elasticity of polymer networks[3,4] to predict the electrical behavior of elastic TFTs. We consider TFTs under uniaxial and biaxial deformation assuming stretchable elements for contacts, dielectrics, and the semiconducting layer. Comparisons of the expectations for TFTs and organic electrochemical transistors (OECTs) are also presented. Our model shows that in addition to the development of new materials for stretchable

electronics there is a pressing need for the development of circuit designs that maintain their functionality under mechanical deformation.

The majority of semiconducting polymers have limited mechanical elasticity relative to insulating elastomers. A material in the elastic regime recovers its initial dimensions after removal of an applied stress. A material that is stretchable can either recover its initial dimensions or plastically deform after removal of an applied stress.[13] The mechanical behavior of polymers depends on their structural order and the temperature relative to their glass transition temperature, T_g. The molecular structure of most high-performance semiconducting polymers leads to a relatively high T_g (e.g., above ~30 °C) and semicrystallinity.[1,14] Poly(3-hexylthiophene), a widely used semiconducting polymer, undergoes plastic deformation without full recovery above strains of ~10%.[15–17] In contrast, simple elastomers are polymer chains crosslinked into a network that exhibit elastic behavior to high strain (>100%) at temperatures above their T_g.[4] Block copolymers, such as styrene–butadiene–styrene (SBS), can also have elastic behavior where some regions are hardened, either by crystallization or by being below their T_g.[13] It is reasonable to believe that semiconducting polymers can be designed to have elastic properties considering that amorphous semiconducting polymers, such as poly(triarylamines), are known.[18–20] Additionally, recent work suggests a design rule for side chain alkylation of conjugated backbones that would lead to stretchable semiconductors that operate around room temperature (i.e., $T_g \leq$ 0 °C).[21] These side chains can be part of long branched groups on select monomers (not on every ring) to avoid crystallization, or inducing an additional T_g for the side chain itself, thus further improving stretchability and elasticity.

The emergence of composites of semiconductors, or conductors, with elastic polymers has enabled exploration of the behavior of stretchable TFTs and circuits.[22] For example, phase-separated blends of semiconducting polymers and elastomers provide a means to form an elastic semiconducting channel. In blends with elastomers, such as poly(dimethylsiloxane) (PDMS) and polystyrene-block-poly(ethylene-co-butylene)-block-polystyrene (SEBS), phase-separated fiber-like aggregates of semiconducting polymers accommodate deformation by bending and stretching within the elastic matrix.[10,22–25] Such blends can have effective carrier mobilities in TFTs near 1 $cm^2 V^{-1} s^{-1}$ depending on the composition and processing.[24] Single wall carbon nanotubes (SWCNTs) supported by SEBS allow for stretchable electrode materials without overly large injection barriers to organic semiconductors.[7] The mechanical recovery of these composites is imperfect, but the associated device characteristics of TFTs show intriguing resilience to deformation.[2,24]

Despite efforts to form stretchable electronics, there has not been significant investigation into basic models for the electrical behavior of elastic, or stretchable, TFTs. Without a clear device model that predicts the current–voltage characteristics of TFTs with deformation, it is difficult to understand the behavior of novel materials and device structures. Given the questions of non-idealities on the extraction of carrier mobility of polymers from TFTs in conventional devices,[26–28] it is particularly important to understand the expectations for their limiting behavior. Here using a standard model for the mechanical behavior of elastic polymers, we examine the expectations for the current–voltage characteristics of TFTs and OECTs (Figure 4.1). The model provides predictions for the behavior of TFTs deformed by both uniaxial

and biaxial stresses as a function of direction with respect to the geometry of the device.

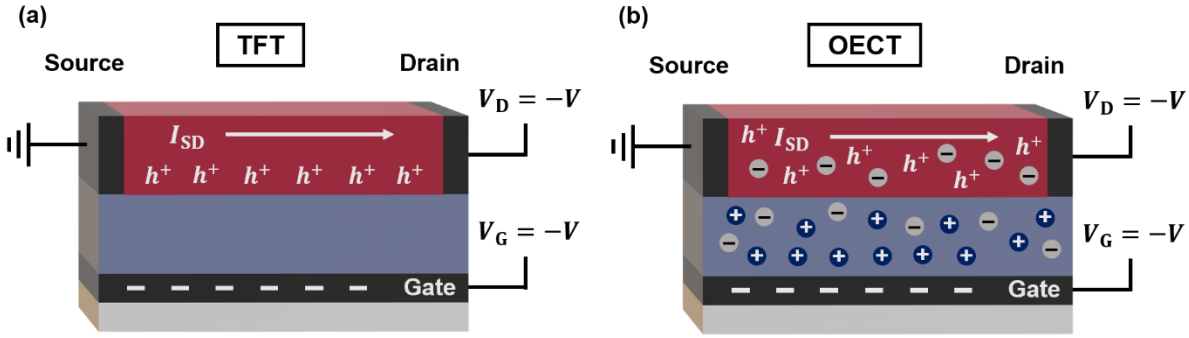

Figure 4.1 Schematic of a p-type (a) TFT and (b) OECT. Holes, h^+, accumulate and flow at the semiconductor–dielectric interface in the former whereas holes accumulate in the bulk of the semiconductor in the latter due to infiltration of ions from the electrolyte gate.

4.3 Results and Discussion

Elastic thin film transistors

The electrical behavior of elastic TFTs can be modeled in the simplest form using the gradual channel model for the current–voltage (I–V) characteristics. The gradual channel model for a TFT with carrier mobility (μ), a gate capacitance per area (C_G), a channel width (W), and a channel length (L) is given by Eqn (4.1) in the linear regime and Eqn (4.2) in the saturation regime where the source–drain bias (V_{SD}) exceeds the magnitude of the difference between the gate to source voltage (V_G) and a threshold voltage (V_T).[26,28]

$$I_{SD} = \frac{W}{L} C_G \mu \left[(V_G - V_T) V_{SD} - \frac{{V_{SD}}^2}{2} \right] \qquad |V_{SD}| < |(V_G - V_T)| \tag{4.1}$$

$$I_{SD} = \frac{W}{L} C_G \mu \left[\frac{(V_G - V_T)^2}{2} \right] \qquad |V_{SD}| \geq |(V_G - V_T)| \tag{4.2}$$

The geometry of the TFT along with the coordinate system used for the deformations is given in Figure 4.2. If elastic materials are used for the electrodes, semiconductor, and dielectric then the changes of the *I*–*V* characteristics of a TFT as a function of deformation can be derived under assumptions about the mechanical and electrical properties of the materials.

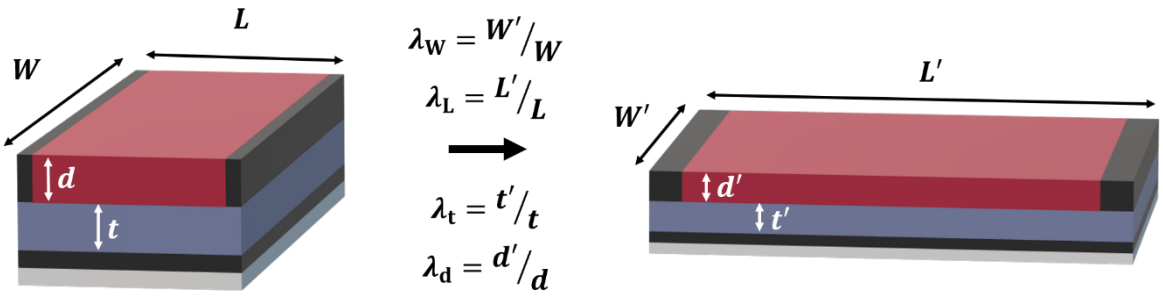

Figure 4.2 Schematic of the deformation of an elastic TFT with the initial dimensions, final dimensions, and extension ratios, λ, defined.

For the mechanical behavior of the materials in the TFT we assume that the materials are incompressible, i.e., they have Poisson's ratio of 0.5, and are isotropic. Such behavior is an excellent approximation for amorphous polymer networks used as dielectrics.[4,13] For ordered semiconducting polymers, the assumption of an isotropic response is not necessarily valid because of the mixture of crystalline and disordered regions, but we expect that it should hold for amorphous semiconducting polymers. We also assume that electrodes made from composites, e.g., SWCNTs supported by or blended in SEBS, will follow this behavior as well. For polymers that undergo high deformation it is common to define an extension ratio, λ, rather than strain. The extension ratio is defined as the ratio of the deformed dimension (x_i') to its initial dimension (x_i) in a particular direction, i, and is given by $\lambda_i = x_i'/x_i$. Here we model the TFT using a deformation along the channel direction, λ_L, along the width,

λ_W, in the thickness of the semiconducting layer, λ_d, and in the thickness of the dielectric layer, λ_t. With Poisson's ratio of 0.5, the product of the extension ratios is unity, i.e., $\lambda_W\lambda_L\lambda_t = 1$.[4] We assume that deformation throughout the TFT is uniform, i.e., the channel, dielectric, and electrodes have equivalent deformation (although the mechanical stress in each layer might be different due to differences in mechanical moduli). We also assume the TFT is free to move in all directions other than that of the applied deformation. Note that this assumption can be invalidated in practice if a TFT is not deformed in a controlled fashion, e.g., in true uniaxial or biaxial strain.

For the electrical properties of the materials in the TFT, we make several important assumptions. The dielectric constant of the gate dielectric is modeled as independent of deformation, which is a reasonable assumption assuming the chain dimensions are not strongly perturbed. We also assume that the mobility of the semiconductor does not vary with extension; this assumption is reasonable for an amorphous polymer at deformations that do not strongly perturb the chain dimensions relative to the initial state. At high extension ($\lambda \gg 1$), changes in the mobility are expected because the polymer chains extend which could lead to variations in the transport pathways and the energetic disorder.[15] We also assume that the accumulation layer is sufficiently thin, e.g., ~1 nm, relative to the thickness of the undeformed semiconductor that the change in dimension does not affect the operation of the device. Our model does not incorporate the role of contact resistances in transistors, which are ignored in the basic gradual channel model, and we comment on the potential effects for various cases of deformations below.

Uniaxial deformation of TFTs

The first case we consider for the electrical behavior with deformation is simple uniaxial extension, or compression, either along the direction of the channel or across it. The full derivation of the model is given in Appendix C and we highlight here the most critical factors. The gate capacitance can be shown to vary as $\sqrt{\lambda}C_G$ with uniaxial deformation along the channel length, or the width, therefore under compression the capacitance will decrease and under extension it will increase. We model change in V_T of the TFT by assuming that the amount of trapped charge per area, q_{trap}, does not change with deformation. In this case, V_T will be a function of C_G because $q_{trap} = V_T C_G$ (assuming that the device turns on in the sub-threshold regime near V_G = 0 V). The expression for the current in the saturation region for change in channel dimensions W and L is given by Eqn (4.3) for deformation along the channel direction and Eqn (4.4) for deformation across the channel with comparable expressions for the linear regime (see Appendix C).

$$I_{SD} = \frac{1}{\lambda_L}\frac{W}{L} C_G \mu \left[\frac{1}{2}\left(V_G - \frac{1}{\sqrt{\lambda_L}} V_T\right)^2\right] \tag{4.3}$$

$$I_{SD} = \lambda_W{}^2 \frac{W}{L} C_G \mu \left[\frac{1}{2}\left(V_G - \frac{1}{\sqrt{\lambda_W}} V_T\right)^2\right] \tag{4.4}$$

The effect of uniaxial deformation is strikingly different in the two cases despite the similar modification of V_T. The relative current ($I_{SD,\lambda}/I_{SD,\lambda=1}$) in the saturation regime upon deformation of a model p-type TFT with W/L = 1, C_G = 5 nF cm^{-2}, and V_T = −10 V and V_G = −40 V is shown in Figure 4.3a. Because the mobility is constant, it does not impact the relative current. The current scales as ~1/λ_L, at small V_T relative to

V_G, as the device is stretched along the channel length, L, because the change in the width and thickness of the dielectric compensate each other. The current scales as $\sim\lambda_W^2$ for extension along the channel width, W, due to the shortening of the channel length and the decrease in thickness of the gate dielectric. This result also holds for the saturation regime at small V_T relative to V_G (see Appendix C). It can be seen from the plots that deformation along the channel length produces a smaller change in the output current of the TFT than deformation along the channel width; note that if the I–V characteristics are plotted on a log scale to show the on-to-off characteristic then such changes would be more difficult to see than in the case where the deformation is along the width of the TFT.

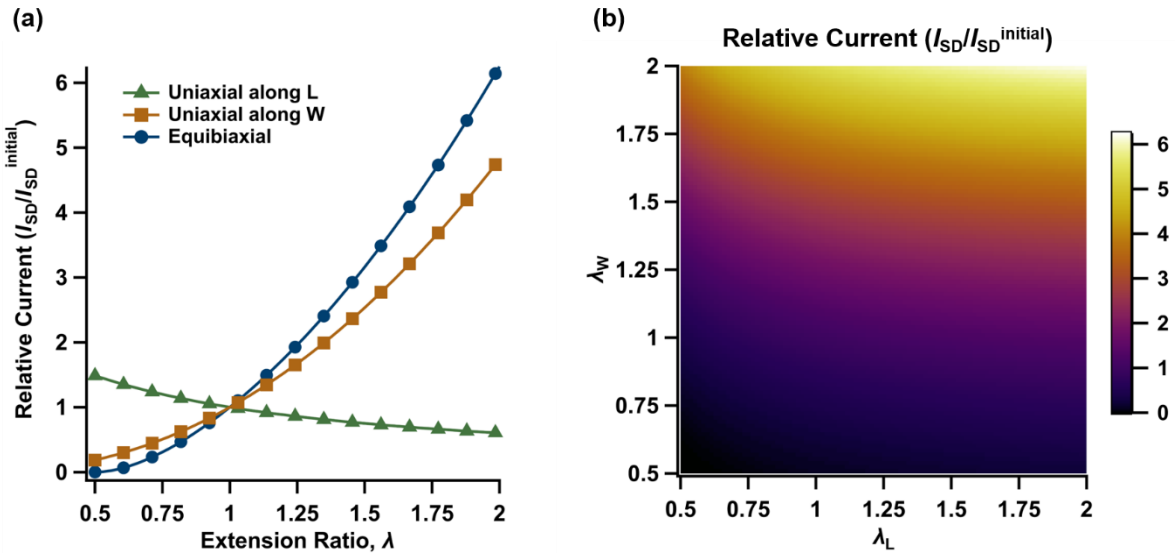

Figure 4.3 (a) Relative I_{SD} of a TFT in the saturation regime as a function of extension ratio for uniaxial deformation along L (triangles) and W (squares) and equi-biaxial deformation along L and W (circles). (b) Two-dimensional plot of the relative current for biaxial deformation. The TFT was modeled with the following parameters: $W/L = 1$, $C_G = 5 \times 10^{-9}$ F cm^{-2}, and a $V_T = -10$ V with $V_G = -40$ V.

As a TFT undergoes deformation, the resistance of the channel will change. As the channel length increases the current drops under the condition of a vanishingly

small contact resistance. However, in practical organic TFTs the contact resistance may be comparable to the channel resistance depending on the initial dimensions of the device, i.e., for short channel lengths or if there is a substantial injection barrier.[28] Upon extension, the channel resistance increases leading to a smaller influence of a fixed contact resistance as the device is stretched along L, but has an increasing effect upon compression as the channel resistance drops. The change in channel resistance differs with deformation along W and could, in principle, lead to apparent differences in mobility extracted from a device with a contact resistance that is competitive with the channel resistance. Given that contact resistances are known to strongly influence the extraction of the apparent carrier mobility in high performance TFTs,[26,28] the best practice would be to evaluate the contact resistance using a variety of channel lengths before interpreting changes in mobility upon deformation. One expects that larger devices, e.g., L > 100 μm, would be preferable for studies of the elastic behavior of TFTs particularly without reasonable models of the injection barrier using elastic conducting composites as electrodes.

Biaxial extension

If a TFT is deformed along both the width and length of the channel in biaxial deformation, Eqn (4.5) shows that the current in the saturation regime scales with $\sim\lambda_W^2$. This behavior can be understood by considering the changes under biaxial extension. The thickness of the dielectric changes as the product $1/\lambda_W\lambda_L$ thereby modifying the gate capacitance. This change compensates for the change in L and the device outputs a current that is surprisingly dominated by changes in W at high V_G relative to V_T despite the biaxial deformation. The relative current with deformation

for the case of equi-biaxial deformation along L and W is given in Figure 4.3a and that for the full spectrum of biaxial deformation is given in Figure 4.3b.

$$I_{SD} = {\lambda_W}^2 \frac{W}{L} C_G \mu \left[\frac{1}{2}\left(V_G - \frac{1}{\lambda_L \lambda_W} V_T\right)^2\right] \quad (4.5)$$

A striking prediction of the model is that if the device is compressed then the effective V_T could increase enough to shut the TFT off. Given the assumption in the model that shifts in V_T are dominated by the change in the gate capacitance, this condition occurs when $V_T/V_G = \lambda_L\lambda_W$. The switch to the off-state could occur at relatively low compression of both directions, e.g., $\lambda \sim 0.7$, at low values of V_G and suggests that such TFTs would be highly sensitive to deformation near this operational condition.

Comparisons to literature

We can compare the model to some results reported in literature, however we note that no truly elastic semiconducting polymers have been reported to our knowledge. The most widely studied stretchable TFTs use composites to achieve elastic behavior. The apparent mobility of stretchable TFTs formed with SEBS/(diketopyrrolopyrole-based semiconducting polymer) blends, SWCNTs supported by SEBS as electrodes, and an SEBS dielectric was reported to be roughly constant based on extraction of the I–V characteristics.[2] The current of the TFTs dropped with extension along the channel length in agreement with the model here, but was nearly constant with deformation along the width to extension of ~1.75 in contrast to predictions here for uniaxial deformation along W.[2] An explanation for the difference would be that the inhomogeneous polymer aggregates in the SEBS matrix did not fill the channel as W

increased, i.e., the number of semiconducting pathways between the source and drain did not change with deformation in the blend. We can also compare the model to TFTs formed with an elastic PDMS dielectric, PDMS-encapsulated SWCNT electrodes, and amorphous indacenodithiophene-co-benzodiathiazole polymer (IDTBT). These TFTs show a decrease in current with extension along *L*, but a more complex behavior with extension along W where the current decreases then increases again.[29] The apparent mobility of the TFT was reported to decrease with deformation in both directions; this could arise from changes in the morphology of the semiconductor or potentially a change in injection from the SWCNT composite electrodes. Considering that the gate capacitance of SEBS dielectrics does change as expected by the model,[24] detailed analysis of stretchable TFTs using the model here should help to reveal the physical origin of changes in the *I*–*V* characteristics.

Predictions for the behavior of circuits

The model for the *I*–*V* characteristics of TFTs with deformation also shows that the layout of a circuit with respect to the deformation direction will have a significant impact on the performance of a stretchable circuit. We consider the case of a complementary inverter with n- and p-type TFTs with the physical layouts shown in Figure 4.4. In digital circuits inverters are used to change the sign of the input voltage, V_{in}, as an output voltage, V_{out}.[30] In analog circuits the inverter can be used as a simple amplifier when operated near an input value referred to as the inverting voltage, V_{inv}, where both the n- and p-type TFTs are in saturation (see Figure C1, Appendix C).[30] Complementary inverters made with organic TFTs have been studied to understand the impacts of gate bias stress and other factors on their operation.[31,32]

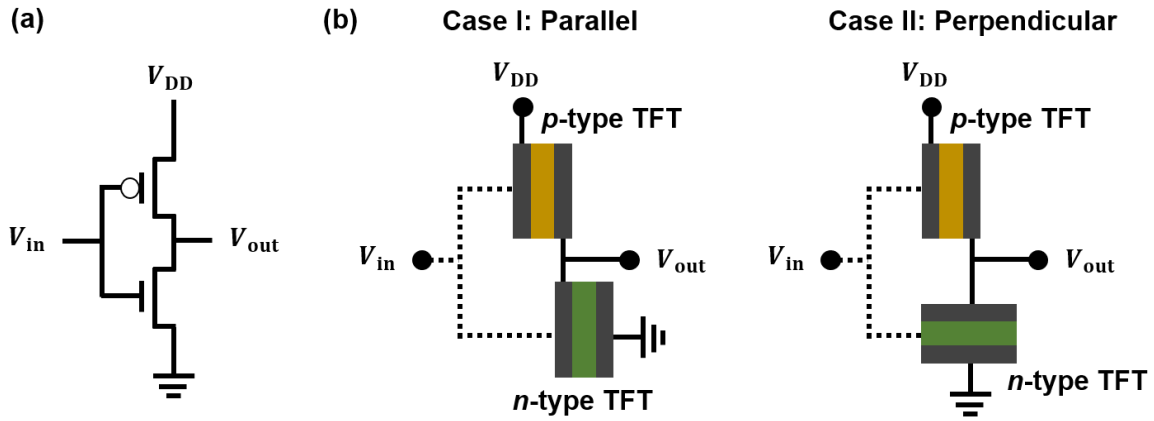

Figure 4.4 (a) Diagram of a complementary inverter circuit with n- and p-type TFTs. VDD is the supply voltage. (b) Top view of the physical layouts of an inverter circuit where the channels of the TFTs are oriented parallel to each other (Case I) and perpendicular to each other (Case II). The dashed line indicates connections to the gate electrodes of the TFTs.

In Case I the TFTs are arranged such that deformation affects both devices in the same way whereas in Case II the TFTs are laid out perpendicular to each other. The operation of circuits such as inverters depends on changes in the resistance, i.e., I_{SD}, of the TFTs upon deformation, which occur even if the mobility of the semiconductor is constant. For Case I, a stability criterion for V_{inv} can be derived from the behavior as a function of uniaxial extension. Eqn (4.6) gives the expected value of V_{inv} with deformation along L (see Appendix C for derivation).

$$V_{inv} = \frac{V_{DD} - \frac{1}{\sqrt{\lambda_L}}|V_{T,p}| + \frac{1}{\sqrt{\lambda_L}}V_{T,n}\sqrt{\beta_n/\beta_p}}{1+\sqrt{\beta_n/\beta_p}} \tag{4.6}$$

In these expressions, β is equal to $(W/L)\mu C_G$ for the n- and p-type TFTs. Eqn (4.7) gives the resulting stability criterion such that V_{inv} is invariant with λ_L that forces the dimensions of the n- and p-type TFTs to be set by the ratio of V_T for the n- and p-type TFTs. This expression is valid for deformation along W with substitution of λ_W for λ_L because the behavior depends only on the change in V_T with deformation. Here

we ignore changes in V_T due to gate bias stress, which has been considered previously and depends on the functional form of the shift in V_T.[31]

$$\sqrt{\beta_n / \beta_p} = \frac{|V_{T,p}|}{V_{T,n}} \tag{4.7}$$

In contrast to Case I, no stability criterion can be found in Case II because the dimensions of the two TFTs change differently with extension. Here V_{inv} is given by Eqn (4.8) in this case for deformation, λ, along the channel of the p-type TFT and the width of the n-type TFT.

$$V_{inv} = \frac{V_{DD} - \frac{1}{\sqrt{\lambda}}|V_{T,p}| + \frac{1}{\sqrt{\lambda}} V_{T,n} \lambda^{3/2} \sqrt{\beta_n / \beta_p}}{1 + \lambda^{3/2} \sqrt{\beta_n / \beta_p}} \tag{4.8}$$

Figure 4.5 shows the inverter characteristics in both Case I and II along with a plot of V_{inv} with n- and p-type TFTs with device parameters comparable to typical TFTs with polymeric gate dielectrics. For both cases the gain (the slope near V_{inv}) varies with deformation with the most severe changes occurring for Case II. In both cases, if the input voltage is well away from V_{inv}, the circuit will still operate as an inverter, but the operational window is substantially affected by deformation in Case II. Such characteristics will lead to a relatively poor noise margin in complex circuits.[30–32] The model does show that if the mechanical deformation is predictable, e.g., for a circuit in a device that is constrained to deform along a particular direction, then circuits and driving voltages may be designed to compensate for mechanical strain. Additionally, the behavioral predictions from the model can be used to design high sensitivity strain/pressure sensors with built-in response, such as the Case II layout, in which V_{inv} varies significantly with deformation. More complex circuit layouts with multiple

inverters can potentially be designed to detect and deconvolute strains in multiple directions.

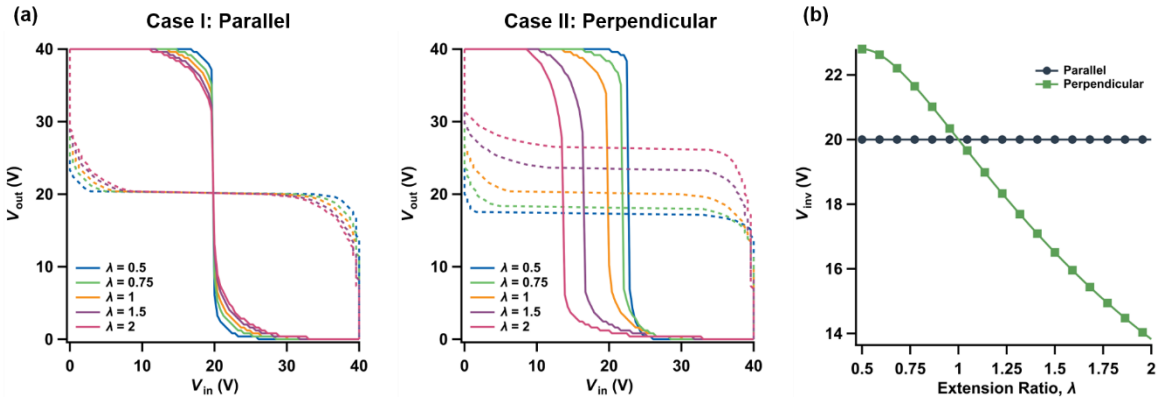

Figure 4.5 (a) Characteristics for an inverter with the Case I and Case II layouts as described in Fig. 4.4. The solid line shows the output voltage, V_{out}, with respect to the input voltage, V_{in}, and the dashed lines are transformations of the circuit performance to highlight the eye of the operational regime of the circuit. (b) Inverting voltage, V_{inv}, with deformation for Case I and Case II showing stability when the TFTs are oriented in the same direction with respect to the deformation and instability when they are not.

Elastic electrochemical transistors

In addition to TFTs, other types of transistors known as organic electrochemical double layer transistors (EDLTs) and organic electrochemical transistors (OECTs) are under investigation.[33–35] In contrast to TFTs, the gate dielectric in EDLTs and OECTs is formed from a fluid or solid-state electrolyte with mobile ions that respond to the gate voltage. In OECTs the current of the transistor flows through the bulk of the semiconducting layer due to infiltration of ions into the semiconductor (Figure 4.1), but in EDLTs ions cannot infiltrate the semiconductor and current flows at the surface of the semiconductor. These devices have advantages over conventional organic TFTs because the operating voltages are low due to the high capacitance of the ionic

dielectric. OECTs in particular are being examined widely in bioelectronics because of their high transconductance.[36]

We can model EDLTs and OECTs with similar assumptions to TFTs, but with a few key differences. We assume that the capacitance of the electrochemical gate is not affected by deformation because the motion of ions to form the double layer, or to penetrate the bulk, should be relatively insensitive to the thickness of the dielectric. The model should be valid for both solid-state electrolytes and for solvent-based electrolytes. We note that we have ignored the effect of swelling of the semiconductor by the ions, which is typically small (a few percent change in volume);[37,38] however for precise modeling at small deformations such changes should be considered as well. The model predicts the I–V behavior at steady state and ignores the speed of the formation of the EDL or the kinetics of infiltration of ions into the channel in an OECT.[36,39,40] We also note that in EDLT and OECT devices parasitic capacitances can play a significant role due to the large double layer capacitance of the dielectric. These effects will also be modified by deformation due to changes in the area of the electrodes,[40] but we ignore their contribution because they are very specific to the exact device design and here only focus on the limiting behavior where the channel controls the operation of the transistor.

In the case of an EDLT, charge is accumulated in a thin layer of the semiconductor at the interface of the dielectric and semiconductor due to formation of an electrochemical double layer. Dimensional changes in the thickness of the semiconductor are not a factor in the operation of EDLTs. For uniaxial deformation, the current of the EDLT varies more strongly than for the TFT because of differences

in the behavior of the dielectric. Eqn (4.9) and (4.10) give the results for the I–V behavior in the saturation regime upon uniaxial deformation along L and W, respectively. Here there is no dependence of the V_T upon deformation assuming no change in the trap density because of the constant C_G. Under biaxial strain, the change in I_{SD} depends only on the ratio of the deformations along L and W leading to stable operation with equi-biaxial deformation (Eqn (4.11)).

$$I_{SD} = \frac{1}{{\lambda_L}^{3/2}} \frac{W}{L} C_G \mu \left[\frac{(V_G - V_T)^2}{2}\right] \tag{4.9}$$

$$I_{SD} = {\lambda_W}^{3/2} \frac{W}{L} C_G \mu \left[\frac{(V_G - V_T)^2}{2}\right] \tag{4.10}$$

$$I_{SD} = \frac{\lambda_W}{\lambda_L} \frac{W}{L} C_G \mu \left[\frac{(V_G - V_T)^2}{2}\right] \tag{4.11}$$

The current between the source and drain in OECTs depends on the thickness of the semiconducting layer, d, because it flows through the bulk due to infiltration of ions from the gate dielectric. Models for the detailed I–V characteristics of OECTs are under investigation and here we use the simplest case where a volumetric capacitance of the semiconductor, C^*, determines I_{SD} with applied gate bias.[35] C^* is determined by the carriers per volume in the semiconductor and is limited for a given material by the number of repeat units in the polymer, i.e., there are a maximum number of valence (or conduction) electrons that can be removed (added) to the polymer. We assume that C^* is unaffected by deformation, which is reasonable because there is no change in monomers per volume. The I–V behavior of an OECT in saturation is given by Eqn (4.12) where d is the thickness of the semiconducting layer.

$$I_{SD} = \frac{W}{L} dC^* \mu \left[\frac{(V_G - V_T)^2}{2}\right] \quad (4.12)$$

Upon deformation the resistance of the OECT changes with the dimensions of the semiconductor. The conduction through the bulk of the semiconductor leads to a fixed V_T because we assume that the number of trap states does not change with deformation. Given these assumptions, the expectations for the I–V behavior in the saturation regime with uniaxial deformation along L and W and biaxial deformation are given by Eqn (4.13)–(4.15). Comparable expressions will hold for the linear regime of operation.

$$I_{SD} = \frac{1}{\lambda_L{}^2} \frac{W}{L} dC^* \mu \left[\frac{(V_G - V_T)^2}{2}\right] \quad (4.13)$$

$$I_{SD} = \lambda_W \frac{W}{L} dC^* \mu \left[\frac{(V_G - V_T)^2}{2}\right] \quad (4.14)$$

$$I_{SD} = \frac{1}{\lambda_L{}^2} \frac{W}{L} dC^* \mu \left[\frac{(V_G - V_T)^2}{2}\right] \quad (4.15)$$

The variation in the current for OECTs can be seen in Figure 4.6 where both uniaxial and biaxial deformation leads to substantial changes in the current. Due to the scaling of the dimensions, the biaxial case (Eqn (4.15)) shows no dependence on λ_W because of the constraint from the thickness of the semiconductor.

The model allows us to determine if there are potential advantages of OECTs vs. TFTs for elastic circuits. First, OECTs have lower operating voltages than TFTs and the current can be much higher than TFTs because of the conduction through the bulk of the device.[34] For current-driven circuits, such as an organic light emitting diode (OLED) connected to an OECT, the output current will vary substantially upon

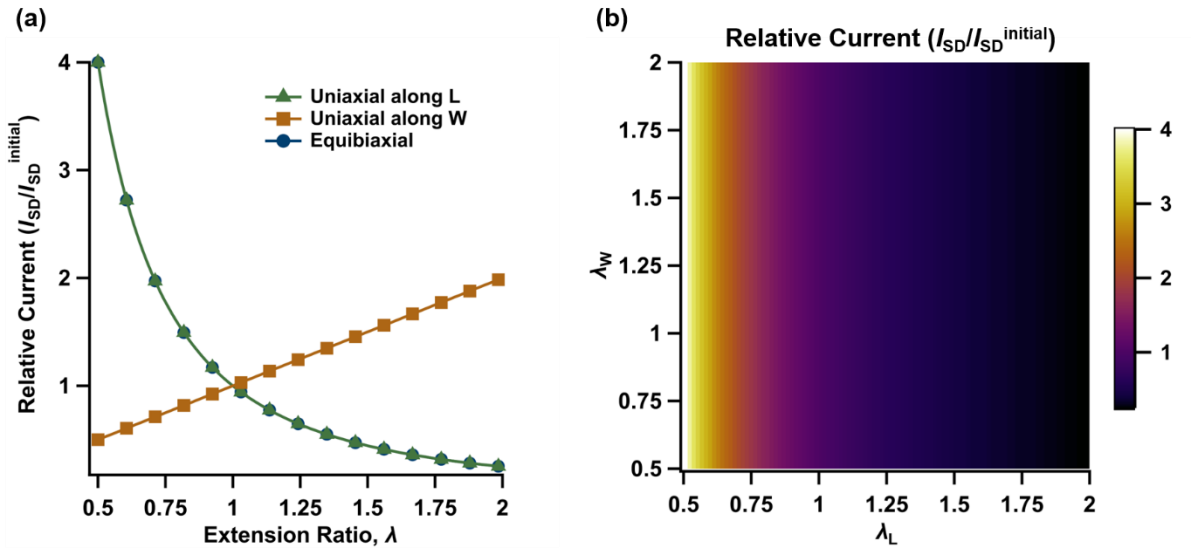

Figure 4.6 (a) Relative I_{SD} of an OECT in the saturation regime as a function of extension ratio for uniaxial deformation along L (triangles) and W (squares) and equi-biaxial deformation along L and W (circles). (b) Two-dimensional plot of the relative current for biaxial deformation. The OECT was modeled with the following parameters: W/L = 1, C^* = 40 F cm^{-3}, d = 100 nm, and V_T = −0.5 V with V_G = −3 V.

deformation and would lead to significant changes in the operation, e.g., brightness, of an OLED. In contrast, for a digital circuit like a complementary inverter, it is possible to find conditions where the parameters of the OECTs can be set to provide a stable value of V_{inv} with deformation for both Case I and Case II (see Appendix C). The predicted behavior of OECT-based inverters with respect to deformation is given in Figure 4.7. The condition for a stable inverter is the same in both cases because of the assumption in the model that V_T is independent of deformation. This would suggest that for some digital circuits the layout of OECTs relative to the deformation direction could be more forgiving than for conventional TFTs. Note that we have not considered the frequency-dependent behavior of OECTs where the kinetics of ion motion could couple with mechanical motion, which could be a fruitful area to pursue for unique electrical behavior for sensing. The overall results suggest that elastic OECTs are

worth pursuing for circuit applications and should have unique behavior relative to TFTs.

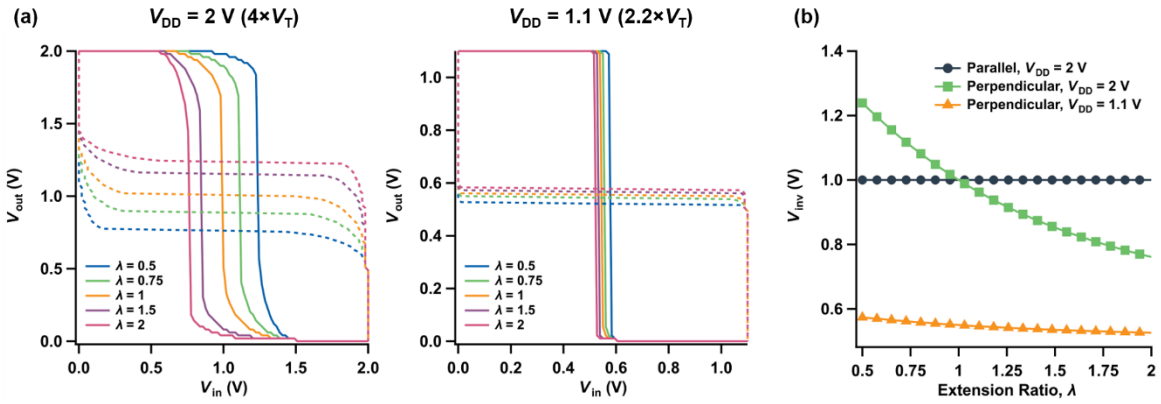

Figure 4.7 (a) Characteristics for an OECT inverter with the Case II (perpendicular) layout, with two different supply voltages: 2 V (farther from the stability criterion) and 1.1 V (closer to the stability criterion). (b) Inverting voltage, V_{inv}, with deformation for Case I and Case II (at the two different supply voltages) showing higher stability for the Case II device operated near the stability criterion.

4.4 Conclusion

A model for the electro-mechanical behavior of elastic TFTs was derived under the assumption of uniform deformation of the semiconductor, dielectric, and electrodes each having the mechanical behavior of incompressible elastic polymer networks. While the model is simple, it provides a means to interpret changes in the electrical operation of TFTs with deformation. Both conventional and electrochemical TFTs are predicted to show substantial changes in their I_{SD} with deformation due to changes in the dimensions of the channel and dielectric. This behavior should be considered in the physical layout of stretchable circuits along with the mechanical strains that the circuit may experience under operation.

Many reports of stretchable TFTs focus on the mobility of the semiconducting material, but the behavior of circuits strongly depends on changes in the absolute

resistance of the circuit elements with deformation. The negative effects of strain have been noted for silicon-based circuits[41] and led to the design of rigid TFTs with stretchable interconnects that have a negligible contribution to the circuit operation.[42,43] If fully stretchable electronics are desired, then circuit designs that are less sensitive to precise current levels and shifts in V_T will be essential. Some neuromorphic elements and designs, such as Schmitt triggers,[44] can compensate for variations in input voltages and such designs may prove to be important for elastic organic devices. Because the behaviors of elastic TFTs and OECTs differ substantially upon deformation, improved models of the $I–V$ behavior of OECTs will benefit the design of future bioelectronic systems. We also expect that new circuit designs for stretchable electronics could lead to improved performance in sensing where the physical behavior of the materials is used beneficially.

4.5 Acknowledgements

This work was supported by the National Science Foundation through the MRSEC Program of the National Science Foundation through Grant No. DMR-1720256 (IRG-2). V.G.R. gratefully acknowledges the National Science Foundation Graduate Research Fellowship Program under Grant 1650114. We thank Prof. Tse Nga Ng (UC San Diego) for helpful conversations.

4.6 Appendix C

I. Derivation of Electrical Behavior of Elastic Thin Film Transistors with Deformation

To examine the changes in the electrical characteristics of thin film transistors (TFTs) upon mechanical deformation, we use the extension ratio, λ. The extension ratio is

defined as the ratio of the deformed dimension (x_i) to the initial dimension ($x_{i,0}$) in a particular direction, $\lambda_i = x_i/x_{i,0}$. This metric is preferable to strain for the description of large deformations of polymers. For most amorphous polymers Poisson's ratio is essentially equal to 0.5 and the product of the extension ratios is unity, i.e., $\lambda_1\lambda_2\lambda_3 = 1$, because the material is incompressible.

We present here the full derivation for uniaxial deformation along the channel length of an elastic TFT where all of the materials, semiconductor, dielectric, and electrodes, are deformed to the same extent and behave elastically. The following derivation follows the conventional model for polymer elasticity at small deformation, i.e., $\lambda <$ ~2.[4] For a TFT, we define the extension ratios along the channel width (W), length (L) and dielectric thickness (t) such that:

$$\lambda_W\lambda_L\lambda_t = 1 \tag{1}$$

The TFT as a whole is deformed by λ_L by a force along the channel direction. The other directions are unconstrained because no force is applied and their extension ratios are equivalent.

$$\lambda_W = \lambda_t \tag{2}$$

This results in a simple relationship between the extension ratios given by Eqn 3 and 4.

$$\lambda_W\lambda_t = \frac{1}{\lambda_L} \tag{3}$$

$$\lambda_W = \lambda_t = \frac{1}{\sqrt{\lambda_L}} \tag{4}$$

These relationships can be used to derive the change in the gate capacitance per area C_G (F/cm^2) with deformation given by Eqn 5 and 6 where ε_0 is the vacuum permittivity, ε_r is the dielectric constant of the gate dielectric, and t is the thickness of the gate dielectric.

$$C_G = \frac{\varepsilon_0 \varepsilon_r}{t} \tag{5}$$

$$C_{G,\lambda} = \frac{\varepsilon_0 \varepsilon_r}{\lambda_t t} = \sqrt{\lambda_L} \frac{\varepsilon_0 \varepsilon_r}{t} = \sqrt{\lambda_L} C_G \tag{6}$$

The change in W/L of the TFT under uniaxial deformation is given by:

$$\frac{\lambda_W W}{\lambda_L L} = \frac{W}{{\lambda_L}^{3/2} L} \tag{7}$$

We assume that the total amount of trapped charge in the semiconductor is the origin of the threshold voltage V_T and is constant, $q_{trap} = V_T C_G$. This results in the following expressions:

$$C_G V_T = C_{G,\lambda} V_{T,\lambda} \tag{8}$$

$$V_{T,\lambda} = \frac{1}{\sqrt{\lambda_L}} V_T \tag{9}$$

With all of the geometric dependences in hand from Eqn 6, 7, and 9, we can substitute into the gradual channel model for the current-voltage behavior of TFTs to obtain the behavior in the linear and the saturation regimes as a function of uniaxial deformation resulting in Eqn 10 & 11 respectively.

$$I_{SD} = \frac{1}{\lambda_L} \frac{W}{L} C_G \mu \left[\left(V_G - \frac{1}{\sqrt{\lambda_L}} V_T \right) V_{SD} - \frac{{V_{SD}}^2}{2} \right] \tag{10}$$

$$I_{SD} = \frac{1}{\lambda_L}\frac{W}{L}C_G\mu\left[\frac{1}{2}\left(V_G - \frac{1}{\sqrt{\lambda_L}}V_T\right)^2\right] \quad (11)$$

The forms for uniaxial deformation along the channel width, *W*, and biaxial deformation along *W* and *L* can be derived similarly.

II. Derivation of Stability Criterion for Complementary Inverters with TFTs

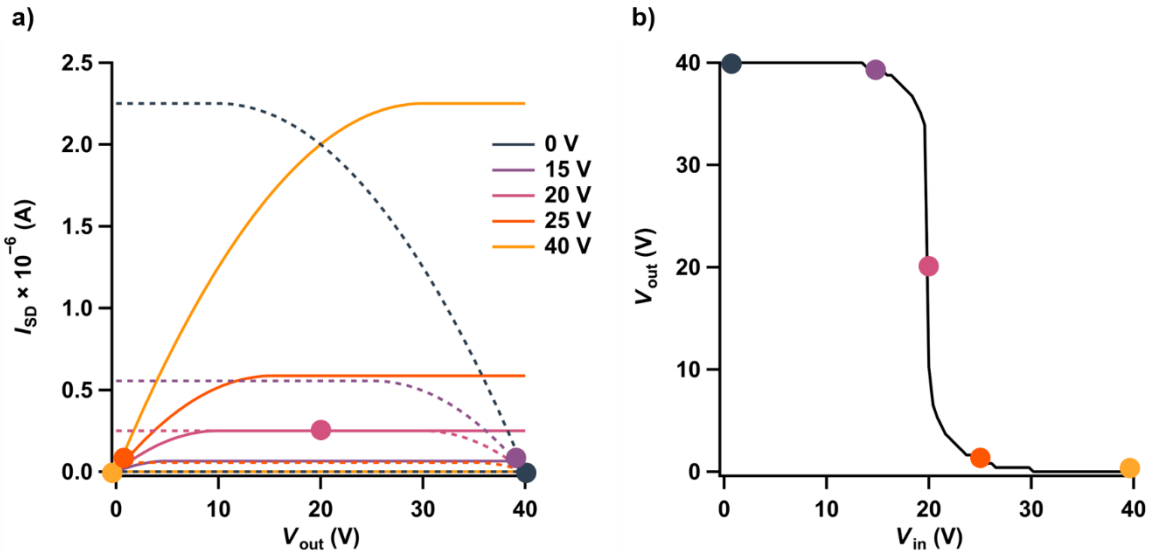

Figure C1 a) Load curves of the n- (solid) and p-type (dashed) TFTs over varying input voltages (V_{in} = 0, 15, 20, 25, and 40 V). b) The voltage transfer curve is created by finding the crossover points of the n- and p-type load curves for a sweep of input voltages.

The value of the inverting voltage, V_{inv}, for a complementary inverter where both the *p*- and *n*- type transistors are in the saturation regime is given by the standard expression in Eqn 12.[30] The device parameters of the two TFTs are given by Eqn 13.

$$V_{inv} = \frac{V_{DD} - |V_{T,p}| + V_{T,n}\sqrt{\beta_n/\beta_p}}{1 + \sqrt{\beta_n/\beta_p}} \quad (12)$$

$$\beta_n/\beta_p = \frac{W_n/L_n \mu_n C_G}{W_p/L_p \mu_p C_G} \quad (13)$$

For uniaxial deformation of an inverter with both TFTs oriented in the same direction, V_{inv} is given by Eqn 14. Here the value of V_T with deformation is assumed to be given by Eqn 9.

$$V_{inv} = \frac{V_{DD} - \frac{1}{\sqrt{\lambda_L}}|V_{T,p}| + \frac{1}{\sqrt{\lambda_L}} V_{T,n} \sqrt{\beta_n / \beta_p}}{1 + \sqrt{\beta_n / \beta_p}} \tag{14}$$

The condition for stability of V_{inv} with deformation can be found by determining when:

$$\frac{dV_{inv}}{d\lambda_L} = 0 \tag{15}$$

The resulting stability criterion is given by Eqn 16 that sets the design parameters for the two TFTs.

$$\sqrt{\beta_n / \beta_p} = \frac{|V_{T,p}|}{V_{T,n}} \tag{16}$$

If the TFTs are laid out into a circuit such that the *p*-type device is deformed along L and the *n*-type device is deformed by the same amount along W given by λ, then the resulting expression for V_{inv} is given by:

$$V_{inv} = \frac{V_{DD} - \frac{1}{\sqrt{\lambda}}|V_{T,p}| + \frac{1}{\sqrt{\lambda}} V_{T,n} \lambda^{3/2} \sqrt{\beta_n / \beta_p}}{1 + \lambda^{3/2} \sqrt{\beta_n / \beta_p}} \tag{17}$$

The derivative of this function has terms with varying powers of λ and a solution to satisfy Eqn 15 that is independent of extension is not possible.

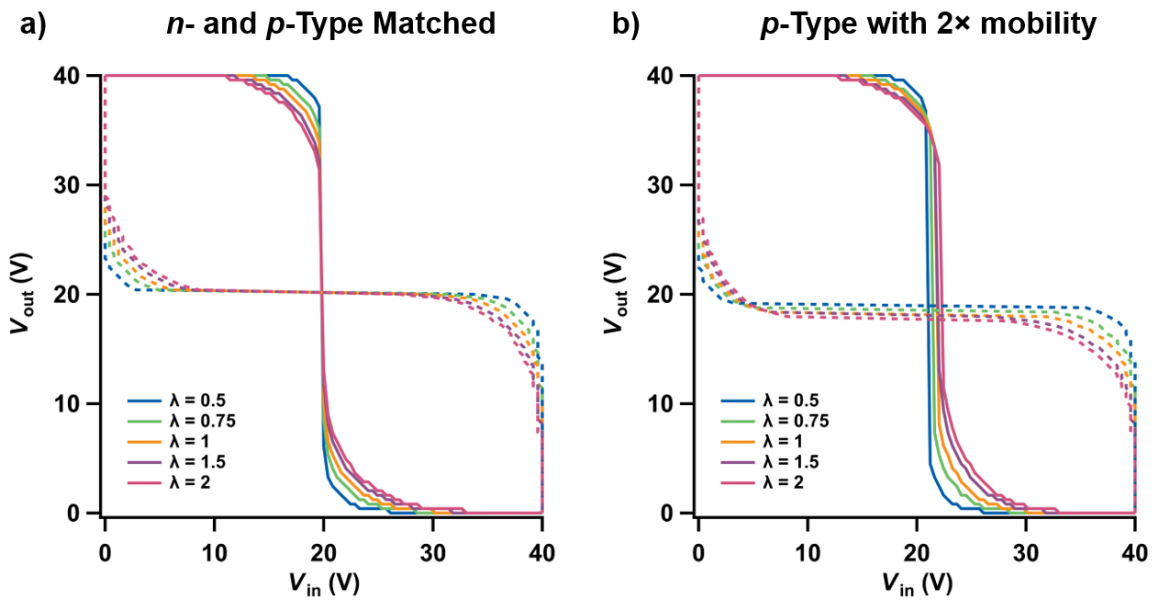

Figure C2 TFT inverter characteristics for a Case I (parallel layout) device deformed uniaxially along L with a) matched n- and p-type TFT specifications, satisfying the above defined stability criterion, and b) mis-matched n- and p-type TFT specifications (with the p-type TFT having double the mobility of the n-type). Note that the mis-matched device (not satisfying the stability criterion) suffers from drift in V_T with deformation.

III. Inverter with Organic Electrochemical Transistors (OECTs)

In the case of organic electrochemical transistors, we assume that V_T is not dependent on deformation, unlike the TFT case. Here the only term in Eqn 12 that will vary with deformation is the ratio of device parameters given in Eqn 13. For a circuit with OECTs laid out with their channels in the same direction (Case I in the main text), V_{inv} is always stable to deformation because both devices deform in the same way.

In the case that they are laid out in different directions (Case II in main text), V_{inv} can be given by the following:

$$V_{inv} = \frac{V_{DD} - |V_{T,p}| + V_{T,n}\lambda^{3/2}\sqrt{\beta_n/\beta_p}}{1 + \lambda^{3/2}\sqrt{\beta_n/\beta_p}} \quad (18)$$

The condition for stability given by Eqn 15 is given by:

$$V_{DD} = \left|V_{T,p}\right| + V_{T,n} \tag{19}$$

This condition limits the value of V_{DD}, which in turn affects the possible gain of the inverter but does lead to stable digital inverting operation.

4.7 References

1. Root, S. E., Savagatrup, S., Printz, A. D., Rodriquez, D. & Lipomi, D. J. Mechanical Properties of Organic Semiconductors for Stretchable, Highly Flexible, and Mechanically Robust Electronics. *Chemical Reviews* 117 6467–6499 (2017).
2. Wang, S. et al. Skin electronics from scalable fabrication of an intrinsically stretchable transistor array. *Nature* 555, 83–88 (2018).
3. Ward, I. M. & Sweeney, J. Mechanical Properties of Solid Polymers. Wiley (2013).
4. Treloar, L. R. G. The Physics of Rubber Elasticity, 3rd Ed. Oxford University Press, Oxford, UK (2005).
5. Kleinschmidt, A. T. & Lipomi, D. J. Stretchable Conjugated Polymers: A Case Study in Topic Selection for New Research Groups. *Accounts of Chemical Research* 51, 3134–3143 (2018).
6. Kong, D. et al. Capacitance Characterization of Elastomeric Dielectrics for Applications in Intrinsically Stretchable Thin Film Transistors. *Advanced Functional Materials* 26, 4680–4686 (2016).
7. Matsuhisa, N., Chen, X., Bao, Z. & Someya, T. Materials and structural designs of stretchable conductors. *Chemical Society Reviews* 48 2946–2966 (2019).
8. Cai, L., Zhang, S., Miao, J., Yu, Z. & Wang, C. Fully Printed Stretchable Thin-Film Transistors and Integrated Logic Circuits. *ACS Nano* 10, 11459–11468 (2016).
9. Zhang, G. et al. Versatile Interpenetrating Polymer Network Approach to Robust Stretchable Electronic Devices. *Chemistry of Materials* 29, 7645–7652 (2017).
10. Kim, H. J., Thukral, A., Sharma, S. & Yu, C. Biaxially Stretchable Fully Elastic Transistors Based on Rubbery Semiconductor Nanocomposites. *Advanced Materials Technologies* 3, 1800043 (2018).
11. Oh, J. Y. et al. Intrinsically stretchable and healable semiconducting polymer for organic transistors. *Nature* 539, 411–415 (2016).
12. Kang, B. et al. Stretchable Polymer Gate Dielectric with Segmented Elastomeric Network for Organic Soft Electronics. *Chemistry of Materials* 30, 6353–6360 (2018).
13. Strobl, G. The Physics of Polymers. Springer-Verlag Berlin Heidelberg (2007).

14. Lang, A. S., Muth, M. A., Heinrich, C. D., Carassco-Orozco, M. & Thelakkat, M. Pendant perylene polymers with high electron mobility. *Journal of Polymer Science, Part B: Polymer Physics* 51, 1480–1486 (2013).
15. O'Connor, B. et al. Anisotropic Structure and Charge Transport in Highly Strain-Aligned Regioregular Poly(3-hexylthiophene). *Advanced Functional Materials* 21, 3697–3705 (2011).
16. Moulton, J. & Smith, P. Electrical and mechanical properties of oriented poly(3-alkylthiophenes): 2. Effect of side-chain length. *Polymer* 33, 2340–2347 (1992).
17. Koch, F. P. V. et al. The impact of molecular weight on microstructure and charge transport in semicrystalline polymer semiconductors-poly(3-hexylthiophene), a model study. *Progress in Polymer Science* 38, 1978–1989 (2013).
18. Thelakkat, M., Hagen, J., Haarer, D. & Schmidt, H. W. Poly(triarylamine)s-synthesis and application in electroluminescent devices and photovoltaics. *Synthetic Metals* 102, 1125–1128 (1999).
19. Zhang, W. et al. Systematic improvement in charge carrier mobility of air stable triarylamine copolymers. *Journal of the American Chemical Society* 131, 10814–10815 (2009).
20. Aitken, B. S., Wieruszewski, P. M., Graham, K. R., Reynolds, J. R. & Wagener, K. B. Control of charge-carrier mobility via in-chain spacer length variation in sequenced triarylamine functionalized polyolefins. *ACS Macro Letters* 1, 324–327 (2012).
21. Xie, R. et al. Glass transition temperature from the chemical structure of conjugated polymers. *Nature Communications* 11, 893 (2020).
22. Song, E. et al. Stretchable and Transparent Organic Semiconducting Thin Film with Conjugated Polymer Nanowires Embedded in an Elastomeric Matrix. *Advanced Electronic Materials* 2, 1500250 (2016).
23. Shin, M. et al. Highly stretchable polymer transistors consisting entirely of stretchable device components. *Advanced Materials* 26, 3706–3711 (2014).
24. Xu, J. et al. Highly stretchable polymer semiconductor films through the nanoconfinement effect. *Science* 355, 59–64 (2017).
25. Shin, M. et al. Polythiophene nanofibril bundles surface-embedded in elastomer: A route to a highly stretchable active channel layer. *Advanced Materials* 27, 1255–1261 (2015).
26. Choi, H. H., Cho, K., Frisbie, C. D., Sirringhaus, H. & Podzorov, V. Critical assessment of charge mobility extraction in FETs. *Nature Materials* 17, 2–7 (2018).
27. McCulloch, I., Salleo, A. & Chabinyc, M. Avoid the kinks when measuring mobility. *Science* 352, 1521–1522 (2016).
28. Paterson, A. F. et al. Recent Progress in High-Mobility Organic Transistors: A Reality Check. *Advanced Materials* 30, 1801079 (2018).
29. Zheng, Y. et al. An Intrinsically Stretchable High-Performance Polymer Semiconductor with Low Crystallinity. *Advanced Functional Materials* 29, 1905340 (2019).

30. Rabaey, J. M. Digital Integrated Circuits: A Design Perspective. Prentice Hall (1996).
31. Chow, M. J. et al. Transistor sizing for Bias-Stress instability compensation in Inkjet-Printed organic complementary inverters. *IEEE Electron Device Letters* 37, 1438–1441 (2016).
32. Ng, T. N. et al. Electrical stability of inkjet-patterned organic complementary inverters measured in ambient conditions. *Applied Physics Letters* 94, 233307 (2009).
33. Kim, S. H. et al. Electrolyte-gated transistors for organic and printed electronics. *Advanced Materials* 25, 1822–1846 (2013).
34. Andersson Ersman, P. et al. All-printed large-scale integrated circuits based on organic electrochemical transistors. *Nature Communications* 10, 5053 (2019).
35. Rivnay, J. et al. High-performance transistors for bioelectronics through tuning of channel thickness. *Science Advances* 1 (2015).
36. Rivnay, J. et al. Organic electrochemical transistors. *Nature Reviews Materials* 3, 17086 (2018).
37. Thomas, E. M. et al. X-Ray Scattering Reveals Ion-Induced Microstructural Changes During Electrochemical Gating of Poly(3-Hexylthiophene). *Advanced Functional Materials* 28, 1803687 (2018).
38. Giridharagopal, R. et al. Electrochemical strain microscopy probes morphology-induced variations in ion uptake and performance in organic electrochemical transistors. *Nature Materials* 16, 737–742 (2017).
39. Said, E., Larsson, O., Berggren, M. & Crispin, X. Effects of the ionic currents in electrolyte-gated organic field-effect transistors. *Advanced Functional Materials* 18, 3529–3536 (2008).
40. Zare Bidoky, F. & Frisbie, C. D. Parasitic Capacitance Effect on Dynamic Performance of Aerosol-Jet-Printed Sub 2 V Poly(3-hexylthiophene) Electrolyte-Gated Transistors. *ACS Applied Materials & Interfaces* 8, 27012–27017 (2016).
41. Ahn, J. H. et al. Bendable integrated circuits on plastic substrates by use of printed ribbons of single-crystalline silicon. *Applied Physics Letters* 90, 213501 (2007).
42. Rogers, J. A., Someya, T. & Huang, Y. Materials and mechanics for stretchable electronics. *Science* 327 1603–1607 (2010).
43. Lacour, S. P., Wagner, S., Narayan, R. J., Li, T. & Suo, Z. I. Stiff subcircuit islands of diamondlike carbon for stretchable electronics. *Journal of Applied Physics* 100, 014913 (2006).
44. Bubel, S., Menyo, M. S., Mates, T. E., Waite, J. H. & Chabinyc, M. L. Schmitt trigger using a self-healing ionic liquid gated transistor. *Advanced Materials* 27, 3331–3335 (2015).

4.8 Permissions and Attributions

Chapter 5: Simulation-guided resonant soft X-ray scattering for determining microstructure of triblock copolymers

5.1 Abstract

Resonant soft X-ray scattering (RSoXS) probes structure with chemical sensitivity that is useful for determining the morphology of multiblock copolymers. However, the hyperspectral data produced by this technique are challenging to interpret. Here, we use computational scattering pattern simulations to extract triblock microstructure from the energy-dependent signals observed in RSoXS. Through quantitative

evaluation of a physics-informed set of model morphologies against experimental data, we find a best-fit microstructure of hexagonally-packed core–shell cylinders. We find excellent agreement with electron density reconstruction from hard X-ray scattering data. These results demonstrate the utility of simulation-guided scattering analysis to study complex microstructures that are challenging to image by microscopy.

5.2 Introduction

Block copolymers are a class of soft materials that self-assemble into mesocrystals, with applications ranging from nanoporous membranes to lithographic templates and drug-eluting coatings for biomedical devices.[1,2] As the design space of multiblock copolymers grows through emerging synthetic methods that can address predictions from theory[3–6], there is a growing need for new characterization techniques that reveal greater structural insights than conventional methods provide.[7] This is especially true as the number and type of blocks grows[8]; for example, ABC triblock terpolymers form a significantly more diverse family of structures than AB diblocks.[1,9]

Numerous methods are used to study the microstructure of block copolymers with a variety of mechanisms to achieve contrast between blocks for structure determination. Transmission electron microscopy (TEM) produces images of very thin films with contrast determined primarily by relative electron densities. For organic materials, it is often necessary to enhance contrast by staining with a heavy metal such as osmium or ruthenium that selectively segregates into one domain; challenges then arise for multi-material systems in which certain components may be difficult to stain selectively (or at all).[10,11] Atomic force microscopy (AFM) maps the

surface of a sample through height, phase, or viscoelasticity contrast, which may or may not reflect the bulk structure of a material.[12–14] Near-field scanning optical microscopy (NSOM)—a less common approach—can achieve sufficiently high resolution for imaging block copolymer self-assembly, but contrast often must be enhanced through fluorescence labeling or polarization modulation.[15,16] As a complement to real-space microscopy techniques, X-ray and neutron scattering probe microstructure in reciprocal space.

Conventional, single-energy (hard) X-ray scattering can reveal substantial structural information, however, if the blocks have similar electron densities or if there is insufficient long-range order, definitively identifying the unit cell is difficult. Recently, resonant soft X-ray scattering (RSoXS, alternatively called anomalous scattering at hard X-ray energies) has been used to selectively probe the structure of multiblock copolymers with chemical sensitivity by varying X-ray energy across specific elemental absorption edges. Like differences in electron density, resonant contrast is linked to material chemistry, but it can have a substantially higher magnitude by tuning the incident energy.[17] This effect improves the scattering signal from thin films, which typically exhibit a low intensity due to a small sample volume.[18] The energy dependence of RSoXS patterns is then linked to changes in the structure factor (e.g., two blocks each forming different lattices) and/or the form factor (e.g., a core–shell cylinder which alternately scatters as a solid or hollow cylinder depending on material contrast).[19,20]

RSoXS performed at the carbon edge revealed structural details such as core–shell domains and nested hexagonal lattices of cylinders formed by a poly(1,4-

isoprene)-*block*-polystyrene-*block*-poly(2-vinyl pyridine) triblock copolymer.[19] Another demonstration involving anomalous scattering at the bromine edge showed that in polystyrene-*block*-poly(4-hydroxystyrene) (PS-*b*-PHS), added brominated PHS homopolymer segregated to the PS–PHS interface in a core–shell structure.[20] RSoXS is also valuable in studying membrane microstructures, where disentangling signals from microphase separation/chemical heterogeneity and void structure or surface roughness is challenging in single-energy measurements.[21,22] One important signal in the resonant scattering of block copolymers is variation in the relative peak intensities with energy. Quantitative extraction of energy-variant parameters from RSoXS data has been used to determine the crystalline packing of conjugated polymers.[23] A similar quantitative approach to analyzing the resonant scattering of block copolymers would represent an advance in the interpretation of energy-dependent relative peak intensities. Computational scattering simulations of polarized resonant soft X-ray scattering (P-RSoXS) have been used to characterize molecular orientation at interfaces in organic photovoltaic doner-acceptor blends and polymer-grafted nanoparticles.[24,25] By combining simulations and experiments, structure models can be quantitatively evaluated against experimental data.

Here, we present a technique for studying the structure of block copolymers using simulation-guided scattering analysis. Investigations into block copolymer structure are typically accompanied by microscopy or tomography to identify a single model that can be applied to interpret the data; instead, we leverage high-throughput computation to evaluate many models as an alternative to expensive experimental characterization. A fast scattering pattern simulation software that exploits

computational acceleration with graphics processing units (GPUs) is applied to an ABC triblock terpolymer formed from poly(4-methylcaprolactone) (P4MCL), poly(2,2,2-trifluoroethylacrylate) (PTFEA), and poly(dodecylacrylate) (PDDA), P4MCL-*block*-PTFEA-*block*-PDDA (Figure 5.1).

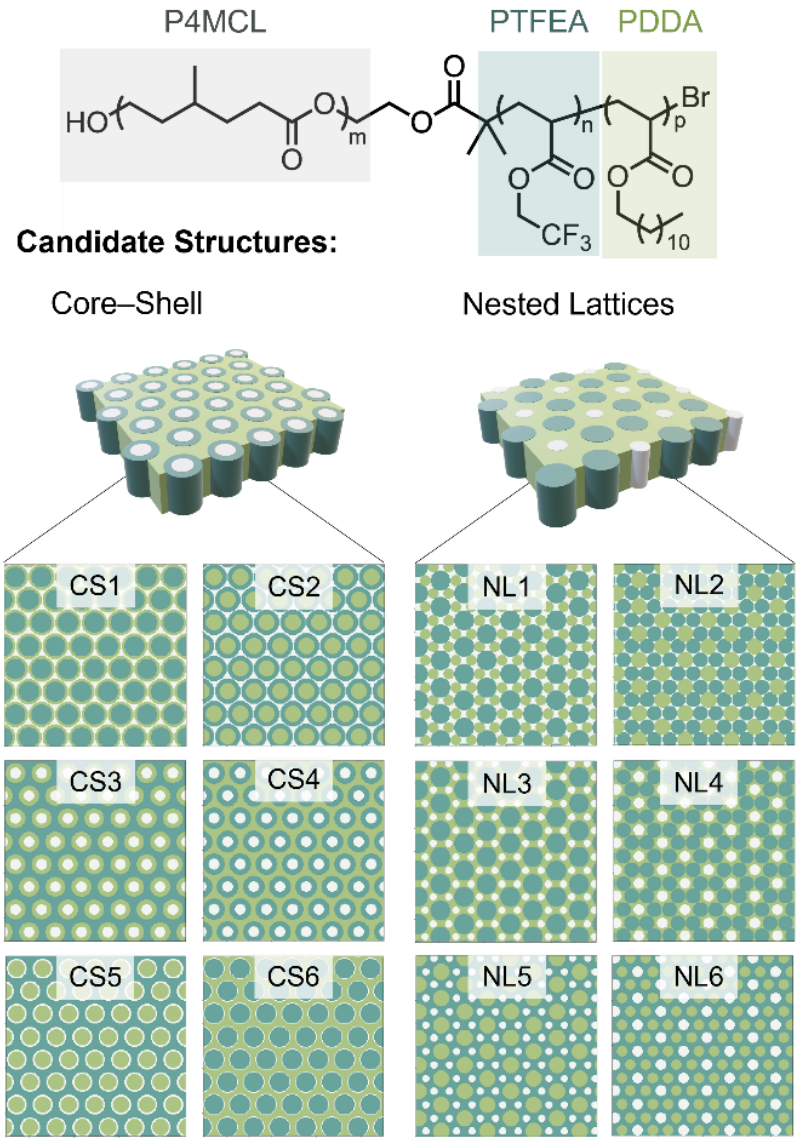

Figure 5.1 The set of candidate structures includes two types previously observed in ABC triblocks (core–shell cylinders and nested lattices). Within each type, there are 3! morphologies representing different arrangements of the blocks. All candidate structures were considered, irrespective of block ordering.

This triblock has a useful chemical handle for RSoXS—the fluorine-containing PTFEA block exhibits high contrast relative to P4MCL and PDDA at the fluorine edge (685 eV). By evaluating a physics-informed set of candidate structures against experimental data, a best-fit structure is found (hexagonally-packed core–shell cylinders with a PDDA matrix, PTFEA shell, and P4MCL core). This conclusion is in good agreement with electron density reconstruction of bulk small-angle X-ray scattering (SAXS) data evaluated against the same candidate structure set. In summary, we demonstrate an approach to scattering analysis which uses modern computation to rapidly evaluate many models against experimental data.

5.3 Experimental Methods

Synthesis & Characterization. The P4MCL-*b*-PTFEA-*b*-PDDA ABC triblock terpolymer was isolated by automated flash chromatography of a parent triblock, which produces well-defined fractions after separation with a low dispersity and negligible homopolymer impurities.[3] The parent P4MCL-*b*-PTFEA-*b*-PDDA triblock was synthesized by sequential anionic ring-opening polymerization (ROP) and photo-initiated atom-transfer radical polymerization (photoATRP) starting from the bifunctional initiator 2-hydroxyethyl 2-bromoisobutyrate (HEBIB). The as-synthesized triblock had molecular weights of P4MCL/PTFEA/PDDA = 14/13/5.0 kDa with volume fractions $\langle f_{P4MCL} \rangle$ = 0.48, $\langle f_{PTFEA} \rangle$ = 0.33, and $\langle f_{PDDA} \rangle$ = 0.19. While the parent triblock morphology could not be definitively assigned by SAXS, the fractionated material with f_{P4MCL} = 0.13, f_{PTFEA} = 0.51, and f_{PDDA} = 0.36 exhibits clear reflections that index to a hexagonal crystal system. Based on the high-quality SAXS pattern, this fraction was identified as a candidate for RSoXS analysis. The PTFEA,

P4MCL, and PDDA block chemistries were chosen because microphase separation is observed between all three pairs at reasonable degrees of polymerization, which is important for self-assembly kinetics. Each block has a low glass transition temperature ($T_{g,P4MCL} \approx -60$ °C, $T_{g,PTFEA} \approx 1$ °C; $T_{g,PDDA}$ cannot be resolved due to an overlap with the melting temperature, but the homopolymer is a liquid under ambient conditions)[26–28] and the resulting triblock is a soft solid which is readily annealed thermally or using solvent vapor.

Small-Angle X-ray Scattering. SAXS measurements of bulk samples were conducted using a custom-built SAXS diffractometer at the Materials Research Laboratory (MRL) X-ray facility (University of California, Santa Barbara). For these experiments, 1.54 Å Cu Kα X-rays were generated using a Genix 50 W X-ray microsource (50 μm micro-focus) equipped with FOX2D collimating multilayer optics (Xenocs, France) and high efficiency scatterless single crystal/metal hybrid slits.

Thin Film Preparation. P4MCL-*b*-PTFEA-*b*-PDDA thin films for RSoXS were prepared by spin coating 3 w/w% solution in toluene directly onto a silicon nitride window (Norcada Inc.). To increase long-range order, the sample was solvent vapor annealed for 1 hour using 1 mL of toluene in a 75 mL glass jar. The PLA-*b*-PTFEA diblock thin film sample for Near-Edge X-ray Absorption Fine Structure (NEXAFS) spectroscopy was prepared by spin coating 5 w/w% solution in chlorobenzene onto quartz and floating the film in deionized water onto a silicon nitride window. The diblock thin film had a thickness of 139 nm as measured by spectral reflectance (Filmetrics F20) on a separate section of the film floated onto silicon.

RSoXS and NEXAFS. RSoXS and NEXAFS measurements were taken at the Spectroscopy Soft and Tender (SST-1) beamline at the National Synchrotron Light Source II.[29] The measurements were taken in vacuum with the incident beam normal to the substrate. Two-dimensional scattering patterns were recorded on a charge-coupled device (CCD) detector sensitive to soft X-rays (greateyes GmbH). The sample was positioned such that the incident beam encountered the silicon nitride membrane before the polymer thin film.

5.4 Results and Discussion

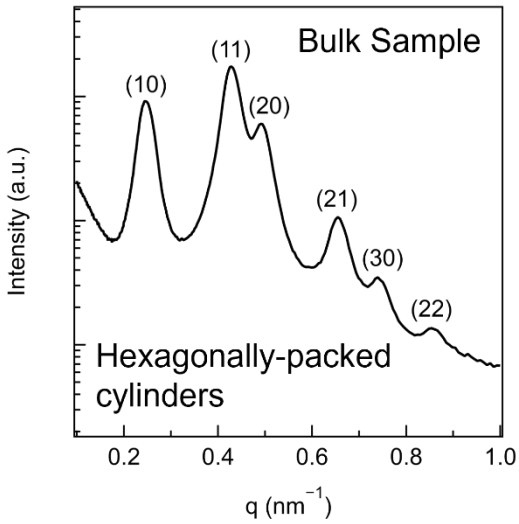

Figure 5.2 Radially-integrated SAXS pattern of P4MCL-*b*-PTFEA-*b*-PDDA thermally annealed in bulk under vacuum at 130 °C for 12 h, 70 °C for 24 h, and RT for 5 h.

In both bulk SAXS (Figure 5.2) and thin-film RSoXS (Figure 5.3a), P4MCL-*b*-PTFEA-*b*-PDDA exhibits peaks (q^*, $\sqrt{3}q^*$, $\sqrt{4}q^*$, $\sqrt{7}q^*$) that indicate a 2D hexagonal plane group (p6mm)[30] with a *d*-spacing ($2\pi/q^*$) of 25 nm. This observation is consistent with two previously observed ABC triblock terpolymer morphologies: core–shell

cylinders and cylinders arranged in nested lattices.[19,31,32] Using the scattering-measured *d*-spacing and NMR-derived volume fractions ($\langle f_{P4MCL} \rangle$ = 0.13, $\langle f_{PTFEA} \rangle$ = 0.51, $\langle f_{PDDA} \rangle$ = 0.36), a set of possible morphologies was generated through geometric analysis (Figure 5.1 and Figure D7, see Appendix D for more details). Core–shell cylinders (CS) and nested lattices (NL) each has 6 possibilities (a permutation of blocks A, B, and C as the matrix, core, and shell for core–shell cylinders or the matrix, lattice 1, and lattice 2 for nested lattices). These real-space models were used to (a) generate the computational scattering pattern simulations for RSoXS analysis and (b) evaluate the electron density reconstruction results relative to expected volume fractions and average electron density. We stress that not all of these possible morphologies are physically realistic given the block connectivity of P4MCL-*b*-PTFEA-*b*-PDDA; as expected and demonstrated below, non-physical options are disfavored by our scattering analysis.

Scattering contrast. The key to interpreting scattering data from multi-material systems such as ABC triblock terpolymers is quantitatively understanding the origin of scattering contrast. The scattering contrast between blocks in conventional (hard X-ray) SAXS is determined by differences in electron density (0.342, 0.436, and 0.316 electrons/Å^3 for P4MCL, PTFEA, and PDDA respectively). Resonant contrast near atomic absorption edges is determined by differences in the energy-dependent complex index of refraction ($\hat{n}(E) = 1 - \delta(E) + i\beta(E)$). This results in the ability to probe structure with varying contrast between blocks; two particularly useful scenarios involve selectively probing a block by either minimizing contrast between the other two blocks (called contrast matching) or maximizing contrast of the block

relative to the other two (leveraging a unique heteroatom, for example). P4MCL-*b*-PTFEA-*b*-PDDA is expected to have variations in contrast at both the carbon and fluorine K edges (284 and 685 eV, respectively). Here, we utilize the fluorine K edge due to the large and unambiguous contrast resulting from fluorine atoms in PTFEA and enhanced resolution accessible at higher energy compared to the carbon K edge.

The refractive index of PTFEA was calculated from the absorption spectrum measured by transmission NEXAFS spectroscopy. This technique requires a thin film of the material prepared on an X-ray transmissive substrate, e.g., silicon nitride. We found that PTFEA did not readily form a thin film, likely due to surface energy, as spin coating resulted in severe de-wetting (Figure D2, Appendix D). To perform the measurement, we instead used a diblock of PTFEA with poly(lactide) (PLA), PLA-*b*-PTFEA, which readily formed a suitable thin film (Figure D2, Appendix D). PLA-*b*-PTFEA was synthesized using sequential photoATRP and ROP from HEBIB (synthetic details available in Appendix D). The imaginary part of the refractive index β of the diblock was calculated using Beer's law from the sample thickness and optical density ($O.D. = -\ln(I/I_0)$ where I is the transmitted intensity and I_0 is the incident intensity, taken as the intensity measured through a blank silicon nitride substrate).[33] The real part of the refractive index δ was calculated via a Kramers–Kronig transform, using the open-source software KKcalc.[34] The refractive index of PTFEA was extracted by subtracting the calculated PLA contribution (estimated using the Henke atomic scattering factors[35]), assuming the index of refraction is a volume-fraction average ($\hat{n} = \sum_i \phi_i \hat{n}_i$, where $\hat{n}$ is the complex index of refraction and ϕ is the volume fraction of each block i). Further details are provided in Appendix D. The refractive indices of

the two blocks without fluorine (P4MCL and PDDA) were estimated using the Henke atomic scattering factors.[35] Figure D3 (Appendix D) shows the resulting optical constants for the three homopolymers. PTFEA has one broad absorption peak centered around 693 eV resulting from the trifluoromethyl groups. This feature provides a region of high contrast between both P4MCL–PTFEA and PDDA–PTFEA (see Figure D4 in Appendix D for the pairwise contrast functions, $(\Delta\beta^2 + \Delta\delta^2)/\lambda^4$).

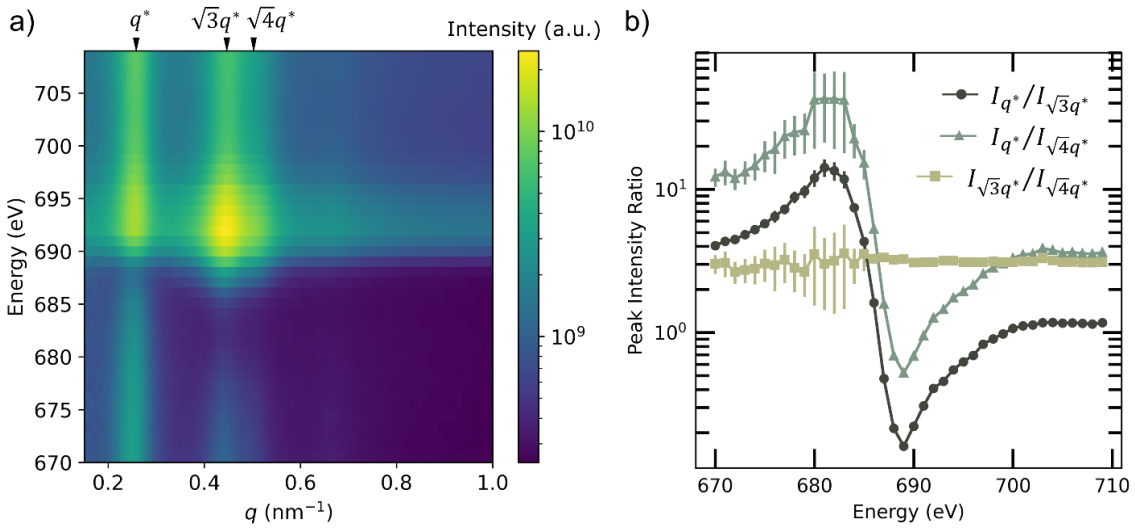

Figure 5.3 a) Scattering intensity of P4MCL-*b*-PTFEA-*b*-PDDA at energies across the fluorine edge. b) Pairwise peak intensity ratios show a strong energy dependence which is related to block contrast and structure. The error bars represent the standard error from peak fitting; larger error bars in the 670–685 eV range arise from challenges in fitting the low intensity $\sqrt{4}q^*$ peak.

Resonant soft X-ray scattering. The scattering intensity of P4MCL-*b*-PTFEA-*b*-PDDA at energies across the fluorine edge is shown in Figure 5.3a. As the X-ray energy is varied, there is a marked change in the relative intensities of the peaks (see Figure D8 in Appendix D for the radially-averaged scattering profiles). The baseline, which is linked to X-ray fluorescence,[36] shifts significantly as well. The peak intensities at q^*, $\sqrt{3}q^*$, and $\sqrt{4}q^*$ were extracted at each energy by least-squares fitting Gaussian

functions along with a cubic polynomial baseline (the intensity of the $\sqrt{7}q^*$ peak was too low to reliably fit). These three peaks were fit simultaneously to ensure a consistent baseline and to deconvolute the $\sqrt{3}q^*$ and $\sqrt{4}q^*$ peaks (further details are provided in Appendix D and an example fit is shown in Figure D9). Peak intensity ratios were calculated in a pairwise manner ($I_{q^*}/I_{\sqrt{3}q^*}$, $I_{q^*}/I_{\sqrt{4}q^*}$, and $I_{\sqrt{3}q^*}/I_{\sqrt{4}q^*}$). Figure 5.3b shows the variation of these peak intensity ratios across the energies near the fluorine edge. We hypothesize that these energetic signatures can be used to identify the most likely structure among a simulation set.

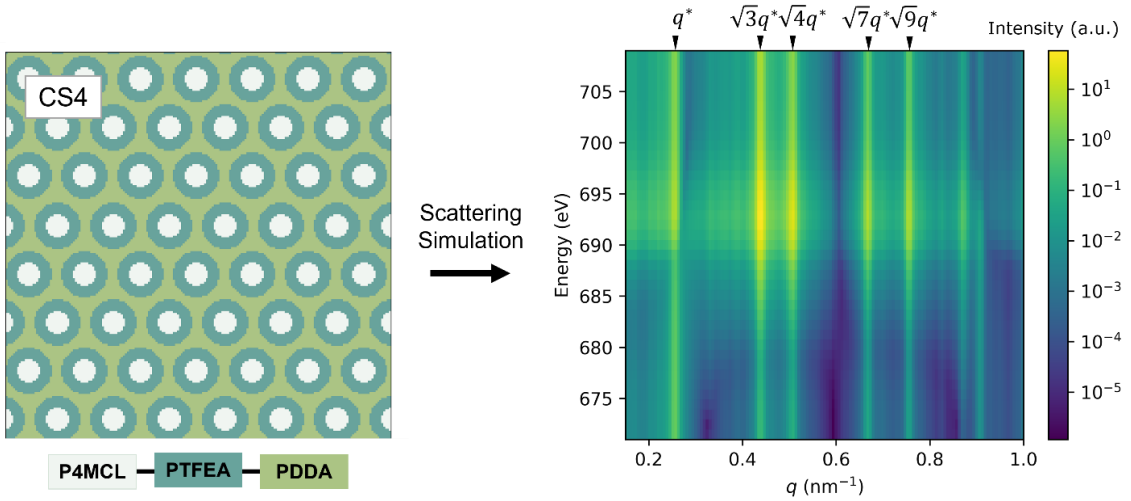

Figure 5.4 *Left*: Composition map representing a 200 × 200 voxel subset of the simulation input for model CS4. *Right*: Simulated scattering intensity of model CS4 at energies across the F edge.

Computational scattering pattern simulations. Inputs to the scattering simulations are real-space composition maps of the models (Figure D7, Appendix D) and optical constants of each block (Figure D3, Appendix D). The composition maps are composed of voxels (each representing 1 nm^3) and are procedurally generated using custom code (hosted on GitHub, access available by request). This numerical approach enables greater flexibility for representing complex geometries relative to

derived analytical models. Additionally, the voxel-based models do not need to be centrosymmetric—a common restriction for models considered in Fourier synthesis approaches in order to limit the number of possible reconstructions.[37] The scattering simulations produce 2D scattering patterns with a resolution in reciprocal space determined by the dimensions of the input image. The simulations are fast due to the parallel processing of different energies; a 40-energy simulation with a 1024 × 1024 × 1 voxel morphology takes ~8 s on the computing cluster used in this work. Figure 5.4 shows the simulated scattering intensity over energies across the fluorine edge for an example morphology, CS4 (see Appendix D for the full set of scattering simulations, Figures D10–D21). The baselines vary with energy in a similar manner to the experimental data, but one notable difference is the pronounced shape of the form factor visible in the simulated profiles. Because the simulated profiles have discrete peaks without overlap, peak intensities were extracted from intensity values at specified q values rather than peak fitting. Then, the pairwise peak intensity ratios were calculated at each energy in a manner similar to the experimental data analysis.

The simulated peak intensity ratios were evaluated against the experimental data using a mean squared error, $\frac{1}{n}\sum_{i=1}^{n}\left(ratio_{exp} - ratio_{sim}\right)^2$. The goodness-of-fit for each simulation was evaluated by summing the mean squared errors of the three ratios. Figure 5.5 shows the distribution of summed mean squared errors for the simulation set and the $I_{q^*}/I_{\sqrt{3}q^*}$, $I_{q^*}/I_{\sqrt{4}q^*}$, and $I_{\sqrt{4}q^*}/I_{\sqrt{3}q^*}$ ratios vs. energy for the best-fit structure CS4 compared to experiment (complete set of ratio overlays available in Appendix D, Figures D10–D21). The best-fit model is a core–shell structure with a PDDA matrix, PTFEA shell, and P4MCL core. This block arrangement is consistent

with the molecular connectivity of the P4MCL-*b*-PTFEA-*b*-PDDA triblock terpolymer. The variation in peak intensity ratios for this core–shell structure represents differences in the form factor of the scattering bodies (circle-like vs. ring-like) as contrast changes with energy. For the $I_{q^*}/I_{\sqrt{3}q^*}$ and $I_{q^*}/I_{\sqrt{4}q^*}$ ratios, the simulation matches the inversion points observed experimentally around 689 eV and captures the line shape well but has a lower magnitude over much of the energy range. Two possible explanations for this are disorder and varying orientations of cylinders in the experimental sample, which can impact the relative peak intensities. The models represent cylinders oriented perpendicular to a substrate (X-ray beam parallel to the long axis of the cylinders). The experimental sample is likely to contain crystalline domains at many orientations; the impact of this discrepancy is expected to be primarily on the magnitude of the peak intensity ratios (further discussion provided

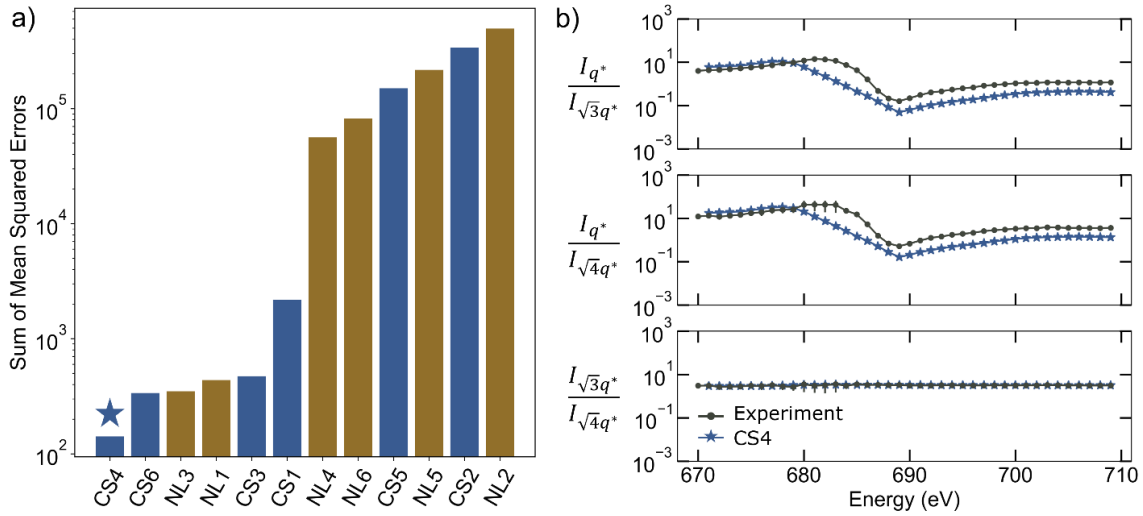

Figure 5.5 a) Sum of the mean squared errors in peak intensity ratios across energy for the simulation set evaluated against experimental data. b) The simulated energy-dependent $I_{q^*}/I_{\sqrt{3}q^*}$ (top), $I_{q^*}/I_{\sqrt{4}q^*}$ (middle), and $I_{\sqrt{4}q^*}/I_{\sqrt{3}q^*}$ (bottom) ratios of the best-fit model CS4 plotted against experimental data. By eye, CS4 captures the experimental line shapes well.

in Appendix D). The $I_{\sqrt{3}q^*}/I_{\sqrt{4}q^*}$ ratio showed excellent agreement in line shape and magnitude between simulation and experiment.

Electron density reconstruction from hard X-ray scattering. The relatively large number of peaks present in the bulk SAXS measurement (Figure 5.2) and sufficiently high electron density contrast enables density reconstruction through Fourier synthesis.[26,38,39] The electron density $\rho(x,y)$ of a two-dimensional morphology can be expressed as the inverse Fourier transform (Eqn 5.1):

$$\rho(x,y) = \bar{\rho} + \sum_{hk}^{N} F_{hk} e^{2\pi i(hx+ky)} \tag{5.1}$$

where $\bar{\rho}$ is the average electron density in the unit cell, N is the number of reflections, x and y are the fractional coordinates in the unit cell, and F_{hk} is the structure factor at given Miller indices h and k (including all symmetry-equivalent reflections). The structure factor at a Bragg reflection hk is given by Eqn 5.2:

$$F_{hk} = |F_{hk}|e^{i\varphi_{hk}} = A \cdot \sqrt{I_{hk}}e^{i\varphi_{hk}} \tag{5.2}$$

where I_{hk} is the integrated intensity with Lorentz and multiplicity corrections, A is a scaling factor arising from the arbitrary intensity measured in scattering experiments, and φ_{hk} is the phase of the reflection.[40,41] The phase of each reflection is inherently ambiguous in X-ray scattering measurements and solving this phase problem is critical to determining the underlying microstructure. Since the morphologies of interest here are all centrosymmetric, the values for φ_{hk} in Eqn 5.2 are limited to 0 and π ($e^{i\varphi_{hk}} = \pm 1$).[41] The complexity of the phase problem is significantly reduced as

only the sign of each Fourier coefficient must be determined. The expression for electron density can be simplified to Eqn 5.3:

$$\rho(x,y) = \bar{\rho} + A \cdot \sum_{hk}^{N} \pm\sqrt{I_{hk}}\cos\big(2\pi(hx+ky)\big) = \bar{\rho} + A \cdot \rho_{\varphi}(x,y) \qquad (5.3)$$

where $\rho_{\varphi}(x,y)$ corresponds to the summation of Fourier terms over N reflections for a given set of phases. Although this expression for electron density is accurate in the limit as N approaches infinity, the finite number of reflections in the bulk SAXS data (N = 6) necessitates approximation of the electron density map by truncation of the Fourier series. Because of this truncation, all possible phase combinations can be enumerated for a total of $2^6 = 64$. The electron density map synthesized from one such phase combination, φ = + − − + + +, is shown in Figure 5.6a.

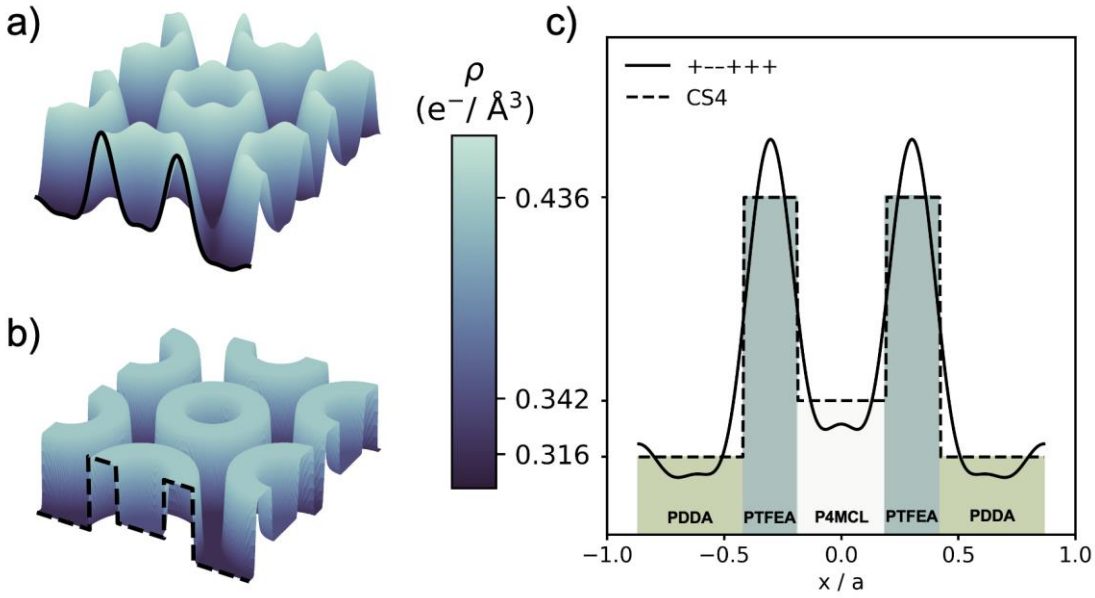

Figure 5.6 a) Electron density reconstruction using phase (φ = + − − + + +). b) Electron density model of the core–shell morphology CS4 with a P4MCL core, PTFEA shell, and PDDA matrix. c) 1D slice along the *x* axis (normalized by the lattice constant *a*) of the most likely reconstruction (φ = + − − + + +, solid) and model (CS4, dashed).

Reported procedures for the phase determination of similar morphologies via electron density reconstruction often utilize prior chemical or physical information about the system to qualitatively determine the most likely phase combination. In many cases, a model is assumed or determined experimentally with supplementary techniques such as TEM.[39,40,42] Complementary techniques, such as histogram-matching,[43–45] are insufficient as this analysis only specifies the distribution of electron density, not the location of electron density in the unit cell. Therefore, a simple yet quantitative approach to evaluating reconstructions against many possible models is necessary. All 64 electron density reconstructions were calculated and compared to the set of 12 real-space volume fraction informed models (Figure 5.1) for a total of 768 comparisons. The models (e.g., core–shell model CS4 shown in Figure 5.6b) assume perfect phase separation between domains of constant electron density. Each model–reconstruction pair was evaluated by performing a least-squares regression of a reconstruction to a given model by varying the scaling factor, A, to simultaneously minimize squared error at each xy coordinate while conserving the average electron density:

$$\min_{A} \sum_{xy} \left(\rho_{model} - \rho_{fit}\right)^2 = \min_{A} \sum_{xy} \left(\rho_{model} - \bar{\rho} - A \cdot \rho_{\varphi}\right)^2 \tag{5.4}$$

By fitting to the model morphologies, the volume fractions and overall electron density constraints inherent to the triblock are being enforced. Poorly fitting reconstructions are indicative of an unphysical electron density profile. The coefficient of determination (R^2) was used as a goodness-of-fit metric for each model–

reconstruction pair as shown in Figure 5.7. The values of R^2 range from 0 to 1, with the best-fit pairs indicated by the values of R^2 closest to 1.

The best-fit model–reconstruction pairs in Figure 5.7 suggest CS4 as the most likely morphology, in agreement with the RSoXS analysis. We can also conclude that the reconstruction φ = + − − + + + best matches the experimentally determined volume fraction and electron density constraints. Cross-sections of electron density from the CS4 model and reconstruction (φ = + − − + + +) show good agreement (Figure 5.6c). Because hard X-ray scattering relies on electron density contrast between adjacent domains[46], determining the three-phase ordering using this reconstruction technique is best suited to morphologies that maximize contrast between adjacent domains (e.g., if the P4MCL and PDDA blocks were adjacent, the low contrast between the two may be limiting).

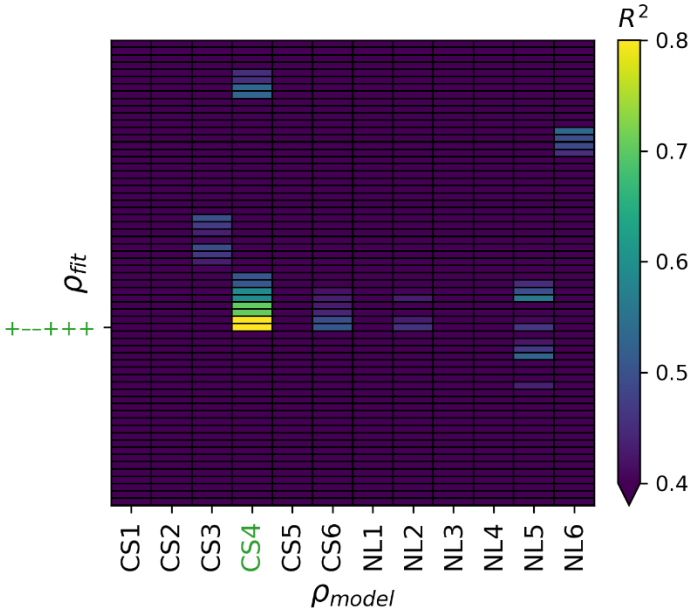

Figure 5.7 Coefficient of determination matrix for each $\rho_{model} - \rho_{fit}$ combination. The best fitting model–reconstruction pair (CS4 and + − − + + +) is highlighted in green.

5.5 Conclusion

We developed an approach to RSoXS and electron density reconstruction analysis which leverages modern computation to evaluate many models against experiment. The RSoXS data workflow combines scattering simulations and experiments to predict ABC triblock terpolymer microstructure from the energy-dependent variation in peak intensity ratios. The results, based on the pairwise ratios of the scattering peaks in RSoXS, show excellent agreement with electron density reconstruction of bulk SAXS data. This approach to characterizing the microstructure of self-assembled thin films may be valuable in analyzing samples with weak signals in conventional SAXS measurements or complex multiblock designs. The procedural generation of candidate structures and GPU-accelerated scattering simulations, paired with fast RSoXS measurement capabilities,[29] provide a means to rapidly extract the microstructure of large block copolymer libraries. This demonstration of simulation-guided RSoXS analysis can also act as a benchmark for systems with more ambiguous scattering, such as semicrystalline polymers containing crystalline domains dispersed in an amorphous matrix.

5.6 Acknowledgements

This research was supported by the National Science Foundation through Award No. DMR-1808622 (RSoXS analysis, M.L.C.) and under Award No. DMR-1844987 (Synthesis and SAXS, C.M.B.). V.G.R. thanks the National Science Foundation Graduate Research Fellowship Program under Grant 1650114. Use was made of computational facilities purchased with funds from the National Science Foundation

(OAC-1925717) and administered by the Center for Scientific Computing (CSC). The CSC is supported by the California NanoSystems Institute and the Materials Research Science and Engineering Center (MRSEC; NSF DMR-1720256) at UC Santa Barbara. The research reported here made use of shared facilities of the UC Santa Barbara MRSEC (NSF DMR-1720256), a member of the Materials Research Facilities Network (http://www.mrfn.org).

5.7 Appendix D

Materials

All reagents were used as received except where noted. Toluene and copper (II) bromide ($CuBr_2$) were purchased from Sigma Aldrich. Dodecyl acrylate (DDA, >98%), 2,2,2-trifluoroethyl acrylate (TFEA), and 2,2,2-trifluoroethanol (TFE) were purchased from TCI chemicals. Tris[2-(dimethylamino)ethyl]amine (Me_6Tren) was obtained from Alfa Aesar. Tin(II) 2-ethylhexanoate ($Sn(Oct)_2$, Aldrich, 92.5–100%) was fractionally distilled 3× under reduced pressure (50 mtorr, 150 °C) and stored in a nitrogen filled glovebox before use. 4-methylcaprolactone (4MCL) was prepared according to literature, purified by fractional distillation 3× from calcium hydride (CaH_2, Fisher Scientific, 93%), from $Sn(Oct)_2$ under reduced pressure (50 mtorr, 50 °C), and stored in a nitrogen filled glovebox before use.[47] Monomers were passed through a column of basic alumina to remove inhibitor prior to use.

Molecular characterization

^{1}H nuclear magnetic resonance (NMR) spectra were recorded on a Varian VNMRS 600 MHz spectrometer and a Bruker 500 MHz spectrometer. Chemical shifts (δ) are

reported in ppm relative to residual $CHCl_3$ (7.26 ppm). The photo-induced atom-transfer radical polymerization (ATRP) light source (UV: $\lambda_{max} \approx 360$ nm) was a commercial nail curing lamp (Thermal Spa, obtained online from Amazon) equipped with 3 × 16 W bulbs.

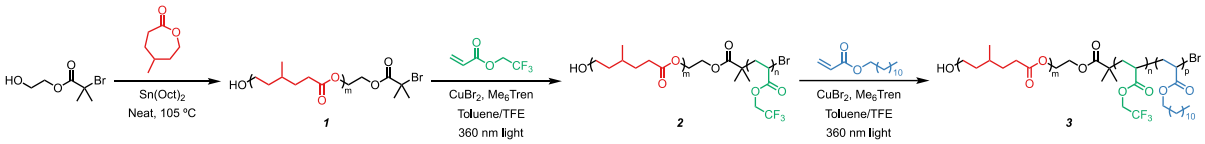

Scheme D1. Synthesis of P4MCL homopolymer (**1**), P4MCL-*b*-PTFEA diblock copolymer (**2**), and P4MCL-*b*-PTFEA-*b*-PDDA triblock terpolymer (**3**).

Synthesis of poly(4-methyl caprolactone) (P4MCL) homopolymer

Synthesis of the initiator, 2-hydroxyethyl 2-bromoisobutyrate (HEBIB), was implemented according to a reported literature procedure.[48] In a nitrogen filled glovebox, 4-methyl caprolactone (5.0 g, 39 mmol), HEBIB (7.4 mg, 35 mmol), and $Sn(Oct)_2$ (7.9 mg, 0.020 mmol) were added to a microwave vial. The vial was sealed, taken out of the glovebox, and placed in a 105 °C oil bath until 70% conversion was achieved, as monitored by ^{1}H NMR. The vial was quenched in an ice bath to stop the reaction. The viscous mixture was dissolved in a minimal amount of dichloromethane and precipitated into cold methanol (500 mL x 3). The final product was obtained by drying the precipitate under vacuum for 12 h. ^{1}H NMR (600 MHz, $CDCl_3$) δ 4.13 – 4.04 (m, 216H), 2.35 – 2.23 (m, 218H), 1.92 (s, 6H), 1.66 (m, 218H), 1.59 – 1.53 (m, 109H), 1.45 (m, 219H), 0.90 (d, J = 6.6 Hz, 330H).

Synthesis of poly(4-methyl caprolactone)-b-poly(2,2,2-trifluoroethyl acrylate) (P4MCL-b-PTFEA) diblock copolymer

A solution of $CuBr_2$ (2.4 mg, 0.011 mmol) and Me_6Tren (17 μL, 0.063 mmol) was prepared in 2 mL of TFE and sonicated for thirty minutes. In a scintillation vial, previously prepared P4MCL homopolymer (0.51 g, 0.04 mmol) was added and dissolved in 2.1 mL of toluene. TFEA (0.78 g, 3.7 mmol) and 0.49 mL of the TFE stock solution were added to the vial. The solution was degassed with nitrogen for fifteen minutes. With stirring, the polymerization mixture was irradiated ($\lambda \approx 360$ nm) in a commercial UV nail lamp until 60% conversion was achieved, as monitored by ^{1}H NMR. The viscous mixture was diluted with dichloromethane, filtered through basic alumina to remove residual copper, and dried under vacuum for 12 h to obtain the desired diblock copolymer. ^{1}H NMR (600 MHz, $CDCl_3$) δ 4.54 – 4.40 (m, 167H), 4.17 – 4.04 (m, 215H), 2.46 (m, 81H), 2.38 – 2.23 (m, 225H), 2.06 (m, 37H), 1.82 – 1.72 (m, 89H), 1.72 – 1.63 (m, 228H), 1.62 – 1.53 (m, 138H), 1.52 – 1.42 (224H), 1.19 – 1.11 (m, 6H), 0.92 (d, J = 6.6 Hz, 2H).

Synthesis of poly(4-methyl caprolactone)-b-poly(2,2,2-trifluoroethyl acrylate)-b-poly(dodecyl acrylate) (P4MCL-b-PTFEA-b-PDDA) triblock copolymer

A solution of $CuBr_2$ (2.4 mg, 0.011 mmol) and Me_6Tren (17 μL, 0.063 mmol) was prepared in 2 mL of TFE and sonicated for thirty minutes. In a scintillation vial, previously prepared P4MCL-*b*-PTFEA diblock copolymer (0.64 g, 0.02 mmol) was added and dissolved in 4 mL of toluene. DDA (0.26 g, 1.1 mmol), 0.48 mL of the TFE stock solution, and an additional 0.5 mL TFE were added to the vial. The solution was

degassed with nitrogen for fifteen minutes. With stirring, the polymerization mixture was irradiated (λ ≈ 360 nm) in a commercial UV nail lamp until 50% conversion was achieved as monitored by ^{1}H NMR. The viscous mixture was purified via dissolution in a minimal amount of dichloromethane and precipitated into cold methanol (200 mL x3). The final product was obtained by drying the precipitate under vacuum for 12 h. ^{1}H NMR (600 MHz, $CDCl_3$) δ 4.52 – 4.38 (m, 168H), 4.15 – 4.04 (m, 228H), 4.04 – 3.89 (m, 32H), 2.54 – 2.37 (m, 84H), 2.37 – 2.21 (m, 241H), 2.11 – 1.95 (m, 39H), 1.79 – 1.71 (m, 89H), 1.71 – 1.61 (m, 252H), 1.61 – 1.50 (m, 129H), 1.45 (m, 236H), 1.33 – 1.19 (m, 349H), 0.90 (d, *J* = 6.6 Hz, 329H), 0.86 (t, *J* = 7.1 Hz, 63H).

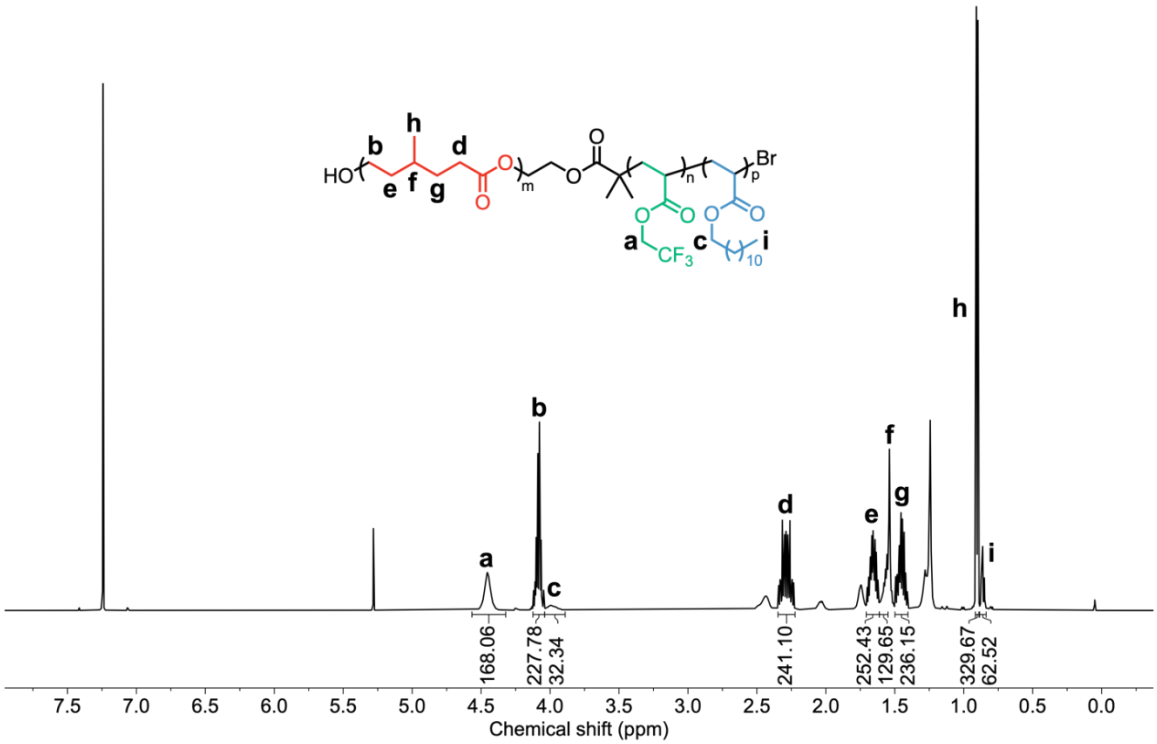

Figure D1 ^{1}H NMR of P4MCL-*b*-PTFEA-*b*-PDDA triblock terpolymer in $CDCl_3$.

Synthesis of poly(2,2,2-trifluoroethyl acrylate) homopolymer (PTFEA)

For the following experiment, a stock solution of copper(II) bromide (14.0 mg, 0.062 mmol) and Me_6Tren (8.6 mg, 100 μl, 37.4 mmol) in 1 mL of trifluoroethanol (TFE) and sonicated until complete dissolution. TFEA (4.76 g, 30.90 mmol) and 2-hydroxyethyl 2-bromoisobutyrate (70 mg, 0.33 mmol) were added to a scintillation vial containing 4.76 mL TFE and 40 μl of the Cu(II)/TFE stock solution. The vial was capped with a rubber septum and the solution purged with argon for 15 minutes. With stirring, the reaction mixture was irradiated ($\lambda \approx 360$ nm) until 70 % conversion of monomer was achieved as monitored using ^{1}H NMR through end group analysis. Upon completion, the reaction mixture was run through a basic alumina column and the resulting polymer was isolated as a viscous liquid following purification via precipitation into hexanes. ^{1}H NMR (500 MHz, $CDCl_3$) δ 4.62 – 4.40 (m, 125H), 3.88 – 3.78 (m, 2H), 2.48 (s, 61H), 2.09 (m, 29H), 1.79 (m, 63H), 1.70 – 1.56 (m, 32H), 1.21 (dt, J = 22.6, 2.4 Hz, 6H).

Synthesis of poly(lactide)-b-poly(2,2,2-trifluoroethyl acrylate) diblock copolymer (PLA-bPTFEA)

In a nitrogen filled glove box, (±) lactide (0.58 g, 3.86 mmol), triethylaluminum (0.05M, 520 μl) and mL toluene were added to a microwave vial containing previously prepared PTFEA (0.50 g, 0.05 mmol, $M_{n,NMR}$ = 9700 KDa). The vial was sealed with a crimp cap and the reaction was heated to 90 °C in an oil bath for 2.5 h (80% conv.) and subsequently quenched with hydrochloric acid (1M, 0.2 mL). The resulting diblock was isolated via precipitation in MeOH (50 mL, x3). ^{1}H NMR (500 MHz,

$CDCl_3$) δ 5.31 – 5.12 (m, 93H), 4.50 (m, 6.0 Hz, 125H), 2.58 – 2.41 (m, 60H), 2.07 (m, 28H), 1.79 (m, 63H), 1.67 – 1.53 (m, 308H).

Fractionation of P4MCL-b-PTFEA-b-PDDA triblock via automated flash chromatography

Automated flash chromatography was performed using a Biotage Isolera One purification system equipped with an evaporative light scattering detector (ELSD). A Biotage SNAP KP-Sil 50 g cartridge was used with a flow rate of 40 mL/min. The parent block copolymer was dissolved in hexanes and loaded onto a samplet using a syringe. The screw-top cap was then removed and the samplet was dried at 60 °C overnight. The column was equilibrated with three column volumes of hexanes. After equilibration was complete, the solvent dispersant head insert was detached and the loaded samplet was inserted. The parent block copolymer was eluted with a programmed hexanes/ethyl acetate gradient. All chromatographic solvents were ACS grade or better and used without further purification. Fractions were monitored by a light scattering detector and collected in 15 mL increments. Volume fractions of the fractionated materials were calculated by ^{1}H NMR by comparing the integrations of the three blocks to their respective homopolymer densities at 25 °C.

Synthesis of poly(2,2,2-trifluoroethyl acrylate) homopolymer (PTFEA)

For the following experiment, a stock solution of copper(II) bromide (14.0 mg, 0.062 mmol) and Me_6Tren (8.6 mg, 100 μl, 37.4 mmol) in 1 mL of trifluoroethanol (TFE) and sonicated until complete dissolution. TFEA (4.76 g, 30.90 mmol) and 2-hydroxyethyl 2-bromoisobutyrate (70 mg, 0.33 mmol) were added to a scintillation

vial containing 4.76 mL TFE and 40 μl of the Cu(II)/TFE stock solution. The vial was capped with a rubber septum and the solution purged with argon for 15 minutes. With stirring, the reaction mixture was irradiated ($\lambda \approx 360$ nm) until 70 % conversion of monomer was achieved as monitored using ^{1}H NMR through end group analysis. Upon completion, the reaction mixture was run through a basic alumina column and the resulting polymer was isolated as a viscous liquid following purification via precipitation into hexanes.

Synthesis of poly(lactide)-b-poly(2,2,2-trifluoroethyl acrylate) diblock copolymer (PLA-b-PTFEA)

In a nitrogen filled glove box, (±) lactide (0.58 g, 3.86 mmol), triethylaluminum (0.05M, 520 μl) and mL toluene were added to a microwave vial containing previously prepared PTFEA (0.50 g, 0.05 mmol, $M_{n,NMR} = 9700$ KDa). The vial was sealed with a crimp cap and the reaction was heated to 90 °C in an oil bath for 2.5 h (80% conv.) and subsequently quenched with hydrochloric acid (1M, 0.2 mL). The resulting diblock was isolated via precipitation in MeOH (50 mL, x3). ^{1}H NMR (500 MHz, $CDCl_3$) δ 5.32 – 5.10 (m, 92H), 4.60 – 4.39 (m, 125H), 2.48 (s, 61H), 2.08 (s, 28H), 1.79 (d, J = 7.6 Hz, 62H), 1.59 (s, 308H).

Optical microscopy of thin films for NEXAFS measurement

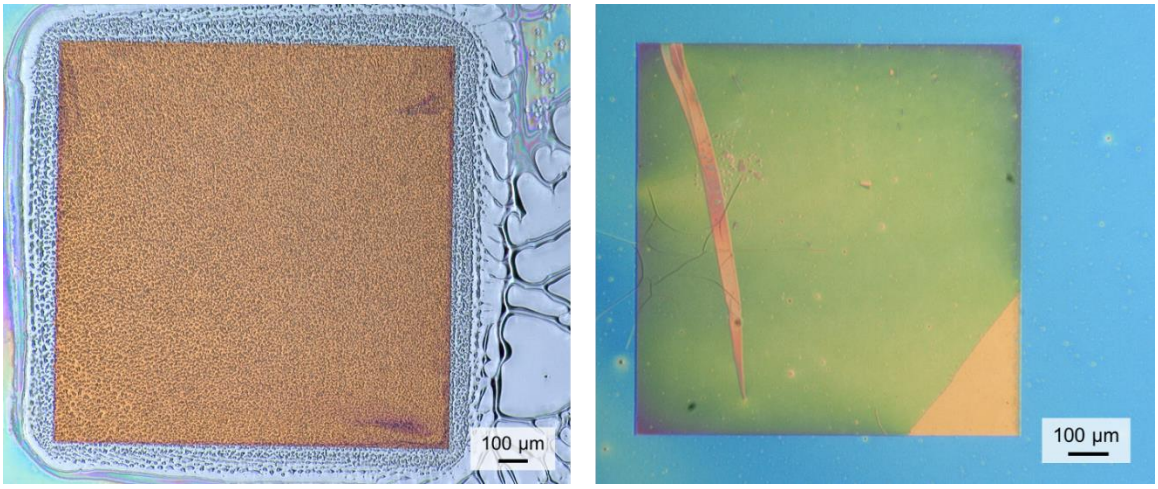

Figure D2 *Left*: Optical micrograph of PTFEA homopolymer de-wetted from a silicon nitride substrate after spin coating. The sample was spin coated from 3 w/w% solution in 2,2,2-trifluoroethanol (TFE) (10 µL, 45 s, 1500 acceleration, 2500 RPM). *Right*: Optical micrograph of a PLA-*b*-PTFEA diblock thin film on a silicon nitride substrate. The diblock thin film was spin coated from 5 w/w% solution in chlorobenzene (60 µL, 45 s, 1500 acceleration, 2500 RPM) onto a quartz substrate. The film was then floated off of the quartz substrate using a bath of deionized water and transferred to the silicon nitride substrate.

Refractive index of mixtures calculation

The equations below show the calculation of the refractive index of block A from the measured refractive index of an AB diblock, using the known refractive index of block B and the assumption that the refractive index of the diblock is a volume-fraction average. This analysis assumes the components do not interact electronically such that the spectra are additive.[49] In the equations below, $\hat{n}$ is the complex index of refraction ($\hat{n} = \delta + i\beta$) and ϕ is the volume fraction.

$$\hat{n} = \sum_i \phi_i \hat{n}_i$$

$$\delta_A = \frac{1}{\phi_A}(\delta_{diblock} - \phi_B \delta_B)$$

$$\beta_A = \frac{1}{\phi_A}(\beta_{diblock} - \phi_B \beta_B)$$

We additionally assumed that density is a volume-fraction average ($\rho_{diblock} = \phi_A \rho_A + \phi_B \rho_B$, where ρ is density).

Complex refractive indices of P4MCL, PTFEA, and PDDA

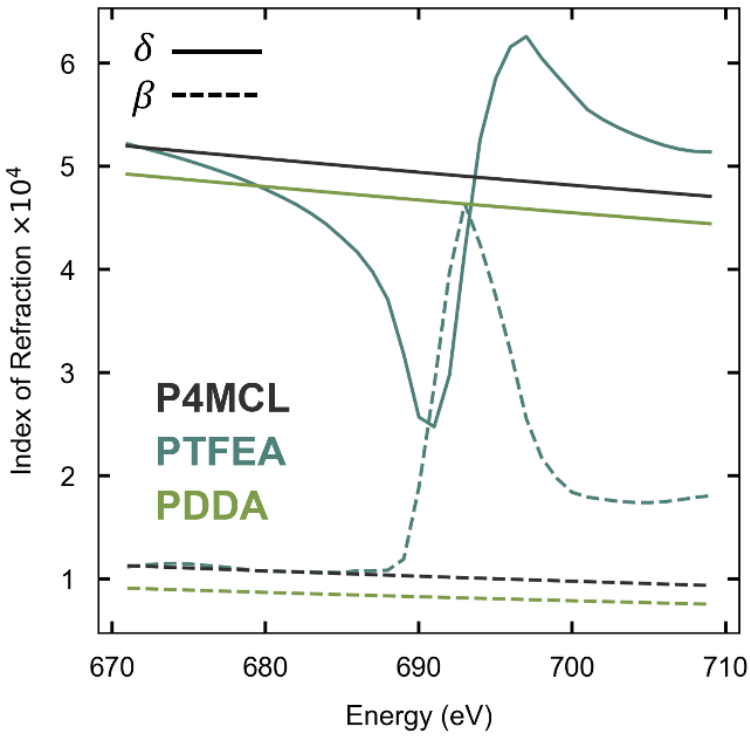

Figure D3 The real (δ) and imaginary (β) components of the complex index of refraction for the three block chemistries. The optical constants for P4MCL and PDDA were estimated using the Henke atomic scattering factors, while those for PTFEA were measured by transmission NEXAFS.

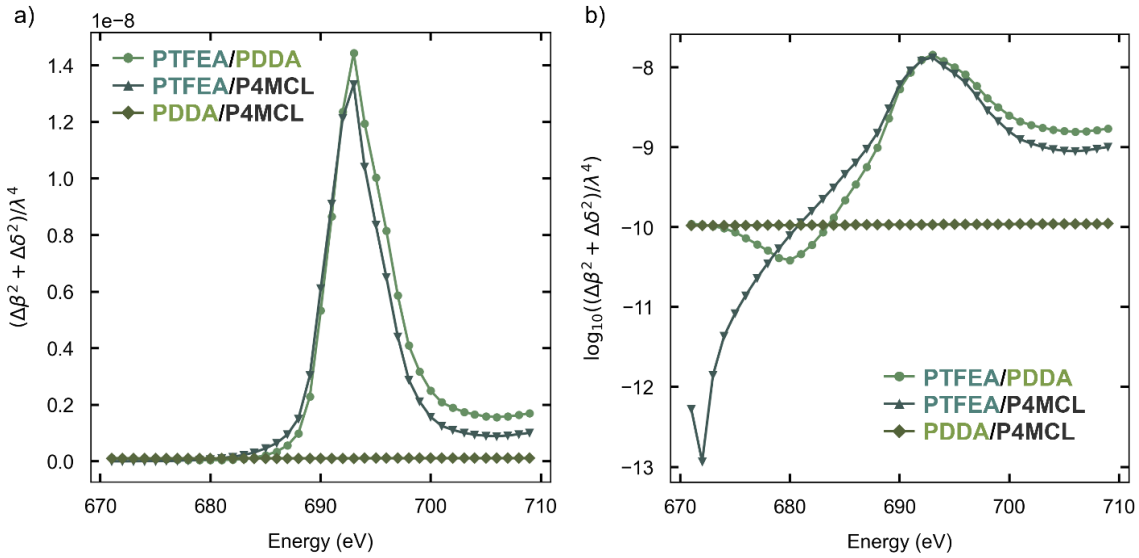

Figure D4 a) Pairwise contrast functions ($(\Delta\beta^2 + \Delta\delta^2)/\lambda^4$) of PTFEA, PDDA, and P4MCL over the fluorine edge. b) Logarithm of the pairwise contrast functions. The contrast between PDDA and P4MCL stays roughly constant on the order of 10^{-10}, while the contrast between PTFEA and the other two has a maximum on the order of 10^{-8} from fluorine resonance. The PTFEA and P4MCL are contrast-matched around 672 eV.

Geometric derivations for microstructure models

Dimensional calculations for hexagonally-packed cylinder morphologies using the scattering-derived d-spacing and the NMR-derived volume fractions.

d: d-spacing

a: lattice parameter

$A_{unit\ cell}$: area of the unit cell

$$d = \frac{2\pi}{q^*}$$

$$a = \frac{2}{\sqrt{3}} d$$

$$A_{unit\ cell} = a^2 \cos 30°$$

I. Core-Shell Cylinders

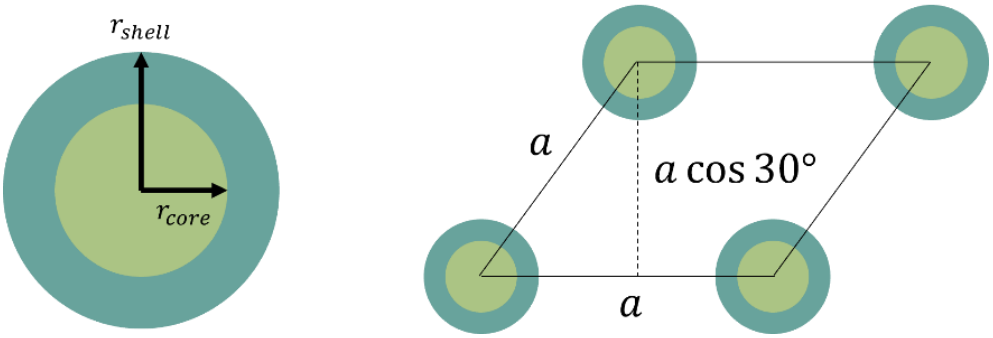

Figure D5 Schematic for the derivation of core-shell dimensions.

Derivation of r_{core} and r_{shell} (note that r_{shell} is defined as the distance from the center of the core-shell cylinder; the shell thickness $t_{shell} = r_{shell} - r_{core}$):

f_{core}: volume fraction of the core material

f_{shell}: volume fraction of the shell material

f_{matrix}: volume fraction of the matrix material

$$f_{core} + f_{shell} + f_{matrix} = 1$$

$$A_{core-shell} = (f_{core} + f_{shell}) \cdot A_{unit\ cell}$$

$$r_{shell} = \sqrt{\frac{A_{core-shell}}{\pi}}$$

$$\frac{A_{core}}{A_{core-shell}} = \frac{f_{core}}{f_{core} + f_{core-shell}}$$

$$r_{core} = \sqrt{\frac{A_{core}}{A_{core-shell}}} \cdot r_{shell}$$

II. Nested Lattices

Derivation of r_1 (larger spacing sub-lattice, green) and r_2 (smaller spacing sub-lattice, blue):

f_1: volume fraction of the sub-lattice #1 material (green)

f_2: volume fraction of the sub-lattice #2 material (blue)

f_{matrix}: volume fraction of the matrix material

$$f_1 + f_2 + f_{matrix} = 1$$

In the nested lattices case, we define the unit cell as:

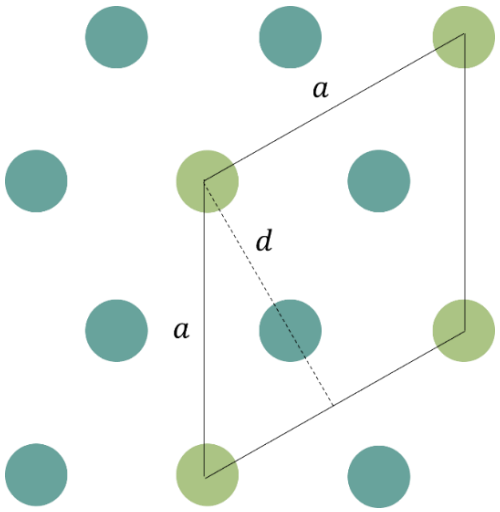

Figure D6 Schematic for the derivation of nested lattices dimensions.

There is one full cylinder of the material on sub-lattice #1 in the unit cell (green). There are 2 full cylinders of the material on sub-lattice #2 in the unit cell (blue).

$$r_1 = \sqrt{\frac{f_1 \cdot A_{unit\ cell}}{\pi}}$$

$$r_2 = \sqrt{\frac{f_2 \cdot A_{unit\ cell}}{2\pi}}$$

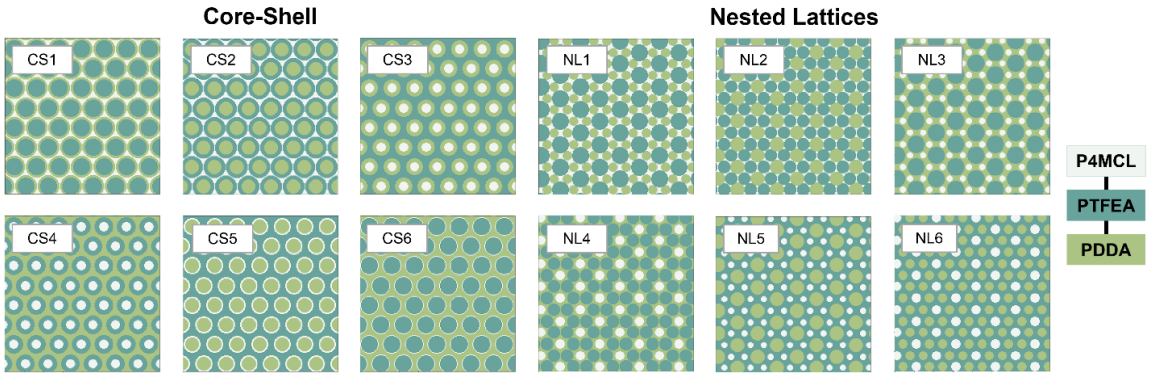

Figure D7 Representative 200 × 200 voxel sections of composition maps of the 12 possible morphologies included in the simulation set. Each full image is 1024 × 1024 × 1 voxels, with each voxel representing 1 nm^3 (minimum length scale determined by the diffraction limit at the fluorine edge). The block identities are as follows: light grey – P4MCL, blue – PTFEA, green – PDDA.

Data reduction & peak fitting

The 2D scattering patterns were reduced to 1D line profiles using Nika, an Igor Pro-based package for SAXS/WAXS data reduction.[50] The sample-to-detector distance was calibrated using a silver behenate standard.

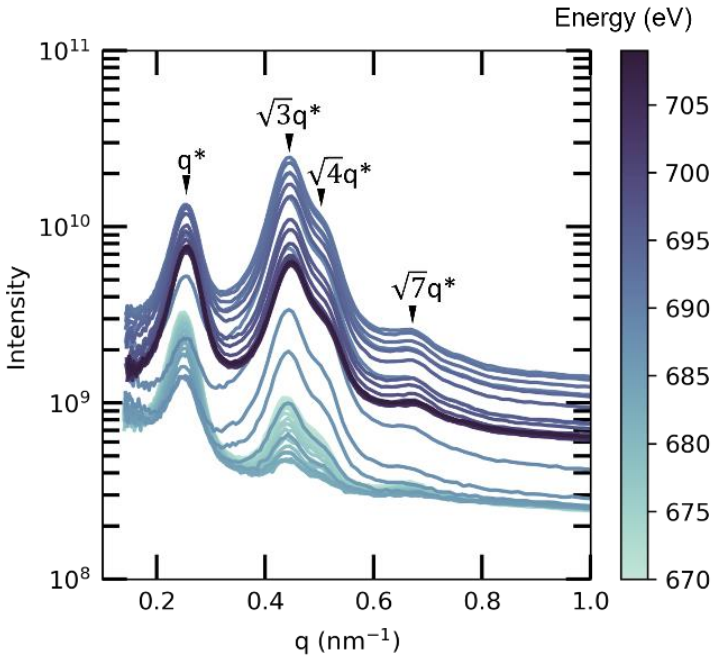

Figure D8 Radially-averaged resonant soft X-ray scattering profiles of P4MCL-b-PTFEA-b-PDDA collected across the fluorine edge.

One challenge in extracting the peak intensity ratios over energy from the experimental RSoXS dataset is the selection and fit of an appropriate baseline. The data were fit using 3 Gaussian peaks and a cubic polynomial baseline (Figure D9). The fitting was performed using lmfit, an open-source Python package.[51] The baseline was allowed to vary across energies (but kept consistent for a single energy). For the peaks, σ was kept constant ($\sigma_{q^*} = 0.023, \sigma_{\sqrt{3}q^*} = 0.027, \sigma_{\sqrt{4}q^*} = 0.022$) while the amplitude was allowed to vary. The q^* and $\sqrt{3}q^*$ peak centers were generally allowed to vary and remained consistent, within $< 3\%$ variation. Due to the convoluted nature of the $\sqrt{3}q^*$ and $\sqrt{4}q^*$ peaks and the relatively low intensity of the $\sqrt{4}q^*$ at certain energies, the $\sqrt{4}q^*$ peak center was held constant relative to the $\sqrt{3}q^*$ peak center.

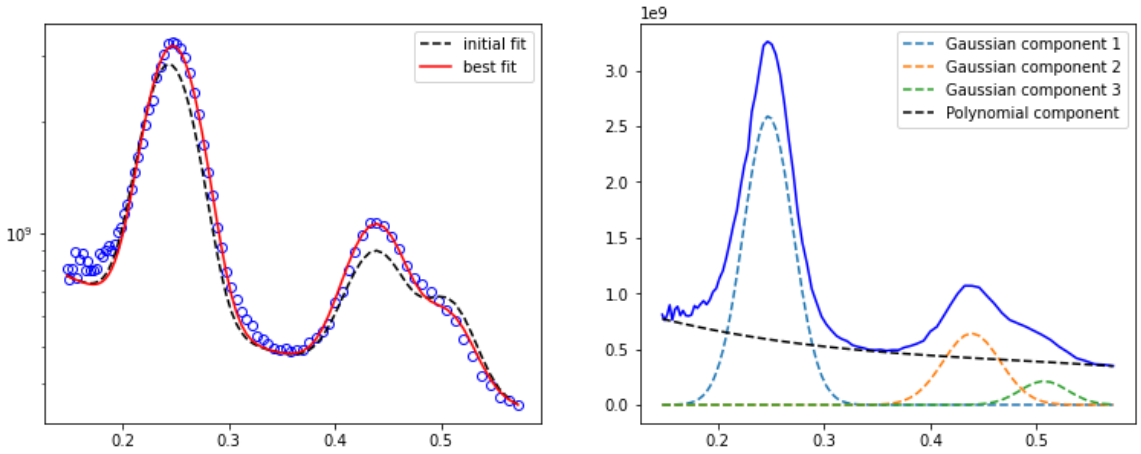

Figure D9 Example fit of a cubic polynomial baseline and 3 Gaussian peaks at 670 eV.

We additionally calculated intensity ratios through (1) extraction of peak intensities at set q values with no background subtraction or peak fitting and (2) automated fitting of a constant + exponential baseline ($C + Ae^{-q/\tau}$) and 3 Gaussian peaks, in which user input was limited to the initial parameter guesses and subsequent guesses were generated using the optimized parameters from the previous energy. In both of these approaches, the lowest-error model was consistent (CS4).

CS1

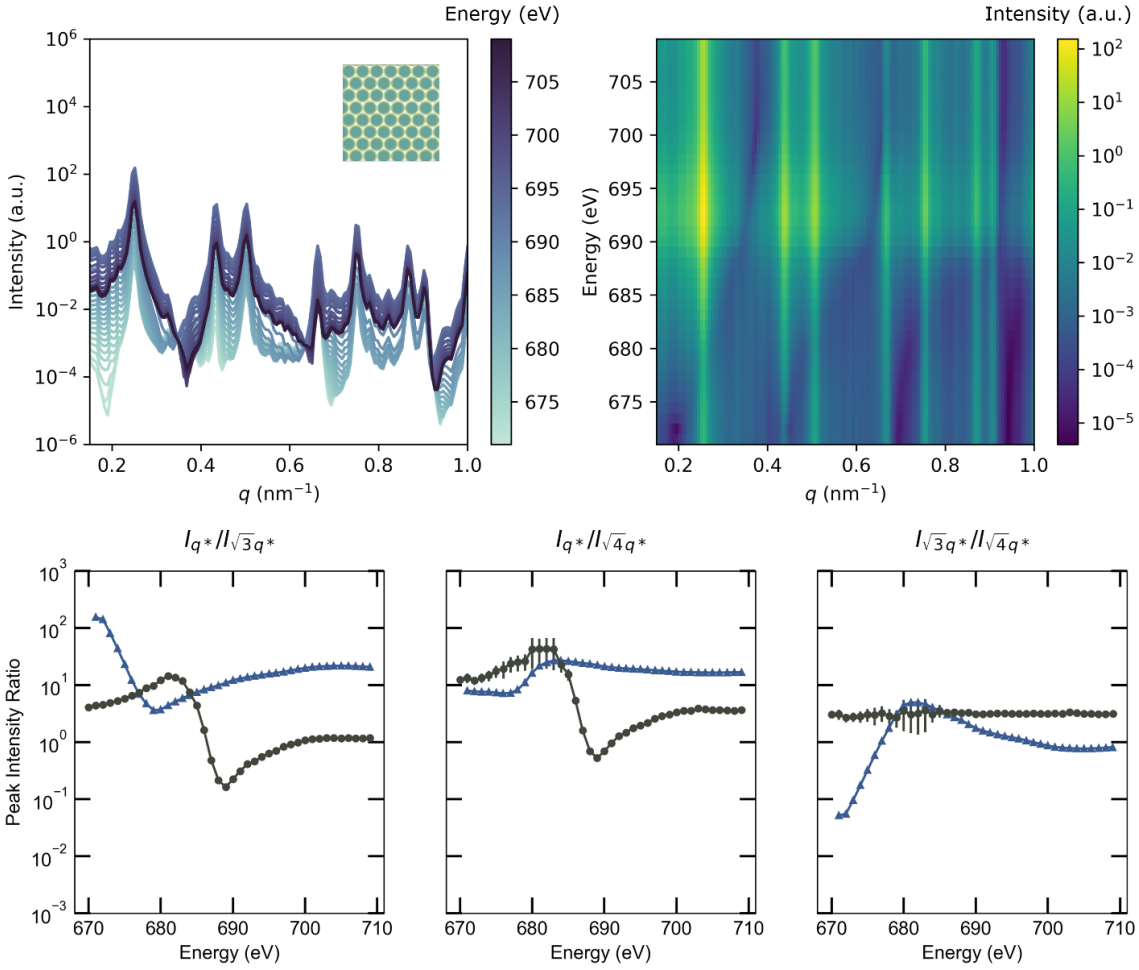

Figure D10 Scattering simulation results for CS1. *Top left*: Radially-averaged simulated RSoXS profiles at energies along the F edge (*inset*: 200 × 200 voxel subset of the model); *Top right*: intensity map of the simulated RSoXS profiles; *Bottom*: energy dependence of peak intensity ratios (dark grey circles: experiment; blue triangles: simulation).

CS2

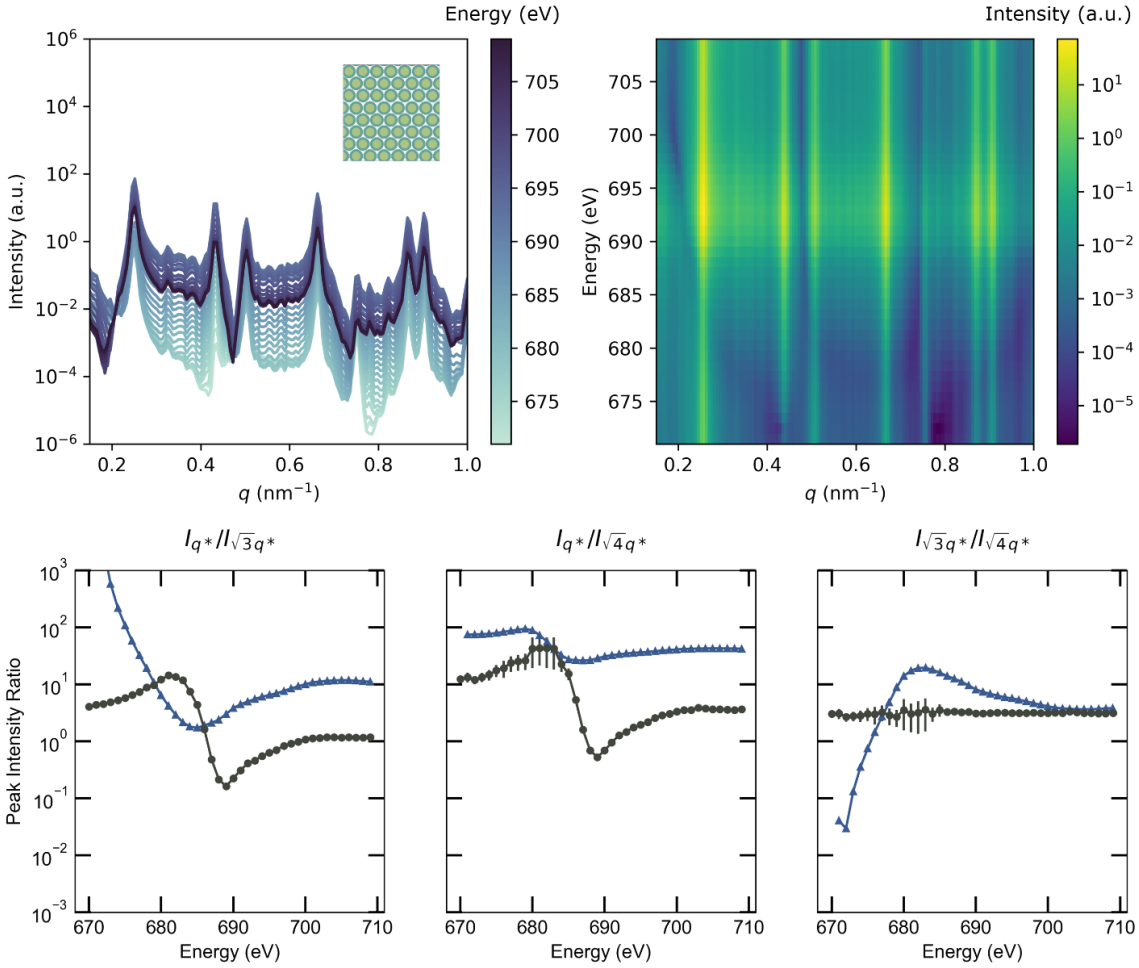

Figure D11 Scattering simulation results for CS2. *Top left*: Radially-averaged simulated RSoXS profiles at energies along the F edge (*inset*: 200 × 200 voxel subset of the model); *Top right*: intensity map of the simulated RSoXS profiles; *Bottom*: energy dependence of peak intensity ratios (dark grey circles: experiment; blue triangles: simulation).

CS3

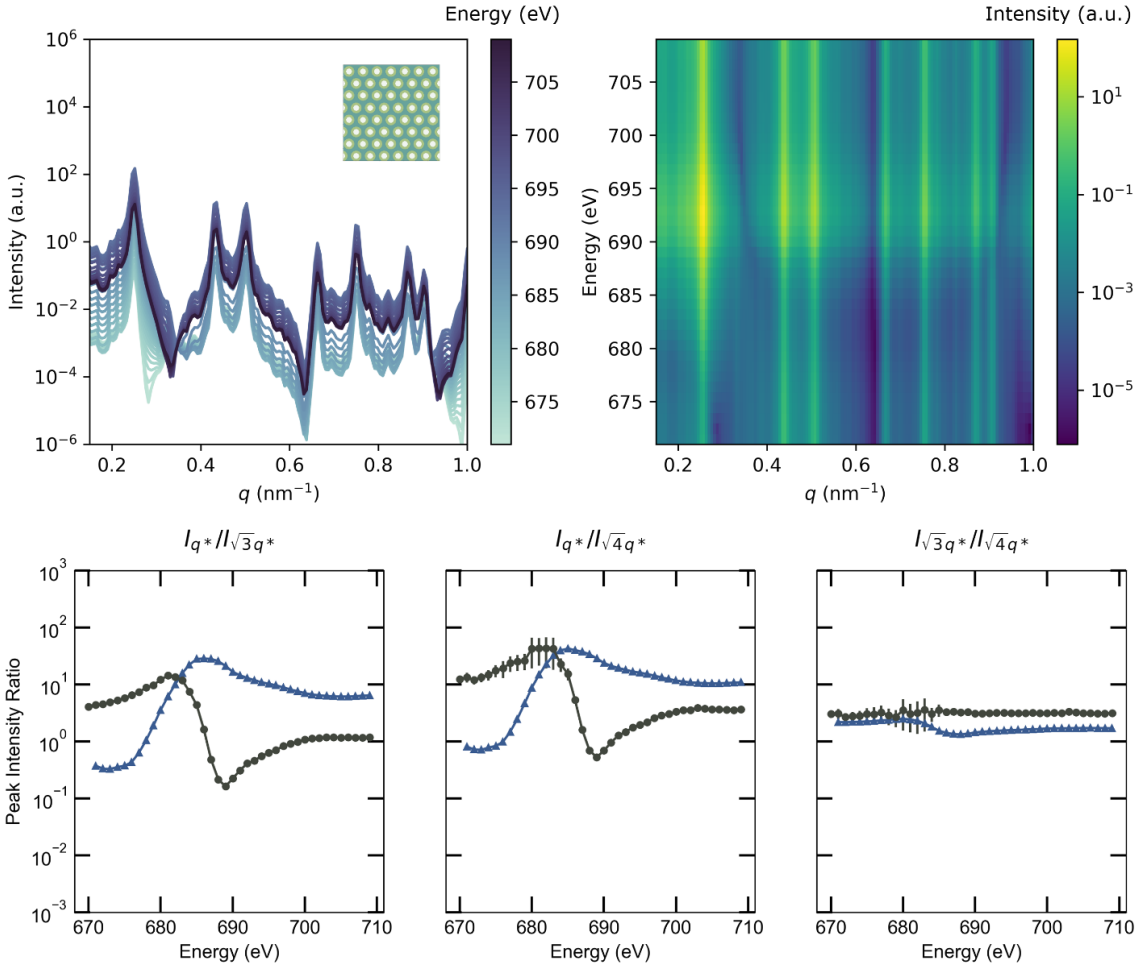

Figure D12 Scattering simulation results for CS3. *Top left*: Radially-averaged simulated RSoXS profiles at energies along the F edge (*inset*: 200 × 200 voxel subset of the model); *Top right*: intensity map of the simulated RSoXS profiles; *Bottom*: energy dependence of peak intensity ratios (dark grey circles: experiment; blue triangles: simulation).

CS4

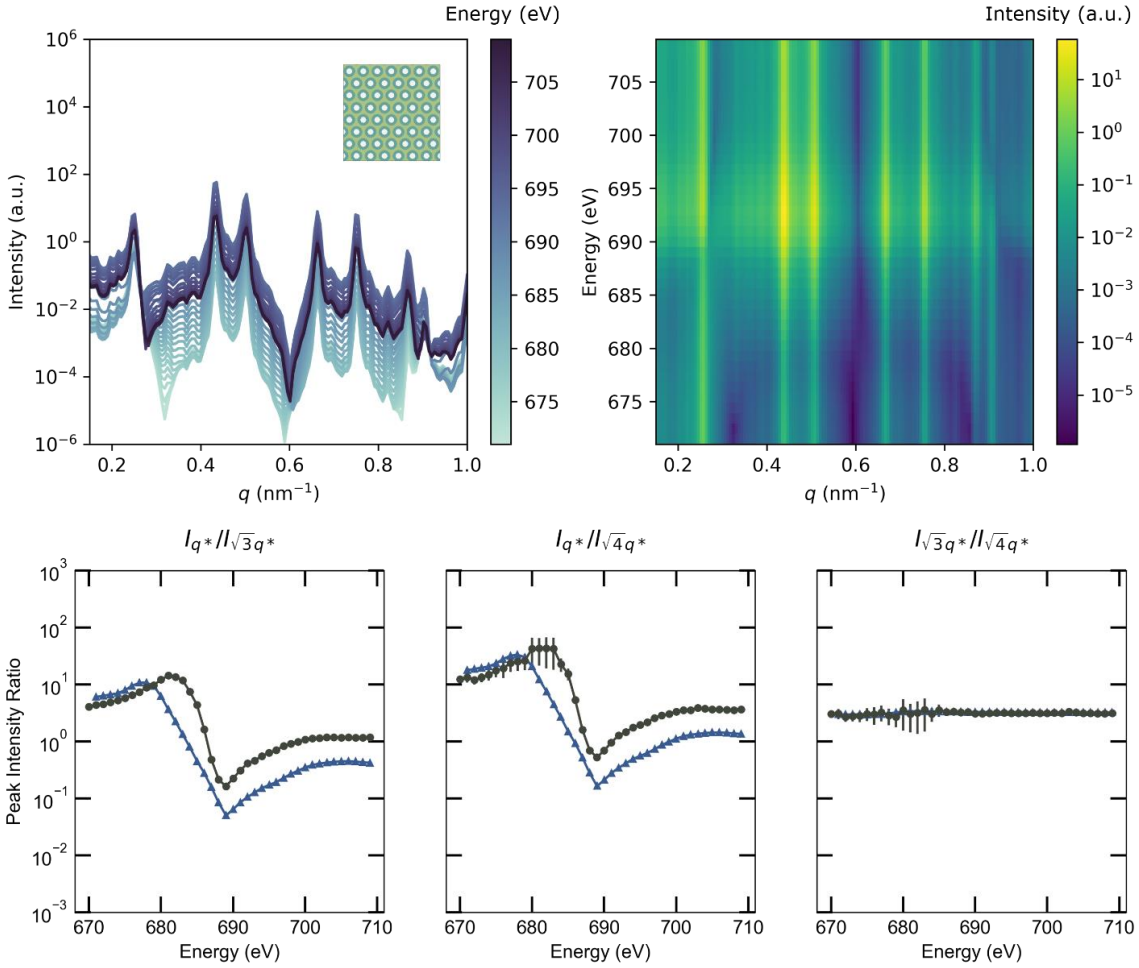

Figure D13 Scattering simulation results for CS4. *Top left*: Radially-averaged simulated RSoXS profiles at energies along the F edge (*inset*: 200 × 200 voxel subset of the model); *Top right*: intensity map of the simulated RSoXS profiles; *Bottom*: energy dependence of peak intensity ratios (dark grey circles: experiment; blue triangles: simulation).

CS5

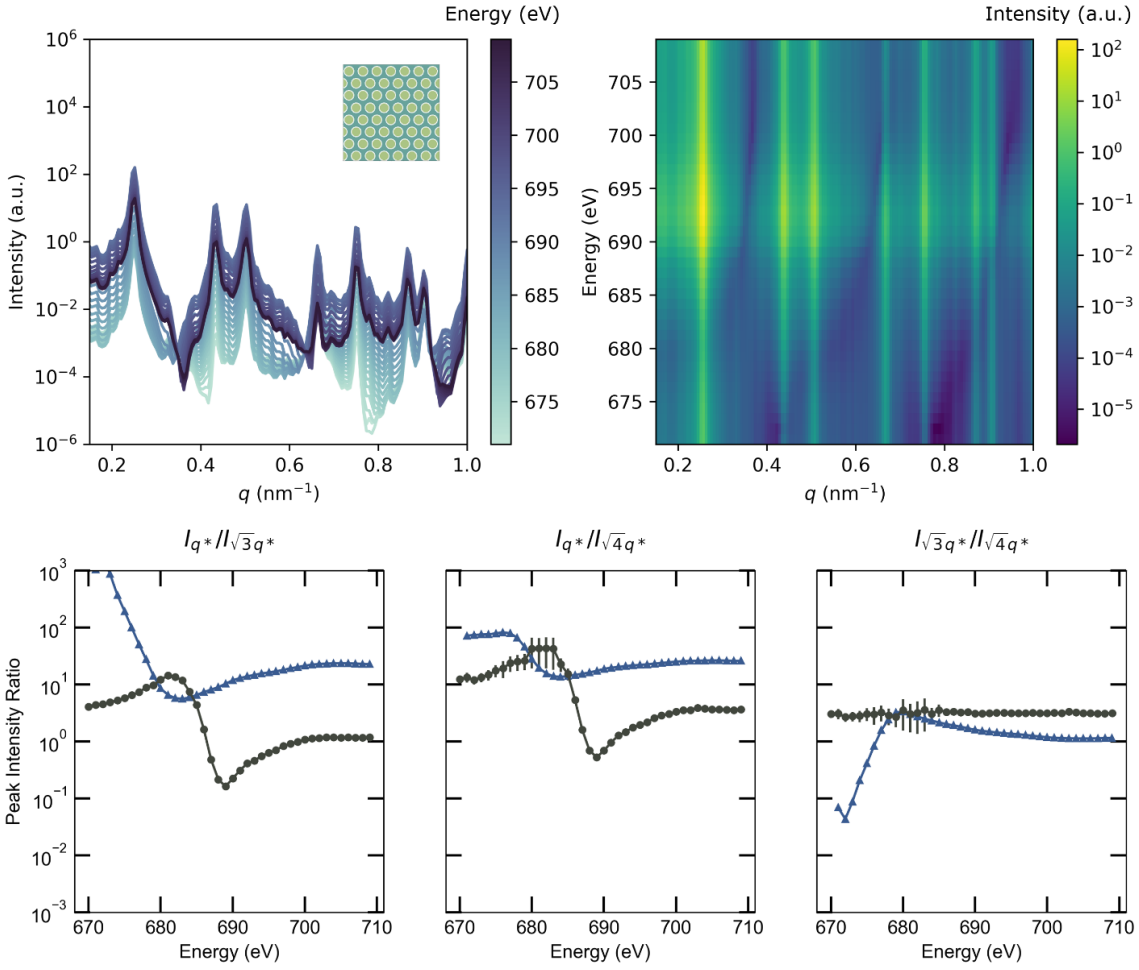

Figure D14 Scattering simulation results for CS5. *Top left*: Radially-averaged simulated RSoXS profiles at energies along the F edge (*inset*: 200 × 200 voxel subset of the model); *Top right*: intensity map of the simulated RSoXS profiles; *Bottom*: energy dependence of peak intensity ratios (dark grey circles: experiment; blue triangles: simulation).

CS6

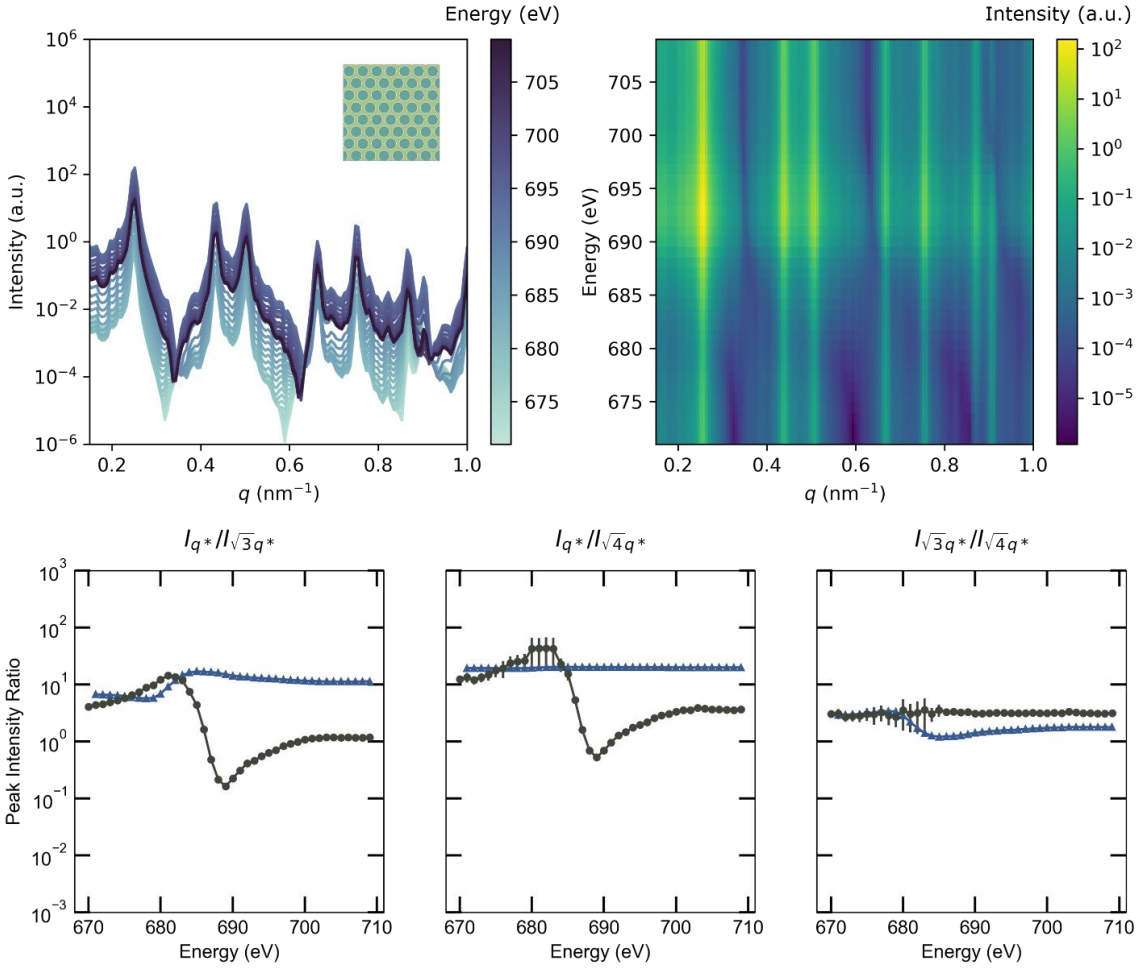

Figure D15 Scattering simulation results for CS6. *Top left*: Radially-averaged simulated RSoXS profiles at energies along the F edge (*inset*: 200 × 200 voxel subset of the model); *Top right*: intensity map of the simulated RSoXS profiles; *Bottom*: energy dependence of peak intensity ratios (dark grey circles: experiment; blue triangles: simulation).

NL1

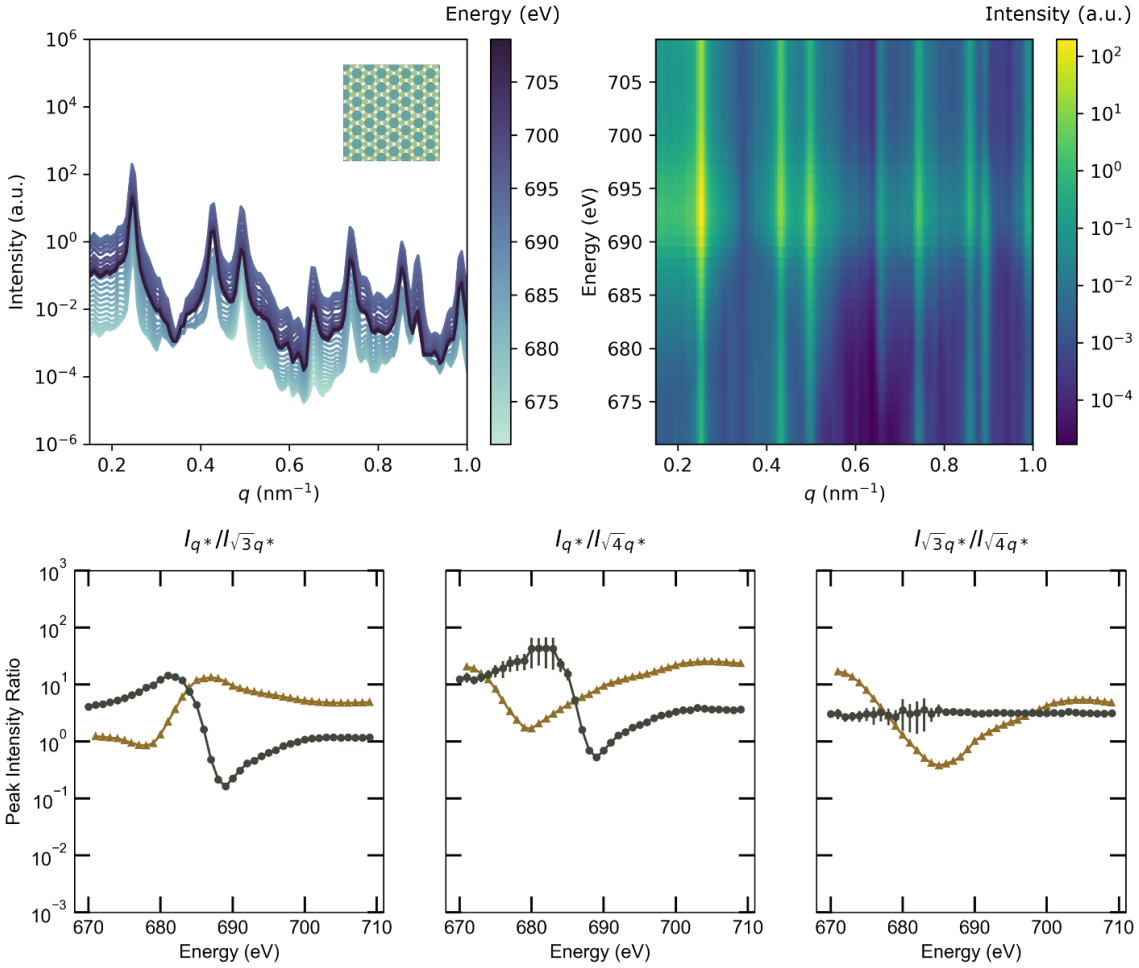

Figure D16 Scattering simulation results for NL1. *Top left*: Radially-averaged simulated RSoXS profiles at energies along the F edge (*inset*: 200 × 200 voxel subset of the model); *Top right*: intensity map of the simulated RSoXS profiles; *Bottom*: energy dependence of peak intensity ratios (dark grey circles: experiment; gold triangles: simulation).

NL2

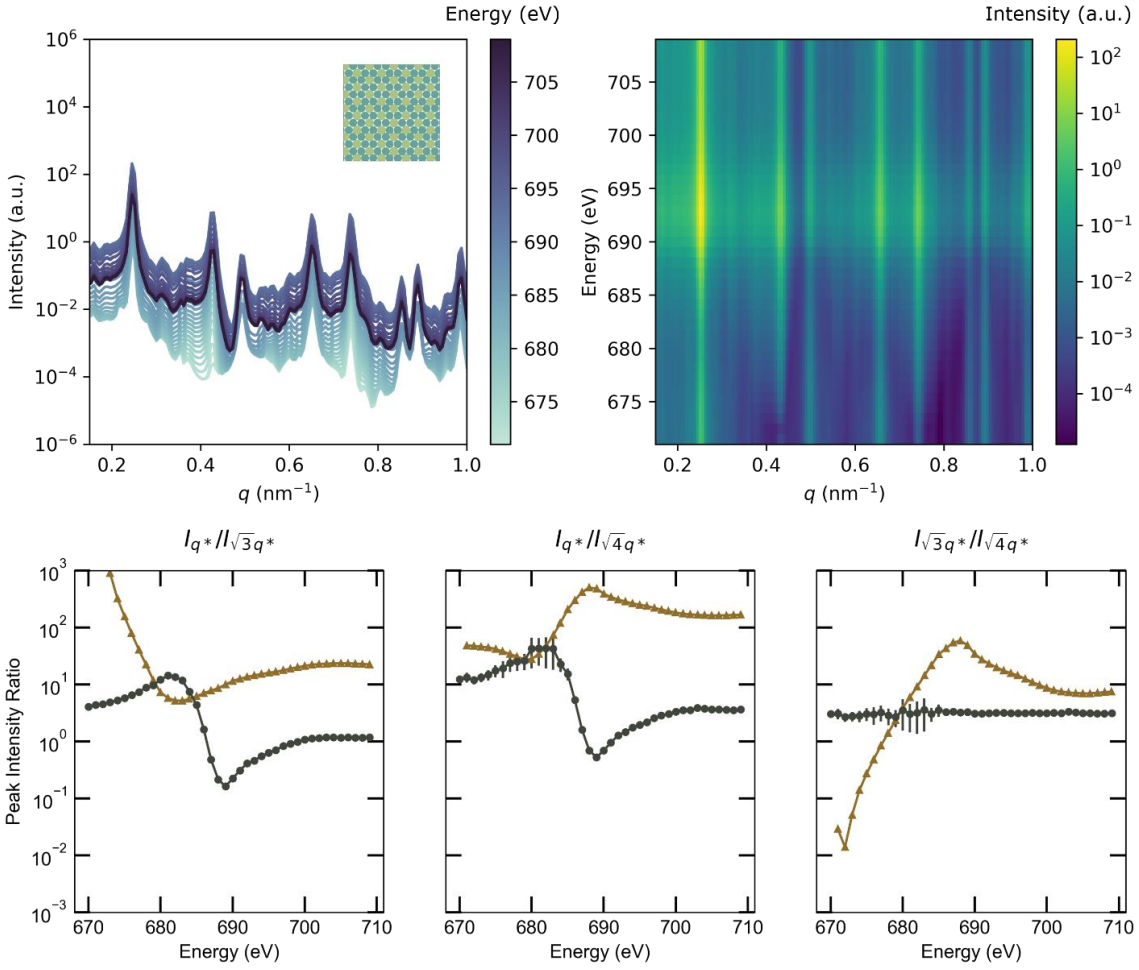

Figure D17 Scattering simulation results for NL2. *Top left*: Radially-averaged simulated RSoXS profiles at energies along the F edge (*inset*: 200 × 200 voxel subset of the model); *Top right*: intensity map of the simulated RSoXS profiles; *Bottom*: energy dependence of peak intensity ratios (dark grey circles: experiment; gold triangles: simulation).

NL3

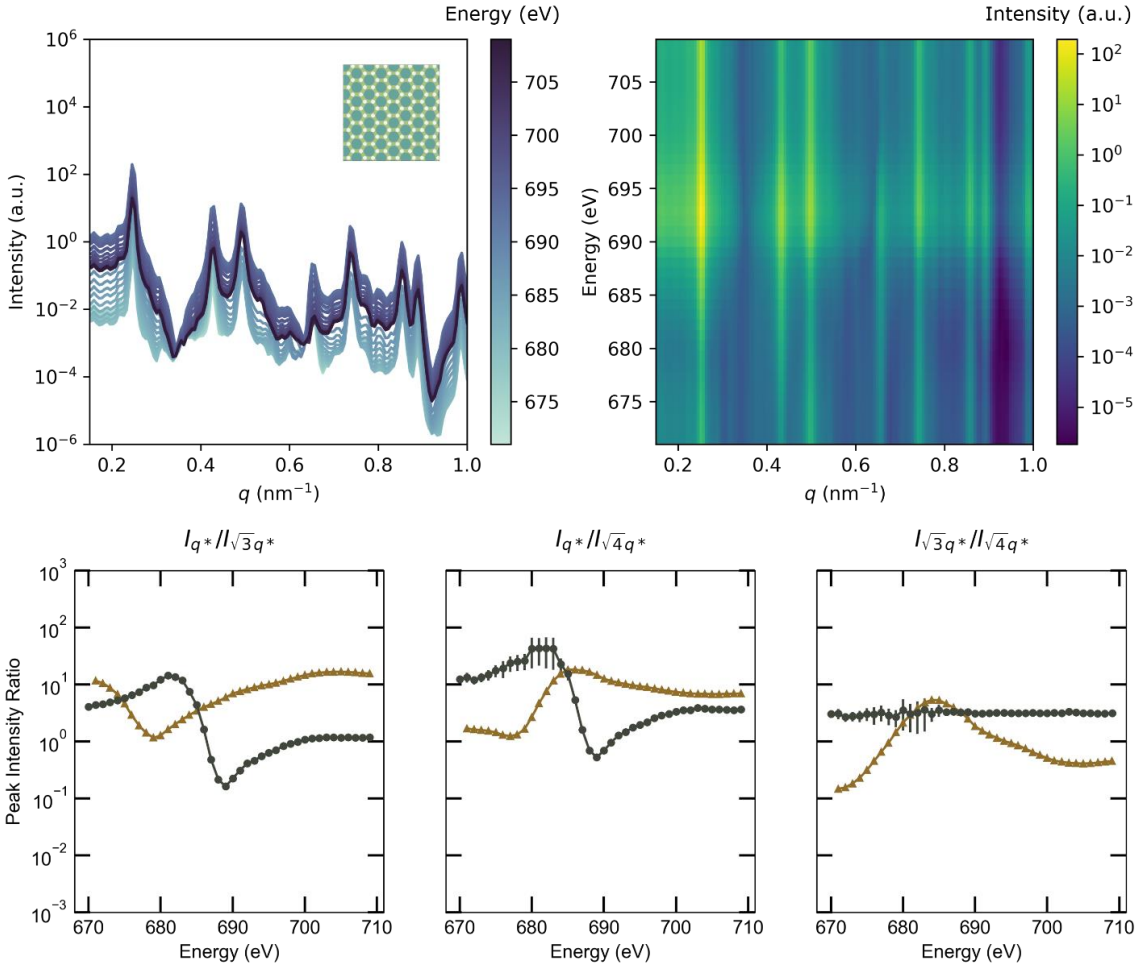

Figure D18 Scattering simulation results for NL3. *Top left*: Radially-averaged simulated RSoXS profiles at energies along the F edge (*inset*: 200 × 200 voxel subset of the model); *Top right*: intensity map of the simulated RSoXS profiles; *Bottom*: energy dependence of peak intensity ratios (dark grey circles: experiment; gold triangles: simulation).

NL4

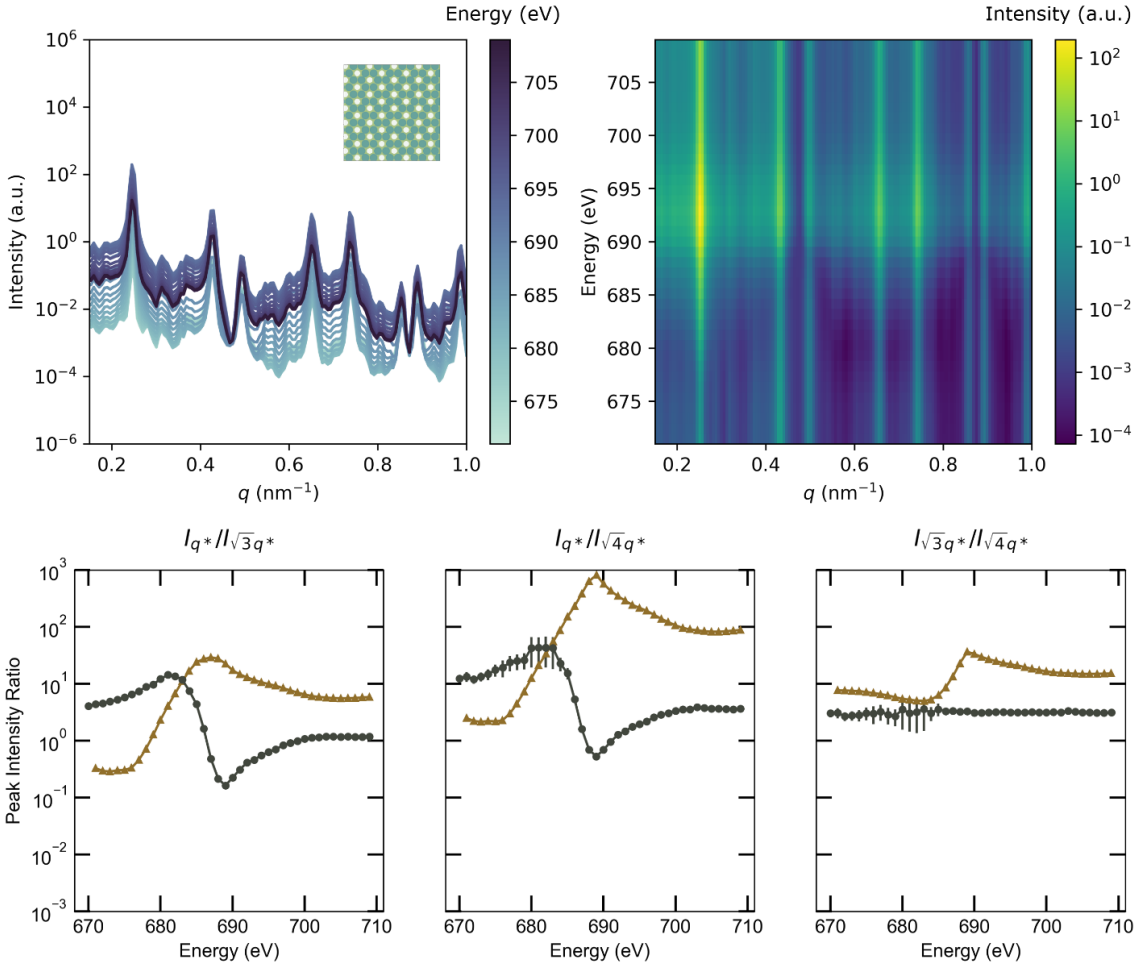

Figure D19 Scattering simulation results for NL4. *Top left*: Radially-averaged simulated RSoXS profiles at energies along the F edge (*inset*: 200 × 200 voxel subset of the model); *Top right*: intensity map of the simulated RSoXS profiles; *Bottom*: energy dependence of peak intensity ratios (dark grey circles: experiment; gold triangles: simulation).

NL5

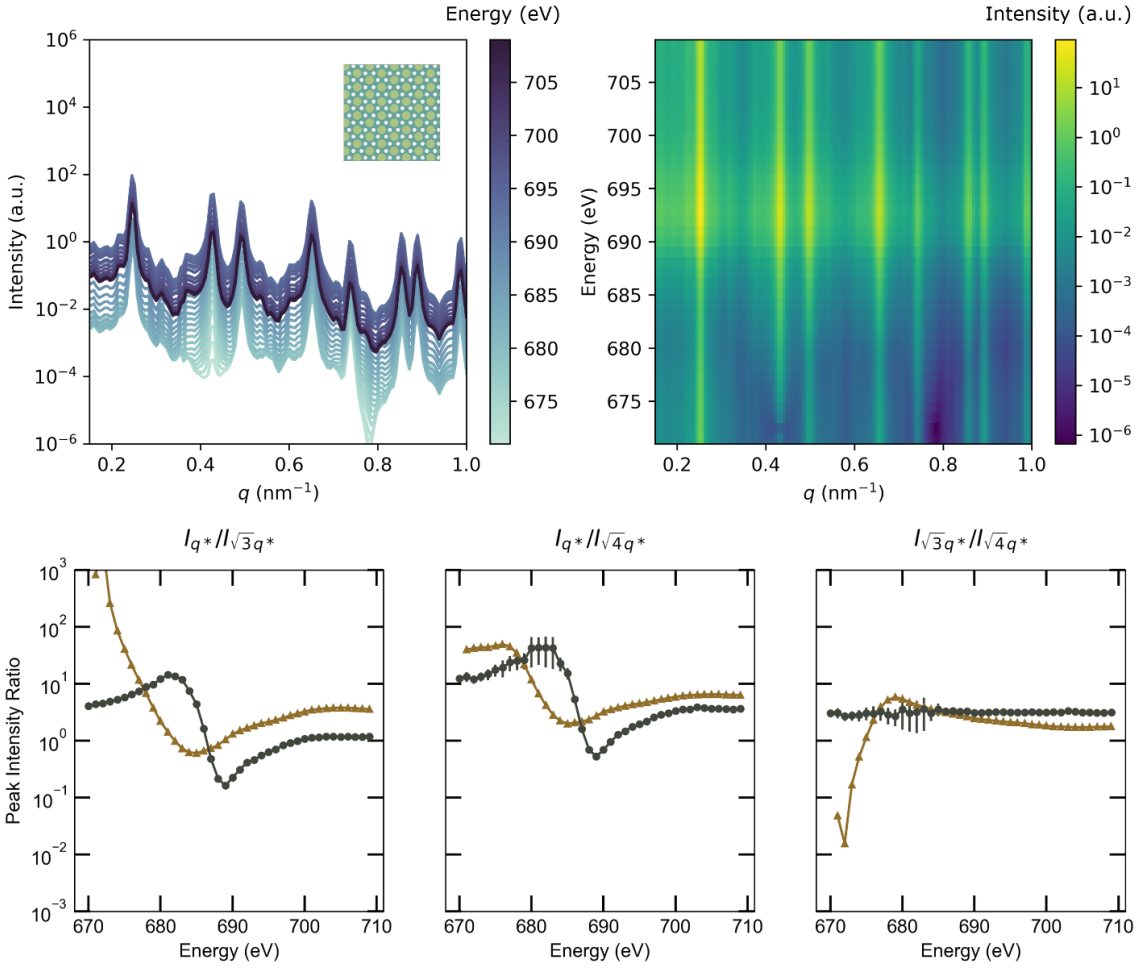

Figure D20 Scattering simulation results for NL5. *Top left*: Radially-averaged simulated RSoXS profiles at energies along the F edge (*inset*: 200 × 200 voxel subset of the model); *Top right*: intensity map of the simulated RSoXS profiles; *Bottom*: energy dependence of peak intensity ratios (dark grey circles: experiment; gold triangles: simulation).

NL6

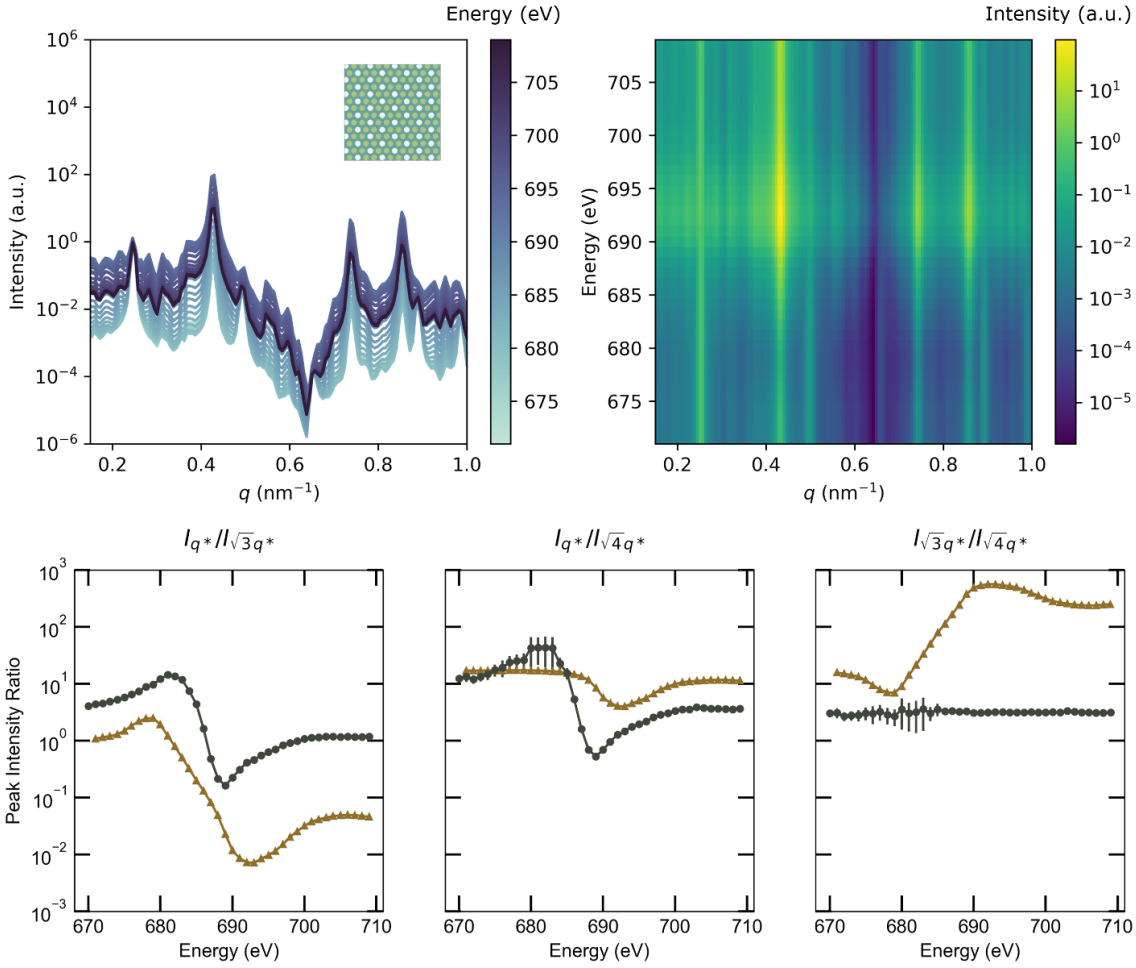

Figure D21 Scattering simulation results for NL6. *Top left*: Radially-averaged simulated RSoXS profiles at energies along the F edge (*inset*: 200 × 200 voxel subset of the model); *Top right*: intensity map of the simulated RSoXS profiles; *Bottom*: energy dependence of peak intensity ratios (dark grey circles: experiment; gold triangles: simulation).

Impact of cylinder orientation

The simulated morphologies represent cylinders oriented perpendicular to the substrate, but experimental samples may contain grains of cylinders oriented in many different directions relative to the substrate. We explored the impact of orientation by integrating the analytical expression for the particle form factor $P(q)$ of a cylinder[52] over different angular ranges. Relative to an isotropic distribution of cylinder orientations, perpendicular cylinders have a form factor which is lower in overall magnitude, higher in amplitude (difference between maximum and minimum values), and similar with respect to the locations of the minima in q-space. We expect that these differences could cause the magnitude of our simulated intensity ratios to be off relative to a typical (polycrystalline) experimental sample, but that the line shape of the ratios vs. energy will be similar.

$J_1(x)$ = first order Bessel function of the first kind

R = cylinder radius

L = cylinder length

α = angle between the cylinder axis and the scattering vector ($\alpha = \frac{\pi}{2}$ for cylinders oriented perpendicular to the substrate)

$$P(q) = \int_{\alpha_1}^{\alpha_2} \left[\frac{2 \cdot J_1(q \cdot R \cdot \sin\alpha)}{q \cdot R \cdot \sin\alpha} \cdot \frac{\sin((q \cdot L \cdot \cos\alpha)/2)}{(q \cdot L \cdot \cos\alpha)/2} \right]^2 \sin\alpha \, \mathrm{d}\alpha$$

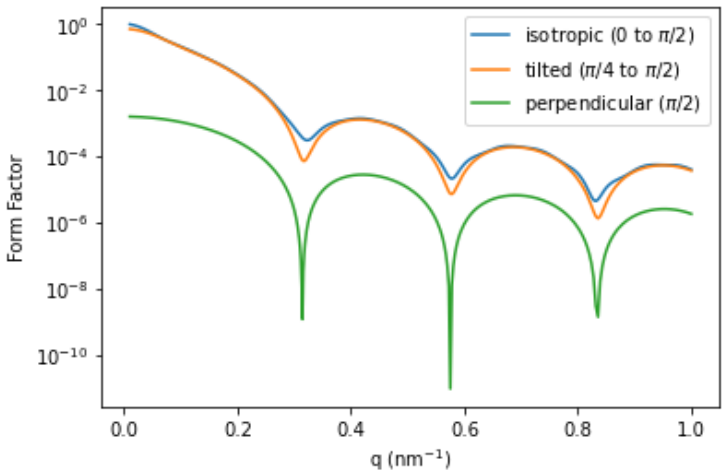

Figure D22 Calculated particle form factor for cylinders with varying orientation distributions.

5.8 References

1. Bates, C. M. & Bates, F. S. 50th anniversary perspective: Block polymers—pure potential. *Macromolecules* 50 3–22 (2017).
2. Bang, J., Jeong, U., Ryu, D. Y., Russell, T. P. & J Hawker, C. Block copolymer nanolithography: Translation of molecular level control to nanoscale patterns. *Advanced Materials* 21, 4769–4792 (2009).
3. Zhang, C. et al. Rapid Generation of Block Copolymer Libraries Using Automated Chromatographic Separation. *Journal of the American Chemical Society* 142, 9843–9849 (2020).
4. Khadilkar, M. R., Paradiso, S., Delaney, K. T. & Fredrickson, G. H. Inverse Design of Bulk Morphologies in Multiblock Polymers Using Particle Swarm Optimization. *Macromolecules* 50, 6702–6709 (2017).
5. Zhu, Y. et al. Multiblock Polyesters Demonstrating High Elasticity and Shape Memory Effects. *Macromolecules* 51, 2466–2475 (2018).
6. Tyler, C. A., Qin, J., Bates, F. S. & Morse, D. C. SCFT study of nonfrustrated ABC triblock copolymer melts. *Macromolecules* 40, 4654–4668 (2007).
7. Reddy, A., Feng, X., Thomas, E. L. & Grason, G. M. Block Copolymers beneath the Surface: Measuring and Modeling Complex Morphology at the Subdomain Scale. *Macromolecules* 54, 9223–9257 (2021).
8. Bates, F. S. et al. Multiblock Polymers: Panacea or Pandora's box? *Science* 336, 434–440 (2012).
9. Xie, N. et al. Macromolecular metallurgy of binary mesocrystals via designed multiblock terpolymers. *Journal of the American Chemical Society* 136, 2974–2977 (2014).
10. Tang, C. et al. Square packing and structural arrangement of ABC triblock copolymer spheres in thin films. *Macromolecules* 41, 4328–4339 (2008).

11. Breiner, U., Krappe, U., Abetz, V. & Stadler, R. Cylindrical morphologies in asymmetric ABC triblock copolymers. *Macromolecular Chemistry and Physics* 198, 1051–1083 (1997).
12. Balsamo, V., Collins, S. & Hamley, I. W. Nanopatterned surfaces obtained with semicrystalline ABC triblock copolymers. *Polymer* 43, 4207–4216 (2002).
13. Elbs, H. et al. Microdomain Morphology of Thin ABC Triblock Copolymer Films. *Macromolecules* 32, 1204–1211 (1999).
14. Benaglia, S., Amo, C. A. & Garcia, R. Fast, quantitative and high resolution mapping of viscoelastic properties with bimodal AFM. *Nanoscale* 11, 15289–15297 (2019).
15. Aoki, H., Kunai, Y., Ito, S., Yamada, H. & Matsushige, K. Two-dimensional phase separation of block copolymer and homopolymer blend studied by scanning near-field optical microscopy. *Applied Surface Science* 188, 534–538 (2002).
16. Fasolka, M. J. et al. Measuring Local Optical Properties: Near-Field Polarimetry of Photonic Block Copolymer Morphology. *Physical Review Letters* 90, 016107 (2003).
17. Collins, B. A. & Gann, E. Resonant soft X-ray scattering in polymer science. *Journal of Polymer Science* (2021).
18. Virgili, J. M., Tao, Y., Kortright, J. B., Balsara, N. P. & Segalman, R. A. Analysis of order formation in block copolymer thin films using resonant soft X-ray scattering. *Macromolecules* 40, 2092–2099 (2007).
19. Wang, C. et al. Defining the nanostructured morphology of triblock copolymers using resonant soft X-ray scattering. *Nano Letters* 11, 3906–3911 (2011).
20. Hamamoto, H., Takagi, H., Akiba, I. & Yamamoto, K. Analysis of Homopolymer Distribution in a Polymer Blend Thin Film by Anomalous Grazing Incidence Small-Angle X-ray Scattering at the Bromine K-Edge. *Macromolecules* 54, 488–498 (2021).
21. Wong, D. T., Wang, C., Beers, K. M., Kortright, J. B. & Balsara, N. P. Mesoporous block copolymer morphology studied by contrast-matched resonant soft X-ray scattering. *Macromolecules* 45, 9188–9195 (2012).
22. Culp, T. E. et al. Probing the Internal Microstructure of Polyamide Thin-Film Composite Membranes Using Resonant Soft X-ray Scattering. *ACS Macro Letters* 7, 927–932 (2018).
23. Freychet, G., Gann, E., Thomsen, L., Jiao, X. & McNeill, C. R. Resonant Tender X-ray Diffraction for Disclosing the Molecular Packing of Paracrystalline Conjugated Polymer Films. *Journal of the American Chemical Society* 143, 1409–1415 (2021).
24. Gann, E. et al. Origins of polarization-dependent anisotropic X-ray scattering from organic thin films. *Journal of Synchrotron Radiation* 23, 219–227 (2016).
25. Mukherjee, S. et al. Polarized X-ray scattering measures molecular orientation in polymer-grafted nanoparticles. *Nature Communications* 12, 4896 (2021).
26. Zhang, C. et al. Emergence of Hexagonally Close-Packed Spheres in Linear Block Copolymer Melts. *Journal of the American Chemical Society* 143, 14106–14114 (2021).

27. Barbon, S. M. et al. Architecture Effects in Complex Spherical Assemblies of (AB)n-Type Block Copolymers. *ACS Macro Letters* 9, 1745–1752 (2020).
28. Self, J. L. et al. Dynamic Bottlebrush Polymer Networks: Self-Healing in Super-Soft Materials. *Journal of the American Chemical Society* 142, 7567–7573 (2020).
29. Gann, E. et al. A NIST facility for resonant soft x-ray scattering measuring nano-scale soft matter structure at NSLS-II. *Journal of Physics: Condensed Matter* 33, 164001 (2020).
30. Hamley, I. & Castelletto, V. Small-Angle Scattering of Block Copolymers in Soft Matter Characterization. 1021–1081, Springer, Dordrecht (2008).
31. Hückstädt, H., Göpfert, A. & Abetz, V. Influence of the block sequence on the morphological behavior of ABC triblock copolymers. *Polymer* 41, 9089–9094 (2000).
32. Elbs, H., Drummer, C., Abetz, V. & Krausch, G. Thin film morphologies of ABC triblock copolymers prepared from solution. *Macromolecules* 35, 5570–5577 (2002).
33. Yan, H., Wang, C., McCarn, A. R. & Ade, H. Accurate and facile determination of the index of refraction of organic thin films near the carbon 1s absorption edge. *Physical Review Letters* 110, 177401 (2013).
34. Watts, B. Calculation of the Kramers-Kronig transform of X-ray spectra by a piecewise Laurent polynomial method. *Optics Express* 22, 23628–23639 (2014).
35. Henke, B. L., Gullikson, E. M. & Davis, J. C. X-ray interactions: Photoabsorption, scattering, transmission, and reflection at E = 50–30,000 eV, Z = 1–92. *Atomic Data and Nuclear Data Tables* 54, 181–342 (1993).
36. Ferron, T., Pope, M. & Collins, B. A. Spectral Analysis for Resonant Soft X-Ray Scattering Enables Measurement of Interfacial Width in 3D Organic Nanostructures. *Physical Review Letters* 119, 167801 (2017).
37. Hamley, I. W. et al. Hexagonal Mesophases between Lamellae and Cylinders in a Diblock Copolymer Melt. *Macromolecules* 26, 5959–5970 (1993).
38. International Tables for Crystallography. Kluwer Academic Publishers (1995).
39. Peterca, M. et al. Self-assembly, structural, and retrostructural analysis of dendritic dipeptide pores undergoing reversible circular to elliptical shape change. *Journal of the American Chemical Society* 128, 6713–6720 (2006).
40. Flodström, K., Teixeira, C. V., Amenitsch, H., Alfredsson, V. & Lindén, M. In situ synchrotron small-angle X-ray scattering/X-ray diffraction study of the formation of SBA-15 mesoporous silica. *Langmuir* 20, 4885–4891 (2004).
41. Impéror-Clerc, M. Three-dimensional periodic complex structures in soft matter: investigation using scattering methods. *Interface Focus* 2, 589–601 (2012).
42. De, J., Bala, I., Gupta, S. P., Pandey, U. K. & Pal, S. K. High Hole Mobility and Efficient Ambipolar Charge Transport in Heterocoronene-Based Ordered Columnar Discotics. *Journal of the American Chemical Society* 141, 18799–18805 (2019).

43. Baerlocher, C., McCusker, L. B. & Palatums, L. Charge flipping combined with histogram matching to solve complex crystal structures from powder diffraction data. *Zeitschrift für Kristallographie* 222, 47–53 (2007).
44. Balagurusamy, V. S. K., Ungar, G., Percec, V. & Johansson, G. Rational design of the first spherical supramolecular dendrimers self-organized in a novel thermotropic cubic liquid-crystalline phase and the determination of their shape by X-ray analysis. *Journal of the American Chemical Society* 119, 1539–1555 (1997).
45. Percec, V. et al. Elucidating the structure of the pm3̄n cubic phase of supramolecular dendrimers through the modification of their aliphatic to aromatic volume ratio. *Chemistry—A European Journal* 15, 8994–9004 (2009).
46. Garstecki, P. & Hołyst, R. Scattering Patterns of Multiply Continuous Cubic Phases in Block Copolymers. II. Application to Various Triply Periodic Architectures. *Macromolecules* 36, 9191–9198 (2003).
47. Watts, A., Kurokawa, N. & Hillmyer, M. A. Strong, Resilient, and Sustainable Aliphatic Polyester Thermoplastic Elastomers. *Biomacromolecules* 18, 1845–1854 (2017).
48. White, M. A., Johnson, J. A., Koberstein, J. T. & Turro, N. J. Toward the syntheses of universal ligands for metal oxide surfaces: Controlling surface functionality through click chemistry. *Journal of the American Chemical Society* 128, 11356–11357 (2007).
49. Ade, H. & Urquhart, S. NEXAFS Spectroscopy and Microscopy of Natural and Synthetic Polymers in Chemical Applications of Synchrotron Radiation Part I: Dynamics and VUV Spectroscopy. ed. Sham, T., 285–355, World Scientific Publishing Co. (2002).
50. Ilavsky, J. Nika: Software for two-dimensional data reduction. *Journal of Applied Crystallography* 45, 324–328 (2012).
51. Newville, M. & Stensitzki, T. Non-Linear Least-Squares Minimization and Curve-Fitting for Python. (2018).
52. Th. Zemb, P. Lindner, Ed. Neutrons, X-rays and Light: Scattering Methods Applied to Soft Condensed Matter. Elsevier (2002).

Chapter 6: Lessons learned

6.1 Introduction

Over the course of my research career, my appreciation of scientific progress has been paralleled by an appreciation of the methods that we use to make scientific progress. Literature review, experimental design, benchtop protocols, and custom code are important aspects of research often reported with a level of detail that does not reflect the tremendous knowledge they encompass. This chapter details some of the lessons that I learned through my research and practice of the scientific method.

6.2 Electro-mechanical testing of soft and stretchable electronics

Characterizing the behavior of soft and stretchable devices combines the challenges of electrical and mechanical measurement. It is critical to minimize electrical interference from the mechanical set-up (e.g., capacitive interference from a moving metal object) and mechanical interference from the electrical set-up (e.g., applied stress from wiring to the device). There has been some progress in the careful consideration of test design for stretchable electronics[1], but more standardized guidance is needed as the field grows. I share below some aspects of experimental design that I found to be important for the accurate measurement of device behavior:

Use hardware parameters to guide device design.

For the capacitive pressure sensor research described in Chapter 2, we designed the sensors with in-house test capabilities in mind. This was particularly important for our work with super-soft materials that have moduli beyond the limits of what is typical for conventional mechanical measurements. To simultaneously measure the change in capacitance and the applied stress, we had to keep in mind the measurement limits of two different pieces of equipment: (1) the inductance–capacitance–resistance (LCR) meter and (2) the load cell of the compression testing set-up. Additionally, the lower limit of displacement rate achievable by the motor of the compression testing set-up in combination with the maximum sampling rate of the LCR meter dictated the strain regime measurable for a given dielectric thickness. These measurement limits,

along with limitations of the quantity of material available to us, guided our selection of device geometry.

Pay close attention to interfaces.

Rough or uneven interfaces (for example, between an electrode and dielectric layer) impact both the electrical and mechanical behavior of the device. We took great care to mold and cure the dielectric elastomer layers in a way that created smooth, level faces to which the electrodes were applied. Additionally, we used a transparent and flexible conductive film (Indium Tin Oxide-coated poly(ethylene terephthalate) or ITO-coated PET, Thorlabs, Inc.) so that the elastomer–electrode interface was easily inspected. Through optimization of elastomer curing and sensor fabrication, we were able to eliminate visible gaps in elastomer–electrode contact. Interfaces are also critical when measuring materials properties such as dielectric constant using impedance spectroscopy. In this case, it may be necessary to cure the elastomer between polished electrodes to ensure an ideal interface.

Shield and ground your test environment to improve signal.

Capacitance measurements are particularly sensitive to electromagnetic interference. Capacitors can be used as proximity sensors in addition to strain/pressure sensors because the approach of an object (e.g., a human finger) will cause an increase in measured capacitance. This is a result of the approaching object modulating the fringe field of the capacitor. Proximity sensitivity is undesirable, however, during electro-mechanical testing which aims to characterize strain/pressure sensitivity in a calibrated manner (e.g., creating a sensor response curve of relative change in capacitance vs. applied pressure). To minimize interference, we found it beneficial to

add a grounded metal plate beneath the sensor, which was electrically isolated on top and bottom with dielectric spacers (the top spacer additionally distributed the applied force evenly across the sensor surface).

6.3 The compliance–conductivity trade-off

When we set out to create super-soft conductive composites with carbon nanotubes (Chapter 3), one initial question that I explored was: is there some way that a particle network could impart conductivity without increasing modulus? The brief literature summary that follows describes the origin of the compliance–conductivity trade-off for composites, with particular focus on the concept of the *bound layer*.

Polymer composites are omnipresent in modern life, from the classic example of the car tire to newer applications such as carbon fiber composite aircraft fuselages. Although composites made with nanoscale particles comprise an active field of modern research, the idea underpinning their promise has been around for almost a century. The first academic paper linking improved properties of rubber to size reduction of the particle filler (pursuing the "finest state of division") was published in 1920 by C. Olin North of the Goodyear Tire Company.[2] This report followed an industrial switch to carbon black for rubber compounding, prompted by zinc oxide shortages during World War I.[3] The rapid advances in particle size reduction processing that resulted from this switch led to the development of nanocomposites (although they were not necessarily recognized as such at the time). Carbon black is prepared through a combustion process and generally takes the form of spherical primary particles clustered in aggregates. With proper compounding and dispersion, it readily reduces to nanoscale proportions. Immense practical knowledge has been

built around composites of rubber and carbon black. Many of the concepts investigated in modern academic research were developed decades ago with industrial inspiration. One particularly interesting and important concept is that of the bound layer. The idea originated from the observation that the incorporation of carbon black imparted a degree of solvent resistance to rubber.[4] From this perspective, the bound layer was defined as polymer chains which are effectively permanently bound to the particle filler. The concept has evolved over time and is now known to play a key role in mechanical reinforcement. In the last decade, researchers have developed unprecedented understanding about the properties and impact of the bound layer, particularly as it relates to electrical and mechanical/rheological percolation.

Recent research has sought to advance understanding of the bound layer through multifaceted application of modern analytical techniques. Three primary areas of focus are 1) characterization of molecular dynamics in the bound layer, 2) accurate measurement of bound layer thickness, and 3) quantification of the impact of the bound layer on rheological transitions. Three impactful papers are highlighted below, each of which has advanced knowledge in one of these three focus areas. All three studies use the same model polymer/particle system for their experiments and analyses: poly(2-vinylpyridine) (P2VP) with silica nanoparticles. This combination is a model system due to its strongly attractive polymer/particle interaction, enabled by hydrogen bonding between the nitrogen of the pyridine ring in the P2VP and the silanol groups present on the surface of the silica nanoparticles.[5] This favorable chemical interaction enables facile dispersion of the silica nanoparticles into the polymer matrix. Additionally, silica nanoparticles can be prepared by a sol-gel process

which enables well-controlled particle growth and correspondingly high monodispersity. The collective focus on this model system has delivered a comprehensive suite of experimental data that can be analyzed holistically and comparatively.

Molecular Dynamics in the Bound Layer

Historically, the bound layer has often been described as being immobilized or frozen. This conception has been challenged and disproven in recent years. In "Dynamics at the Polymer/Nanoparticle Interface in Poly(2-vinylpyridine)/Silica Nanocomposites," Holt et al. tackled the question of bound layer dynamics by pairing glass transition measurements by temperature-modulated differential scanning calorimetry (TMDSC) with dielectric relaxation measurements by broadband dielectric spectroscopy (BDS).[6] Prior literature relied heavily on glass transition measurements to gain insights into the change or spread of molecular dynamics following nanoparticle inclusion.[6] The glass transition is commonly defined as the onset of collective segmental motion in macromolecular systems. The characteristics of a material's glass transition are directly linked to molecular mobility; of particular relevance to the investigation of the bound layer is the broadness of the transition, which is telling of the homogeneity (or heterogeneity) of segmental mobilities represented in the material. The state-of-the-art technique to measure glass transition calorimetrically is TMDSC, which applies a sinusoidal perturbation over a linear temperature ramp to deconvolute the heat capacity signal from kinetic contributions. Holt et al. measured a series of P2VP/silica nanocomposites of varying particle loadings by TMDSC and isolated the polymer component of the heat capacity through the subtraction of silica contributions.[6] Their

data demonstrate that with increased particle loading, the glass transition broadens without a decrease in glass transition strength, indicating there is no population of truly immobilized chains.[6]

Holt et al. complemented their calorimetric study with BDS, a technique which probes molecular motions through dielectric relaxation measurement.[6] The technique works by sweeping an AC input signal through a range of frequencies and collecting the complex dielectric response. Peaks in the frequency response of the imaginary component can be attributed to various polarization mechanisms, some of which can be linked to specific types of molecular motion. Relevant to the question at hand is the feature commonly known as the α peak, which is linked to segmental relaxation in polymer systems. Holt et al. showed that with increased particle loading, the α peak broadens in the low frequency regime and decreases intensity otherwise, indicating the existence of a population of slower-moving (but not immobilized) polymer segments.[6] Holt et al. fit their data with the Havriliak–Negami relaxation model (a modification of the Debye relaxation model commonly used for polymer systems) and found that two peaks are needed to achieve a good fit of the particle-filled systems, with one being attributed to the bulk polymer and the other to the bound layer.[6] From their analysis, they concluded that segmental mobility in the bound layer is approximately two orders of magnitude lower than in the polymer bulk, but not immobilized.[6]

Dimensions of the Bound Layer

A variety of techniques have been employed to measure bound layer thickness, each with its own strengths and weaknesses. X-ray scattering techniques have been used

on semi-crystalline composites with the assumption that increased amorphous content seen upon particle inclusion is representative of the bound layer.[7] Calorimetric methods have been used to quantify the mass fraction of a rigid amorphous phase (assumed to be the bound layer), with thickness extracted by assuming ideal particle dispersion and material density.[8] Yet another technique extracts thickness from a model fit to positron annihilation lifetime spectroscopy (PALS) data, with an assumption that the bound layer does not exhibit thermal expansion.[9] One of the most common methods due to experimental accessibility is based on thermogravimetric analysis (TGA), a simple technique which measures mass loss through a defined temperature ramp.[10] For systems with components of adequately different thermal stabilities (such as an organic polymer and an inorganic particle), TGA can be used to measure the mass fraction of individual components. To measure bound layer thickness with TGA, a polymer–particle composite is taken through several solvent washing steps to isolate the particles and the polymer chains securely attached to them. This material is heated in the TGA and the mass fraction of polymer is measured. To extract a bound layer thickness, a density must be assumed for the bound layer polymer. This assumption is a large source of uncertainty for the method; most often, the density of the bulk polymer is used.[10] Additionally, this technique assumes that the washing steps remove all other chains while preserving the physically or chemically attached chains.

In “Bound Polymer Layer in Nanocomposites,” Jouault et al. checked the validity of the TGA technique by comparing it with two alternative methods.[10] One of the alternative methods used is dynamic light scattering (DLS), a technique which

calculates particle size from the velocity of Brownian motion in a dilute solution environment—the velocity of particle motion scales inversely with size. This calculation employs the Stokes–Einstein relationship, extracting hydrodynamic radius from a measurement of the translational diffusion coefficient (the metric of velocity of Brownian motion) with only the temperature and solution viscosity as additional inputs. To measure bound layer thickness with DLS, a dilute solution of the particle and polymer is prepared in a theta solvent (in which the polymer chains should not be swollen relative to their conformation in the melt state).[10] The average particle size measured for this system is then compared to that of a particle-only solution and bound layer thickness is calculated by simple subtraction.[10] This technique has the advantage of averaging over many particles and does not require an assumption of density. It does, however, require the assumption that chain morphology in a dilute solution with the chosen solvent accurately represents morphology in the melt. The other alternative method was based on image analysis of transmission electron microscopy (TEM) images of the nanocomposite.[10] In this method, a correlation function is calculated from which average interparticle spacing may be extracted.[10] The authors then fit the correlation function with an interaction pair potential model based on the de Gennes model of a polymer brush on a flat surface through iterations of a Monte Carlo simulation.[10] The two parameters optimized in the fitting process represent grafting density and brush thickness, the latter of which is taken to be the bound layer thickness.[10] Although calculation of bound layer thickness by this method is relatively indirect, this is the only method presented with data from a bulk sample rather than isolated particles.

These three methods of thickness measurement were compared over a range of nanoparticle sizes.[10] The values obtained by the DLS and TEM interaction pair potential methods were in good agreement despite being measured in quite different and unrelated ways. These values were 3–5 times higher than the values obtained by the TGA method.[10] This discrepancy implies that the TGA method may underpredict bound layer thickness and therefore should be paired with or replaced by alternative techniques for accurate measurement.

Impact of the Bound Layer on Rheology

The recent developments in measuring bound layer properties have helped researchers better connect macroscale properties of interest to nanoscale morphology and behavior. Most relevant to the development of compliant conductors is the topic of rheological percolation (and the potential to alter or avoid it). Two simple extremes in composite rheological behavior would be a fully polymer-dominated response on one end (far below the percolation threshold) and a fully particle-dominated response on the other (far above the percolation threshold). Particle loading for compliant conductors should be optimized closely around the percolation threshold to achieve conductivity with minimal impact to rheological behavior. To move beyond the trade-off curve rather than optimize along it, it may prove fruitful to develop a nanoscale perspective on rheological impact through the spectrum of polymer- to particle-dominated behavior.

In "Network dynamics in nanofilled polymers," Baeza et al. examined the changes in rheological behavior of P2VP/silica nanocomposites with increasing particle loading.[5] They sought clarity regarding a long-standing question of whether

mechanical reinforcement observed in polymer nanocomposites is due to particle clusters alone or a network of particles and polymer chains.[5] Based on rheological data, the authors proposed two transition points in rheological behavior. At low nanoparticle loadings, there is a polymer-dominated response with added friction due to the polymer/particle interfaces.[5] The rheological master curves at these conditions exhibit typical viscoelastic liquid behavior with an entanglement plateau and low frequency drop-off. Within this regime, increased nanoparticle loading begins to increase the plateau modulus without affecting other features. As nanoparticle loading is increased further, the system transitions to a gel-like state with a broadened plateau region.[5] The third regime exhibits particle-dominated (permanently percolated) behavior defined by a dependence of the storage modulus on $\omega^{0.2}$, shown to be independent of molecular weight.[5] The authors worked to understand the transition points between these regimes by comparing average interparticle spacings of various loadings to polymer dimensions. They propose that the transition point for polymer-dominated to gel-like behavior is when bound layers bridge particles, which they link to the point when interparticle spacings become comparable to the entanglement tube diameter of the polymer.[5] For the transition from gel-like to particle-dominated, they propose that behavior changes when interparticle spacings are reduced to the Kuhn length of the polymer, meaning only small numbers of adsorbed Kuhn segments bridge particles.[5] These proposed transition points are a first step toward mechanistic understanding of rheological changes through the spectrum of polymer- to particle-dominated behavior.

In summary, modern understanding of the bound layer reveals the reason why mechanical/rheological percolation occurs before electrical percolation in particle–polymer composites. This indicates that in pursuit of soft conductive composites, particle loading must be carefully optimized to balance modulus and conductivity. The studies referenced above focused on spherical silica particles. There are further opportunities in studying composites prepared with high aspect ratio particles such as carbon nanotubes to investigate the impact of particle geometry on bound layer behavior. Unique interactions have been observed in carbon nanotube–polymer systems, including polymer crystallization perpendicular to nanotube surfaces and individual polymer chains wrapping around nanotubes.[11] It is interesting to consider the nature of the bound layer in systems where the particle has a similar size and aspect ratio to an individual polymer chain.

6.4 Methods for preparing polymer–particle composites

The most important aspect of composite processing is dispersion of particles in the polymer matrix. This often involves particle size reduction (e.g., breaking up carbon black agglomerates into aggregates or carbon nanotube bundles into individual nanotubes), achieved through shearing forces. In pursuit of a solid polymer–particle composite, one major decision is whether to perform dispersion processing in solution (solvent-added, lower viscosity) or bulk (solvent-free, higher viscosity). Methods for dispersion of low viscosity mixtures include rotor–stator mixing, ultrasonication, and high pressure pneumatic processing. The ability to control viscosity through solvent

addition is useful, but drawbacks include the need for a surfactant/dispersant to prevent particle reaggregation and, in the case of preparing a solid composite, the need to remove solvent after processing. Methods for dispersion of higher viscosity mixtures include centrifugal mixing, three roll milling, and twin-screw extrusion. Dispersion without solvent means the material can be used immediately after mixing and the mixture is less susceptible to reaggregation (due to limited particle mobility in the high viscosity polymer). However, this route has high sensitivity to the viscosity of the polymer/particle mixture.

Equipment availability is often a factor when choosing a dispersion method. The equipment necessary for many of the methods listed above may be more commonly found in an industrial lab than an academic one. In the shared facilities at UCSB, I found ultrasonicators and centrifugal mixers available. Ultrasonicators are common in labs which process aqueous biological samples but for this reason, are often located on the benchtop. For samples containing organic solvents, dispersion equipment must be located in an appropriately-ventilated space such as a fume hood. A cup horn sonicator configuration allows for sample processing in sealed containers but these are typically made of commodity polymers with poor solvent resistance such as polystyrene and polypropylene. Processing bulk polymer avoids the complication of finding a solvent compatible with both the polymer and dispersion equipment. The practical considerations of equipment availability and solvent compatibility led to our choice of centrifugal mixing for the work described in Chapter 3.

One challenge common to both low and high viscosity dispersion processing is heat generation. This is an inevitable byproduct of effective dispersion and care must

be taken to avoid excessive temperature rise. Thermal mitigation is particularly important for temperature-sensitive systems (e.g., a polymer that will react or degrade at elevated temperatures). For lab-scale dispersion, it is useful to have an ice bath on hand and to process in short time increments with cooling breaks in between.

6.5 Beyond scripting: developing scientific code

There are many excellent resources on scientific code development but diving into this area can nevertheless be intimidating. Below I share a handful of lessons that helped me improve the robustness and usability of my code. Word of caution: I am an amateur "scientist who codes" and my advice should be taken with a grain of salt.

Organize variables with classes.

A class defines a type of object, grouping together properties and relevant functions. I found it useful (and satisfyingly logical) to organize the inputs to my calculations using classes. For example, I might have a function for calculating the kinetic rate of a photoisomerization reaction that requires a number of inputs: sample thickness, concentration of the isomers in the sample, extinction coefficients of the isomers, quantum yields, thermal side reactions, and wavelength and irradiance of the light used in the experiment. These inputs can be conceptually grouped into 3 classes: (1) the sample (dimensions, concentrations), (2) the photoactive species (extinction coefficients, quantum yields, thermal reactions), and (3) the light source (wavelength, irradiance). The segments of code below show this implemented in Python.

```
class Sample():
      """Define a solid-state sample.
      Instance Variables:
```

```
        l (float): Sample thickness (nm)

        A_0 (float): Initial concentration of isomer A (M)

        B_0 (float): Initial concentration of isomer B (M)

    """

    def __init__(self, l: float, A_0: float, B_0: float):

        self.l = l

        self.A_0 = A_0

        self.B_0 = B_0

        self.concentration = A_0 + B_0


class Photoswitch():

    """Define the isomers involved in the photoisomerization, the
    quantum yields of the forward and reverse reactions, and
    (optionally) associated thermal reactions.

    Instance Variables:

        label_A (str): Label of isomer A

        epsilon_A (float): Extinction coefficient of isomer A (M^-1
        cm^-1)

        label_B (str): Label of isomer B

        epsilon_B (float): Extinction coefficient of isomer B (M^-1
        cm^-1)

        phiForward (float): Initial guess for the quantum yield of the
        forward reaction (between 0-1)

        phiReverse (float): Initial guess for the quantum yield of the
        reverse reaction (between 0-1)

    """

    def __init__(self, label_A: str, epsilon_A: float, label_B: str,
    epsilon_B: float, phiForward: float, phiReverse: float):

        self.label_A = label_A

        self.epsilon_A = epsilon_A

        self.label_B = label_B

        self.epsilon_B = epsilon_B

        self.phiForward = phiForward

        self.phiReverse = phiReverse

        self.thermalrxns = []
```

```
        def addThermalRxn(self, direction: str, order: int, k: float):
        """ Add thermal reactions that accompany the photoisomerization.
        Each thermal reaction is defined by a list with the structure:
        [direction, order, k]
        Inputs:
              direction (str): Direction of the thermal reaction: 'forward'
              or 'reverse'
              order (int): Order of the thermal reaction (options: 0, 1, 2)
              k (float): Rate constant of the thermal reaction
        """
        if direction == 'forward':
              sign = 1
        elif direction == 'reverse':
              sign = -1
        self.thermalrxns.append([sign, order, k])


class Light():
        """Define a light source.
        Instance Variables:
              wavelength (float): Wavelength of the light source (nm)
              irradiance (float): Irradiance of the light source (mW/cm^2)
        """
        def __init__(self, wavelength: float, irradiance: float):
              self.wavelength = wavelength
              self.irradiance = irradiance
              h = 6.62607015E-34 # J s
              c = 299792458 # m/s
              # Calculate photon flux in photons / s cm^2
              self.flux = self.irradiance * (1/1000) * ((self.wavelength *
              (10**-9)) / (h*c))
              # Calculate the photon energy in J / photon
              self.photonEnergy = (h*c)/(self.wavelength*(10**-9))
```

These three objects can then be combined to create a model:

```
class Model():
      """Contains the parameters necessary to model a photoisomerization
      reaction in the solid state.
      Instance Variables:
            description (string): Label of the experiment
            light (Light)
            photoswitch (Photoswitch)
            sample (Sample)
      """
      def inputParameters(self, description, light: Light, photoswitch:
      Photoswitch, sample: Sample):
            self.description = description
            self.light = light
            self.photoswitch = photoswitch
            self.sample = sample
```

With this framework, it is simple to create a model object through scripting. Streamlining model creation is useful when running sets of calculations in an interactive computing environment like a Jupyter Notebook.

```
light = Light(wavelength = 300, irradiance = 0.6)
photoswitch = Photoswitch(label_A = 'Open Form', epsilon_A = 23394,
label_B = 'Closed Form', epsilon_B = 19731, phiForward = 0.42, phiReverse
= 0.28)
photoswitch.addThermalRxn(direction = 'reverse', order = 2, k = 0.0015465)
sample = Sample(l = 550, A_0 = 0.58081, B_0 = 0)
model = Model()
model.inputParameters(description = 'Test', light = light, photoswitch =
photoswitch, sample = sample)
```

Organizing variables using classes makes it straightforward to run automated "virtual experiments" mapping large parameter spaces, which can be defined within

or beyond experimental confines. For example, you might want to maximize your reaction rate by changing the wavelength of your light source. You could ask two different questions:

(1) I have 3 light sources available to me in the lab (365 nm, 405 nm, and 625 nm)—which will achieve the fastest reaction rate?
(2) Which wavelength in the range of 200–700 nm using 1 nm increments will achieve the fastest reaction rate?

The first question seeks to optimize rate among a set of experimentally-accessible light sources while the second question seeks to optimize rate with no experimental bounds. These two sets of light source objects can be defined independent of each other and used to compare the two scenarios.

Write functions with troubleshooting in mind.

When creating a function that performs a lengthy calculation, it is useful to make a pen & paper plan first. Unit mistakes are easy to make. I found it convenient to implement unit conversions as-needed to simplify input and output (e.g., you have an equation using light irradiance in W/m^2 but the power meter used in lab for measuring irradiance outputs the value in mW/cm^2 – convert the units in-function rather than making the user convert their units each time). For a multi-step calculation, there is a trade-off between minimizing memory use and maximizing accessibility of intermediate values in the calculation for troubleshooting. This same issue manifests as a trade-off between minimizing lines of code and maximizing code readability. In cases where memory is not an issue, I prefer to err on the side of maximum data accessibility and code readability.

I share an example function below that calculates the concentration profile of a photoisomerization reaction occurring in a solid-state sample over time and depth using a finite difference method according to the following equations[12]:

E_e = irradiance of the light source (mW/cm^2)

λ = wavelength of the light source (nm)

Φ_t = transmitted flux ($photons/s \cdot cm^2$)

Φ_i = incident flux ($photons/s \cdot cm^2$)

Φ_a = absorbed flux ($photons/s \cdot cm^2$)

dz = layer thickness (m)

ε_A = extinction coefficient of the A isomer ($1/M \cdot cm$)

$[A]$ = concentration of the A isomer (M)

ε_B = extinction coefficient of the B isomer ($1/M \cdot cm$)

$[B]$ = concentration of the B isomer (M)

$I_{incident}$ = incident irradiation ($einsteins/s \cdot cm^2$)

F = photokinetic factor ($einsteins/s \cdot cm^2$)

I_A = amount of irradiation absorbed by species A ($einsteins/s \cdot dm^2$ [=] M/s)

I_B = amount of irradiation absorbed by species A ($einsteins/s \cdot dm^2$ [=] M/s)

$k_i^{reverse}$ = list of reverse (B→A) reaction rate constants

x_i = list of reverse (B→A) reaction orders (0, 1, or 2)

$k_i^{forward}$ = list of forward (A→B) reaction rate constants

y_i = list of forward (A→B) reaction orders (0, 1, or 2)

$\frac{d[B]}{dt}$ = reaction rate (M/s)

$$\Phi_i(z=0) = E_e \cdot \frac{1\ W}{1000\ mW} \cdot \frac{\lambda \cdot 10^{-9}}{hc}$$

$$\Phi_t = \frac{\Phi_i}{10^{dz \cdot 100 \cdot (\varepsilon_A \cdot [A] + \varepsilon_B \cdot [B])}}$$

$$\Phi_a = \Phi_i - \Phi_t$$

$$I_{incident} = \Phi_t \cdot \frac{1}{N_A}$$

$$E = dz \cdot 100 \cdot (\varepsilon_A \cdot [A] + \varepsilon_B \cdot [B])$$

$$F = I_{incident} \cdot \frac{1 - 10^{-E}}{E}$$

$$I_A = F \cdot [A] \cdot \varepsilon_A \cdot \frac{1000\ cm^3}{1\ dm^3}$$

$$I_B = F \cdot [B] \cdot \varepsilon_B \cdot \frac{1000\ cm^3}{1\ dm^3}$$

$$\frac{d[B]}{dt} = \phi_{forward} \cdot I_A - \phi_{reverse} \cdot I_B - \sum_{i=1}^{n} k_i^{reverse} \cdot [B]^{x_i} + \sum_{i=1}^{m} k_i^{forward} \cdot [A]^{y_i}$$

$$[B](t) = [B](t-1) + \frac{d[B]}{dt}(t) \cdot dt$$

```
def calculateConcentrationProfile(*, t: List[float] = None, z: List[float]
= None, A_0: float = None, B_0: float = None, flux_0: float = None,
epsilon_A: float = None, epsilon_B: float = None, phiForward: float =
None, phiReverse: float = None, thermalrxns: List[List[float]] = None):

      """Calculate the concentration profile using a finite difference
      method. Note: np = NumPy

      t (List[float]): time mesh in seconds, list of time points at which
      to evaluate the concentration profile; must include t = 0

      z (List[float]): depth mesh in meters, list of depth points at which
      to evaluate the concentration profile; must include z = 0 (which
      corresponds to the sample surface) and be evenly spaced

      A_0 (float): Initial concentration of isomer A (M)

      B_0 (float): Initial concentration of isomer B (M)

      flux_0 (float): Incident photon flux in photons / s cm^2

      epsilon_A (float): Extinction coefficient of isomer A (M^-1 cm^-1)

      epsilon_B (float): Extinction coefficient of isomer B (M^-1 cm^-1)

      phiForward (float): Quantum yield, forward reaction (between 0-1)

      phiReverse (float): Quantum yield, reverse reaction (between 0-1)

      thermalrxns (List[List[float]]): List of thermal reactions, each
      defined as [sign, order, k]

      """

      dz = z[1]
```

```
A_tz = A_0*np.ones((len(t), len(z)))

B_tz = B_0*np.ones((len(t), len(z)))

concentration = A_0 + B_0

def calculateFluxProfile(A_z, B_z, flux_0, epsilon_A, epsilon_B):

      """Given a depth-dependent concentration profile at a single
      point in time, calculate the incident, transmitted, and
      absorbed photon flux for each layer."""

      # Pre-allocate arrays to contain the results

      flux_i_z = np.zeros(len(z))

      flux_t_z = np.zeros(len(z))

      flux_a_z = np.zeros(len(z))

      # Initialize the flux arrays at the surface (z = 0)

      flux_i_z[0] = flux_0

      flux_t_z[0] = flux_0

      flux_a_z[0] = 0

      for i in range(1, len(z)):

            # The incident flux of the current slice = the
            transmitted flux of the last slice

            flux_i_z[i] = flux_t_z[i-1]

            flux_t_z[i] = flux_i_z[i] / (10**(dz * 100 * ((epsilon_A
            * A_z[i]) + (epsilon_B * B_z[i]))))

            flux_a_z[i] = flux_i_z[i] - flux_t_z[i]

            return flux_i_z, flux_t_z, flux_a_z

flux_i_tz = np.zeros((len(t), len(z)))

flux_t_tz = np.zeros((len(t), len(z)))

flux_a_tz = np.zeros((len(t), len(z)))

# Initialize the fluxes for time = 0 in photons / (s * cm^2)

flux_i_tz[0,:], flux_t_tz[0,:], flux_a_tz[0,:] =
calculateFluxProfile(A_tz[0,:], B_tz[0,:], flux_0, epsilon_A,
epsilon_B)

# Calculate the concentration profile over the depth of the sample
at each timepoint

for i in range(1, len(t)):

      # I_incident is the incident irradiation in einsteins / (s *
      cm^2)

      I_incident = flux_i_tz[i-1,:] * (1/6.02214076E23)
```

```
        # F is the photokinetic factor in einsteins / (s * cm^2)

        E = dz * 100 * (epsilon_A * A_tz[i-1,:] + epsilon_B * B_tz[i-
        1,:])

        F = I_incident * (1 - (10**-E)) / E

        # I_A and I_B are the amounts of irradiation absorbed by the
        species A and B respectively

        # The units are einsteins / (s * dm^3) [=] M/s

        I_A = 1000 * epsilon_A * A_tz[i-1,:] * F

        I_B = 1000 * epsilon_B * B_tz[i-1,:] * F

        # The rate d[B]/dt is in M/s

        # The rate is defined by the state at the previous timepoint

        rate = phiForward*I_A - phiReverse*I_B

        # Add in the thermal reactions

        for thermalrxn in thermalrxns:

        if thermalrxn[0] == -1:

              rate += thermalrxn[0]*thermalrxn[2]*((B_tz[i-
              1,:]**thermalrxn[1]))

        elif thermalrxn[0] == 1:

              rate += thermalrxn[0]*thermalrxn[2]*((A_tz[i-
              1,:]**thermalrxn[1]))

        # The concentration profiles are defined at the current
        timepoint

        B_tz[i,:] = np.add(B_tz[i-1,:], rate[:]*(t[i]-t[i-1]))

        A_tz[i,:] = concentration - B_tz[i,:]

        # The fluxes at the current timepoint are calculated using the
        concentration profiles

        flux_i_tz[i,:], flux_t_tz[i,:], flux_a_tz[i,:] =
        calculateFluxProfile(A_tz[i,:], B_tz[i,:], flux_0, epsilon_A,
        epsilon_B)

# Convert concentration of B to molar fraction of B

B_molFraction_tz = B_tz / concentration

# Calculate the average molar fraction of B over the entire sample
thickness for comparison to experimental data

B_molFractionAvg_t = np.average(B_molFraction_tz, 1)

# The returned data removes z = 0 which was used to define the
surface state for ease of computation

return t, z[1:], flux_i_tz[:,1:], flux_t_tz[:,1:], flux_a_tz[:,1:],
A_tz[:,1:], B_tz[:,1:], B_molFraction_tz[:,1:], B_molFractionAvg_t
```

This function stores and returns many intermediate values. Some are redundant but I found that sometimes this is practical when creating code that will be used interactively. Figure 6.1 shows a visualization of the concentration profiles calculated by the function above for an example model:

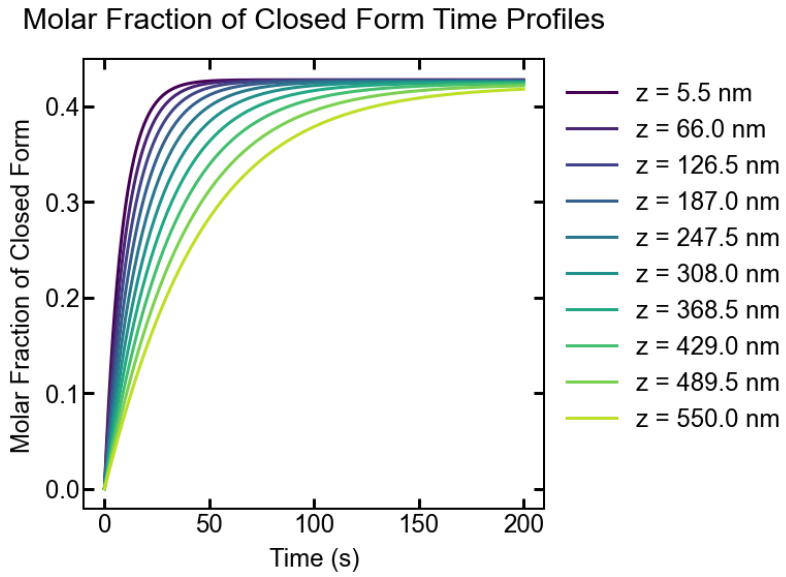

Figure 6.1 Molar fraction of the closed form (isomer B) over time at varying depths.

Avoid repeating code to the greatest extent possible.

If you start copying and pasting code, a single change needs to be replicated in many places. I found the best way to avoid this is to write every bit of code that could be reusable as a function. The function shown above was structured to enable (1) straightforward calculation of concentration profiles given a model (Figure 6.1) and (2) iterative calculation of the depth-averaged concentration profile for use in a secondary function which applies a least-squares fitting method to refine model parameters (e.g., quantum yields) against experimental data (Figure 6.2).

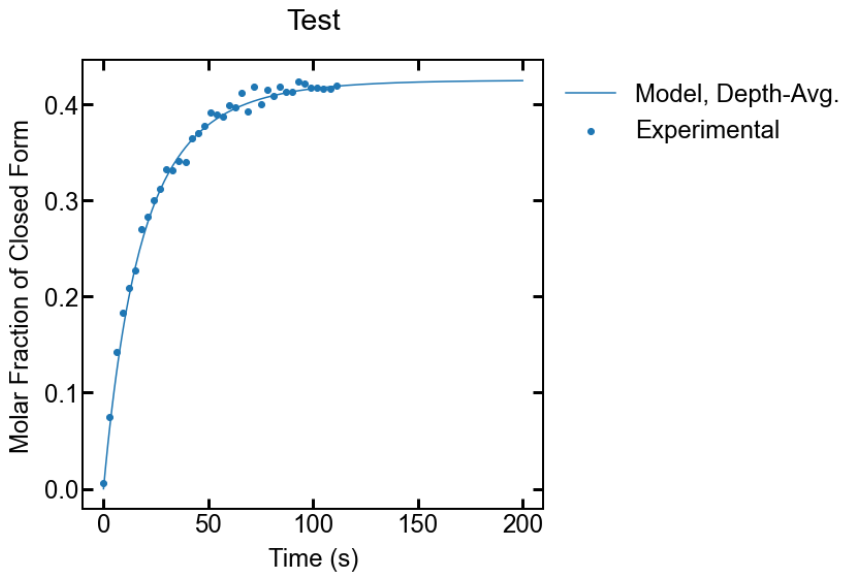

Figure 6.2 Depth-averaged molar fraction over time of a refined model plotted against experimental data. By structuring the inputs of the function appropriately, the code implementing the calculation did not need to be repeated to use within a fitting function.

Optimize only as-needed.

It is a good idea to understand how the time and space required to run your function will scale with input size (called time and space complexity, often described using Big O notation). However, if you are able to answer your scientific question using the code at-hand (unoptimized) then optimizing the code is not necessary.

6.6 References

1. Klein, S. A. et al. Mechanical testing for stretchable electronics. *ASME International Mechanical Engineering Congress and Exposition Proceedings* 10, 80–83 (2016).
2. North, C. O. The Effect of Compounding Ingredients on the Physical Properties of Rubber. *Rubber Age Tire News* 7, 461–465 (1920).
3. Goodyear Corporate History. https://corporate.goodyear.com/en-US/about/history.html. Accessed 2018.
4. Dannenberg, E. M. Bound Rubber and Carbon Black Reinforcement. *Rubber Chemistry and Technology* 59, 512–524 (1986).
5. Baeza, G. P. et al. Network dynamics in nanofilled polymers. *Nature Communications* 7, 11368 (2016).

6. Holt, A. P. et al. Dynamics at the polymer/nanoparticle interface in poly(2-vinylpyridine)/silica nanocomposites. *Macromolecules* 47, 1837–1843 (2014).
7. Chen, L. et al. Double glass transitions and interfacial immobilized layer in in-situ-synthesized polyvinyl alcohol/silica nanocomposites. *Macromolecules* 43, 1076–1082 (2010).
8. Sargsyan, A., Tonoyan, A., Davtyan, S. & Schick, C. The amount of immobilized polymer in PMMA SiO2 nanocomposites determined from calorimetric data. *European Polymer Journal* 43, 3113–3127 (2007).
9. Harton, S. E. et al. Immobilized polymer layers on spherical nanoparticles. *Macromolecules* 43, 3415–3421 (2010).
10. Jouault, N. et al. Bound polymer layer in nanocomposites. *ACS Macro Letters* 2, 371–374 (2013).
11. Grady, B. P. Effects of carbon nanotubes on polymer physics. *Journal of Polymer Science, Part B: Polymer Physics* 50, 591–623 (2012).
12. Mauser, H. and Gauglitz, G. Photokinetics: Theoretical Fundamentals and Applications. Elsevier (1998).

Chapter 7: Conclusion

In summary, this Dissertation demonstrates the value of application-driven materials development for soft and stretchable electronics, guided by electro-mechanical modeling. The macromolecular chemistries and architectures accessible through modern synthetic chemistry are a rich resource for scientists and engineers engaged in applied research. Electro-mechanical modeling is a guiding force for intelligent materials selection and materials-aware device design.

Chapter 2 described a new class of capacitive pressure sensors prepared with bottlebrush elastomers, which have extremely low moduli that enable high sensitivity. The approach of using inherently super-soft elastomers is a valuable alternative to approaches using air–elastomer composites (micropatterned or microporous layers) made with conventional elastomers. Benefits of sensors prepared with bottlebrush

elastomers include simple processing, tolerance to changes in relative humidity or liquid submersion, and sensitivity enhancement over a large pressure range. This work showed how novel materials can enhance device performance through an understanding of device physics and materials mechanics.

Chapter 3 detailed methods for making super-soft conductive composites through the dispersion of carbon nanotubes in a bottlebrush elastomer matrix. Despite an inevitable increase in modulus inherent to percolated particle networks, the resulting composites made with this approach have lower moduli than are accessible using conventional linear polymers due to the super-soft nature of bottlebrush elastomers. The network chemistry enabled solvent-free dispersion processing (via a "temporary plasticizer" which reduced viscosity during processing but was subsequently incorporated into the network), efficient thermal crosslinking, and thermal reprocessability.

Chapter 4 introduced an electro-mechanical model for the behavior of elastic thin film transistors and electrochemical transistors. In this theoretical framework, we applied the equations of rubber elasticity to the gradual channel model for transistor behavior. We found that deformation mode is predicted to have a dramatic impact on the relative stability of a transistor being deformed. In the analysis of a complementary inverter formed by stretchable transistors, we found that organic electrochemical transistors may provide a stability advantage over thin film transistors. This model can be used to identify targets for new materials development and guide circuit design based on materials behavior.

Chapter 5 described a new workflow for studying block copolymer microstructure using resonant soft X-ray scattering, guided by scattering simulations. Block copolymers are an important class of materials with applications including 3D-printable and thermoplastic elastomers. Block copolymers with 3 or more blocks (e.g., ABC triblock terpolymers) can form complex microstructures that can be difficult to identify using conventional techniques but are intimately linked to material properties. Resonant soft X-ray scattering, which probes structure with chemical sensitivity, can be used to investigate the fine domain structure of block copolymers. Our simulation-guided approach to extracting block copolymer microstructure from resonant soft X-ray scattering data can help build process–structure–property relationships for these self-assembled systems.

The work summarized in this Dissertation showed the utility of application-driven materials development and there remains tremendous opportunity in further development of new materials for stretchable electronics. As synthetic chemists continue to access novel macromolecular designs, materials scientists will have a critical role to play in characterizing the unique properties of new materials and developing methods for processing them. There are additional opportunities for applied scientists and engineers to use prototyping and device modeling to highlight materials needs in the field.

One interesting area of development is 3D-printable materials for stretchable electronics. Additive manufacturing enables rapid design iteration for prototyping and personalized manufacturing (e.g., a wearable device or medical implant tailored to an individual). Our team has recently demonstrated that bottlebrush block copolymers

which exhibit yield-stress behavior can be 3D printed via direct ink writing.[1] Further development of 3D-printable materials with a variety of electrical and mechanical properties will enable flexibility and speed in trialing new device configurations. Another opportunity lies in the use of high-throughput characterization and computation to identify materials candidates for challenging applications like stretchable electronics that demand unique combinations of materials properties. Modern materials research leads to the generation of a large volume of data, but it is not typically organized and shared in a way that allows for it to be used collectively. The growing field of materials informatics, bolstered by recent advances in machine learning, has the potential to enable targeted materials design using data-driven predictions.[2]

As the community continues to develop new materials and models for stretchable electronics, there will be growing opportunities in the commercialization of these devices for medical and consumer electronics applications. The technologies that inspire work in this field not only hold promise for the advancement of society but also bring to light interesting materials challenges that will push the boundaries of materials properties to the benefit of many research areas.

7.1 References

1. Xie, R. et al. Room temperature 3D printing of super-soft and solvent-free elastomers. *Science Advances* 6, eabc6900 (2020).
2. Ramprasad, R., Batra, R., Pilania, G., Mannodi-Kanakkithodi, A. & Kim, C. Machine learning in materials informatics: recent applications and prospects. *npj Computational Materials* 3, 54 (2017).